



Contents lists available at ScienceDirect

Progress in Materials Science

journal homepage: www.elsevier.com/locate/pmatsci

Shear localization in metallic materials at high strain rates

Na Yan^a, Zezhou Li^b, Yongbo Xu^c, Marc A. Meyers^{b,*}^a School of Physical Science and Technology, Northwestern Polytechnical University, Xi'an 710072, China^b Departments of Nanoengineering and Mechanical and Aerospace Engineering, University of California, San Diego, CA 92093-0411, USA^c Shenyang National Laboratory for Materials Science, Institute of Metal Research, Chinese Academy of Sciences, Shenyang 110016, China

A B S T R A C T

Three factors govern adiabatic shear localization: strain hardening (or softening), strain-rate hardening, and thermal softening. It is typically associated with large shear strains (>1), high strain rates (10^3 – 10^7 s⁻¹), and high temperatures (40–100% of melting point), all of which happen within narrow regions with widths of about 1–200 μ m.

It is often an undesirable phenomenon, leading to failure, but there are situations where it is desirable, e. g., the generation of machining chips. Here, we review the development of both theoretical and experimental achievements, from the initiation of shear bands to their propagation with emphasis on three aspects: novel experimental techniques, novel materials, and nano/microstructural effects. The principal characteristics of adiabatic shear bands in metallic materials at the nano- and micro-scale are described. Bands that were formerly identified as transformed actually consist of nanocrystalline/ultrafine grains. These grains result from the breakup of the microstructure by a rotational recrystallization process.

The evolution of the microstructure inside shear bands and their interactions for hcp, bcc, and fcc alloys, high-entropy alloys, nanocrystalline alloys, and metallic glasses are analyzed mechanistically.

The gaps in the field and opportunities for future research are identified. Modern experimental characterization and computational techniques enable a more profound and predictive understanding of adiabatic shear localization and its avoidance in advanced materials.

1. Introduction

Elastic deformation is constrained by the geometry of the material and applied tractions; it is homogeneous in simple geometries when wave-propagation effects are absent. As elasticity gives way to permanent deformation, inhomogeneities gradually develop in the accumulated strain and thermal excursion and will generate spatial differences in the evolution of the strengthening or softening. Thus, deformation localizes. One prominent way by which localization takes place is by the formation of two-dimensional interfacial regions. These are commonly referred to as shear bands, since they have a particular 'banded' appearance when observed in a two-dimensional section. The gradient of deformation in these regions often leads to the accumulation of damage (in brittle materials) or to a decrease in the flow stress (in ductile materials) leading to further concentration of deformation. This most often leads to shear failure, a most important mechanism of fracture. If the body containing a weakened region is exposed to tension, tensile failure by the nucleation and growth of voids in the softened region may occur.

There are special circumstances and materials that do not undergo shear localization, and this leads to extraordinarily high tensile ductility. This is usually induced by high work hardening rate or strain-rate sensitivity. Typical examples are covalent and metallic glasses, at higher temperatures, where the viscosity is sufficiently low (10^{-4} Pa.s). The strain-rate sensitivity, m , defined as $\frac{d \ln \dot{\epsilon}}{d \ln \dot{\gamma}}$, is in the range 0.5–1. A number of alloys also exhibit this behavior at prescribed regimes of temperature and strain rates, and this phenomenon is known as superplasticity. The latter is enabled by a small grain size, in which grain-boundary sliding is the dominating mechanism of

* Corresponding author.

E-mail address: mameyers@eng.ucsd.edu (M.A. Meyers).

<https://doi.org/10.1016/j.pmatsci.2020.100755>

Received 28 January 2020; Received in revised form 27 September 2020; Accepted 8 October 2020

Available online 24 November 2020

0079-6425/© 2020 Published by Elsevier Ltd.

Nomenclature

σ	normal stress
σ_0	initial flow stress
ε	strain
$\dot{\varepsilon}$	strain rate
$\dot{\varepsilon}_0$	reference strain rate
τ	shear stress
γ	shear strain
$\dot{\gamma}$	shear strain rate
T	temperature
T_0	initial absolute temperature
ρ	material density
C_v	specific heat at constant volume
C_p	specific heat at constant pressure
n	strain-hardening exponent
m	strain-rate sensitivity
β	rate of conversion of deformation energy into heat (Taylor-Quinney factor)
k	wave number for the initial perturbation
λ	thermal conductivity
κ	thermal diffusivity
h	thermal softening coefficient
\bar{t}	characteristic time for the complete nucleation
t_{cr}	critical time at which complete shielding effect occurs
Q	activation energy for diffusion
D	diffusion coefficient
γ_{GB}	grain-boundary energy
D_B^V	vacancy diffusion coefficient in the grain boundary
D_{B_0}	grain-boundary diffusion coefficient
Ω	atomic volume
Q_B	activation energy for grain boundary diffusion
μ	shear modulus
δ	shear band thickness
v	motion velocity of grain boundary
ρ_m	mobile dislocation density
R	gas constant
k_B	Boltzmann constant

deformation.

A simple approach to the mechanics of shear-band formation is to consider the shear stress, τ , to be a function of shear strain, γ , shear strain rate, $\dot{\gamma}$, and temperature, T [1]:

$$\tau = f(\gamma, \dot{\gamma}, T) \quad (1)$$

The change in shear stress, $d\tau$, can be expressed in terms of partial derivatives [2]:

$$d\tau = \left(\frac{\partial \tau}{\partial \gamma} \right)_{\dot{\gamma}, T} d\gamma + \left(\frac{\partial \tau}{\partial \dot{\gamma}} \right)_{\gamma, T} d\dot{\gamma} + \left(\frac{\partial \tau}{\partial T} \right)_{\gamma, \dot{\gamma}} dT \quad (2)$$

The three partials represent work hardening (or softening), strain-rate sensitivity, and thermal softening (or, in rare cases, hardening). These effects establish whether $d\tau$ is positive or negative. If $d\tau$ is positive, deformation is homogeneous. However, if $d\tau < 0$, instability will take place. This will lead to, eventually, localization. The difference between these two terms will be discussed later, in Section 3.1 and Fig. 4.

The first term, work hardening, in general decreases with strain for metals. The absence of work hardening (work softening) leads to localization. Such is the case of nanocrystalline metals, which have very limited ductility; therefore, deformation readily localizes into bands in compression. There are also other situations where work softening is observed, especially when the existing dislocation substructure is unstable and collapses, upon deformation. This occurs when some metals are first deformed at low temperature and then at a higher one [3]. It has also been observed in shock loaded nickel when it is subsequently deformed quasistatically [4].

The second term represents the effect of strain rate. If the strain-rate sensitivity is high, localization is inhibited, and the material can experience large strains in stable fashion. This is the case of superplasticity.

The third term represents thermal softening. In quasistatic deformation, where the heat extraction rate is equal to the heat

generation rate, the temperature can be considered constant and this term disappears. However, as the strain rate increases, a smaller and smaller fraction of the heat is extracted, leading to an increased temperature and associated softening. At sufficiently high rates of deformation, the extracted heat can be neglected, and one has an adiabatic condition. This is the reason why shear bands occurring in this regime are called adiabatic. There are very rare cases of thermal hardening; dynamic strain aging of steels, which is briefly described in Section 11.7, is one such case [5,6]. There is another situation, in which the rate controlling mechanism for plastic flow is no longer the thermal activated overcoming of short-range obstacles by dislocations, but viscous drag. Zaretsky and Kanel [7] conducted shock loading experiments on silver between 10^4 and 10^7 s $^{-1}$ and observed an increase in flow stress with temperature (through the evaluation of the elastic precursor) that became more intense as the temperature approached the melting point. Calculations by El Ters and Shehadeh [8] on shock loading of BCC iron using multiscale dislocation dynamics simulations into which molecular dynamics were injected, predicted an increase in flow stress with temperature, whereas at low strain rates this effect was reversed. Austin [459] developed a dislocation-based model of high-rate metal plasticity and found the temperature-dependence of elastic/plastic wave structure, which is consistent with experimental measurements of evolving wave profiles at 300–933 K in shock-compressed aluminum. Hence, thermal hardening can affect the formation of shear bands under extreme conditions. This effect has hereto not been investigated and deserves attention.

The formation of shear bands is more prevalent at high strain rates than in conventional, low strain rate deformation, because the thermal softening term becomes increasingly important. The condition for instability is $d\tau/d\gamma = 0$. If the experiment is conducted at a constant strain rate, $\dot{\gamma}$, that is, $d\dot{\gamma} = 0$, Eq. (2) is reduced to the following, after dividing the terms by $d\gamma$ and rearranging terms :

$$\left(\frac{\partial\tau}{\partial\gamma}\right)_T = - \left(\frac{\partial\tau}{\partial T}\right)_\gamma \frac{dT}{d\gamma} \quad (3)$$

The decrease in stress with strain, at constant temperature, is determined by thermal softening and by the generation of heat from the plastic strain. These bands are a precursor to failure and therefore their study has been pursued extensively. The yearly number of papers published on this subject over the past 5 years is around 100, without any marked change, as presented in Fig. 1 (a). The number of citations from web of science has increased remarkably during recent 20 years as is demonstrated in Fig. 1 (b). Since the concept was

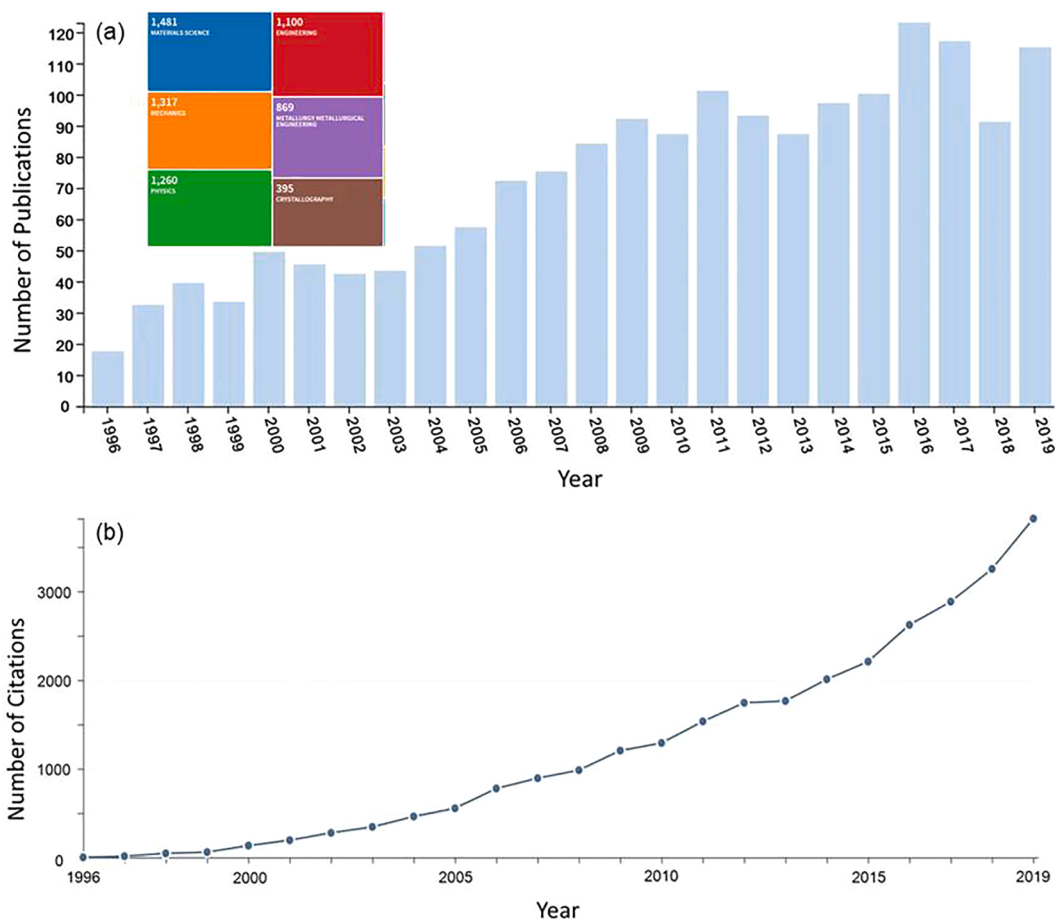


Fig. 1. (a) Yearly number of publications since 1996 on adiabatic shear bands or adiabatic shear localization; (b) total number of citations per year [From Web of Science].

introduced, over 2,000 papers on the subject were published. Approximately 1,400 papers are classified into the category of Materials Science and about 1,300 ones can be ascribed to the field of Mechanics. Meanwhile, such topic is also related to the main fields of Physics, Engineering, Metallurgical Engineering or Crystallography. The total citations are approaching 40,000 up to 2020. One should understand that these numbers are fairly high and that papers do not necessarily address adiabatic shear bands. In this review, we try to systematize the vast literature on the subject without claiming it to be exhaustive. Indeed, the number of our references is only approximately 460.

Table 1 shows the principal books [9–14] and reviews [15–27] on the subject. We comment briefly on the books here. The focus of Bai and Dodd's the first book is a balanced treatment of the microstructural aspects in historical perspective. Dodd and Bai's second book, published in 2012, is a collection of chapters by co-authors that overview most of the fields and a variety of materials linked to adiabatic shear localization. Their third book [11] published in 2014 is an enhanced and updated student-friendly edition of the first one. Wright's [12] approach is highly mathematical and separates instability, which has the onset at the maximum stress, from localization, a later phenomenon which results in the adiabatic shear band. Chen and Song [13] systematically describe the general principles of Kolsky bars (split Hopkinson bars), which are widely used for obtaining dynamic material properties. More details are focused on the modification of instruments, obtaining of reliable data as well as the experiment design or challenges for different classes of materials (brittle, ductile, soft, etc) and for different loading conditions (tension, torsion, triaxial, high/low temperatures, intermediate strain rate, etc). Shukla et al. [14] discuss the topic of dynamic loading and its effect on material and structural failure in their book. In addition to these six important contributions, a number of more focused works have been published, addressing specific aspects of shear localization. We will not reproduce these extensive studies but focus on principles, important recent developments, and microstructural evolution mechanisms.

2. Historical aspects

This section reviews some of the major steps in the development of our understanding of ASBs. An excellent article on the foundational contributions to the understanding of adiabatic shear bands was written by Walley [21].

Henri Tresca [28] first described the observation of heat generated during the dynamic plastic deformation and the localization of

Table 1

Books and reviews on the subject of adiabatic shear bands.

Books	Authors	Title	Year	Publisher
1	Bai Y.L., Dodd B.	Adiabatic shear localization: occurrence, theories, and applications	1992	Pergamon Press
2	Dodd B., Bai Y.L.	Adiabatic shear localization: frontiers and advances	2012	Elsevier
3	Dodd B., Bai Y.L.	Introduction to adiabatic shear localization (Revised Edition)	2014	Imperial College Press
4	Wright T.W.	The physics and mathematics of adiabatic shear bands	2002	Cambridge University Press
5	Chen W.N., Song B.	Split Hopkinson (Kolsky) Bar <i>Design, Testing and Applications</i>	2011	Springer
6	Shukla A., Ravichandran G., Rajapakse Y.D.S.	Dynamic Failure of Materials and Structures	2010	Springer
Reviews	Authors	Title	Year/volume/ pages	Journal
1	Rogers H.C.	Adiabatic plastic deformation	1979/9(1)/28 3–311	Annul Review of Materials Science
2	Timothy S.	The structure of adiabatic shear bands in metals: a critical review	1987/35(2)/3 01–306	Acta Metallurgica
3	Gilman J.J.	Micromechanics of shear banding	1994/17(2–3)/ 83–96	Mechanics of Materials
4	Klepaczko J.	Remarks on impact shearing	1998/46(10)/ 2139–2153	Journal of the Mechanics and Physics of Solids
5	Meyers M.A., et al.	Shear localization in dynamic deformation of materials: microstructural evolution and self-organization	2001/317(1–2)/ 204–225	Materials Science and Engineering: A
6	Ben-Dor G., Dubinsky A., Elperin T.	Ballistic impact: recent advances in analytical modeling of plate penetration dynamics-a review	2005/58(6)/355- 371	Applied Mechanics Reviews
7	Walley S. M.	Shear localization: a historical overview	2007/38(11)/ 2629–2654	Metallurgical and Materials Transactions A
8	Armstrong R.W., Walley S.M.	High strain-rate properties of metals and alloys	2008/53(3)/ 105–128	International Materials Reviews
9	Xu Y.B., et al.	Shear localization in dynamic deformation: microstructural evolution	2008/39(4)/811- 843	Metallurgical and Materials Transactions A
10	Greer A.L., Cheng Y.Q., Ma E.	Shear bands in metallic glasses	2013/74(4)/ 71–132	Materials Science and Engineering R
11	Antolovich S.D., Armstrong R. W.	Plastic strain localization in metals: origins and consequences	2014/59/1–160	Progress in Materials Science
12	Monlinari A.	Shear band analysis	1988/3-4/ 447–468	Solid State Phenomena
13	Salvado F.C., et al.	A review on the strain rate dependency of the dynamic viscoplastic response of FCC metals	2017/88/ 186–231	Progress in Materials Science

plastic flow into a shape of an X during the forging of platinum in 1878. This was subsequently demonstrated by Harold Massey [29] in 1921, and the first image depicting the heat cross was achieved by Johnson et al. [30]. The X-shaped region corresponds to the outline of largest shear stress and is expected to orient at 45° to the impact direction. This could be the precursor of the formation of adiabatic shear bands [31]. Then, in 1928, Kravz and Tarnavskii [32] described a true adiabatic shear band, which was once known as “Kravz-Tarnavskii effect” in various kinds of steels by drop-weight impact. Their contribution is critically evaluated by Dodd et al. [33] in a review of the major steps in our understanding of adiabatic shear bands.

In 1934, Taylor and Quinney [34] carried out deformation experiments which demonstrated that about 90% of the work during plastic deformation was transformed into heat. Shortly after, Davidenkov and Miroslubov [35] proposed two different mechanisms of shear localization and explored the influence of initial microstructure on the initiation of shear bands.

Thermal softening as the principal mechanism for shear banding was first proposed by Zener and Hollomon [36]. This classic work was part of the US war effort. WW2 military research produced a large volume of research on this subject. They recognized that the shear localization can be initiated at the peak of the stress–strain curve but failed to express this mathematically. Recht [1] developed an equation based on the thermoplastic properties of materials which enabled comparison of their adiabatic shear sensitivities. This will be presented in the Section 4.1. The values of strain rate required to initiate shear localization are derived and the critical strain rate is defined. The critical strain rates for titanium and its alloys were found to be less than one thousandth of those for mild steel [37,38]. Many other alloys have shown similar behavior. Culver [2] correlated the occurrence of shear localization with a critical shear strain, when the slope of the adiabatic stress–strain curve becomes 0. Argon [39] took the effect of adiabatic heating into account during the instability analysis of inhomogeneous deformation. Staker [40] extended the instability criterion to a wide variety of alloys assuming a parabolic stress–strain response and incorporated the dependence of the strain rate upon the flow stress. The Staker equation for the critical shear strain for ASB formation is expressed as:

$$\gamma_c = \frac{n}{-C_v^{-1} \rho^{-1} \left(\frac{\partial \sigma}{\partial T} \right)_{\dot{\gamma}} - \frac{m(d\dot{\gamma}/d\dot{\gamma})}{\dot{\gamma}}} \approx \frac{C_v \rho n}{\left(\frac{\partial \sigma}{\partial T} \right)_{\dot{\gamma}}} \quad (4)$$

The parameters are: n , work hardening; m , strain rate sensitivity; C_v , heat capacity at constant volume; ρ , density; Staker [40] mentions that the second term in the denominator can be ignored and thus his expression ignores the strain-rate sensitivity. However, it is well established that even a modest strain-rate sensitivity leads to a delay in the localization process. He found, for ferrous alloys, that two important material parameters, the temperature dependence of flow stress and strain hardening exponent, are significant to the onset of shear band formation, whereas the effect of strain-rate sensitivity is negligible due to a small variation in most ferrous materials. The bimodal microstructure of Ti-6Al-4V alloys with the thickest α lamellar in the transformed β matrix showed the lowest susceptibility of the formation of adiabatic shear band since its higher strain hardening ability suppresses the thermal softening effect revealed by Zheng et al. [460,465]. Rogers [15] pointed out that the above investigations bring the question of whether a “critical strain rate” exists for the adiabatic shear band to form in a material. He also demonstrated that large strains can be achieved quasi-statically in steel without the formation of a shear band. Once a critical strain is attained, a critical strain rate, above which temperature can increase above the value for transformation to occur, can be revealed.

Burns and Trucano [41] considered thermal softening, strain hardening, and strain-rate sensitivity in their constitutive equation. They investigated the growth of small perturbations and included time-dependent coefficients in the linear ordinary differential equations. Such analysis for the critical shear strain was restricted to a special condition: a Newtonian-like fluid with temperature-dependent viscosity. This treatment did not consider microstructure evolution effects during adiabatic shear band formation. Clifton [42] and Bai [43] developed separate perturbation analyses incorporating heat transfer during the occurrence of shear localization. The principal equations will be presented in Section 4. Bai [43,44] later involved the dynamic aspect in a similar way. Ordinary differential equations with constant coefficients were used. The critical strain rate for the formation of a shear band can be described simply once the constitutive equation has an explicit expression, which marks a significant theoretical advance.

3. Experimental methods

Shear localization is usually associated with severe plastic deformation. This dynamic phenomenon is usually obtained in high strain-rate loading experiments using momentum trapping devices, pulse shaping equipment, and strain measurement techniques [45]. Over the past decades, several techniques have been developed to investigate the dynamic behavior of metallic materials. Prominent ones among these are the split-Hopkinson pressure bar [46–54], cylinder imploding and exploding techniques [55–61], ballistic impact [62–68], drop-weight tower [69–71], and high-power pulsed laser shock [72–77].

In these experimental techniques, the formation of shear bands depends mainly on the geometry of the specimens. Meanwhile, the material characteristic is of great importance to the dynamic behavior of specimens [78]. It is commonly accepted in the literature that either forced shear localization or spontaneous shear localization can occur. For the forced shear localization, the regions where shear bands appear are controlled by the specimen geometry or the loading conditions. For example, the hat-shaped specimens are the most widely applied geometry for studying the forced shear localization in different materials. Forced shear localization takes place in most materials when using the hat-shaped specimens [79–87]. Spontaneous shear localization can occur in a symmetrical structure, like cylindrical or spherical specimens, when they are subjected to internal or external symmetrical loadings. There are no predictable locations to induce shear localization within symmetrical specimens or under symmetrical loading. Arrays of shear bands can be obtained in various positions with a specific spacing that is related to some inherent features of materials. This is treated in Sections 6

and 11.6.

We first provide in this section a brief introduction to the experimental methods based on different facilities as well as unique specimen geometries. The current thrusts are to obtain in situ real time information on the temperature, microstructural evolution, strain, and their spatial variations. This is a challenge requiring ever more sophisticated equipment and advanced diagnostics with greater temporal and spatial capabilities.

3.1. Split-Hopkinson pressure bar (SHPB)

The Kolsky bar, or split-Hopkinson pressure bar, presented in Fig. 2, is an important technique for dynamic testing of materials. A comprehensive treatment of Hopkinson bars is given in the book authored by Chen and Song [13]. The Hopkinson bar has its origin in the work of John Hopkinson [88] who studied the dynamic response of iron. Upon his death in a tragic biplane accident piloted by him, his son Bertram Hopkinson, a lawyer by training, took his position at Cambridge and continued his work prior to succumbing to a climbing accident in the Alps. He is credited with the design of the first Hopkinson pressure bar and time-resolved measurement to record a pressure-pulse profile [89]. Kolsky [90] made a great contribution by improving the technique incorporating two elastic bars between which the specimen is sandwiched. This is called the split-Hopkinson (or Kolsky) bar and enabled obtaining the stress-strain curves at high strain rates. The stress profiles in the bars are measured and the stress, strain, and strain-rates of the specimen are extracted by a one-dimensional elastic wave analysis based on the technique proposed by R. M. Davies [91] and later by E. Davies and Hunter [47]. The difference between two pulses in incident and transmitted bars provides the inelastic path in specimen.

The split-Hopkinson pressure bar can also be used in tension testing owing to the modification by Hauser and, later, Lindholm and Yeakley, by subjecting the specimen to uniaxial tension [92–94]. Harding [95] contributed to the design of a tensile split Hopkinson pressure bar which can be applied to composite materials. Recently, Mohr and collaborators [96,97] made significant efforts at improving the tensile experiments as seen in Fig. 3 (a,b). They proposed a new technique for testing the high strain-rate tensile response of sheet metal by using a compression Hopkinson bar system. The tensile force as well as the displacement history acting on the specimen are measured with the aid of a high-speed camera system. Another successful tensile bar configuration is shown in Fig. 3 (c), where the projectile is accelerated in the direction opposite to the position of the specimen. This design is due to Isaacs and Nemat-Nasser [98].

Another novel design was introduced by Baker and Yew [99], modifying the split Hopkinson bar for dynamic torsion tests. This was developed to determine the stress evolution process and dynamic stress-strain relationships of materials subjected to high strain-rate torsional loading [46,100]. Although the split Hopkinson bar has been used quite often, shear bands are produced by shear, and the torsional Hopkinson bar is the most rigorous instrument to generate a state of simple shear. The classic experiments by Marchand and Duffy [101] enabled the direct observation of the distortion of a grid in steels and thus, the evolution of shear instability and localization, as shown in Fig. 4. The incorporation of a grid on the specimen and the use of high-speed cameras lead to the photographic series shown in Fig. 4 (b)-(f). One can see that localization takes place at a critical shear strain, evidenced by discontinuities in the lines. Similar experiments were also conducted by Xue, Shen, Xu, and Bai [102]. Fig. 5 (a) shows the experimental setup used by Xue, Shen, and Bai [52]. This experimental technique provides a possible approach for the comparative investigation of macro and microscopic observations and corresponding measurements of shear stress versus shear strain. A clamp holds the incident bar in position, while it is subjected to elastic torsional loading. After the release of the clamp, a shear wave propagates throughout the incident bar and then enters the material, which undergoes rapid plastic deformation. This technique was extended by Chichili et al. [103] who added a compressional stress as demonstrated in Fig. 5 (b).

Meanwhile, the specimen geometry is of great importance to the stress distribution which is a dominant factor during plastic deformation. The simplest geometry is the cylindrical one. Because of the frictional end effects, shear localization often starts and propagates from the ends or edges, forming a cone. Among various testing techniques, the specimens with a geometry discontinuity that further constrains the shear deformation into certain gauge sections [104], are the hat-shaped [105–109], double shear [110–112], single or double notch [113–116], and compact forced simple shear [117] specimens. Other types of specimens use a

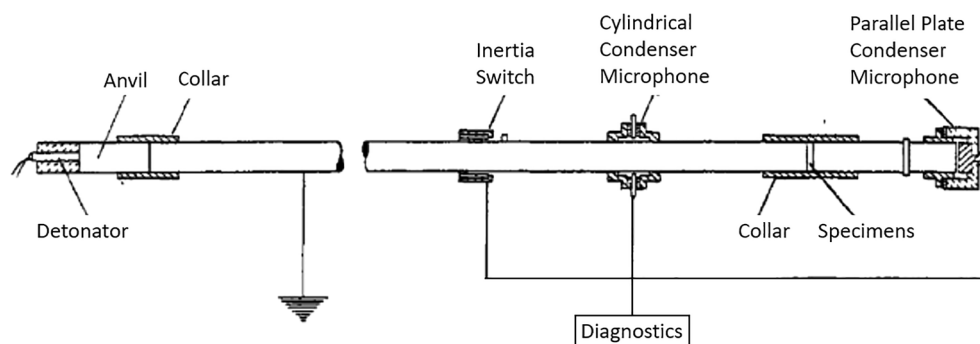


Fig. 2. Schematic of Kolsky's apparatus showing explosive charge accelerating anvil and creating compressive pulse in incident bar and (collared) specimen sandwiched between two bars [90].

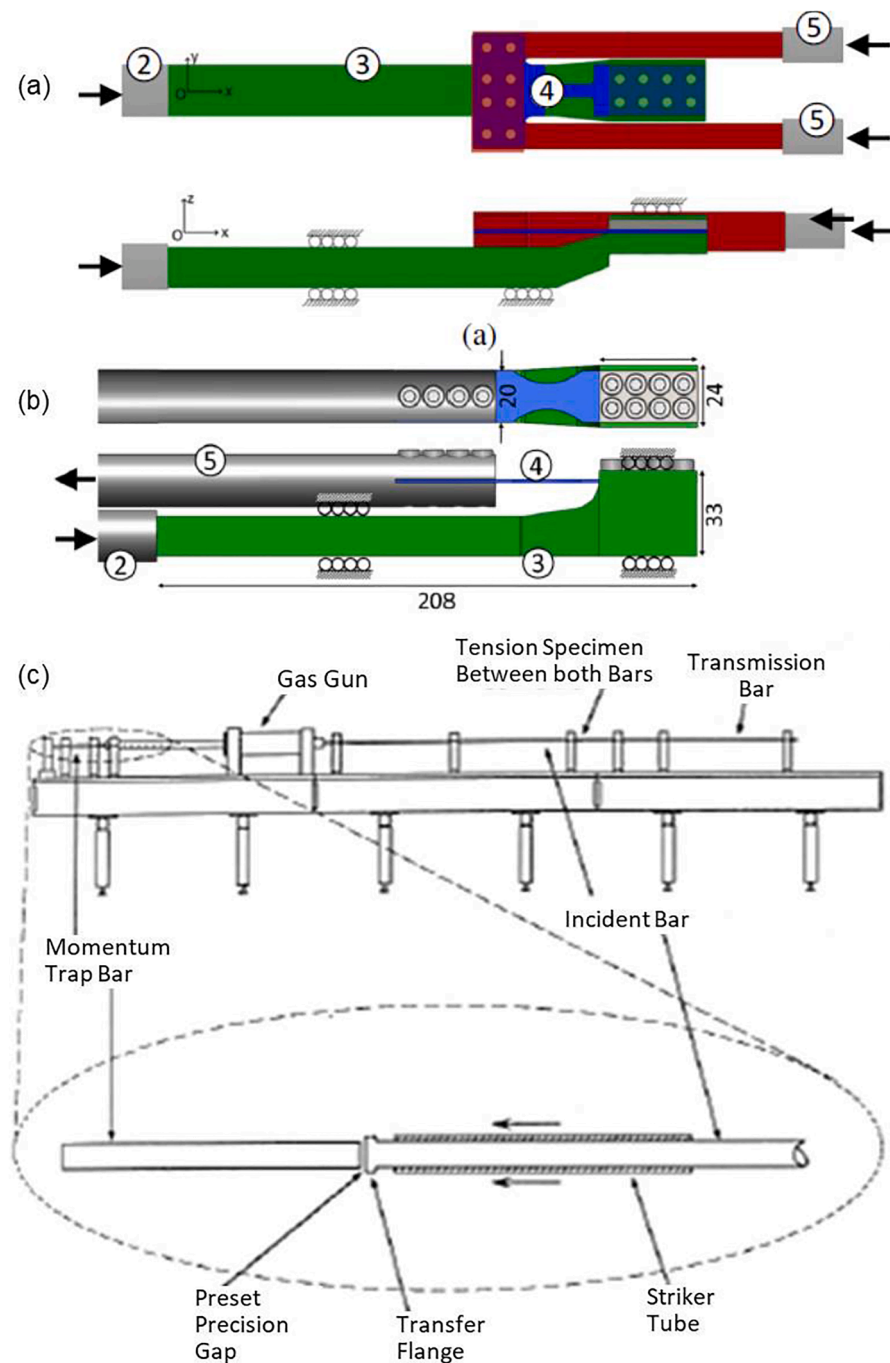


Fig. 3. Schematic of modified SHPB for tensile testing (pulse travels from left to right): (a) compressive pulse in bar ③ generates tension in specimen ④; (b) compressive pulse in bar ② creates tension in specimen ④, while transmitted bar ⑤ will undergo tension; (c) the tensile Hopkinson bar setup developed at UCSD for recovery experiments. Dimensions given are in mm [97,98].

continuous geometry, which can produce the shear deformation by asymmetry or heterogeneity in the deformation fields, like cylindrical compression and shear [37], punch [118], indentation [119], and inclined flyer [120]. Other geometries depend on a combination of the above mentioned two components, such as shear and compression [121,122] and shear and tension [123].

3.1.1. Cylindrical specimen

Specimens with cylindrical geometry are usually used for the investigation of the quasi-static and dynamic mechanical response for different kinds of materials, such as aluminum, titanium, steels as well as foams. Cylindrical specimens can be used to achieve the

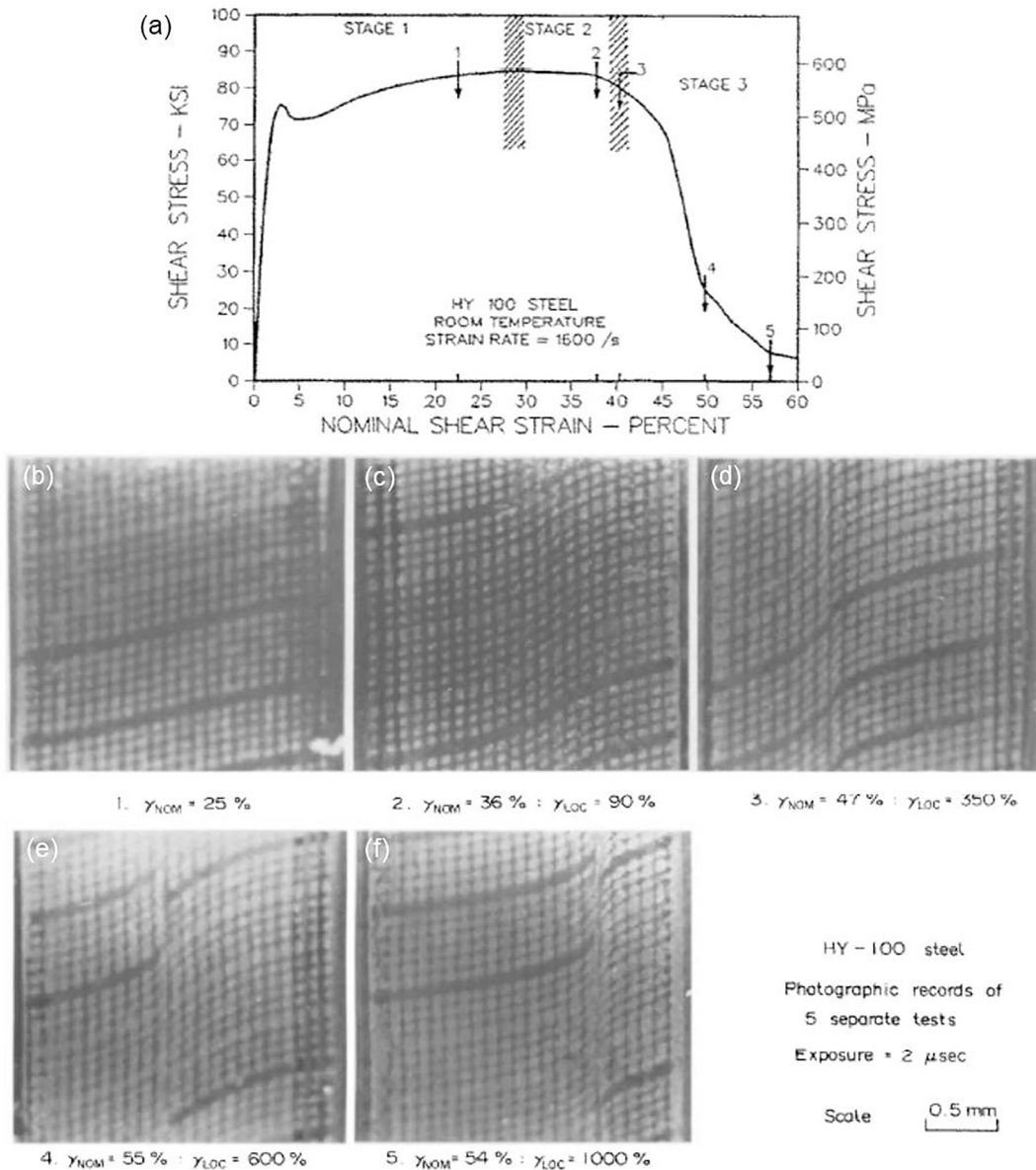


Fig. 4. The evolution process of shear band in HY-100 steel observed in experiments: (a) a typical stress–strain curve showing three stages during formation of shear band at a nominal strain rate of 1600 s^{-1} ; (b)–(f) photographs of the grid patterns obtained in five separate tests at the nominal strain values corresponding to the marked strain values 1–5 in (a) [101].

relationship between yield strength & strain-rate as well as temperature. Cylinders with 5 mm in diameter and 5 to 8 mm in length have been adopted by Meyers and coworkers [124] to investigate the dynamic deformation of ultrafine-grain-sized zirconium. Other geometries are also available [80,125]. In general, the length/diameter ratio in cylindrical specimens in dynamic tests is around 1. This is not an ideal ratio, but produces satisfactory results in spite of the limitations. Inertial and frictional stresses play an important role in dynamic testing. These should be minimized to provide reliable stress strain results. The evaluation of these has led to the size and aspect ratio of specimens. As the strain rate is increased, the specimen dimensions have to be reduced to maintain equilibrium. Miniature Hopkinson bars are used for high strain rates, on the order of 10^5 s^{-1} . Siviour and Walley [126,127] provide equations to calculate inertial and frictional stresses and suggest special geometries to minimize barreling. For instance, for a copper specimen 3.8 mm in diameter and 2.3 mm thick, inertial effects become important at a strain rate of 10^5 s^{-1} .

3.1.2. Hat-shaped specimen

Hat-shaped specimens are used to produce a forced shear band in a specific zone, and provide an approach to clarify the influence of the original microstructure, temperature and strain rate on the development of shear bands [128–130]. The hat-shaped or top-hat

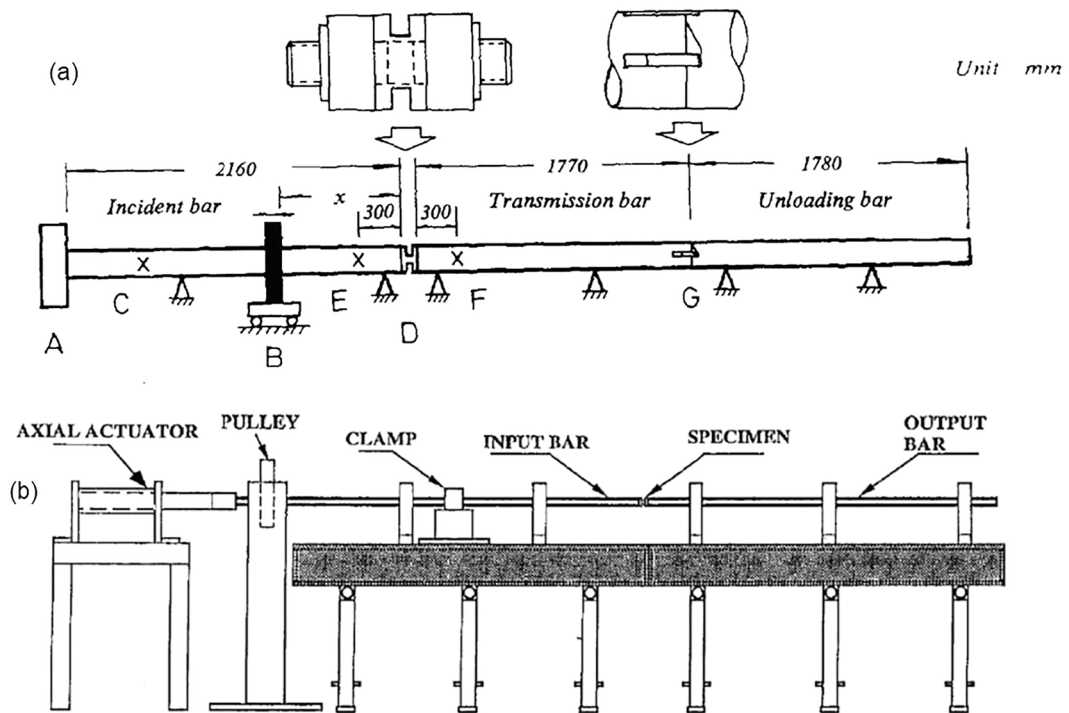


Fig. 5. Schematic diagrams of (a) split-Hopkinson torsional bar apparatus [52] and of (b) compression-torsional split-Hopkinson bar [103].

geometry is an attractive design. It is an axisymmetric specimen consisting of an upper hat part and a lower brim part. When such specimen is subjected to compression, the material between the hat and the brim parts shears [131]. This geometry, first designed by Meyer and Manwaring [132] has been modified several times [129,130] and has been applied to the formation of ASBs in titanium alloys [133], copper alloys [130], tantalum alloys [134,135], aluminum alloys [69], stainless steels [136–138], and other materials.

The hat-shaped specimens have the advantage of generating shear localization even in very ductile materials during the SHPB compression test. Due to its special geometry, extremely large shear strains and high strain rates can be achieved. The displacement of

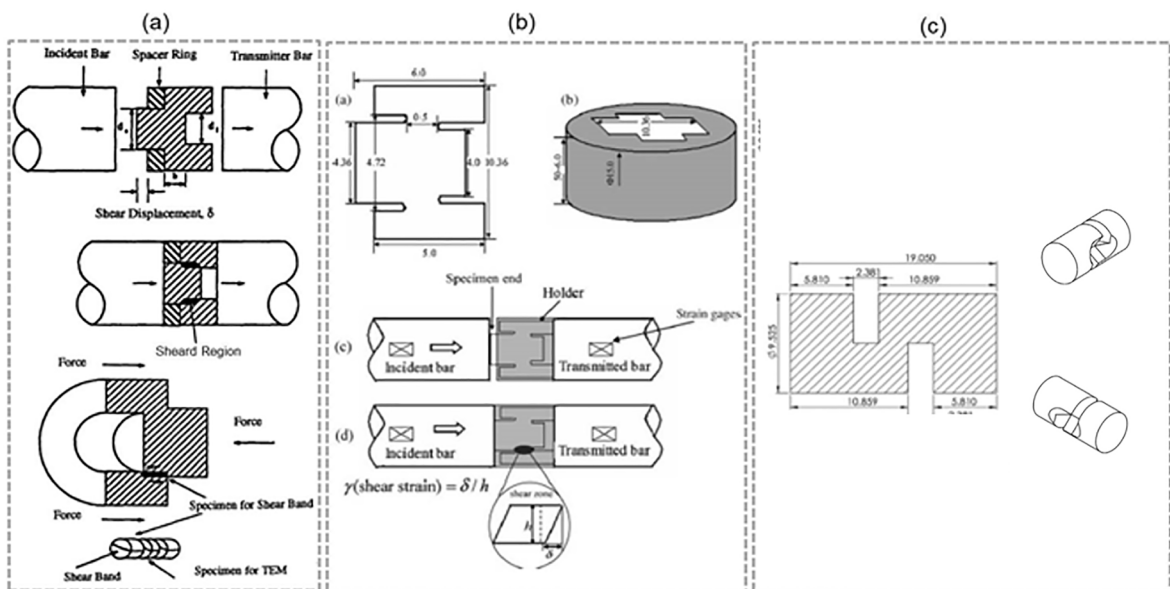


Fig. 6. Schematic illustration of shear test set-up in Hopkinson-bar: (a) the hat-shaped specimen before and after dynamic loading and extraction of specimen for transmission electron microscopy [37]; (b) the hat-like shaped specimen with the holder and the specimen before compression and after compression [144]; (c) the compact-forced-simple-shear specimen with different section views [117]. All dimensions are in mm.

the specimen in the axial direction can be controlled easily with stopper rings to study the dynamic response and microstructure evolution as a function of strain during shear localization.

Such specimens were prepared with different characteristic geometries; for example three specimens with hat heights of 0.75, 1, and 2 mm were used by Kad et al. [124]. Other dimensions of the specimen have been used [139,140]. The deformation time of the shear localization can be estimated by dividing the displacement of the top-hat by the loading velocity, and is about 0.05–0.1 ms. Disregarding hat heights, hat and hole diameters are of approximately the same size [141]. Most investigations are performed on specimens with a slightly larger hat diameter than the hole diameter, resulting in an additional compressive loading state, like a hydrostatic pressure, as demonstrated in Fig. 6(a) [37]. By modifying the specimen geometry, different compression-shear loading states can be generated. In addition, there exist a few investigations in the literature where the hat diameter is smaller than the hole diameter [19,142].

3.1.3. Hat-like-shaped specimen

An early form to the hat-like-shaped specimen is called “plate-shear” specimen, and was first designed by Meyer et al. [143] to conduct shear tests. It can also produce shear bands in a narrow zone and has been used successfully in exploring adiabatic shear localization in many materials [144]. This method forces shear localization forming in a narrow flat region, which is different from the narrow ring-shaped shear zone in hat-shaped specimen.

Liu and Dai et al. [144] examined the influence of strain rate on the evolution of shear localization in Zr-based bulk metallic glasses using hat-like-shaped specimens. The shear displacement is determined by the length of the specimen hat outside the holder, as presented in Fig. 6 (b). By modifying the length and the applied load, different shear deformations can be achieved in the sheared zone. This geometry has been extensively modeled by Finite Element Analysis.

3.1.4. Compact-forced-simple-shear specimen

Fig. 6 (c) shows the schematic drawing of the compact-forced-simple-shear specimen [117]. The objective of this geometry is to explore the large strain constitutive behavior, and damage and failure mechanisms during shear deformation systematically as a function of shear loading for different microstructure orientations. The design is intended to align the single shear plane parallel to the loading direction. This leads to a single narrow plane subjected to simple shear in compression direction. By changing the shear plane positions, the mechanical response under shear deformation and the damage evolution can be investigated systematically on materials

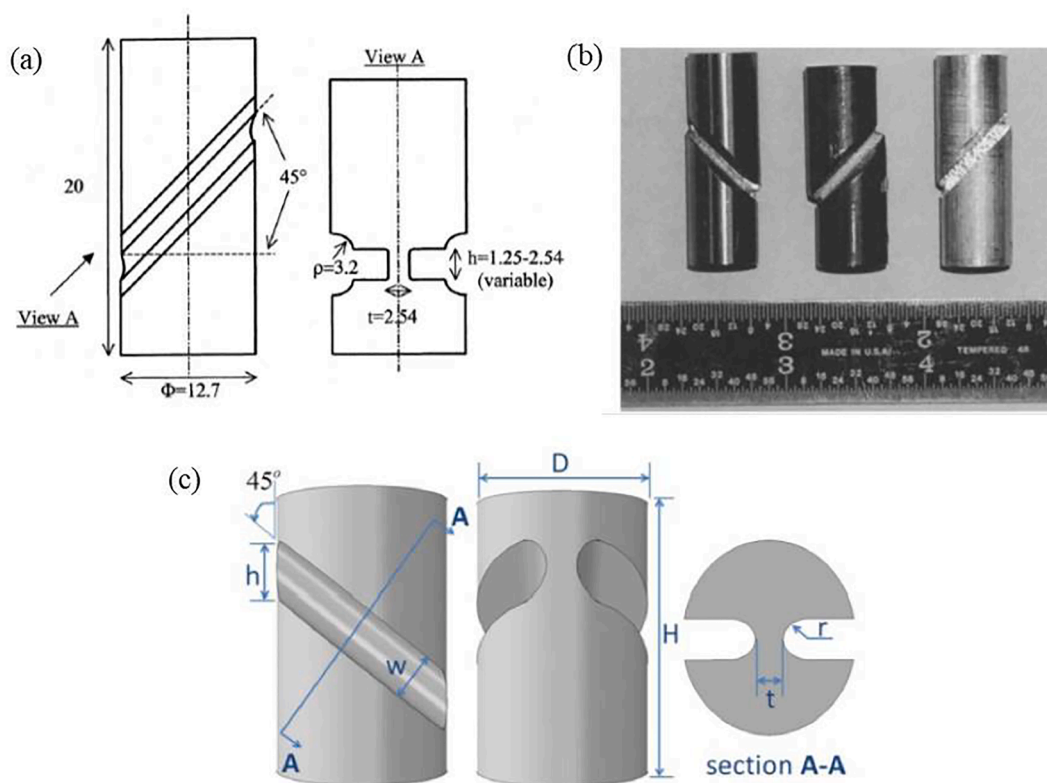


Fig. 7. Schematic representation of the shear compression specimen (SCS): (a) geometrical parameters of the SCS specimens; (b) photographs of three deformed specimens. From left to right, they are annealed Ti-6Al-4V titanium alloy, commercial OFHC copper and 6061-T351 aluminum alloys; (c) schematic for the modified SCS specimen with a circular gauge [121,122].

possessing microstructural or crystallographic anisotropy. This technique has been applied for shear testing of numerous materials correlated to specific orientations with different propensities for shear banding, such as titanium and aluminum alloys, investigated by Vecchio et al. [117,145].

3.1.5. Shear compression specimen

The shear compression specimen (SCS), which provides a combination of shear and compression loading, is shown in Fig. 7 [121,122,146]. It is typically a short cylinder with two slots which are inclined 45° to the longitudinal axis. Under compression, the gauge region undergoes a dominant shear deformation. Such gauge section is defined by its height and thickness. The diameter of cylinder is designed to remain elastically deformed during the test. The cylindrical section transfers the vertical displacements and corresponding loads to the gauge section. A clearance is designed to make visual access and diagnostic of gauge region possible. This clearance has no influence on the load transmission to the gauge. A typical deformation of the specimen is presented in Fig. 7 (a) and (b). It is clear that the gauge region experiences a shear-dominated deformation. The failure strain is dependent on specimen geometry and material properties. The limitation of this geometry is the rectangular nature of the slots, which intrinsically concentrates the stress locally [121]. Later, the original design was modified with two completely opposite semi-circular slots that are different from the two rectangular slots, as shown in Fig. 7 (c). The newly designed specimen was systematically examined under quasi-static and dynamic testing conditions using an elastoplastic material [122]. The comparison between the two slot designs confirmed the improvement of the new geometry at larger strains and the reduction of stress constraint within the rectangular slots. It is indicated that the advantages of semi-circular slot compared with the rectangular slot design can be a larger strain range, failure and fracture within the gauge, and constant Lode parameter during plastic deformation. Besides, the novel configuration of the failure path can be recorded by *in-situ* experiments. Such technique was applied to examine copper, aluminum, as well as steel under quasi-static and dynamic conditions by using the SHPB [121,122].

In addition, a shear-tension specimen was also proposed by Dorogoy et al. [147]. It is composed of a long cylinder and an inclined gauge section provided by two opposite semi-circular slots that are created with an angle of 45° to the longitudinal axis. This provides a flexibility of loading which combines both tension and shear.

3.1.6. Double shear specimen

Campbell and Ferguson [38] employed a double shear specimen (DSS) where the output bar of an SHPB apparatus is designed with a tubular geometry to explore the temperature and strain-rate dependence of shear strength in materials, such as mild steel. Later, Klepaczko [110] introduced an improvement to this technique: one is the removal of the incident bar and the utilization of direct projectile impact; another is the modification of the specimen geometry with an enlarged shear zone to 2 mm. This is a modified double shear specimen which can test the material in a wide range of shear strain rates, up to 10^5 s^{-1} . The transition from isothermal to adiabatic plastic deformation depends on both the geometry of the deformed specimen and the heat extraction rate from the deformed regions. Once the plastic work converts locally into volume heating without heat transfer, the thermal softening during adiabatic shearing can directly induce instability and localization. Oussouaddi and Klepaczko [148] predicted the critical strain rate of such transition for copper, aluminum and mild steel when the thickness of deformed layer is $\sim 2 \text{ mm}$.

A double shear specimen is characterized by two identical rectangular sheared regions forming between a central loading portion and two supporting ends, as illustrated in Fig. 8 [149,150]. The size of the sheared regions can be modified to produce various strain rates. With this design, specimens can be used easily in a split-Hopkinson bar, employing the loading and supporting ends directly attached to the bars. Since the lateral movement is restricted by the fixture, the deformation in the sheared region is one of simple shear. This specimen also facilitates the diagnostics of the evolution of shear localization, such as temperature rise and propagating velocity.

Furthermore, Zhao et al. [53] performed a detailed investigation on the application of the split Hopkinson pressure bar to weak materials. Low impedance bars with high viscoelasticity are required for high-strain-rate testing of foams. They also demonstrated that the technical problems of such application are related to the loading and measurement conditions. A novel method which combines

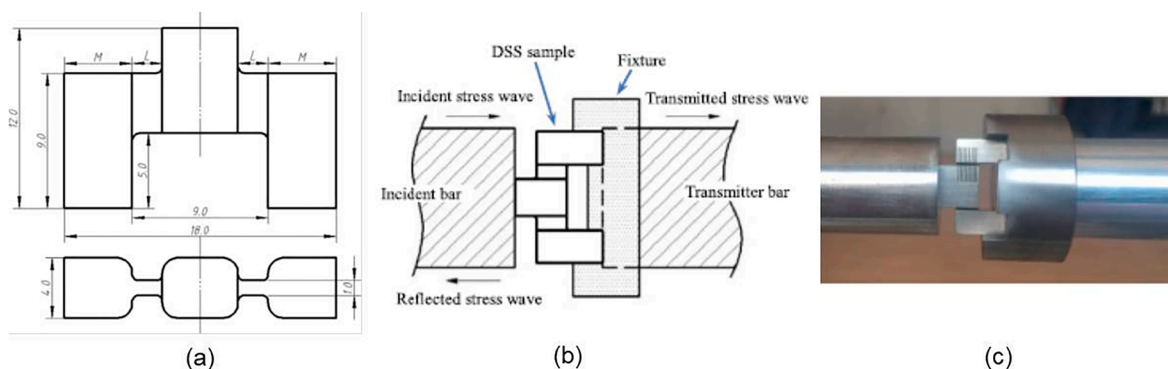


Fig. 8. Schematic diagram of double shear specimen (DSS): (a) the geometrical parameters of the DSS specimens; (b)-(c) the illustration of global experimental set-up with Hopkinson-bar [149,150].

compression and shear loading at high strain rates was developed by Zhao et al. [54]. It is called the split-Hopkinson pressure shear bar (SHPSB), and is shown in Fig. 9.

3.2. Time resolved techniques

The ultimate goal of scientific experiments on shear bands is to connect the evolution of the strength with the temperature rise and changes in the micro and nanostructure. Constant but slow progress is made in this area but there are a few notable recent developments. This requires in situ time resolved measurements of temperature and structure evolution.

X-ray phase contrast imaging technique has been successfully used to document the evolution of fracture in silicon, fiber-epoxy interfacial friction, and ligament-bone interface debonding using the Hopkinson bar in conjunction with the synchrotron at the Advanced Photon Source (Argonne National Laboratory) [151,152]. In the compression mode, sand and grain to grain interaction are photographed. The 100 ps white radiation has to be synchronized with the deformation. A temporal resolution of 0.5 μs and spatial resolution of μm -level were achieved. The setup is straightforward but the timing is critical (Fig. 10) [151].

The measurement of temperature using infrared cameras is also constantly evolving, with measurements that can be made in the shear bands, in contrast with older methodologies that measured a larger area, a fraction of which was covered by the shear band. These more accurate measurements focus on an area significantly smaller than earlier measurements by Guduru et al. [153], in which spatial resolution is only in the order of tens of microns.

In order to enable direct observation, the Meyer-Manwaring hat-shaped specimen of cylindrical shape was replaced by a flat hat-shaped specimen with thickness of 0.8 mm. The shear-band width for 6061-T6 was 30–70 μm . The combination of X-ray measurements using the Advanced Light Source and infrared measurements enabled a complete description of the process (Fig. 11). The temperature reaches the maximum value before the stress is highest and fracture follows immediately upon localization, the front propagates at approximately 1,100 m/s. These experiments exemplify the state-of-the art in shear-band research [154].

3.3. Exploding and imploding cylindrical configurations

The cylindrical geometry is extremely important in the formation of shell fragments. The fragmentation is intimately connected to the formation and spacing of shear bands. The smaller their spacing, the smaller the fragment sizes. Thus, the establishment of shear-band spacing is measured by this geometry. The design and operation of nuclear weapon implosions and the understanding of how symmetrical is the collapse of a hollow sphere are important for the prediction of the yield.

Two distinct experimental configurations have been developed based on explosives which can be placed inside or outside a hollow cylinder. Depending on the loading direction of the explosive driving force, the experiments are classified into the contained exploding cylinder test and the contained imploding cylinder test. This technique can generate strain rates up to 10^6 s^{-1} and large plastic deformation.

Shockey and Erlich [155] described the contained explosive cylinder experiment and applied it to AISI4340 steel in order to establish the distribution of shear bands. Fig. 12 shows the experimental setup of the contained explosive cylinder geometry. There is a plexiglass layer between the steel cylinder under investigation and the massive steel containment annulus that controls the overall deformation which is arrested before complete fragmentation takes place. This configuration was successfully used to determine the statistical distribution of fragments.

The opposite configuration, enabled by an outside explosive, is the collapse of a thick-walled cylinder under controlled and

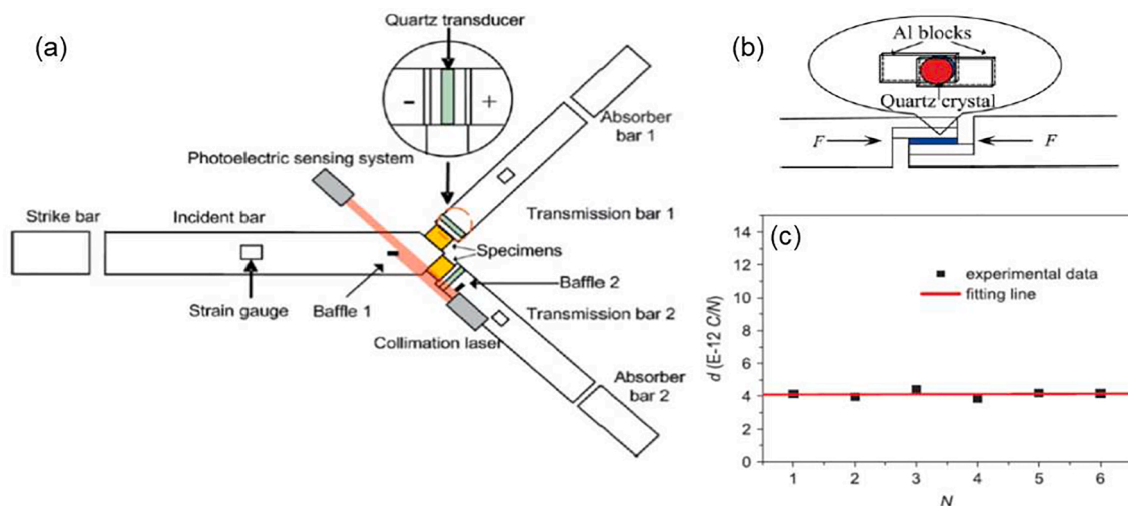


Fig. 9. (a) Schematic of the Y shaped experimental apparatus for generating shear bands simultaneously in two specimens; (b) the calibration experiment setup and (c) the calibration results of the piezoelectric constant [54].

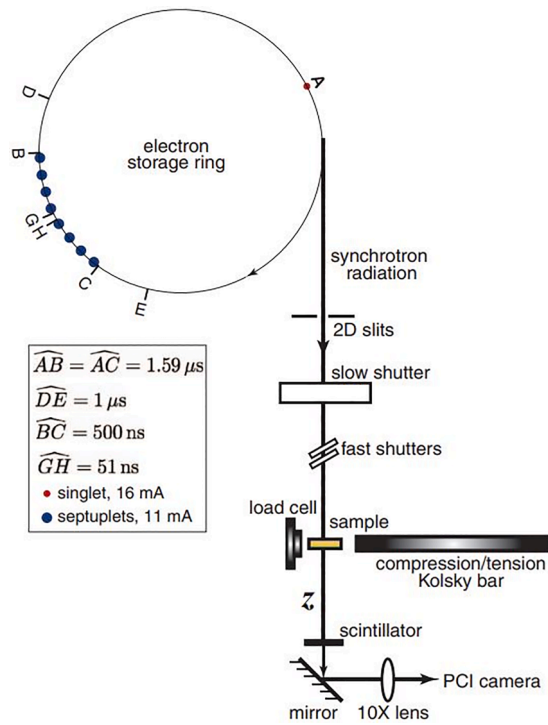


Fig. 10. Synchrotron radiation experimental setup at Advanced Photon Source (Argonne National Laboratory; Hopkinson/Kolsky bar is coupled to light source [151]).

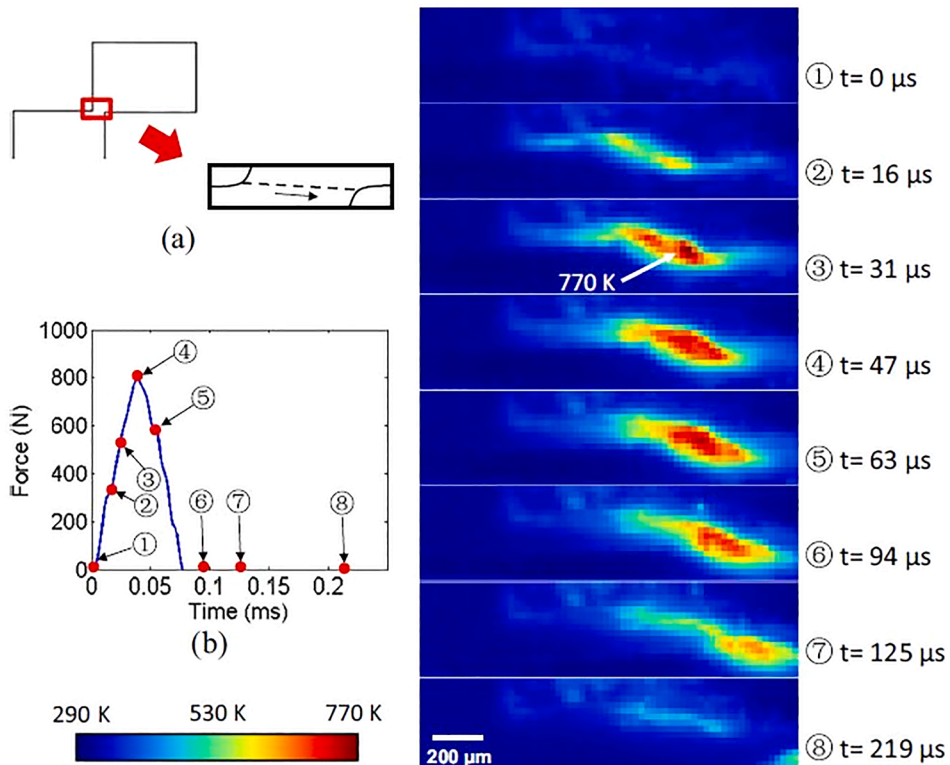


Fig. 11. In situ temperature measurement in 6061-T6 aluminum alloy (flat hat-shaped specimen) using infrared thermal imaging; maximum temperature of 770 K is measured [154].

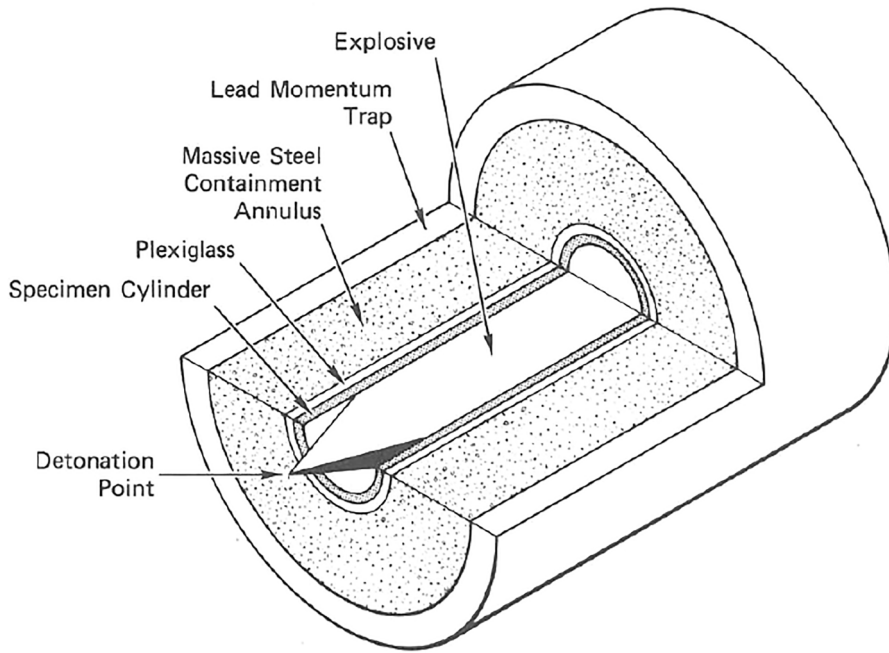


Fig. 12. Schematic of exploding cylindrical experimental setup in expanding geometry [155].

prescribed pressure. It is one of the most important load-geometry combinations for the spontaneous formation of multiple ASBs. This technique was first developed to study the shear bands by Nesterenko and Bondar [55,60], and has been adapted to Ti [156,158], steels [58,157] and tantalum [135] for studying the characteristics and evolution of ASBs. The required loading energy is usually generated through a low detonation velocity explosive, as presented in Fig. 13 [157]. The detonation provides a compressive stress in the radial and circumferential directions. An internal cylinder arrests the deformation.

Later, Stokes et al. [159] carried out experiments on the Pegasus-II facility using electromagnetic forces as the driver for the

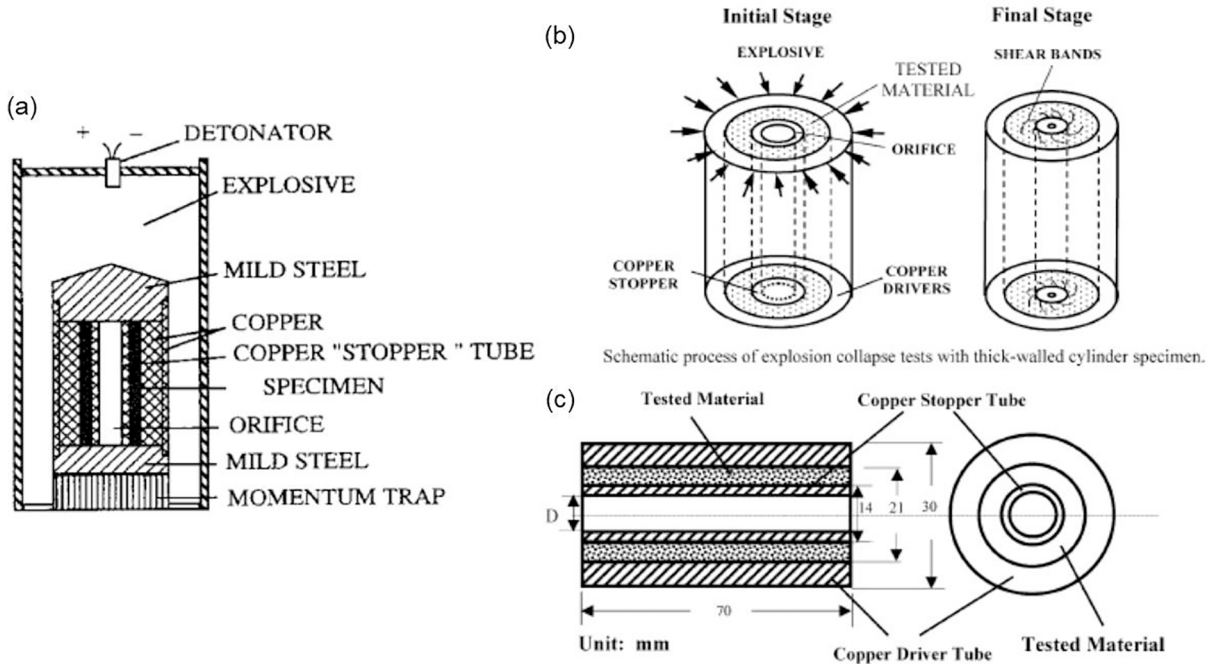


Fig. 13. Experimental configuration for explosive collapse of hollow (thick-walled) cylinder in imploding geometry : (a) schematic of cylinder experiment setup; (b) dynamic process of explosion collapse thick-walled hollow cylinders; (c) dimensions of assembly [157].

collapse of specimens. This shows a distinct advantage of more uniform collapse of the specimen as compared to the explosively driven experiments which present some axial differences due to the directional ignition of the driver. The electromagnetic method has been also used by Lovinger et al. [57] to test the repeatability of the thick-walled cylinder experiments.

Through the variation of the driving forces and the cylinder thickness, strain and strain-rate during the loading test can be adjusted. Shear bands initiate at the internal surfaces of the cylinders (where the strain is highest) and propagate outwards along spiral trajectories, Fig. 13 (b). The cylinder is sandwiched between two cylindrical shells, as presented in Fig. 13 (c). Both the outer and inner shells control the collapse of the specimen [157,158] and determine the maximum strain. In this technique, no stress concentration occurs, and the failure behavior is only material dependent.

Grady and Kipp [160,161], Wright and Ockendon [162], and Molinari [163] established one-dimensional analytical equations to predict the spacing of shear bands. A discontinuous growth mode was proposed by Meyers et al. [108] by considering the interaction between multiple shear bands. These will be presented in Section 11.6. It should be mentioned that these developments have their origin in the classic WW2 Mott experiments which determined the sizes of fragments in exploding munition. The unloading produced by fracture determined the fragment size [164–169].

3.4. Ballistic impact

The ballistic impact is a high velocity collision between the penetrator and target materials, which is accompanied by very large strains, strain rates, pressures and temperature rise as well as their gradients. The penetrator or projectile is generally operated by a light-gas gun or a standard rifle from a certain distance with different velocities, as shown in Fig. 14 [170]. The geometry of the projectiles for plugging test also varies, such as blunt [171,172], cylindrical [173,174], conical [175,176] and hemispherical projectile [177,178], which can generate different shear conditions. The inherent limitation of ballistic experiments is the lack of control of stress, strain and strain rate. Nevertheless, they provide a realistic assessment of how shear bands affect the performance of a target subjected to the impact by a projectile. Meyers and Wittman [179] examined dynamic impact of different plates and revealed the failure mechanisms (shear localization and spall), as shown in Fig. 15 (a) and (b). Fig. 15 (c) and (d) present the increase of penetration depth with the rise of impact velocity and normalized kinetic energy.

There have been numerous approaches aimed at clarifying the mechanics of penetration for a variety of impact situations, such as impact velocity, material properties and projectile/target configurations. A study by Sangoy et al. [64] demonstrated the relationship between hardness and ballistic limit in armor steels, which can be roughly divided into three regimes. For steels with low hardness, the failure of target happens as a consequence of plastic flow, and for steels with high hardness, fracture of projectile happens. In the intermediate region, the failure is controlled by the adiabatic shear process and the ballistic limit reduces with increasing hardness. This means that ASBs significantly influence the ballistic performance of materials.

Solberg et al. [180] also performed investigations of Wieldox (a class of high strength steels with high ductility) steel plates with different yield strengths impacted by hardened steel projectiles. Penetration testing on different materials using blunt projectiles showed that the ballistic velocity limit is reduced with increasing hardness. However, in similar testing with conical and ogival projectiles, the ballistic velocity limit rose with increasing hardness. They also reported that deformed shear bands were found in 12 mm thick Wieldox 460 E plates, while numerous white etched shear bands were revealed in both Wieldox 700 E and 900 E targets with considerably higher strength.

Craig and Stock [181] studied ASB propagation by impacting cylindrical projectiles made by hardened steel onto annealed brass in the velocities ranging from 300 to 600 m/s. The projectile only penetrated a short distance of the brass targets as semi-infinite blocks. The adiabatic shear bands originated near the impact region and propagated through the brass block. White-etching zones were also observed at the surface of the bullet holes. Manganello and Abbott [63] explored the ballistic behavior of heat-treated steel plates, by impacting armor-piercing projectiles and studied the evolution of the white-etched shear bands. They found that as the increase of tempering temperature and the decrease of carbon content, the penetration resistance decreased.

Mishra et al. [107] performed several high strain-rate tests to evaluate the suitability in demonstrating the ballistic penetration behavior for two kinds of aluminum alloys. An inference was drawn from combined observations that the dynamic indentation by gravity drop tower, split-Hopkinson bar, and Taylor tests can represent the actual ballistic impact performance of 7017 and 7055 alloys with regard of adiabatic shear bands evolution, shear-induced cracking, and penetration depth.

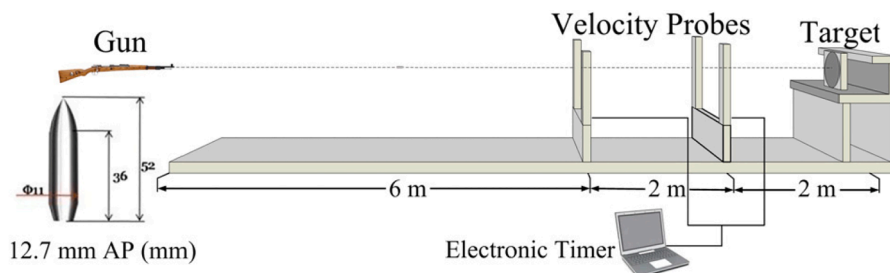


Fig. 14. Schematic of typical experimental setup for ballistic impact [170].

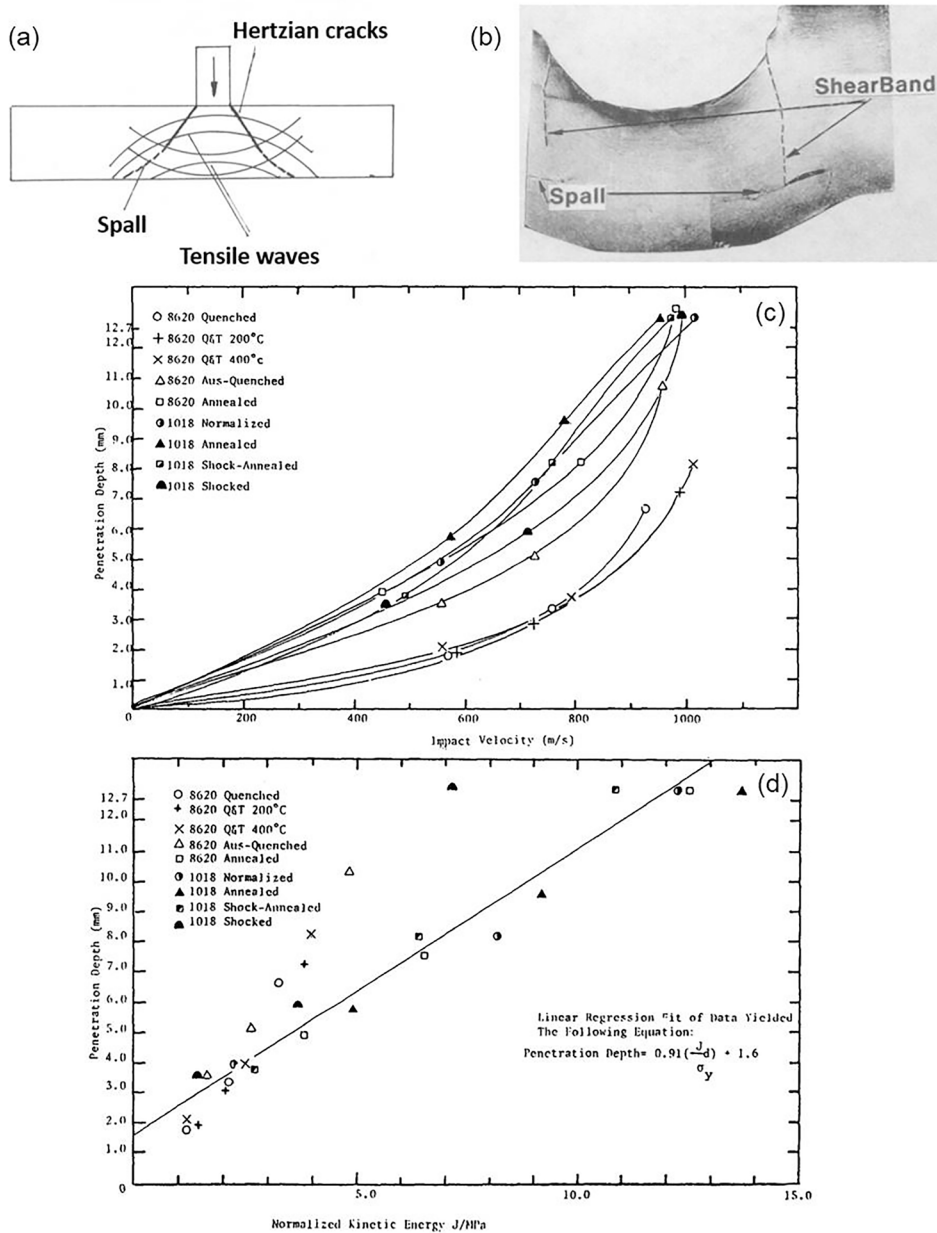


Fig. 15. (a) Schematic showing formation of conoid by combination of Hertzian contact stresses and tensile reflected stresses produced by ballistic impact; (b) Cross section of target AISI 8620 specimen quenched and tempered (shear band highlighted by dashed line); (c) impact velocity vs. measured penetration depth under room-temperature ballistic tests; (d) plot of normalized kinetic energy vs. penetration depth during ballistic tests [179].

3.5. Impact loaded Pre-notched plate

The single-edge and double-edge notched specimens with special geometries have been widely investigated, as shown in Fig. 16. Two geometries are designed with either a slit or a supplementary fatigue crack. A projectile impacting these specimens generates a Mode II shear loading around the crack. As the shear bands propagate, their velocity and the temperature evolution can be monitored and quantified.

Kalthoff and Winkler [182] and Kalthoff [183] investigated the plastic deformation near the crack tip in a prenotched rectangular maraging steel plate. The impact on one side of the notch by a cylindrical projectile along the axis of the notch was also carried out during experiment. Ravichandran and collaborators [115] used this geometry to investigate the initiation and propagation of shear bands. With a two-dimensional high-speed infrared camera, the temperature field evolution was recorded. The optical imaging of

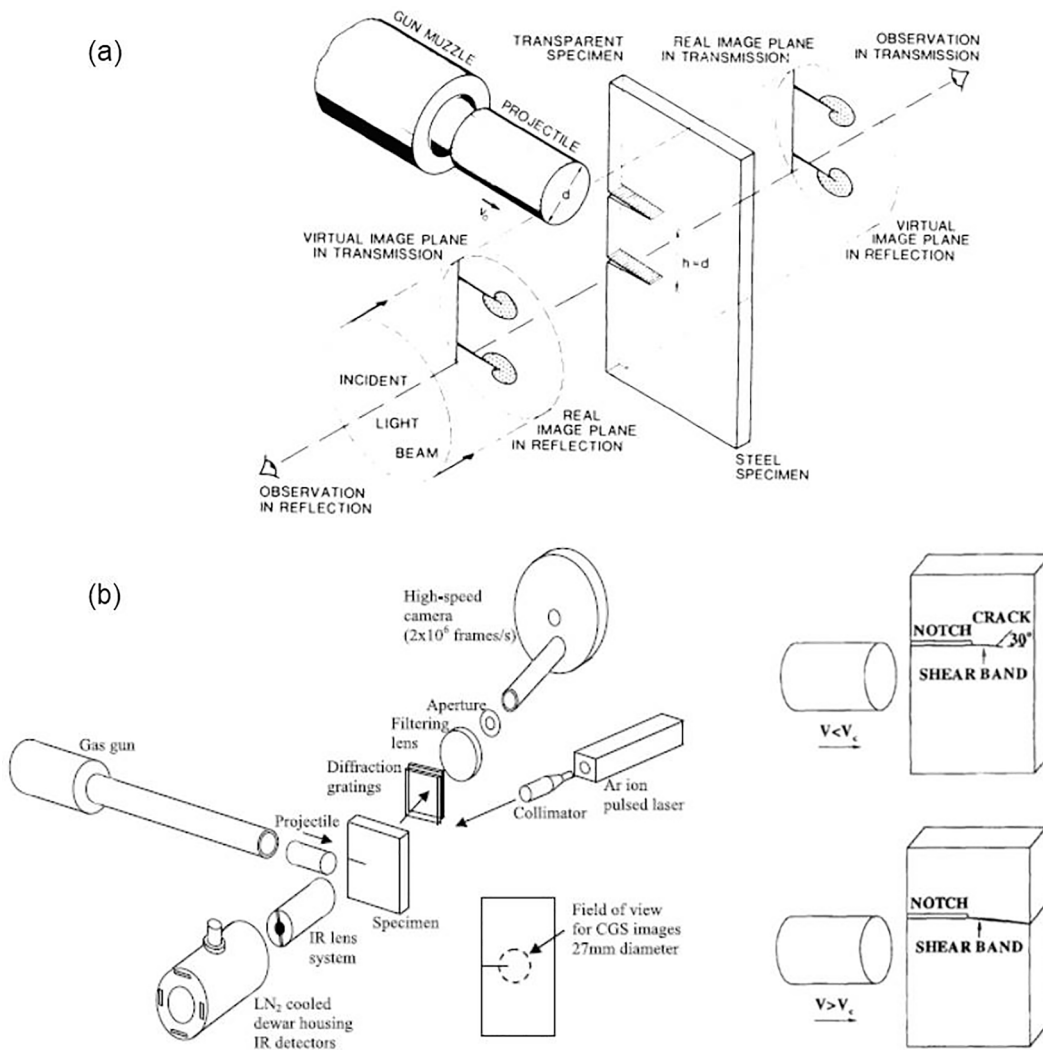


Fig. 16. Schematic illustration of the impacting pre-notched plate experimental setup: (a) double-edge notch specimen loading device and shadow optical arrangement; (b) single-edge notch specimen impact configuration and failure modes [115,153,183].

coherent gradient sensing was used to investigate the development of the mixed mode stress fields. The thermographs exhibited a diffuse shear-band tip and revealed a “hot spot” distribution in propagation direction of a well-developed shear band [153]. This will be shown later in Section 3.8. Such methods provide an effective way to investigate in-situ the entire process of dynamic deformation and shear failure. With the aid of an ultrahigh-speed camera and digital image correlation, the strain fields which describe the kinematics induced by both shear localization and crack propagation can be established. This provides a powerful approach to study the propagation and evolution of shear bands as well as cracks.

3.6. Mechanical Machining

In the engineering field, materials are often subjected to dynamic loading, such as chip formation during machining [184–188], punching [189], penetration [190–192], forging [193,194], high-speed friction [195], wear tests [196], and bird strikes on jet engines as well as airfoil leading edges [197]. Among them, the formation of ASBs in machining has been paid special attention by many researchers. This has been investigated by both experimental and theoretical methods in titanium [187,198,199], steels [184,200], nickel-based alloys [201], as well as metallic glasses [186,202].

Theoretical analyses on chip formation were carried out by Burns and Davies [203] using a one-dimensional continuum theory of machining initially proposed by Recht [1]. Failure of material linked with internal damage was introduced into the numerical modeling of chip serration based on the Johnson-Cook fracture model. Chen et al. [204] carried out orthogonal cutting testing on Ti-6Al-4V alloys and investigated the serration behavior of chips with an energy-based ductile failure model. Based on the analysis, the levels of peak and valley in serration were found to be proportional to the feeding rate. Calamaz et al. [205] incorporated a constitutive

law with the effect of strain rate, strain, and temperature on the flow stress, as well as a strain softening effect by assuming that the chip segmentations are only induced by ASBs to analyze the chip formation and shear localization during machining of Ti-6Al-4V alloy. Molinari et al. [206,207] investigated the shear localized zones produced along the tool-chip interface by the frictional heating and plastic deformation during continuous cutting processes. They also focused on the influence of the cutting speed and feeding rate on the formation of chip serrations [208]. This will be presented in greater detail in Section 7. Dai et al. [199] proposed a theoretical model based on Ti-6Al-4V alloy to analyze the spacing of segments at different cutting speeds by considering the momentum diffusion during unloading.

However, the accuracy of simulation for machining relies on the choice of the material constitutive equation, since an advanced simulation includes a good prediction of the final chip morphology based on the accurate estimation of the cutting and feeding forces. Calamaz et al. [205] demonstrated that the main reason for the mismatch between simulation and experiment was the choice of the material parameters in the Johnson-Cook equation.

3.7. Other dynamic testing techniques

In this section, we list some of the dynamic testing techniques beyond the ones presented above. Field et al. [209] provide an overview of the principal techniques for dynamically testing materials. Drop hammers, cam plastometers, Taylor impact, and flyer plate impact provide a range of strain rates not accessible through Hopkinson bars. For example, a drop-weight tower can produce a strain rate from 10^2 s^{-1} to 10^3 s^{-1} . O'Donnell and Woodward [69] studied the shear instability and flow behavior of 2024 aluminum alloy using the drop-weight test. The flyer-plate test is generally employed to investigate the shock-Hugoniot behavior at extreme high strain rates from 10^5 to 10^7 s^{-1} [210], in which the tested thin-foil specimen is fixed between an impactor and an anvil. Klepaczko [18] pointed out that since the material thickness is small, extremely high strain rates can be realized, which are much higher than those induced by the split-Hopkinson pressure bar.

Another powerful approach is the use of high-power pulsed lasers to study the materials extreme behavior subjected to pressures of hundreds of GPa up to several TPa in nanoseconds and at strain rates of 10^6 - 10^{10} s^{-1} [72]. It can reveal new mechanisms of plastic deformation [23], phase transformation [211], and even amorphization in materials [75]. This advanced experimental technique, assisted with novel diagnostics, *in-situ* analyses, and multiscale material characterization, helps scientists to answer some fundamental materials science questions, such as the ultimate tensile strength of metallic materials, the slip-twinning transition, dislocation mechanisms of void growth, and the different dislocation velocity regimes, such as the transition from thermally-activated to phonon drag. It also enables us to investigate the dynamic behavior under extreme conditions, especially in those regimes that are encountered in the interior of planets [212–216]. Mikkola and LaRouche [217] were the pioneers to investigate the ultra-short shock compression experiment. They accelerated flyer plates to impact foils with small thickness, producing pressure pulses with a duration time of 0.04 ns. Clauer et al. [73,74] explored the potential application of laser shock to strengthen aluminum alloys and stainless steels for the first time. More recently, Meyers and coworkers [75–77] carried out laser ablation driven shock compression experiments on covalently bonded materials; strain rates of $\sim 10^8 \text{ s}^{-1}$ were obtained by laser shock.

Detailed critical reviews on different types of testing techniques and shear specimens with their advantages and disadvantages have been presented in chapters from the book edited by Dodd and Bai [10] and the review by Meyer and Halle [141]. Meanwhile, the techniques for microstructural characterization within the shear bands have also been developed for several decades, aiming at higher resolution reaching the atomic scale. Antolovich and Armstrong [25] provide a comprehensive review on plastic strain localization, which contains a detailed description of the experimental techniques in the observation of shear bands.

3.8. Diagnostic investigations

A comprehensive understanding of ASBs requires detailed information about the onset of localization, strain, strain rate, and temperature evolution within the shear bands. High-resolution and fast-response infrared detection and optical imaging techniques offer an approach for recording the dynamic deformation process, and provide information not only for the experimental investigation but also for theoretical analysis. The pioneering works conducted by Kalthoff and Winkler [182,183] and by Marchand and Duffy [101] provide exact determinations of shear band propagation and failure mode transition. Detailed measurements of the temperature and strain during shear band evolution were carried out in HY-100 steel.

Since the typical width of shear bands is 1–200 μm , the direct measurement of temperature is quite difficult. One outstanding attempt to detect the temperature within the shear band by applying infrared radiation (IR) thermographic technique was made by Costin et al. [218]. With one single element, the average temperature rise around a 1 mm spot (obtained from a propagating shear band) was measured in low-carbon steel. The calculated temperature increase was only $\sim 100 \text{ }^\circ\text{C}$. Since the width of shear band was much smaller than the detector size, the estimation underestimated the real temperature increase inside the shear band. A more careful examination using a linear array of ten indium antimonide (InSb) IR detectors was performed by Hartley et al. [219] in two low-carbon steels. They found that the widths of shear bands in these steels were typically 150–250 μm and the highest temperature increase obtained was about $450 \text{ }^\circ\text{C}$ using spot sizes of 20 μm . Then, Marchand and Duffy [101] applied a linear array of 12 InSb IR detectors to determine the temperature increase within shear band in a specimen of HY 100 steel. The shear band width was about 10–20 μm and the temperature rise was around $600 \text{ }^\circ\text{C}$. They also assessed the shear-band propagation velocity to be 250–500 m/s. Ranc et al. [220] combined two pyrometer techniques for the measurement of temperature during shear-band propagation. For the low temperature range, 32 photovoltaic InSb detectors are used; meanwhile, for the high-temperature range, an intensified CCD camera with a visible spectral band was used. A detailed measurement approach for the emissivity of material surface that related to the main error in

determination of temperature was also presented. A maximum local temperature of around 1000 °C in the shear band was detected right before failure in dynamic torsion experiment of titanium alloys. Guduru et al. [153] employed coherent gradient sensors and a two-dimensional high-speed array with the acquisition rate of 10^6 frames per second, to investigate the change of the stress intensity factors in mixed mode and temperature distribution during the initiation and propagation of a shear band. The transition of a plastic zone near crack tip to a shear band and the propagation of shear band at the tip were first observed. A non-uniform temperature field with “hot spots” along the well-developed shear band was revealed. They also reported a local temperature rise of up to 600 K in a C-300 maraging steel. A high-speed optical camera was also used to obtain visualized infrared images of shear-band initiation in bulk metallic glasses, like La-based materials [221].

Giovanola [222] determined the temperature, strain, and strain rate evolution, as well as stress–strain curve during shear-band formation using a high-speed photographic technique. A maximum temperature rise of 1100 °C in 4340 steel by SHPB was

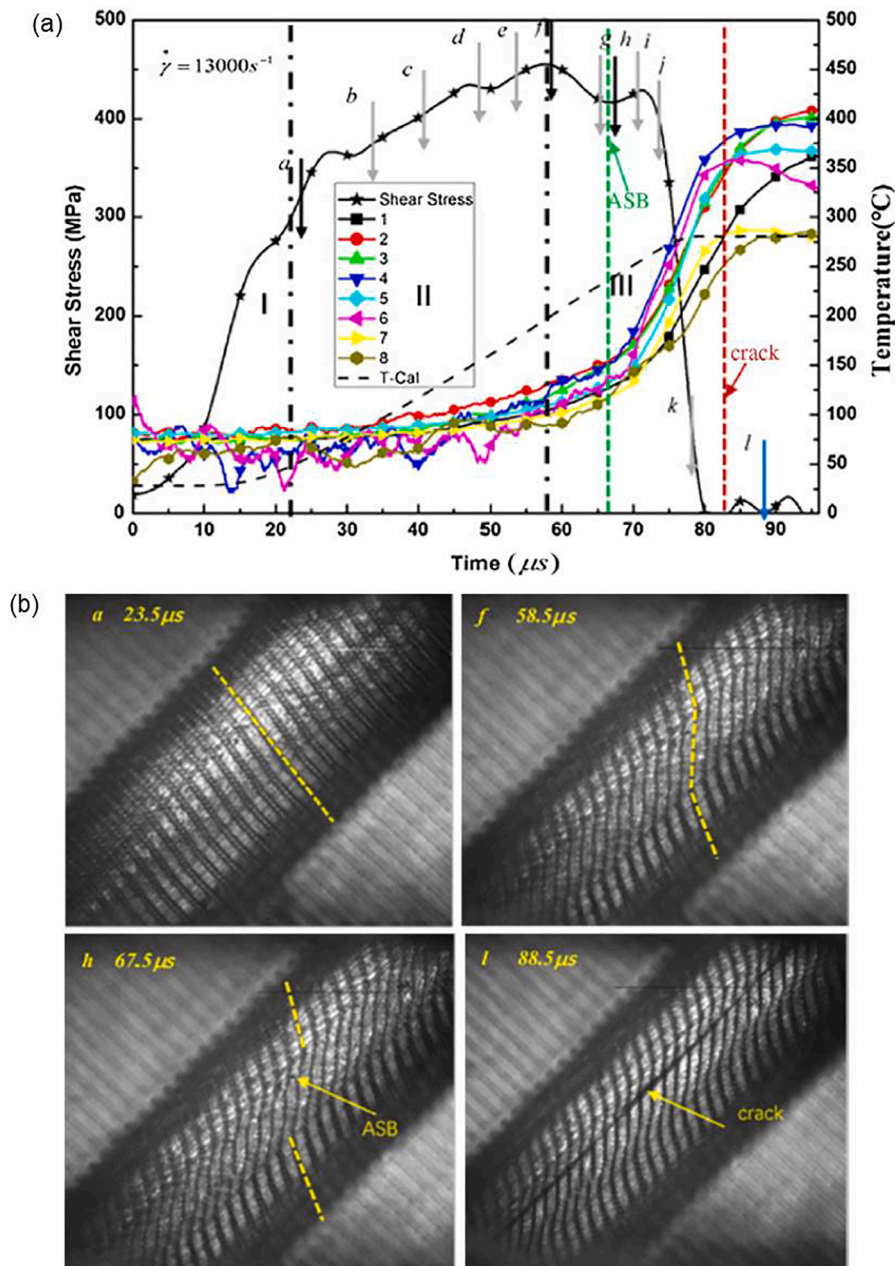


Fig. 17. The evolution of shear band in CP titanium with time during impact loading with SHPB: (a) Deformation and temperature histories of a shear-compression CP titanium specimen; (b) Four representative high-speed photographic snapshots showing the deformation of a shear-compression specimen under dynamic loading [225].

estimated. Zhou et al. [115,116] studied the velocity of shear-band propagation and the corresponding temperature rise using a single-edge notched rectangular plate of C300 maraging steel. Since the shear band initiated from a notch tip, it could be imaged while propagating at speeds up to 1,000 m/s that were measured by employing a high-speed camera. They also found that, at a certain impacting speed, a shear band starts, propagates, arrests within the specimen and a mode I crack forms with an angle of about 35° to the shear band propagation direction from the tip of the arrested shear band. The temperature profile captured within the shear bands can facilitate the modeling of temperature evolution during shear localization. Raabe and his coworkers [223] carried out non-contact measurements with an infrared high-speed thermal camera to record the temperature rise with the increase of strain. Another X-ray digital imaging correlation (XDIC) method was employed to describe the dynamic deformation and fracture behavior in titanium alloys at the Advanced Photon Source by Wu et al. [224]. Additional details of the technique are presented in Section 3.2. This *in-situ*, synchrotron-based, high-speed X-ray phase contrast imaging was applied to map strain fields with adequate results for mesoscopic measurements under dynamic loading. Systematic errors for the displacement and strain measurements were constrained under 0.01 pixel and 0.1%, respectively. XDIC provided small speckles and high spatial resolution for measuring both surface and internal deformation fields, suggesting a promising method for the investigation of shear localization and some other cases in small samples or even very local areas, e.g., welding joints, and precious materials.

Recently, Guo et al. [225] synchronized the SHPB with a high-speed photographic system and an IR temperature measurement system to identify the roles of strain, strain rate, and temperature during adiabatic shear localization in commercial titanium. The temperature measurement system can provide a range from 60 °C to 1200 °C with response time < 1 μs. The deformation evolution of the material was recorded by a high-speed camera with the highest framing rate of 5 × 10⁶ fr/s and spatial resolution of 50 μm. This provided a direct identification of the significant events, such as collapse, strain localization, temperature increase, shear band initiation, and maximum temperature, as shown in Fig. 17. The stress collapse between *i* and *j* in Fig. 17 (a), corresponds only to the onset of temperature rise, suggesting that localization precedes material heating; however, the difference in time is minimal, ~10 μs. There are several possible interpretations for these results. Fig. 17 (b) shows the displacement at times *a*, *f*, *h*, and *l*. The shear-band width increases with strain. The maximum temperature measured was about 400 °C.

4. The formation of shear bands

The development of criteria for shear-band formation has been an important endeavor for the prediction of the stability of the deformation of materials and often incorporated the thermal excursion in a mechanical stability analysis.

The localization of plastic deformation into a shear band, as presented in Section 2, is defined as a competition between the hardening and softening mechanisms. This has been discovered in metals; however, metallic glasses, ceramics and polymers under high strains and strain rates also obey similar laws. It has been established that the thermal and microstructural softening effects are the most dominant component during shear localization. Since most of the plastic work done is translated to heat, the resulting effect is the temperature rise. The associated thermal softening leads to the decrease of the yield stress. Based on this premise, a number of analytical and numerical approaches have focused on the initiation of shear bands. It should be mentioned that shear localization may also form by other softening mechanisms, for example texture development at large strains or ductile void growth. In rocks and ceramics, it occurs by a process of comminution. This was established and modeled for SiC by Meyers and co-workers [226,227].

4.1. Initiation conditions for shear localization

The predictions of shear instability strain and evolution of deformation within a shear region have grown in complexity since they were first introduced in the 60 s. Single expressions have given way to analyses using the perturbation theory and other mathematical and computational tools, especially finite element methods. We will present the principal ones in this section.

It is shown in Eq. (1) that the expression of shear stress τ can be constitutively expressed as a function of shear strain γ , shear strain rate $\dot{\gamma}$, and temperature T . Based on it, Recht [1] proposed that adiabatic shear instability happens when materials “soften” or the shear stress drops with increasing strain γ :

$$\frac{d\tau}{d\gamma} \leq 0 \quad (5)$$

One obtains this classical condition for instability by taking the derivative of Eq. (2) with respect to γ :

$$\frac{d\tau}{d\gamma} = \left(\frac{\partial \tau}{\partial \gamma} \right)_{\gamma, T} + \left(\frac{\partial \tau}{\partial \dot{\gamma}} \right)_{\gamma, T} \frac{d\dot{\gamma}}{d\gamma} + \left(\frac{\partial \tau}{\partial T} \right)_{\gamma, \dot{\gamma}} \frac{dT}{d\gamma} \leq 0 \quad (6)$$

Culver [2] proposed a similar criterion, which led to a critical shear strain γ_c given by:

$$\gamma_c = \frac{n\rho C_v}{\beta \left| \frac{\partial \tau}{\partial T} \right|_{\gamma, \dot{\gamma}}} \quad (7)$$

where, ρ is the density, C_v is the specific heat capacity at constant volume, n represents strain-hardening (or working-hardening) exponent, $\left| \frac{\partial \tau}{\partial T} \right|_{\gamma, \dot{\gamma}}$ is the thermal softening, and β is a constant expressing the ratio of the heat generated by plastic work, which is

equivalent to the Taylor-Quinney conversion and is usually taken as 0.9 for metals. The validity of this assumption will be discussed in Section 4.2.

A similar criterion was proposed by Staker [40]:

$$\gamma_c = \frac{n}{-\frac{1}{C_v \rho} \left(\frac{\partial \tau}{\partial T} \right)_{T, \dot{\gamma}} - \frac{m}{\dot{\gamma}} \frac{d\dot{\gamma}}{d\gamma}} \quad (8)$$

where m is the strain-rate sensitivity. Since $0 \leq m \leq 1$ for larger strain-rates, the second term in the denominator can be neglected and the Staker criterion reduces to the Culver criterion.

Meyers et al. [37] used a constitutive equation based on the Johnson-Cook equation with a power-law thermal softening component to reach the critical shear strain for adiabatic shear localization of titanium at a constant strain rate and temperature:

$$\sigma = (\sigma_0 + B\epsilon^n) \left(1 + C \log \frac{\dot{\epsilon}}{\dot{\epsilon}_0} \right) \left(\frac{T}{T_r} \right)^A \quad (9)$$

where σ , ϵ and $\dot{\epsilon}$ are the normal stress, strain and strain rate, respectively, T and T_r are the examined and reference temperatures (initial, 298 K), σ_0 is the yield stress at the reference temperature, $\dot{\epsilon}_0$ is the reference strain rate, and B , n , C , and A are experimentally determined parameters. The deformation work can be translated into an (adiabatic) temperature rise:

$$dT = \frac{\beta}{\rho C_v} \sigma d\epsilon \quad (10)$$

where β is the Taylor-Quinney factor. By substituting Eq. (10) into Eq. (9), the instability strain ϵ_c can be estimated by $d\sigma/d\epsilon = 0$, one can get:

$$A(\sigma_0 + B\epsilon_c^n)^2 = -Bn\epsilon_c^{n-1} \frac{\rho C_v T_r^A}{0.9} \times \left[T_r^{1-A} + \frac{0.9\epsilon_c(1-A)}{\rho C_v T_r^A} \left(\sigma_0 + \frac{B\epsilon_c^n}{n+1} \right) \right] \quad (11)$$

The corresponding temperature can be obtained from:

$$T = \left[T_r^{1-A} + 0.9(1-A)\epsilon \frac{1 + C \log \frac{\dot{\epsilon}}{\dot{\epsilon}_0}}{\rho C_v T_r^A} \left(\sigma_0 + \frac{B\epsilon^n}{n+1} \right) \right]^{1/1-A} \quad (12)$$

The instability strain can thus be estimated.

Instead of assuming that instability occurs at a critical strain, Clifton [42] presented an elementary linear perturbation analysis of the stability of quasi-static, simple shear, incorporating the effects of heat conduction, strain hardening, strain-rate sensitivity, and thermal softening. The resulting expression has the form:

$$\left[\frac{1}{\tau} \left(\frac{\partial \tau}{\partial \gamma} \right) + \frac{\alpha}{\rho C_v} \left(\frac{\partial \tau}{\partial T} \right) \right] m \dot{\gamma} + \frac{\lambda k^2}{\rho C_v} \leq 0 \quad (13)$$

where k is the wave number for the initial perturbation which is the wavelength divided by 2π .

Bai [43,44] developed a similar perturbation analysis leading to the criterion expressed by the solution of the equation:

$$\rho^2 C_v \alpha^3 + \rho \left[\beta P_0 \dot{\gamma}_0 + (\lambda + C_v R_0) k^2 \right] \alpha^2 + (\lambda R_0 k^2 + \rho C_v Q_0 - \beta \tau_0 P_0) k^2 \alpha + \lambda Q_0 k^4 = 0 \quad (14)$$

where, the subscript 0 is the reference state, α is a perturbation term (reciprocal of the characteristic time), λ is thermal conductivity, $Q = \left(\frac{\partial \tau}{\partial T} \right)_{\dot{\gamma}, T}$ is work-hardening, $R = \left(\frac{\partial \tau}{\partial \dot{\gamma}} \right)_{T, \dot{\gamma}}$ is strain-rate sensitivity, and $P = -\left(\frac{\partial \tau}{\partial T} \right)_{\dot{\gamma}, T}$ is the thermal softening.

Generally the critical strain for initiation decreases with increasing strain rate [228], which results from the increase in strength at higher strain rates [108]. Low strain-rate sensitivity reduces the strain for initiation of shear bands [229]. Shear localization is inhibited by strain hardening [229]. However, it is commonly assumed that the instability of shear bands results from thermal softening [10,12]. Internal heat generation is considered to be vital for the initiation of ASBs, and is incorporated in the classical Johnson-Cook model [230,231], the Kocks-Mecking model [232,233], continuum viscoplasticity models [116,234], and crystal plasticity models [235–237].

In general, the predominant criterion for the onset of adiabatic shear localization is the attainment of a critical strain value. This parameter can also be considered as a failure criterion for the engineering design, which marks the onset of the catastrophic failure.

There are numerous initiation sites for shear bands, which can be due to geometrical or microstructural inhomogeneities. Armstrong [238] and Armstrong and Zerilli [239] proposed that dislocation pile up releases were an important microstructural mechanism of strain and heat localization in BCC metals and could trigger the initiation of shear bands. Indeed, they proved, through calculations [239], that the local temperature rise produced by a pileup upon bursting through a grain boundary was significant. Meyers et al. [37]

commented on other internal inhomogeneities which could give rise to the initiation of shear localization. Fractured second-phase particles, can generate strain concentration in the matrix at the extremities of the fracture. Some grains can undergo orientational softening by rotating towards a lower Schmid factor with plastic strain, decreasing its “effective” flow stress. This results in a concentration of strain in this grain, with an associated temperature increase. In martensitic alloys, such as quenched steels, martensitic lenses or laths are crystallographically oriented within each grain. Inter-lath or inter-lens sliding becomes a favored deformation mechanism because the retained austenite has a lower flow stress than the transformed region. Thus, there will be a tendency for localized heating and shear-band initiation; the same happens in mechanical twinning.

4.2. The Taylor-Quinney conversion parameter

Taylor and Quinney [34] investigated the temperature rise (using thermocouples attached to the specimens) in severe plastic deformation by torsion and compression tests in copper, mild steel, and decarburized mild steel, the latter being essentially equivalent to pure iron. They also performed calorimetric measurements. Their results were consistent and showed that the conversion of plastic work into heat had an efficiency between 80 and 100 percent. This parameter became known as the Taylor-Quinney parameter and is usually designated by β ; it is used in coupled thermomechanical equations to estimate the temperature rise. It should be mentioned that these original, carefully conducted measurements, date from 1934, the year in which dislocations were postulated. The fraction of work stored in the material agrees well with calculations based on dislocation evolution and their self-energy; this value, the stored energy of cold work, represents 10 to 20 pct. of the deformation energy. Fig. 18 (a) shows the evolution of β in aluminum measured with IR detectors during a Hopkinson (Kolsky) bar experiment. The agreement with the early experiments by Taylor and Quinney is evident, in spite of the very large difference in strain rate. Indeed, if the strain rate is above 800 s^{-1} , the process can be assumed to be adiabatic, simplifying the analysis. The results obtained by Mason et al. [240] using IR detectors for titanium were surprising: β increased with plastic strain to close to 1 and then decreased to 0.5 for a strain of 0.17. Similar experiments conducted on 4340 steel, 2024 Al, Ti-6Al-4V, and Inconel 718 confirmed lower values of β in the dynamic regime. The experiments by Smith et al. [241] used simultaneously digital image correlation and IR measurements which, together, can establish the spatial and temporal variation of β in dynamic tension experiments.

The crucial question that needs to be answered is: *where does the deformation energy go, if the temperature increase is significantly lower than the original Taylor-Quinney estimate?* Twinning, phase transformations, nanometer and micrometer sized cracks, can all contribute

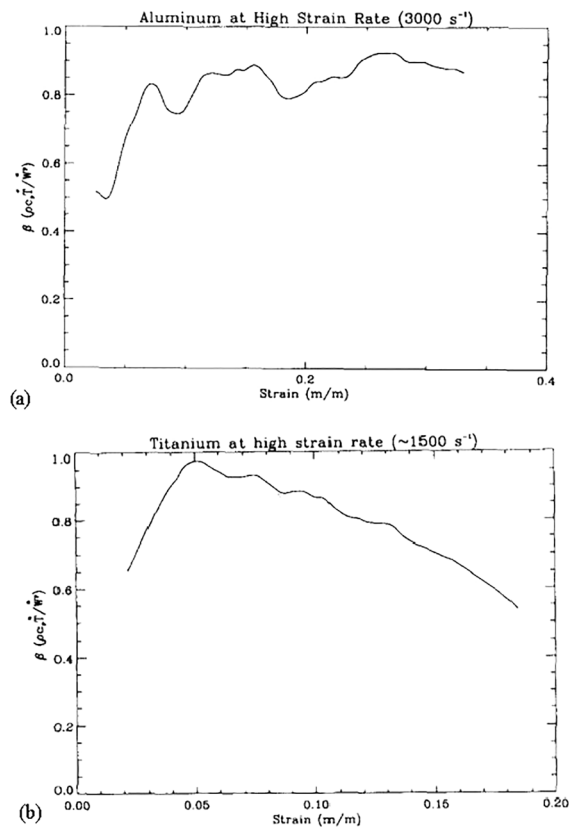


Fig. 18. Taylor-Quinney conversion parameter β expressing fraction of deformation work transformed into heat for (a) 2024 aluminum and (b) Ti-6Al-4V [240].

to permanent deformation and do not necessarily have the same energetics as dislocations. As Taylor and Quinney [34] pointed out in 1934, there are also possible temperature differences between the inside and surface of the specimens which contribute to differences. Importantly, the stress state at the surface is different from the interior as the lateral constraints are relaxed by the boundary conditions (biaxial vs. 3D stress state). This aspect has yet to be considered by researchers. Additionally, the defect evolution of the surface and bulk are different. It is not implausible to think that the dislocations close to the surface exit the specimen, with a decreased work hardening.

4.3. Evolution of shear bands

Critical conditions, orientation directions, and initial growth rate for shear-band formation have been derived through various numerical models for viscoplastic materials including metals and polymers. Shawki et al. [242] developed an ordinary differential equation to describe the local evolution of the plastic strain rate during simple shear deformation in a thermo-viscoplastic material by neglecting the elastic deformation and heat conduction effects. Meanwhile, the shear localization is presented in forms of the qualitative behavior of the aforementioned ordinary differential equation. Molinari and Clifton [229,243] applied a fully nonlinear closed form analysis to predict the critical conditions for shear localization in thermo-viscoplastic materials subjected to simple shear deformation.

These idealizations neglect heat conduction, inertia, and elasticity. The explicit results showed the roles of strain-rate sensitivity, thermal softening, strain hardening rate, and initial imperfections on the shear localization behavior. Burns [244] applied a two-timing asymptotic expansion of a particular constitutive model to consider the time-dependent homogeneous solution in the stability analysis. Anand et al. [245] introduced a tridimensional generalization of the linear perturbation analysis to investigate the initiation of shear localization. The prediction of critical formation conditions, emergent direction, and incipient growth rate of a shear band under both quasi-static isothermal deformation and dynamic adiabatic shear-band deformation conditions was qualitatively correct. Wright et al. [246–249] investigated the problem of shear-band formation around a small initial perturbation in one dimension by applying a fully nonlinear finite element calculation. It also included small variations in initial temperature or in material strength as well as geometrical defects to obtain a further generalization prediction for the initiation of a shear band.

Fressengeas and Molinari [250] presented a novel relative perturbation method accounting for non-steady plastic flow in a thermal-viscoplastic hardening material with heat conduction. It provided the criteria for both instability and localization which showed better agreement with the available nonlinear results and experimental data.

Giovanola [222] concluded that void initiation and development did not occur before the inception of thermomechanical instability. The loss of load-carrying capability was attributed to the void nucleation process. Thus, the softening was due to geometric effects instead of temperature. In agreement with Giovanola [222], Bai, Xue, and coworkers [102,251] also concluded that void or crack nucleation was the factor leading to the loss of load-carrying ability in steels and titanium alloys. The remnants of these elongated voids are seen in the surfaces of the separated parts after Hopkinson torsional bar experiments. Nevertheless, transmission electron microscope examinations of specimens prior to failure (principally, hat-shaped specimens where the forced shear was interrupted at various stages prior to fracture) revealed that dynamic recrystallization preceded void or crack generation, growth, and coalescence. Flockhart et al. [252] proposed an approach by correlating the onset of adiabatic shear failure to the appearance of velocity discontinuities, which can be revealed by the shear strain-rate maxima in the finite element simulation in high-rate deformation problems. Xing et al. [253] investigated the instability evolution in adiabatic shear localization in hot-rolled low-carbon steel both experimentally and numerically. They found that several fine shear bands, which are the shear fluctuations, developed before the onset of the final shear localization and some of these finite amplitude disturbances evolved into fully developed shear bands.

Schoenfeld and Kad [254] described a 2D plane strain model for polycrystalline Ti-6Al-4V alloy by applying the single-crystal theory as a constitutive routine within an explicit finite element code. In their work, both slip and twinning were incorporated, which are related to different local flow stresses, depending on the cell orientation. The influence of anisotropy on ASB formation was explicitly demonstrated. The work of Clayton [255] who considered large strains, thermodynamics, nonlinear elasticity, energy storage mechanisms, and volume changes related to residual stress fields of lattice defects in modelling the dynamic performance of aluminum alloys should also be mentioned. A coarse-grained crystal plasticity model was proposed, indicating that microstructure is instrumental in improving the impact toughness of these materials by increasing their shear strength or by initial processing that enhance the activity of dynamic energy storage mechanisms related to dissipation mechanisms. This was studied numerically by Dolinski et al. [256] and was demonstrated to be successful for a variety of problems involving high strain-rate loading. Kuriyama and Meyers [257] also found that the stress and strain distributions at the tip of a shear band (the ‘process zone’) were non-uniform by applying the finite element method to the elastoplastic material exhibiting softening as shown in Fig. 19. They showed that the “adiabatic” material (Ti) exhibits greater strains than the “parabolic” (continuously hardening) material at the same position and applied traction. The treatments above do not incorporate any structural changes.

Dynamic recrystallization (DRX) has been recognized as an important component during the formation of adiabatic shear localization. Medyanik et al. [258] considered a criterion based on a dynamic recrystallization deformation mechanism. It is formulated in terms of temperature and strain rate to predict the initiation and propagation of dynamic ASBs, as well as the onset of ductile failure. Dynamic recrystallization is presumed to instigate the material to act like a viscous fluid, leading to the collapse of flow stress. This mechanism needs elevated temperatures to trigger dynamic recrystallization and subsequent shear-band formation. Thus, adiabatic shear localization is proposed to influence not only a mechanical instability but also the microstructural softening prior to any softening. The discontinuously evolving damage mechanism cannot be recognized as an abrupt instability by previous theory, and is described as a gradual transition process that contains nucleation, growth, and failure stages [259]. A critical value of the stored energy

of cold work is suggested to dominate the formation of DRX and subsequent shear localization process [260]. In other words, these authors proposed that the microstructure softening transformations dominated by the stored energy by cold working, such as DRX, are responsible for the formation of an adiabatic shear band. Bronkhorst et al. [138] have also modeled the process of adiabatic shear-band formation using DRX as a trigger for the discontinuous drop in the flow stress. Their contribution is discussed in Section 12.

Andrade and Meyers [108] proposed a modification of the Johnson-Cook equation incorporating a discontinuous drop in strength caused by recrystallization. This is shown in Fig. 20, where the flow stresses at the plastic strain 0.3 and different temperatures are presented for cold-worked and shocked-hardened copper. There is a good fit between experimental results and the modified Johnson-Cook equation with a proper choice of parameters. The flow stress decreases discontinuously with a drop at the dynamic recrystallization temperatures: $\sim 600\text{--}700\text{ K}$ ($\sim 0.5 T_{\text{melting}}$).

A physics-motivated model for evaluating the combined roles of thermal softening and microstructural softening through dynamic recrystallization (DRX) in ASB onset was developed by Longère [261]. He also presented a unified method to demonstrate entire processes of deformation, involving different stages of shear localization in the large-scale postulated framework. Two extreme conditions were proposed based on the simulation results: one is for late DRX initiation where ASB onset is determined by thermal softening and the other is for early DRX initiation where ASB onset is mainly attributed to microstructural transformations. Between these two conditions, both softening mechanisms play important roles in the onset of ASB. The dynamic recrystallization mechanism will be presented in detail in Section 12.

Although thermal considerations have been extensively investigated, many aspects related to the formation of ASBs have also been explored both numerically and experimentally. Numerical modeling performed by Needleman and Tvergaard [262] demonstrated that microvoid-induced damage softening is also important in addition to thermal softening during ASB onset. Cowie et al. [263] also revealed that micro-void damage can play an important role in the initiation of shear bands under high strain-rate loading. They observed that failure initiates and develops by progressive nucleation, growth and coalescence of microvoids and microcracks during shear deformation in ultrahigh-strength steels. The sudden drop of flow stress in the deformation area was related to microvoid formation as a softening mechanism. Once the failure initiates, the combination of thermal and microvoid softening effects will compete with the strain hardening effect within the adiabatic shear band.

Kudryashov et al. [264] considered the process of adiabatic shear localization using a one-dimensional model in an infinite slab of incompressible elastic, thermo-visco-plastic material by involving a strain hardening factor. They presented a finite difference approach based on the Courant-Isaacson-Rees scheme which enables observing the processes from initiation of ASB to the final stage. They also concluded that the strain hardening effect changes the quantitative characteristics of the formation of shear bands. The total number of the ASBs and the average distance between them are predicted numerically. It shows that the average distance between ASBs in HY-100 steel tends to follow the Grady-Kipp estimation but that for OFHC copper is closer to Wright-Ockendon and Wright-Zhou-Ramesh estimations. A detailed treatment of ASB spacing will be presented in Section 11.6.

Zhang et al. [265] performed thermo-mechanical crystal plasticity calculations considering internal heat generation to describe the dynamic loading of an HCP polycrystal. They confirmed previous findings presented earlier in this section (Molinari and Clifton [229,243]; Fressengeas and Molinari [250]) that the balance between plastic heat generation and thermal diffusion plays a significant role in controlling thermal softening, strain localization, and ASB formation. The microstructure was considered to play an important role in ASB initiation and propagation, as well as their arrest and disruption. At a higher strain-rate, the heat dissipation rate was higher due to the decreased heat conduction, inducing a much higher temperature, thermal softening, and further slip development as well as

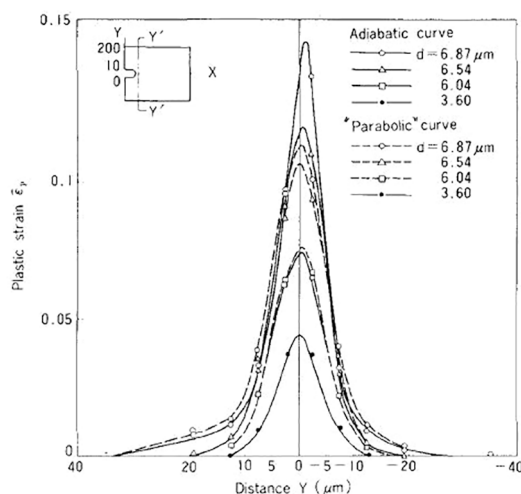


Fig. 19. Comparison of process zone (inferred from plastic strain distributions along $Y'Y'$) between a material with adiabatic stress-strain curve and with monotonic (parabolic) work-hardening curve. The calculated adiabatic curves are full and the parabolic ones dashed. The plastic strains in the adiabatic curve are higher than in the ones for parabolic hardening at the same positions ahead of the band tip. Thus, the propagation is easier for the adiabatic case [257].

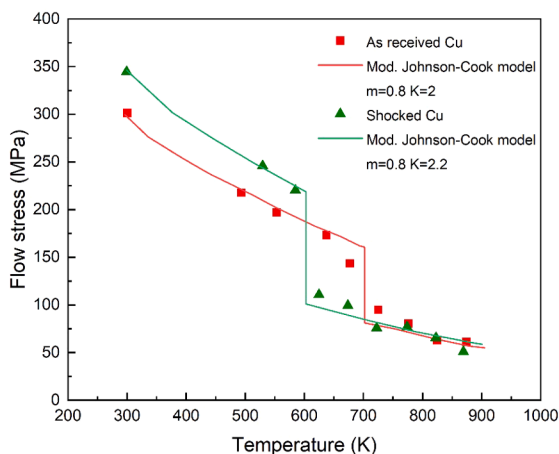


Fig. 20. Experimentally determined and computed flow stress (at a plastic strain of 0.3) as a function of temperature for: (red) cold-worked and, (green) pre-shocked copper. Recrystallization produces a discontinuity in flow stress, with pronounced softening [108]. (For interpretation of the references to color in this figure legend, the reader is referred to the web version of this article.)

enhanced internal heat generation, finally leading to the formation of the ASB. At a lower loading rate, thermal conduction re-distributes temperature fields and inhibits strong softening as well as strain localization, leading to much more diffuse shear bands. They also found that thermal perturbation (“hot spots”), resulting in local sharp temperature gradients developed in strained regions, leading to local thermo-mechanical heterogeneities and to instability and formation of shear bands. As seen in Fig. 21, shear bands develop from the “hot spots” labeled as h1, h2, h3 and h4 and a heterogeneous temperature distribution exists within the shear bands [265]. Using the finite simulation method, Teng et al. [266] proposed that the “hot spots,” where temperature rises more significantly, occur periodically and act as the initiation sites for the crack. It is concluded from both simulation and experimental results that the formation and linkage of micro-cracks within the shear band results in a single major crack.

In addition, Marchand and Duffy [101] proposed that the development of shear banding consisted of three stages: first, the deformation is homogeneous before the onset of shear instability; second, right after the initial instability, plastic strain becomes mildly heterogenous while the plastic deformation zone is retained; third, the deformation zone localizes in a narrower region, the stress drops significantly, and shear localization occurs. Instability originates when stable and homogeneous plastic deformation becomes heterogenous. This is just the inception of the heterogenous deformation instead of the onset of the ASB, while the stress collapse is a fast-growing dynamic process corresponding to the inception and development of ASB. Xu [150] investigated the dynamic deformation behavior of an armor steel at shear strain rates ranging from $5 \times 10^3 \text{ s}^{-1}$ to $4.5 \times 10^4 \text{ s}^{-1}$ using newly-designed double shear specimens. The relationship between shear stress and strain, and the deformation profiles of the specimen are presented in Fig. 22 (a). Three regimes were also defined as the elastic regime, the plastic deformation regime, and the failure regime, corresponding to increasing shear strains in the specimen.

The separation into two stages, instability and localization, was also emphasized by Wright [12] as one of the foundations of ASB formation. Instability sets in when $d\tau/d\gamma < 0$. Localization, with the formation of an adiabatic shear, occurs at a higher strain. This is

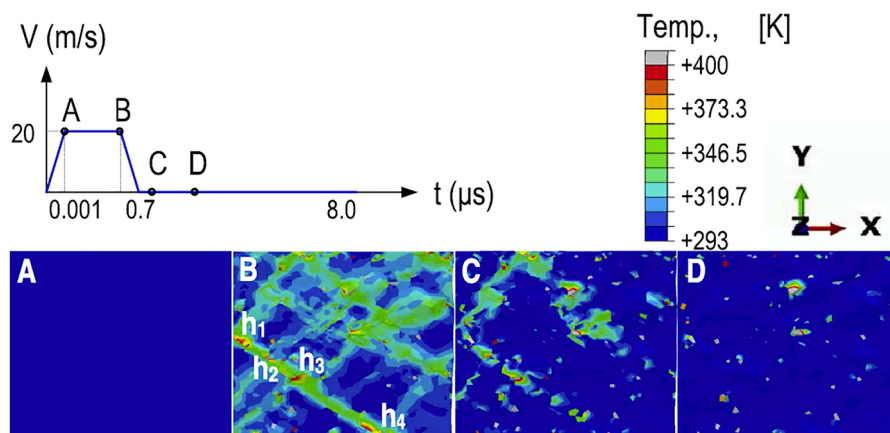


Fig. 21. The simulated temperature variation during loading (A, B) and unloading (C, D) of the polycrystalline specimen. The illustration of temperature distribution corresponds to points A, B, C and D shown in the target velocity–time curve [265].

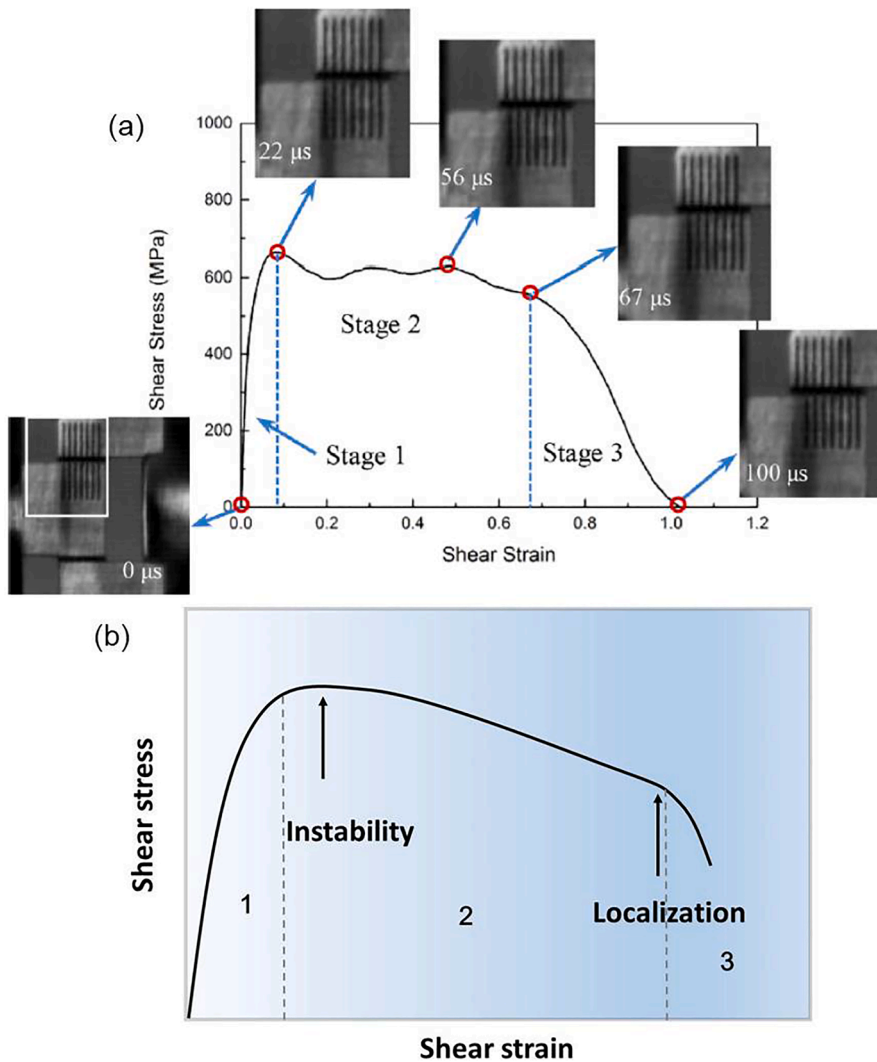


Fig. 22. Sequential stages of adiabatic shear-band formation. (a) Shear stress-shear strain curve for armor steel at the strain rate of $14,000 \text{ s}^{-1}$ [150]; (b) Schematic showing instability (maximum in the curve) followed by localization.

shown in Fig. 22 (b). The distinction between instability and localization was discussed in the early work of Molinari and colleagues between 1985 and 1988; the three stages of the adiabatic shear band process were also described by Molinari and Clifton [243].

Fressengeas and Molinari [250] established, using a relative perturbation method, the criteria for instability and localization for a material with constitutive equation given by:

$$\tau = AT^{\nu}(\dot{\gamma})^m\gamma^n \quad (15)$$

where ν , m , and n are thermal softening, strain rate sensitivity, and work hardening, respectively, and A is a pre-exponential parameter.

Instability: $\nu + n < 0$,

Localization: $\nu + n + m < 0$.

For a material to undergo instability, the thermal softening term ν , which is negative, has to numerically exceed work hardening n . For localization, the thermal softening has to exceed the magnitude of the sum $(m + n)$.

All these works certainly have blazed a trail in the study of the shear localized deformation, but microstructural evolution during shearing was not revealed, and the relationship of the mechanical parameters with the microstructures in the shear bands are of significance, and need to be explored. The original SHPB cannot record the microstructure changes during localization. However, Bai and Xue et al. [52], who have modified the original SHPB (Section 3.1) by incorporating torsion, combined the measurements of the mechanical parameters with corresponding microstructures as well as the formation and evolution processes of shear localization.

Very precise experiments need to be conducted to reveal the relative contributions of thermal softening and microstructural softening to the evolution of shear bands. Dynamic recrystallization (DRX) is the primary microstructural evolution mechanism. The

potentially important role of microstructure (e.g. texture) in both promoting and inhibiting ASB initiation and propagation in materials cannot be ignored. However, the contributions and importance of each mechanism to the overall shear failure process are still incompletely understood.

5. Estimation of characteristic parameters during shear localization

Since the thermo-mechanical history during shear-band formation is rather complex, thermal excursion is an important factor during the initiation of shear localization. Meanwhile, the shear-band thickness is also dominant in the propagation and evolution process of the shear band. Theoretical models have been established to predict the local heat generation, shear-band width, and velocity of propagation; they are discussed in this section.

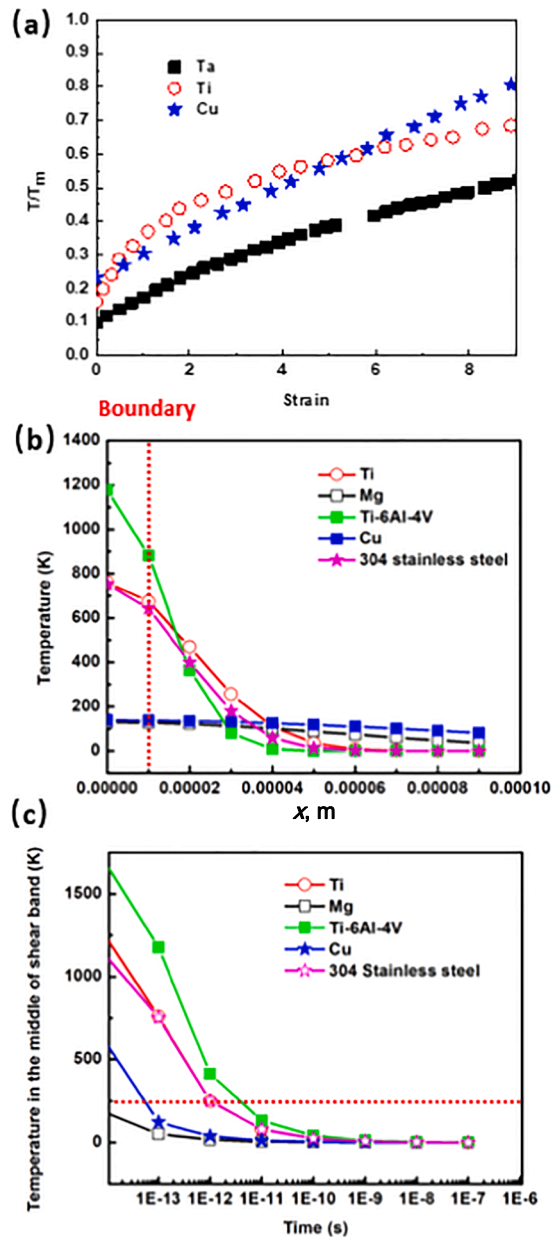


Fig. 23. The calculated temperature evolution of shear bands with (a) strain [19]; (b) distance to the SB center and (c) time in different materials.

5.1. Calculation of temperature rise and cooling rate

The temperature increase and subsequent cooling of the shear band can be calculated at different levels of exactness. A simple situation, based on the Johnson-Cook equation combined with the (adiabatic) temperature rise from deformation energy, will be presented below. The heating process is assumed to be adiabatic, with no heat exchange to the surrounding environment. This leads to an adiabatic temperature rise from a reference temperature T_r . Once the deformation stops, heat transfer to the surroundings starts and the temperature T in the shear band decreases until equilibrium with the surroundings. A semi-infinite body is assumed for simplicity. The temperature T is therefore strictly a function of the true strain ϵ as presented in Fig. 23 (a) for copper, titanium, and tantalum [19]. The temperature rise was estimated with the conversion of the deformation energy to the internal energy by the Taylor-Quinney factor β (this ratio defined in Eq. (10)):

$$\sigma = (\sigma_0 + B\epsilon^n) \left(1 + C \ln \frac{\dot{\epsilon}}{\dot{\epsilon}_0} \right) e^{-A(T-T_r)} \tag{16}$$

$$T = T_0 + \frac{1}{A} \ln \left[e^{-A(T_0-T_r)} + \left(\frac{\beta A}{\rho C_p} \right) \left[1 + C \ln \left(\frac{\dot{\epsilon}}{\dot{\epsilon}_0} \right) \right] \left[\sigma_0 + \left(\frac{B}{n+1} \right) \epsilon^n \right] \epsilon \right] \tag{17}$$

where T_0 describes the initial absolute temperature, and A, B, C and n are parameters in the Johnson-Cook model as have been defined in Eq. (9). This is a slight modification from Eqs. (9) and (12).

Assuming that shear bands are in an infinite environment, one can obtain the cooling temperature as a function of time t and the distance to the middle of shear band x [267]. If the region $-a < x < a$ is initially at constant temperature T_0 and the region $|x| > a$ is initially at zero,

$$T = \frac{1}{2} T_0 \left\{ \operatorname{erf} \frac{a-x}{2\sqrt{\kappa t}} + \operatorname{erf} \frac{a+x}{2\sqrt{\kappa t}} \right\} \tag{18}$$

where κ is the thermal diffusivity, $\kappa = \lambda/\rho C_p$ (ρ represents density, and C_p represents the specific heat capacity at the constant pressure). Calculated temperatures at various positions and times, for Ti, Mg, Ti-6Al-4V alloy, Cu, and 304 stainless steel, are presented in Fig. 23 (b) and (c), respectively. More complex formulations, using finite difference, finite element, and analytical methods reach more exact solutions, but this equation is a very good first approximation.

Another way to calculate the temperature rise inside a shear band with a thickness $2L$ is through the linear heat transfer theory [267]. One assumes that the region $x > 0$ with zero initial temperature and the heat is produced at a constant rate A_0 (where A_0 is heat generation per unit time and per unit volume for $t > 0$) in a region $0 < x < l$, and that there is no outflow of heat at position $x = 0$. The

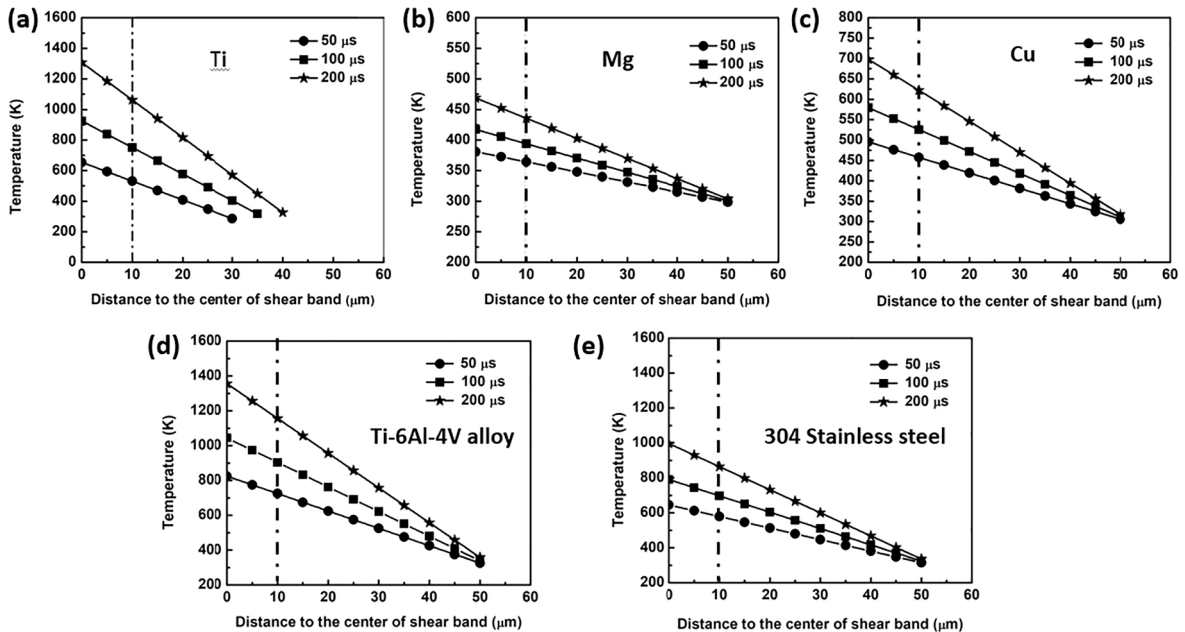


Fig. 24. The calculated temperature profiles within and around shear bands for different times after deformation: 50, 100, and 200 μs : (a) Ti; (b) Mg; (c) Cu; (d) Ti-6Al-4V; (e) AISI 304 Stainless Steel.

temperature rise can be represented by:

$$T = \frac{\kappa A_0 t}{\lambda} \left\{ 1 - 2i^2 \operatorname{erfc} \frac{l-x}{2\sqrt{\kappa t}} - 2i^2 \operatorname{erfc} \frac{l+x}{2\sqrt{\kappa t}} \right\} \quad 0 < x < l \quad (19)$$

$$T = \frac{2\kappa A_0 t}{\lambda} \left\{ i^2 \operatorname{erfc} \frac{x-l}{2\sqrt{\kappa t}} - i^2 \operatorname{erfc} \frac{l+x}{2\sqrt{\kappa t}} \right\} \quad x > l \quad (20)$$

where x is the distance from the center of the ASB. Temperature rises in shear bands with thickness of 20 μm for Ti, Mg, Cu, Ti-6Al-4V and 304 stainless steel as a function of distance to the center are shown in Fig. 24. These are the same materials analyzed in Fig. 23 (b) and (c). They all reach recrystallization temperatures (half of melting temperature) within the time of 200 μs , but more exact experimentally-based heat generation rates A_0 can be applied to the different conditions and materials.

5.2. Shear-Band width prediction

The determination of the shear-band width is an important endeavor. There are essentially four equations predicting it as a function of material parameters.

The Bai-Dodd theory [268] has the following equation to predict the width of the shear band, δ :

$$\delta = 2 \left(\frac{\lambda T}{\tau \dot{\gamma}} \right)^{1/2} \quad (21)$$

Since the Bai-Dodd equation does not consider the thermal softening effect in the shear band, Grady [160] analyzed the shear-band thickness with minimized dissipation corresponding to the fastest growth rate for the shear band and proposed this width as the optimum one. Thus, the width of shear band, incorporating the thermal softening coefficient α , is:

$$\delta = \left(\frac{16\lambda^3}{\tau^3 \alpha^2 C_p \dot{\gamma}} \right)^{1/4} \quad (22)$$

The thermal softening coefficient in shear band, α , assumes a linear behavior:

$$\tau = \tau_0 (1 + \alpha(T_0 - T)) \quad (23)$$

where T_0 the initial temperature, and τ_0 is the reference shear stress. Another slightly modified form of Grady's equation replaces 16 by 9.

The results obtained by Andrade et al. [108] for copper show a reasonable agreement with both Bai et al. [269] and Grady et al. [160] equations (Fig. 25). The experimental thickness of shear bands parallels these two equations. Although both equations describe a reduction in the width of shear bands with the increase of flow stress and shear strain rate, the abrupt drop for the ultrafine-grained (UFG) copper was caused by a change in mechanism causing a loss of mechanical stability. It was attributed to the increased propensity of thermal softening and disappearance of strain-hardening in ultrafine grained materials. As an initial attempt by Grady [161], this

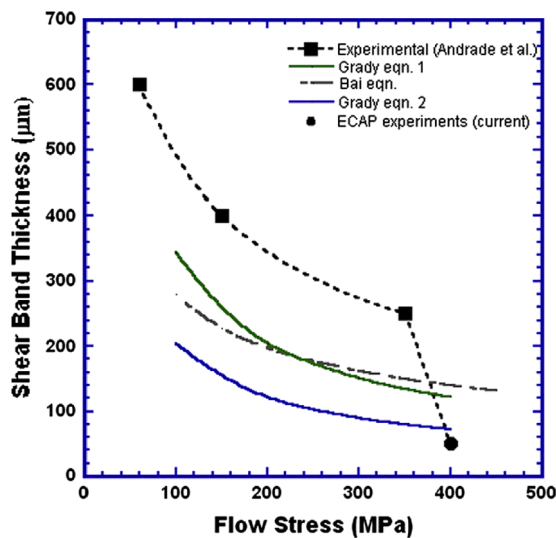


Fig. 25. Shear-band thickness obtained from experiments in ultra-fine-grained copper as compared to prediction by Bai's and Grady's equations. The significantly narrower shear band ($\sim 50 \mu\text{m}$) corresponds to copper subjected to sequential Equal Channel Angular Pressing passes to a strain generating an ultrafine grained structure [82], as seen in Fig. 72.

thermal softening parameter α in Eq. (23) describes a linear thermal softening relationship with the melting temperature. This is labeled Grady Equation in Fig. 25. With the effort to describe a more significant thermal softening effect in the ultrafine-grained copper, it was assumed that the full softening was reached at 400 K [82]. The corresponding results are shown in Fig. 25 and are

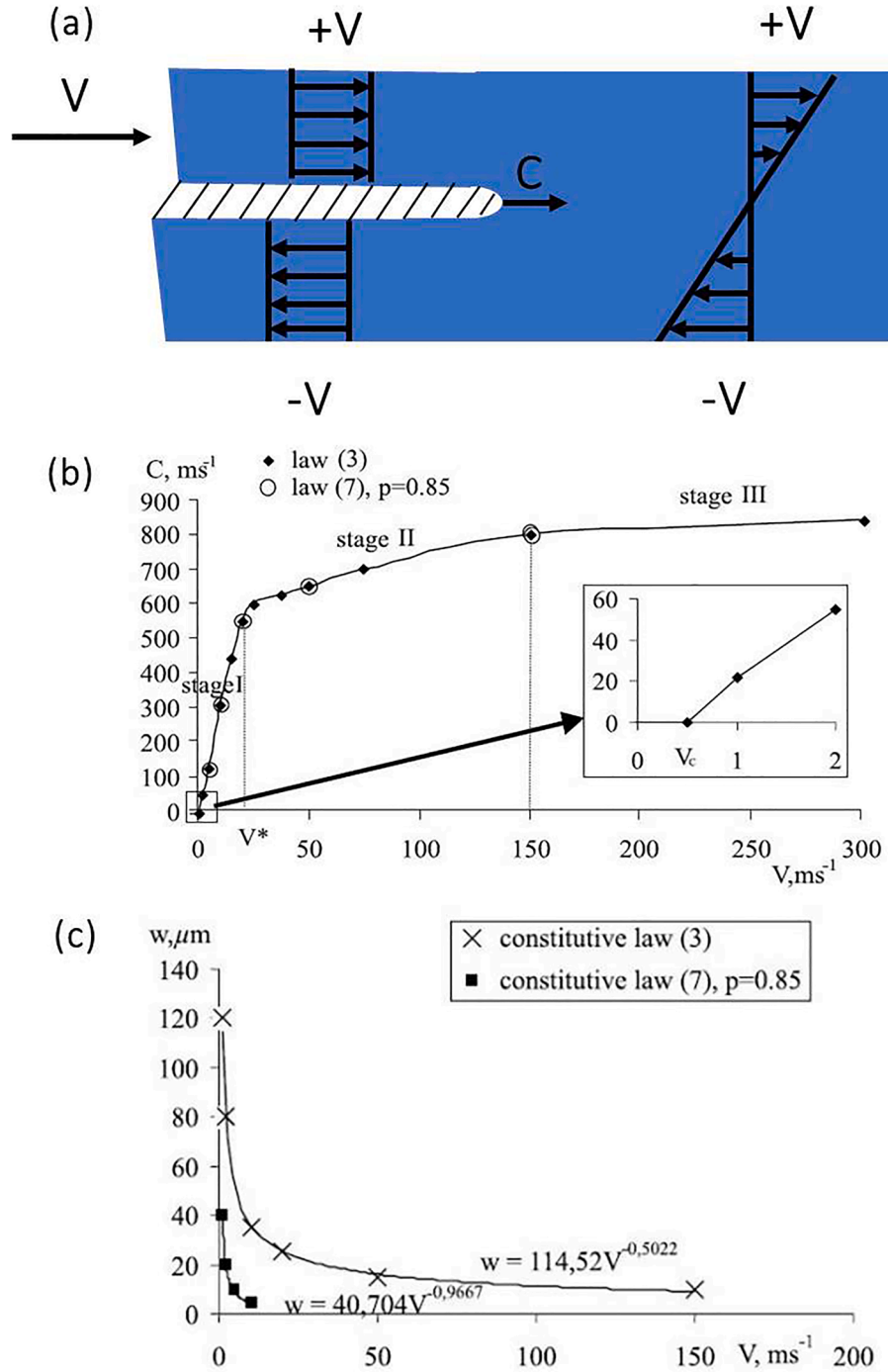


Fig. 26. Schematics for the dependence between imposed shear deformation velocity V and propagation velocity of shear-band front C . (a) Geometry of velocity V and C . C is dependent on V ; (b) Numerical modeling of the effects of the applied velocity V on the stationary shear band speed C for CRS-1018 steel. The enlarged box shows the existence of a critical velocity V_c below which no propagation is observed due to heat conductivity effects: transition from isothermal ($V < V_c$) to adiabatic process ($V > V_c$). Note the presence of three stages. In stage I ($V < V^*$), the band propagation is controlled by external work. In stage III, the propagation is driven by the elastic energy release. (c) Evolution of the shear band width in CRS-1018 steel as a function of the applied velocity V for two different constitutive laws [276].

labeled Eq. (2). A good fit with Grady's equation for the UFG materials has been demonstrated by adopting an accelerated linear thermal-softening.

The shear-band width was also calculated in a more complete manner incorporating strain rate hardening, by Dinartz and Molinari [270], yielding the expression:

$$\delta \approx 6\sqrt{2m} \frac{k_0 T_0}{v_0 a \tau_0} \quad (24)$$

where k_0 is the conductivity, a is the thermal sensitivity and v_0 the relative displacement velocity imparted to the system. The constitutive equation used is similar to Grady's with the addition of the strain rate effect.

An alternative expression was obtained by Dinartz and Molinari to provide direct comparison with the Bai-Dodd equation:

$$\delta \approx \sqrt{6\sqrt{2}} \frac{\sqrt{m}}{\sqrt{a}} \sqrt{\frac{k_0 T_0}{\dot{\gamma} \tau_0}} \quad (25)$$

Wright [12] comments that the experimental results are twice of Bai's equation predictions. Wright and Ockendon [271] have an alternative expression:

$$\delta \approx \frac{2m}{1-m} \frac{k_0 T_0}{v_0 a \tau_0} \quad (26)$$

The ratio $\delta_{D-M}/\delta_{W-O}$ is approximately equal to $3 \times 2^{1/2}$. Thus, the predictions are very close.

5.3. Velocity of propagation of shear band

The determination of the shear-band velocity is an important endeavor, since shear bands do not generate a uniform shear deformation but are the result of the deformation at the front, also known as the "process zone". This has been first measured by Marchand and Duffy [101] for HY-100 steel in the geometry shown in Fig. 4 at a strain rate of 1600 s^{-1} . The speed of propagation was estimated to be 520 m/s. Kalthoff and Winkler [182] studied double-notched plates impacted with a cylindrical projectile. They reported a transition of the failure mode between crack propagation and adiabatic shear band propagation depending on the notch-tip radius and the impact velocity. Grady [160,272] used a simple one-dimensional analysis for a propagating shear band. Batra and Zhang [273] developed a numerical analysis and were able to numerically reproduce the experiments of Marchand and Duffy under different strain rates. They found that the strain rate had a strong effect on the velocity of propagation. Gioia and Ortiz [274] used a boundary layer theory to study the two-dimensional structure of a shear band propagating in a thermo-viscoplastic solid. Zhou et al. [115,116] used impacted pre-notched plates to study numerically and experimentally the propagation of an adiabatic shear band in C-300 steel and Ti-6Al-4V. A strong dependence of shear band speed on impact velocity, at lower impact velocities, and a tendency to saturate at higher impact velocities were observed.

An important advance was made by Mercier and Molinari [275]: they developed an analytical model based on the variational method to determine the speed of propagation in CRS-1018 steel and HY-100 steel (the one used by Marchand and Duffy [101]). They assumed a Mode II configuration in which the shear region is subjected to simple shear (Fig. 26 (a)). Velocities $\pm V$ are applied to the left-hand side, generating a propagation velocity C . In the variational method, the velocity C was obtained as a function of the size of the process zone and the shear-band width. The effects of strain hardening, strain-rate sensitivity, thermal softening and elastic shear modulus were incorporated into their theory but heat conduction was neglected. Their prediction of 905 m/s compared rather favorably with the Marchand and Duffy results of 510 m/s for the HY-100 alloy. For the CRS-1018 steel, they obtained a maximum shear-band velocity of approximately 1300 m/s. Using finite elements, Bonnet-Lebouvier et al. [276] expanded on the analytical model and obtained results incorporating heat conduction. The velocities were somewhat decreased but the analytical model was confirmed: a maximum velocity of ~ 800 m/s was obtained for the same CRS-1018 steel. The finite element prediction of the variation of shear-band velocity C with the velocity imparted to the free surfaces (Fig. 26 (b)) leads to a maximum close to 850 m/s when V is about 300 m/s. At Stage III, the velocity is governed by the rate of elastic energy release. There is also a velocity V below which (provided in the detail of the figure) no propagation takes place. In Stage I, the velocity is controlled by external work. The finite element method also predicted the width of the band, δ . It decreases with V for two constitutive descriptions that simulate CRS-1018 steel but with slight differences in the softening: for this model (#7 in figure) the yield strength becomes equal to zero at the melting point.

The relationship between V and the width δ is provided in Fig. 26 (c) and can be expressed as:

$$\delta = AV^{-(0.5-1)} \quad (27)$$

where A is a parameter. The exponent depends on the constitutive equation adopted. The width decreases rapidly with the increase in velocity, V . This relationship compares with the dependence assumed in Section 5.2 in which the width is expressed as a function of the strain rate, directly related to V .

6. Variables related to shear localization

Many factors, such as geometrical design, microstructural characteristics, material properties, and environment temperature can

influence the transition from homogeneous deformation to shear strain localization under deformation at large strains and high strain rates [126,277]. The effects of some variables on shear localization are discussed in this section.

6.1. Geometrical aspects

For a general geometry of specimens, such as cylinders, the location of the initiation of shear localization cannot be predicted with exactitude. In the forced shear specimen design, such as hat-shaped specimen, the stress concentration in the shear region can take over other influences such as initial defects [278,279]. Thus, the forced shear geometry is excellent for systematically studying the deformation history of adiabatic shear localization. The difficulties in recognizing the random initiation sites of shear bands by a specimen exposed to general dynamic impact can be eliminated [138]. Additionally, such specimens can explore the multi-component stress effect on the microstructural evolution [131].

The dimension ratio or the thickness of the specimen is also an important parameter during dynamic deformation. O'Donnell and Woodward [69] carried out experiments on dynamic loading of aluminum cylindrical samples with a diameter of 4.76 mm. It was revealed that shear failure occurred only in specimens with a height >4 mm and a threshold of aspect length/diameter (L/D) ratio of about 1. This effect was also observed by Walley et al. [126] in armor steels and W alloys in a large direct impact Hopkinson bar. The results showed a clear indication of shear fracture when $L/D > 1$, a fact not observed in specimens with a smaller L/D ratio. Based on these results, it may be concluded that the shear failure of cylindrical specimens under dynamic impact is extremely sensitive to geometry, in addition to their physical properties. These differences are partly due to frictional boundary conditions at the ends and partly due to the existence of a plane at 45° entirely contained in specimen.

Meyer et al. [280] used slightly inclined cylindrical compression specimens with the longitudinal axis at an angle with the direction of loading and observed a dependence of the stress for shear-band initiation on the angle. This design can achieve a wider differentiation of materials compared with the normal compressive loading.

6.2. Microstructural aspects

A significant aspect of microstructural influence on the formation of ASBs which has not yet received sufficient attention is the effect of crystallographic texture, together with the grain size distribution and dispersed phases or particles [81]. For the FCC, BCC and HCP structures, the cubic texture was revealed to inhibit the propagation of shear band advantageously. Clayton [255] pointed out that microstructure was of great importance for the development of shear localization, such as random and rolled cubic textures, in addition

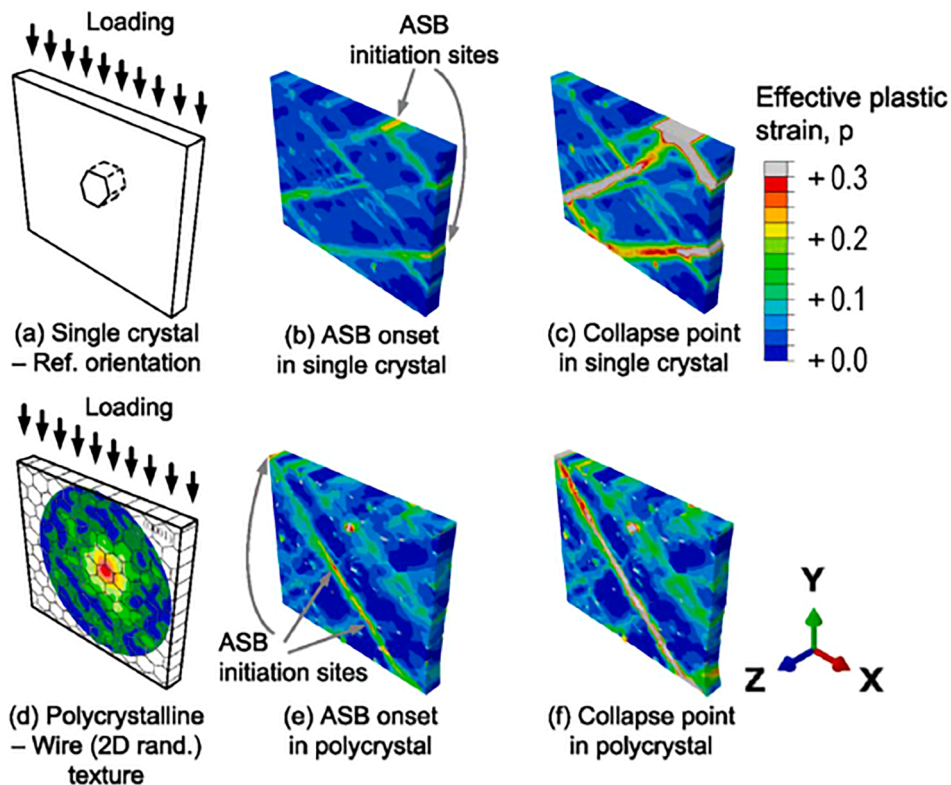


Fig. 27. The evolution process of shear bands in HCP single and polycrystalline specimens under dynamic loading modeled by the finite element method [265].

to stored elastic energy and residual volume changes resulted from lattice defects, dislocations, impurities, and second phases.

Considering the crystallography aspect, the responses to uniaxial dynamic compression of single and polycrystal HCP materials were investigated, as presented in Fig. 27 [265]. For the single crystal, the shear band initiates at the top right side of the cylinder and propagates on prism slip planes to the other boundary. It was mentioned that during the inception of the ASB, wave propagation is the main nucleation source because of the heterogeneous deformation when the wavelength is smaller than the sample size (Fig. 27 (b) and (c)). The nucleation of ASBs in polycrystalline materials takes place in the interior of the specimens, in regions where slip is easier. The ASB tends to propagate in grains with a similar orientation, thus giving a wavy configuration, shown in Fig. 27 (e) and (f). For both single and polycrystal materials under dynamic impact, ASBs usually propagate in the direction of maximum shear stress. This shows that the thickness of the shear band in the single crystal was usually larger than that in polycrystal due to local crystal anisotropy. This leads to a higher heat generation in the narrower local band in the polycrystal, and a higher temperature rise. This is consistent with hot-spot observation as shown in Fig. 28 (a) by Guduru et al. [153] and localized recrystallization by Rittel et al. [281]. These results will be discussed in Section 13. Another conclusion is that both the inception and failure of ASBs are reached earlier in the polycrystal materials. This is also due to the Hall-Petch strengthening effect.

A fascinating and relevant analysis conducted by Molinari and Leroy [282] and applied to the earth's crust predicts a two-dimensional variation in temperature akin to the observations. This analysis applies to any type of material. The particle velocity, if exclusively parallel to the shear-band direction, would not produce spatial variations in the thickness of the band. The analysis used a two-dimensional perturbation. Under certain conditions a two-dimensional flow was generated, which led to a two-dimensional temperature distribution. This condition is given from the constitutive equation below, which contains thermal softening, strain-rate hardening and strain hardening terms:

$$\tau = \tau_0 \exp \left[-\alpha \left(\frac{T}{T_0} - 1 \right) \right] \left(\frac{\dot{\gamma}}{\dot{\gamma}_0} \right)^m \quad (28)$$

This type of instability occurs when thermal softening, expressed by α , equals strain rate sensitivity, expressed by m . The two-dimensional distortion of an initially square grid is evident in Fig. 28 (b). Accordingly, the temperature distribution also has two-

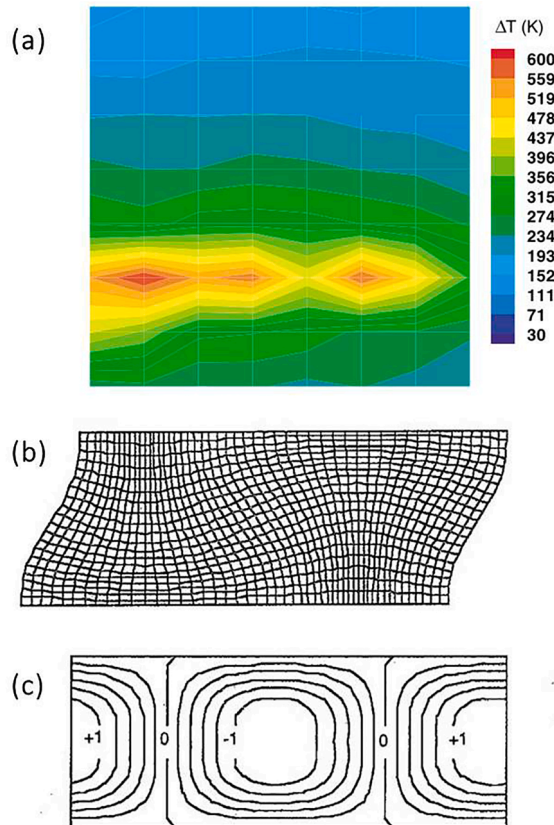


Fig. 28. (a) The thermal image of a shear band showing non-uniform temperature distribution along the length of the band using a two-dimensional high speed infrared camera [153]; (b) Calculated fluctuation in deformation seen from the distortion of an initially rectangular grid using a bi-dimensional flow perturbation analysis for a material simulating earth's outer crust; (c) Iso-temperature distribution lines (arbitrary scale) exhibiting a spatial pattern. The extremes -1 and $+1$ represent an arbitrary temperature scale [282].

dimensional fluctuations as shown in Fig. 28 (c). This is an arbitrary scale varying from -1 to $+1$. This self-organization can lead to the pattern observed by Guduru et al. [153] and to fluctuations in the thickness of the band, to be discussed later (Fig. 76, Section 13).

Particle reinforced metal-matrix composites (MMCs) are also a typical class of microstructure-sensitive materials [283,284]. Experimental investigations have shown that both fraction and size of the reinforcing phase have a significant effect on formation of adiabatic shear bands in MMCs. Lee et al. [285] performed ballistic tests on SiC whisker reinforced aluminum matrix composites and found that the high fraction of SiC whiskers blocks adiabatic shear band propagation. The susceptibility of aluminum alloys to shear localization was found to increase with alumina particulate reinforcement [286]. Dai et al. [287] found a significant effect of particle size on shear localization in SiCp/2024Al matrix composites. As displayed in Fig. 29, the composite reinforced by the smallest SiC particles ($3.5\ \mu\text{m}$) formed well-defined shear bands (Fig. 29 (a)), while the ones with larger particle size of $10\ \mu\text{m}$ (Fig. 29 (b)) and $20\ \mu\text{m}$ (Fig. 29 (c)) tended to deform inhomogeneously without any visible shear band. This indicates that ASBs are more likely to form in

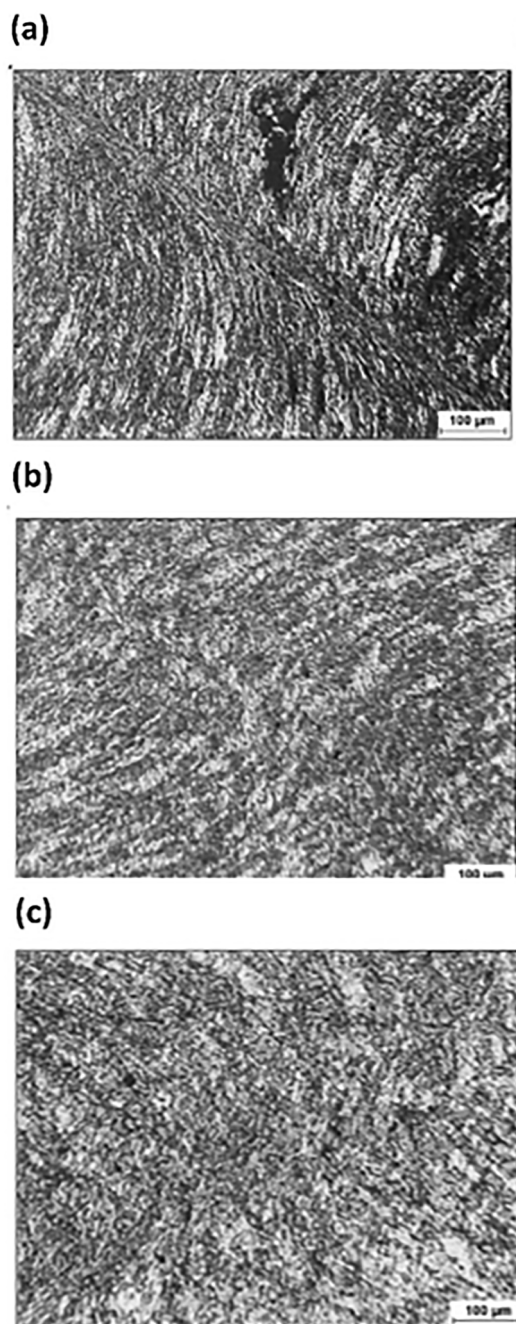


Fig. 29. Deformation patterns of SiCp/2024Al matrix composites: (a) $3.5\ \mu\text{m}$ SiC particle; (b) $10\ \mu\text{m}$ SiC particle and (c) $20\ \mu\text{m}$ SiC particle [287].

the composite reinforced with smaller particles. This size-dependent phenomenon has also been revealed by other researchers [288,289]. Shih et al. [226] examined the shear localization mechanism in granular SiC and found the fragmentation within the shear bands.

The development of ASBs was also observed in AISI 4340 steel for specimens with inhomogeneous microstructure [290]. The study showed that the tempered steel specimens, with an inhomogeneous microstructure composed of precipitated carbides and high-hardness matrix, were more susceptible to the formation of ASBs. Yiadom [277] showed that microstructural inhomogeneities between the precipitated carbides and the ferrite matrix were more prone to the nucleation of ASBs.

Theoretical analysis was performed to reveal the underlying mechanism of size dependent behavior in MMCs, Dai and coworkers [283,291] developed a microscopic mechanism based strain gradient constitutive theory, where the strengthening effects due to statistically stored and geometrically necessary dislocations are considered. The results showed that the smaller the size of particle, the larger the strain gradient and the lower critical instability shear strain in the metal matrix composite. These analytical results are in

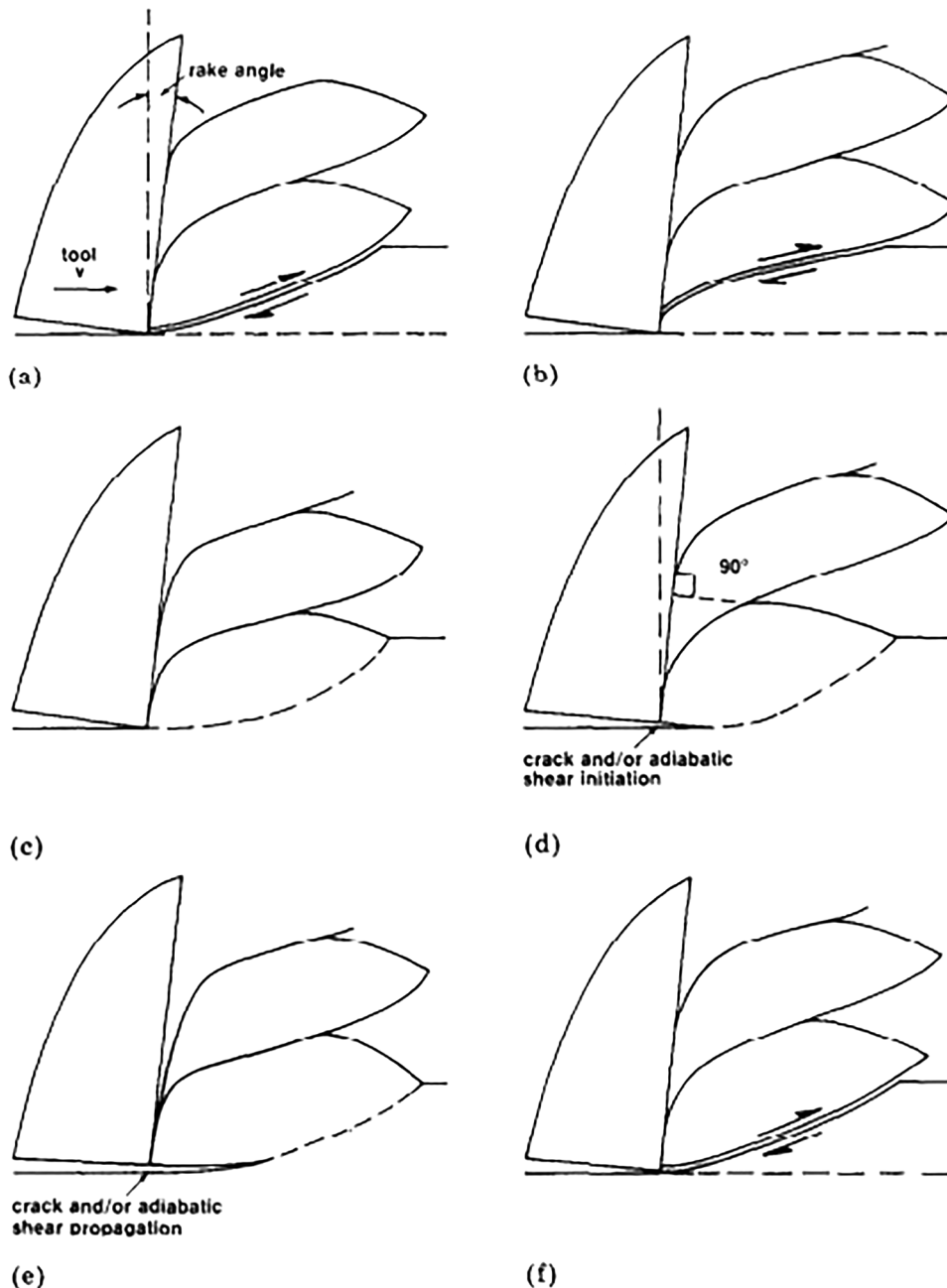


Fig. 30. Sequence of formation of shear bands and chips in machining titanium alloy according to Komanduri and Von Turkovich [198].

good accordance with the aforementioned experimental observations.

Li et al. [81] carried out an investigation on the shear instability in materials with different grain sizes, for example, UFG titanium. Both theory and experiments revealed that initial defects such as precipitates, other phases, inclusions, cracks, and boundaries in layered materials can act as potential inception sites for shear bands [279,292].

6.3. Material properties

As discussed in Section 4, the shear localization was found to be strongly dependent on material variables, including physical and mechanical parameters. Since the thermal softening parameter, strain hardening rate, and strain-rate sensitivity are three dominant effects for the development of shear bands, the thermal-related parameters are first discussed here. It is well recognized that the material will be more sensitive to shear localization if it has a lower heat capacity and lower thermal conductivity. The low heat capacity generates a high rate of temperature rise under the same input of plastic work; meanwhile it also provides a slow thermal diffusion rate of heat into surroundings and accelerates the heat accumulation in a localized area. Metals with low heat capacity and thermal conductivity, such as Ti and titanium alloys ($C = 500 \text{ J/kgK}$, $\lambda = 19 \text{ W/mK}$), are found to be much more prone to shear localization under high strain rate deformation [37]. Correspondingly, those metals with high thermal parameters, for example pure copper ($C = 385 \text{ J/kgK}$, $\lambda = 400 \text{ W/mK}$) and pure aluminum ($C = 903 \text{ J/kgK}$, $\lambda = 238 \text{ W/mK}$), are much less susceptible to adiabatic shear formation [79].

High strain hardening and strain-rate hardening effects may overcome thermal softening and make localized shear deformation impossible. One of the differences between pure metals and their alloys is the lower strain hardening rate for the alloys. For example, in copper alloys, distinctive shear localization has been observed. For copper, shock pre-deformation to a high yield stress and low work hardening are needed, which will be discussed further in Section 15. This is due to the alloying elements which offer more barriers to dislocation slip and result in an increase in flow stress. Once plastic localization develops, the local strain rate increases dramatically. If the materials have a relatively high strain-rate hardening, further development of shear localization may be suppressed. Therefore, Argon [39] pointed out that materials which are sensitive to strain rates are less prevalent to shear localization because they can undergo more homogeneous deformation. This is akin to Newtonian viscous behavior.

Besides, Xu et al. [251] revealed that the critical shear localization strain was significantly influenced by the strength of materials with different microstructures at constant strain rates. The critical strain values for the quenched, quenched and tempered, and normalized steels are found at 0.30, 0.36 and 0.8. This indicates that the steel with quenched martensite has greater propensity to shear localize among the three. Thus, the higher the strength, the easier it is for deformation to localize. A key challenge in the development of armor is to obtain simultaneously a high surface hardness and resistance to shear localization.

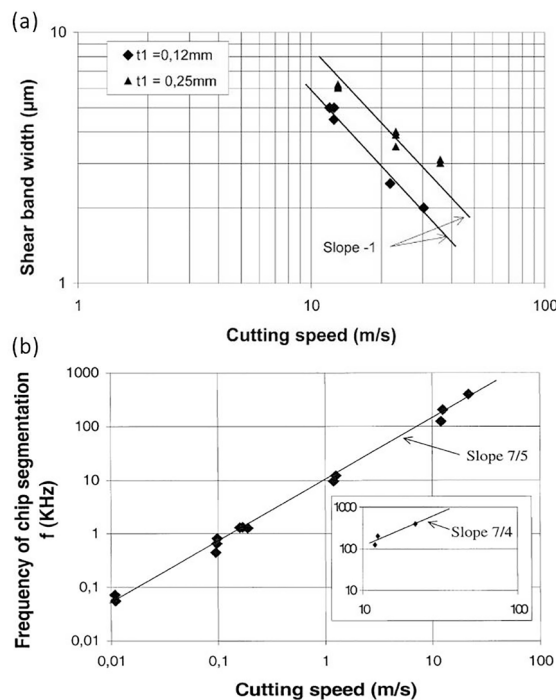


Fig. 31. (a) Adiabatic shear band width as function of the cutting speed for a titanium alloy Ti-6Al-4V for two cutting depths (feed): 0.12 and 0.25 mm. This exponent of -1 is predicted from theory by Molinari et al. [188]. (b) Frequency of chip segmentation in Ti-6Al-4 V alloy as a function of the cutting speed. There is excellent agreement with the theoretical exponent predicted by Eq. (30), especially in the higher velocity regime where the slope is $7/4$.

7. Estimation of shear band parameters in machining

Mechanical machining was introduced in Section 3.6. Here we will summarize some shear-band related properties during the machining process. The breakup of machining chips is a desirable property. Long continuous chips can form something referred to as “birdnesting” and have to be periodically removed by operator, since they will get trapped in the chuck or tool. The breakup of chips occurs by the generation and propagation of shear bands.

Chip formation is especially prevalent in titanium alloys and is a function of material as well as processing parameters. The constitutive equation of the material describes its response to the imparted deformation. The tool/rake angle and velocity are the principal process parameters. The classic work by Komanduri and Von Turkovich [198] describes the sequence of events in chip formation (Fig. 30). As the tool advances it generates a shear band in the material that is being machined (Fig. 30(a)). Further advance and the tool penetrates into virgin material, as significant deformation occurs in the shear band. This concentrated deformation increases with the advance of the tool (Fig. 30 (c)). At a critical strain, a second band is initiated and propagates into the material.

The formation of machining in Ti-6Al-4V was experimentally determined at different tool velocities by Molinari et al. [188]. At low velocities the tool was attached to a universal testing machine. For high velocities, the tool was attached to a compressed air gun providing a velocity of up to 73 m/s. The perturbation analysis which was applied predicted the width of the shear bands as well as their spacing as a function of tool velocity. The width decreases with velocity from a value of 7 μm to <2 μm as shown in Fig. 31 (a). The inverse relationship in log-log plot provides an exponent of -1 .

Using the Molinari perturbation analysis given in Section 5.3 and making a number of approximations, the following expression was obtained for the characteristic spacing of shear bands, L_c :

$$L_c \approx AV^{-3/4} \quad (29)$$

where V is the velocity of the tool. The frequency of chip segmentation, f , which is equal to the number of chips formed per unit time, is obtained from:

$$f = V_N / L_c = (V \sin \phi) / L_c = \frac{\sin \phi}{A} V^{7/4} \quad (30)$$

where ϕ is the angle of the shear-band plane with the surface of the material, which is only weakly velocity dependent. Thus, the theoretical predictions are fully consistent with the experimental observations as shown in Fig. 31 (b). This is particularly the case at higher velocities, where the exponent is 7/4.

Subsequent finite element calculations by Miguélez et al. [293] corroborated the effect of strain rate on shear-band spacing (Fig. 32) and width for the same alloy. It can be concluded that the process of chip formation and separation is well understood experimentally, analytically, and computationally.

8. Shear bands in severe plastic deformation

Shear localization manifests itself in severe plastic deformation processes such as equal-channel angular pressing (ECAP) in which a metallic sample is pushed through a die with two channels making an angle as high as 90°. This redirection of the plastic flow within

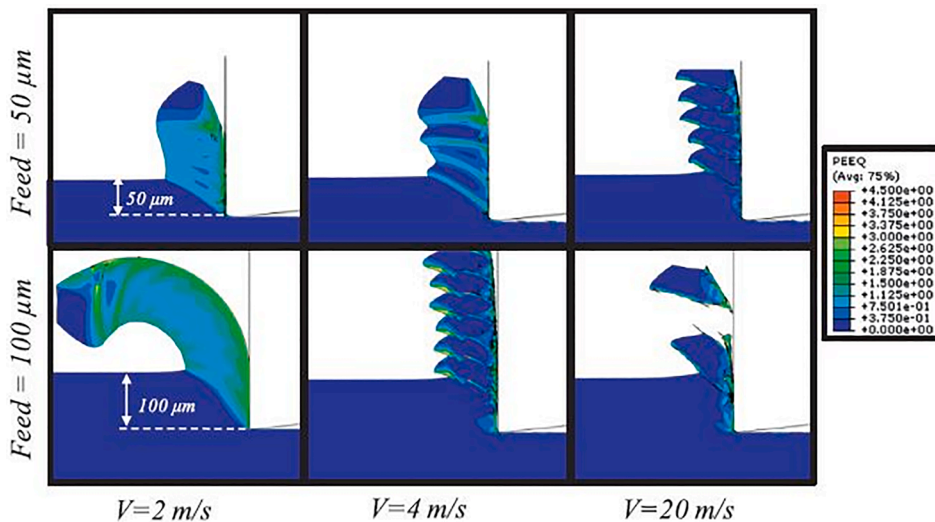


Fig. 32. Chip formation in Ti-6Al-4V alloy modelled by FEM. As cutting speed (depth of cut (feed) is 50 and 100 μm) increases, the chip spacing decreases. Equivalent (or effective) plastic strain level contours are shown [293].

the channel, through a sharp elbow, generates a high local deformation; the shear strain is as high as 1. Successive passes lead to strains that can yield values all the way to 8 or 10. In some cases, when the metal has limited ductility, such as magnesium and its alloys, the sharp angle makes deformation very difficult and generates multiple cracks that are originated from shear bands. Thus, the grain size reduction associated with the severe plastic deformation becomes impossible.

Lapovok et al. [294] applied the perturbation analysis developed by Molinari [163] to AZ31 magnesium alloy processed by ECAP. The strain rate imparted by ECAP was on the order of 0.05 s^{-1} and cylindrical specimens were thus tested at strain rates of 0.03, 0.3, and 3 s^{-1} in compression at $250 \text{ }^\circ\text{C}$ to obtain the parameters in the constitutive description of this alloy, in particular the strain-rate sensitivity. Shear bands were observed in the specimens, whose spacing decreased with increasing strain rate (Fig. 33). The calculated shear-band spacing showed the same deformation velocity dependence as the observed values. The sensitivity of the spacing to the back pressure was also obtained. This study demonstrates that shear bands formed in a quasi-static regime can be modeled by similar methods as the ones developed for high strain-rate deformation.

9. Deformed and transformed bands

Shear bands were traditionally divided to deformed or transformed, based on absence or presence of a shiny phase in optical microscopy. The former one refers to regions with severe deformation or elongation of the grains under dynamic plastic deformation. The transformed band is also called the white-etching band, and has attracted significant attention since it was proposed that a phase transformation occurs inside the band. White-etching shear bands have been reported in steels [295–297], titanium and its alloys [298–300], tantalum and its alloys [301,302], aluminum alloys [303], and magnesium alloys [304].

One of the first observations of shear bands, through transmission electron microscopy, is by Me-Bar and Shechtman [62]. After this landmark paper, detailed aspects on microstructural evolution within ASB have been extensively studied by TEM techniques, revealing a much-refined microstructure with nano-sized grains.

Whenever the rise of the temperature inside the shear band overpasses a solvus line, the phase transformation is thermodynamically favorable. The diffusion time is very limited and phase separation is often not possible due to kinetic effects. However, displacive transformations are much faster. Upon cooling, the opposite takes place, with the possible retention of high temperature phases or occurrence of martensitic transformation. In extreme conditions, an amorphous structure can be formed due to the very rapid cooling, whose times are on the order of milliseconds. These structures often have a shiny appearance because precipitates and second-phase particles were dissolved. However, a great fraction of *transformed bands* is now recognized as *deformed bands*, in which no phase transformation happens. There are also other structures where no obvious boundary line is crossed. The large deformation gives way to dynamic recrystallization, generating a new/ultrafine grain size which cannot be resolved by optical microscopy. This shows an apparent featureless morphology if observation is exclusively conducted by optical microscopy. This phenomenon will be discussed at length in Section 12.1. Here, we clarify that ASBs with phase transformation should continue to be called “transformed bands”, such as the so-called white etching bands in titanium alloys [305,306].

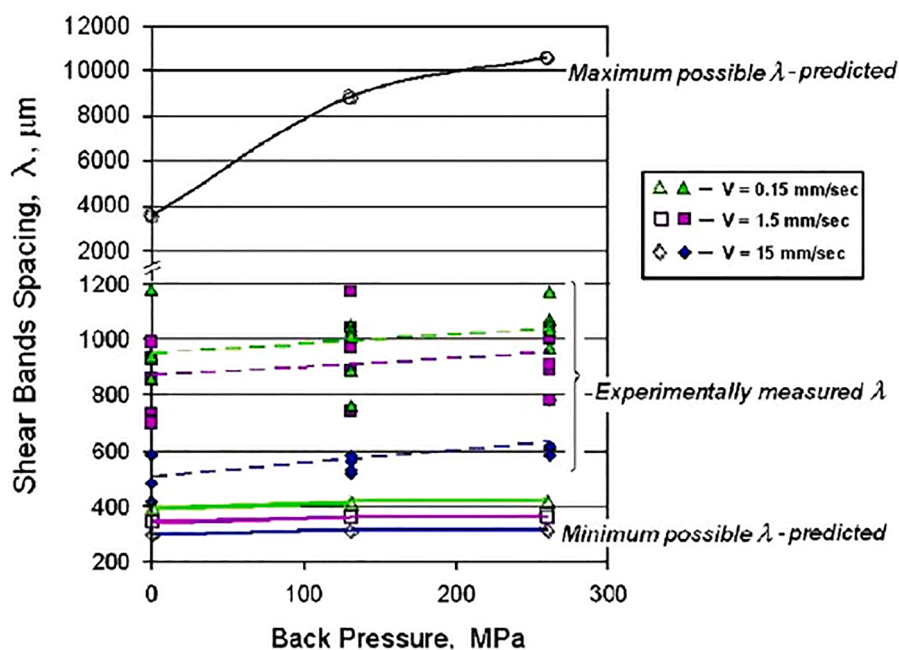


Fig. 33. Effect of ECAP velocity and back pressure on the shear-band spacing in AZ31 magnesium alloy; experimental results are points whereas minimum and maximum shear band spacing (marked as predicted) are calculated by perturbation analysis [294].

The microstructural differences between deformed and transformed bands are caused by different strain levels of deformation. Once material reaches a critical strain, the structure can reorganize itself into ultrafine- or nano-grains. For AM60B magnesium alloys, the shear band is called *deformed* describing the effect of shear deformation. At a larger localized strain, the deformed microstructure is replaced by nanocrystalline grains. The shear band was classified as *transformed* by Zou et al. [68] but obviously no phase transformation occurred. Li et al. [307] also reported two kinds of shear bands in 7075 Al alloys: one is deformed and the other is transformed. Recrystallized grains with 100 nm size were formed in the middle of the band. In addition, the grains were elongated at the edge of the band along the shear direction. The change of microhardness due to microstructure transformation will be discussed in the Section 10.

Trent [308] was the first to observe the white etching bands in steel. The results show that these bands exhibit either slightly yellow or white color in the sheared region. This was attributed to a phase transformation. Later, some researchers confirmed that it was a structure consisting of dislocation cells, while others referred to it as extraordinarily tiny recrystallized grains [179,309]. It is possible that phase transformations could occur. Wang [305] found the orthorhombic α'' -martensite phase and α phase structure coexisting inside the shear band of Ti-5Al-5Mo-5 V-1Cr-1Fe alloy. Therefore, the α'' phase-transformation does indeed occur during shear localization. Further broad investigations by transmission electron microscopy and X-ray diffraction have revealed that the shear band can generate a typical-looking martensite [308], a fine-grain equiaxed delta ferrite [310], or untempered martensite [36].

When revealing the occurrence of phase transformation, the important role of the temperature rise during nucleation and transformation cannot be ignored. It has been proposed that the maximum temperature rise inside shear band can be hundreds of degrees Kelvin compared with the initial value. It is normally derived indirectly from deformation evolution but can also be measured. The temperature evolution can be recorded by using high speed optical or IR detection techniques; this is discussed in Section 3.8. The shear band can be rapidly cooled to the surrounding temperature, and the cooling rates can reach values as fast as 10^7 Ks⁻¹, as shown in Section 5.1.

Recent investigations have also found that ASBs can exhibit a large range of microstructural variations, such as dynamic recrystallization, phase transformations, and even amorphization. Meyers and coworkers [19] also proposed that those shear bands with refined grain sizes formed during recrystallization can be further defined as *recrystallized shear bands*. This mechanism has been confirmed in a broad spectrum of materials, such as steels [179,309,310], titanium [311], aluminum [84,85,312] and magnesium

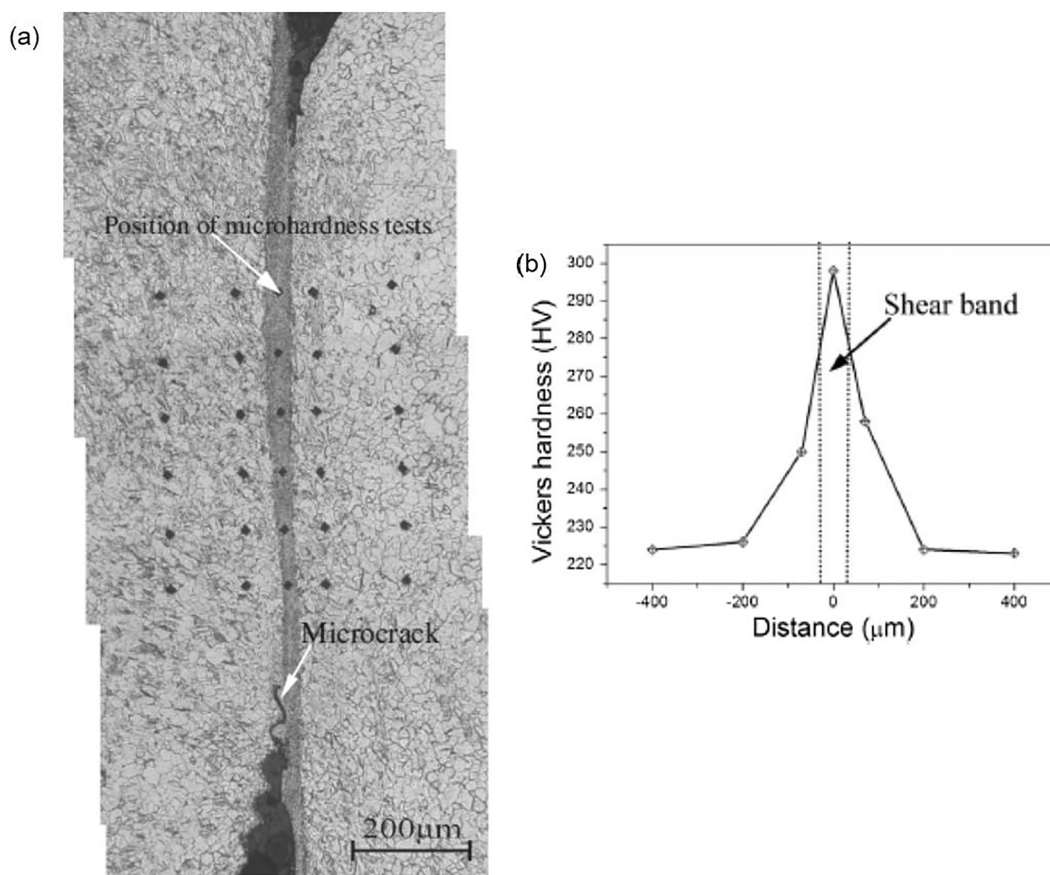


Fig. 34. Optical micrograph showing micro-hardness testing pattern in the shear region of pure titanium: (a) selected measuring locations; (b) micro-hardness of the corresponding selected locations [86].

[313–315]. This will be further documented in Sections 11 and 12.

10. Microhardness distribution inside the shear regions

The increase of hardness in the shear-band area has been observed as early as 1960s and is reported by Rogers [316]. In the early days, it was attributed either to work hardening in the deformed bands or to martensite formation in the transformed bands. But there is another possible reason for the increase in hardness, which is nano-sized grains or ultra-fined equiaxed grains.

Meyers et al. [37] compared the difference between the microstructure adjacent to and within the shear bands in titanium alloys. An enhancement of microhardness in the shear band was observed and caused by the decrease of grain size, which significantly strengthens the materials. Jiang and Yang et al. [86,314] carried out a further investigation on the microhardness in the shear band in annealed pure titanium from several indentations in the different deformation regions. Fig. 34 (a) shows the ASB appearing on the cross section of a hat-shaped specimen. It shows long, straight, and clear interfaces. The shear deformation is significantly localized into an area with a width of about 45 μm . From Fig. 34 (b), it is clear that in the center of shear band, the microhardness is larger than that in the area away from the center of shear band. This was mainly induced by work hardening and reduced grain size. Thus, the shear deformation is inhomogeneously distributed. As the shear band is approached, the shear deformation increases, leading to a higher work hardening. In the middle of ASB, the microhardness is significantly larger than that in the matrix, which is caused by grain refinement through the Hall-Petch effect.

Zou et al. [315] observed that the microhardness within shear bands of magnesium alloy increases significantly and that the microstructure of the shear band becomes nanocrystalline and remains HCP. They also attributed the microhardness enhancement to the reduction of grain size in the shear region. Edwards [312] revealed that for 2024-T351 aluminum alloy, the hardness is different from the hat part to the brim part and the center of shear band. The different values of microhardness in each part of the specimen are attributed to the variation in shear strain. For every sample, there exists a continuous increase of microhardness approaching the shear band, and then a peak value in the center. Microhardness tests in 7075 Al alloys [307] also showed higher values in the band.

However, for glassy materials, such as Zr-based metallic glass, the hardness inside the shear band decreases, indicating softening of the structure, as demonstrated in Fig. 35 [119]. The average hardness profiles in three sites are quite different. This is evidence that the structural variations along the shear direction are dependent on the position; meanwhile, a direct correlation with macroscopic local plastic strain is difficult to be exactly developed.

Similar microhardness tests have been carried out on several kinds of metals, such as titanium and its alloys [37,66], aluminum alloys [307], magnesium alloys [317], pure iron [318], ultrafine-grained iron [319], steels [320,321], copper alloys [322] as well as metallic glasses [119]. Fig. 36 shows the microhardness results for a number of metallic materials. The microhardness is generally enhanced inside shear bands in crystalline materials. The increment of microhardness in the middle of the shear bands in comparison to the matrix varied with material. Most of the hardening inside the shear band in different materials is attributed to grain refinement induced by dynamic recrystallization. The corresponding mechanism of grain size reduction is presented in Section 12.

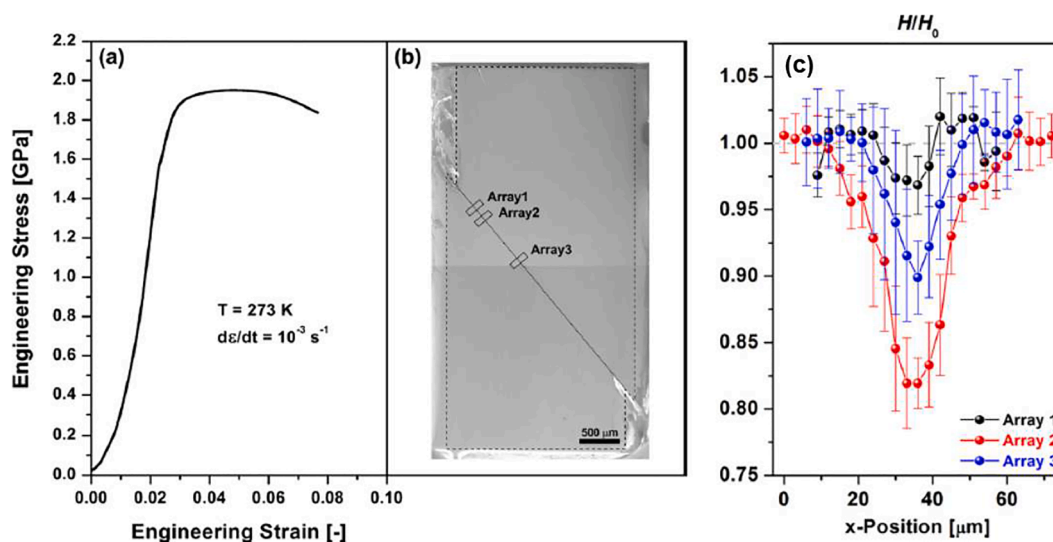


Fig. 35. (a) Stress–strain curve for bulk metallic glass; (b) corresponding SEM micrograph of the polished surface of a $\text{Zr}_{52.2}\text{Ti}_5\text{Cu}_{17.9}\text{Ni}_{14.6}\text{Al}_{10}$ BMG recorded at 273 K; (c) Averaged profiles of the indentation hardness obtained from the three arrays [119].

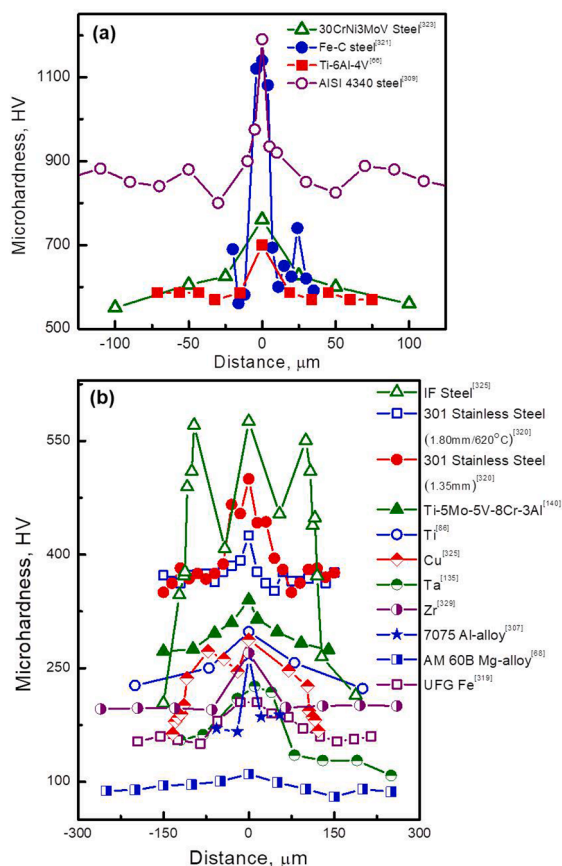


Fig. 36. Micro-hardness within the shear region for different metallic materials: (a) high-strength metallic alloys; (b) medium-strength metallic materials. For most cases, there is a significant increase of hardness in the shear-band region.

11. Microstructural characteristics within shear bands

As mentioned in Section 9, many researchers have observed fine equiaxed grains in many metallic materials, such as steels [323–325], titanium and titanium alloys [326,327], zirconium and zirconium alloys [328,329], tantalum and tantalum alloys [56], copper and copper alloys [104,330], aluminum alloys [70,312], magnesium alloys [317,331], nickel alloys [142], nickel-based superalloys [171], nanocrystalline alloys [81,332], bulk metallic glasses [333–335] and others. The rotational dynamic recrystallization (RDR) mechanism was developed to clarify the microstructural evolution inside the shear bands, consisting mostly of recrystallized ultrafine-grained and nanocrystalline grains. The details of the rotational dynamic recrystallization mechanism developed by Meyers et al. [336] will be discussed in Section 12.

The typical width and equiaxed grain size in the ASBs in different dynamically deformed metallic materials are listed in Table 2. The refined-grain sizes range from 10 to 500 nm, a broad range within the nano to ultrafine grain regime [337].

11.1. Shear bands in conventional alloys

Some of the earliest detailed investigations by TEM on shear bands were conducted in Ti-6Al-4V alloy and commercially pure titanium [338–340]. Fig. 37 demonstrates the characteristics of shear bands in titanium. The shear band in α -Ti had a thickness of about 3–20 μm and the structure is composed of small equiaxed grains. Such microstructure evolution within shear band was also observed in dynamically impacted pure titanium by Meyers and Pak [326] and confirmed by Meyers et al. [37] and Jiang [86]. The selected area diffraction patterns inside and outside the shear band are distinct. Outside the shear band, the diffraction pattern confirms the single crystal structure. Inside the band, a series of rings, typical of nanograined structures, can be seen. At a higher magnification, the equiaxed grains in the core of the shear band are revealed (Fig. 37(c)). The suggestion that the formation of such fine recrystallized equiaxed grains was due to dynamic recrystallization was first made by Meyers and Pak [326]. Later, Toth et al. [341] investigated the texture evolution within an ASB and presented the evidence of dynamic recrystallization in the ASBs in XC-18 steel.

Since crystal structure significantly influences the mechanical response [339], the following sections introduce the microstructural evolution characteristics according to different structures. As seen in Table 2, the microstructures in shear bands for materials with different crystal structures (HCP, FCC and BCC) are actually similar: nearly equiaxed grains with size ranging from 50 to 300 nm. The

Table 2

Typical width and equiaxed grain size in ASBs in some metallic materials.

Alloy	Original grain size (μm)	Experiment methods	Width of SBs (μm)	Equiaxed Grain size within SBs (nm)	Shear strain/ Effective strain	Strain rate (s^{-1})	Source/ Reference
Pure α -Ti (Annealed)	~ 20	SHPB	45	100–500	~ 2.5	3.2×10^4	Jiang-2015 [86]
Pure Ti	61	Ballistic impact test	1–10	50–300	/	/	Meyers-1986 [326]
Ultrafine-grained Ti	~ 0.12	SHPB	2	~ 40	~ 4.5	$\sim 10^3$	Li-2017 [81]
Ti-6Al-4V	3–7	TWC	1–8	~ 200	0.13–0.26	$\sim 10^4$	Xue-2002 [327]
Ti-5Al-5Mo-5 V-1Cr-1Fe	1000(β)	SHPB	~ 25	~ 100	~ 1.64	$\sim 10^5$	Wang-2016 [311]
	4(α),11(β)		~ 10	50–200	~ 0.68		Wang-2015 [305]
Low-alloy steel 30CrNi ₃ MoV	/	Orthogonal cutting	5	50–100	/	/	Duan-2005 [323]
4340 steel	/	Punch impact test in SHPB	6	~ 10	0.5	1.8×10^4	Zurek-1994 [297]
4340 steel	/	SHPB	9	8–20	/	$\sim 10^5$	Beatty-1990 [337]
Fe-10Ni-0.1C	~ 0.15	SHPB	~ 20	~ 300	/	2×10^3	Wang-2009 [324]
Fe-Cr-Ni (AISI 304LSS)	30	TWC	5–50	100–200	1–100	$\sim 10^4$	Meyers-2003 [106]
		SHPB	1–8				
Zirconium (Zircadine 702)	~ 14	SHPB	10–25	200	25–100	$\sim 10^4$	Kad-2006 [124]
8090 Al-Li	/	SHPB	10–30	200	0.17(peak-aged)/0.21(under-aged)	$\sim 10^3$	Xu-2001 [79]
Al-Cu (2A10 Aluminum)	50	Electromagnetic Impact upsetting	150	150	/	$\sim 10^3$	Zhang-2017 [303]
NS Cu-11.14 wt% Al	~ 0.093 (ECAP-8 passes)	SHPB	15	< 50	0.35	$\sim 4 \times 10^3$	Li-2016 [139]
CrMnFeCoNi	~ 8	SHPB	~ 10	100–300	~ 7	1.6×10^3	Li-2018 [346]
CrCoNi	~ 4.7	SHPB	12.5 (298 K) /6.4 (77 K)	~ 300	~ 6.4 (298 K) /5 (77 K)	8×10^4	Ma-2018 [348]
TWIP steel	1–10	Ballistic Impact test	10	10–100	/	$\sim 10^5$	Li-2011 [376]
Shocked Cu	~ 70	SHPB	200	~ 100	3–4	$\sim 10^4$	Andrade-1994 [108]

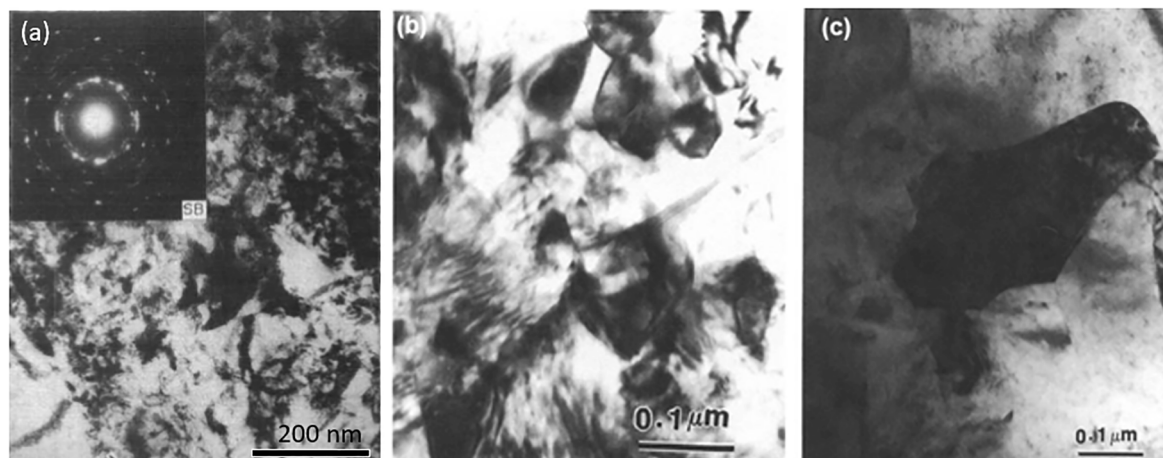


Fig. 37. TEM images of hat-shaped commercial purity Ti specimen (a) showing the formation of recrystallized grains with the diffraction pattern; (b) equiaxed micro-grains; (c) equiaxed micro-grains with low dislocation density [37].

mechanism of formation of this nanocrystalline/ultrafine grain structure will be presented in Section 12.

11.1.1. HCP alloys

Titanium, magnesium and zirconium alloys with HCP crystal structure are more resistant to plastic deformation, thus strain localization can be easily initiated at high strain-rates. Transmission electron microscopy observations in the shear bands of HCP structured materials are shown in Figs. 37–40.

Meyers et al. [37] performed dynamic testing on α -titanium hat-shaped specimens in a compression SHPB. As mentioned in Section 4.3 (Fig. 22 (b)), that shear bands develop in two steps: one is instability, caused by thermal softening and the increment of the thermal assistance in the motion of dislocations; the other is localization, requiring softening because of major microstructural changes (recovery and dynamic recrystallization) in the material. The shear band width varied from about 3–20 μm and increased with plastic strain. Near the shear band, elongated grains were found, which transformed to subgrains approaching the middle of band. The breaking-up of the subgrains led to the formation of equiaxed grain microstructure ($\sim 200\text{ nm}$) with a relatively low dislocation density (Fig. 37).

The microstructure within shear bands in AM60B magnesium alloys was revealed by Zou et al. [68]. They reported both deformed and transformed shear bands in Mg alloy under dynamic loading, as presented in Fig. 38. The white lines in Fig. 38 (a) and (d) show boundaries of the shear-band zones. Severely deformed small grains were found inside shear bands in Fig. 38 (b). Elongated grains along the shear direction can be clearly seen. The asterism in the diffraction spots in Fig. 38 (c) is due to the crystal misorientation within severely deformed grains. Meanwhile, recrystallized and equiaxed grains with sizes between 50 and 200 nm are observed, as shown in Fig. 38 (e); the ring-like selected electron diffraction pattern reveals the large misorientation within these grains. The indexed diffraction pattern in Fig. 38 (f) shows that only HCP structure is detected, without phase transformation. Thus, this is truly a recrystallized band.

Jiang et al. [331] showed a similar microstructure evolution inside shear bands in the peak aged ZK-60 magnesium by exploding a cylindrical tube specimen. The shear band is clearly presented in Fig. 39 (a). The boundary of shear bands was clear. The width of the ASB is about 9 μm , while the structure inside the shear band cannot be resolved by optical microscopy. There is a large difference in the microstructure between the shear band and matrix, as demonstrated by TEM analysis in Fig. 39 (b) and (c). The matrix is severely deformed and stretched in the shear direction. A high dislocation density near the boundary of the ASB was observed (Fig. 39 (b)), forming dense dislocation cells. Fig. 39 (c) presents the morphology in the middle of the ASB, which exhibits fine equiaxed grains with low dislocation density. The selected electron diffraction patterns in positions 1, 2 and 3 located at the matrix, boundary and shear band in Fig. 39 (b) are shown in Fig. 39 (d). The orientation difference among the fine grains is significant in the core of the ASB and a continuous diffraction ring was found. Near the boundary of band, the continuous diffraction rings become less obvious indicating a

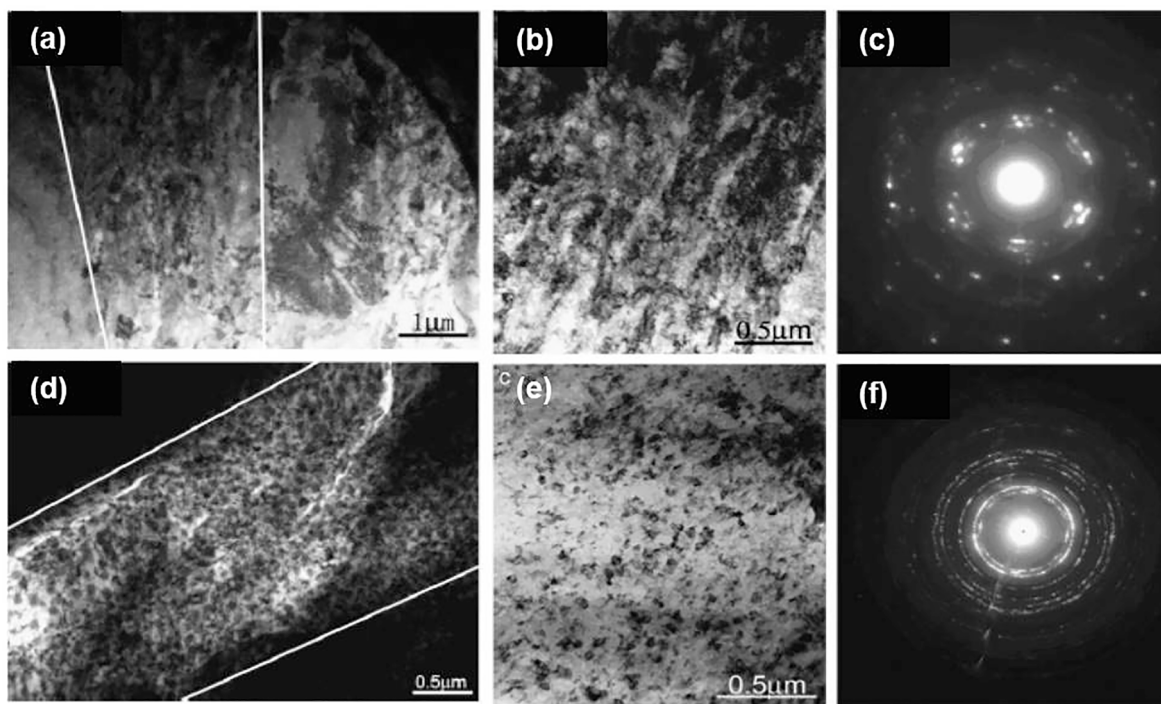


Fig. 38. TEM images of ASBs in AM60B magnesium alloy target impacted by steel projectile at a velocity of $0.5\text{ km}\cdot\text{s}^{-1}$: (a) deformed bands; (b) typical microstructure of deformed band; (c) corresponding SAED; (d) transformed bands; (e) typical microstructure of nanocrystalline (dynamically recrystallized) bands; (f) corresponding SAED [68].

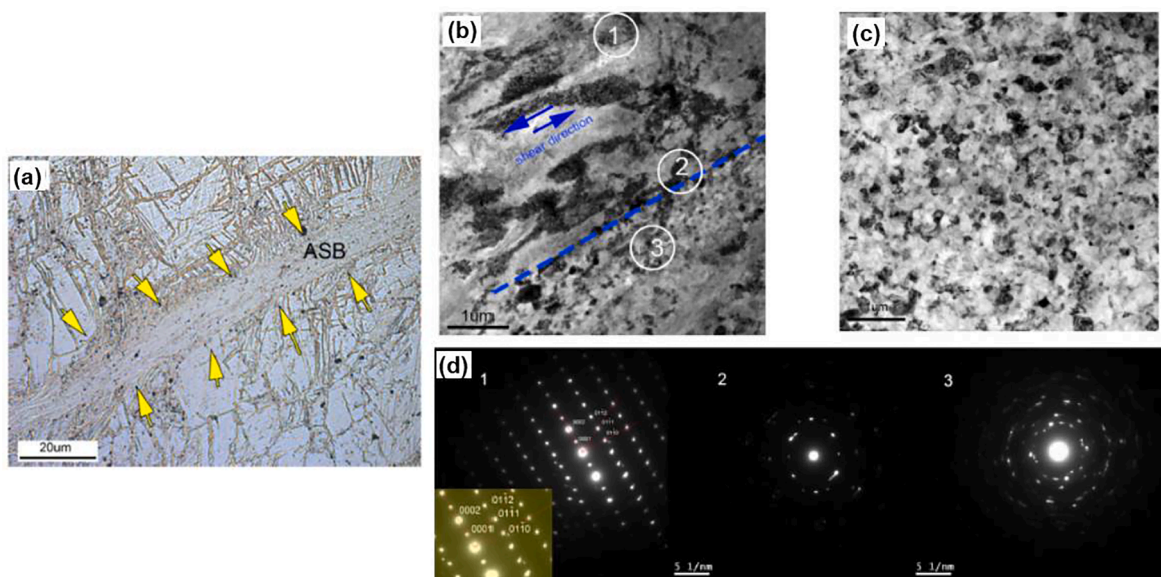


Fig. 39. Microstructure of ZK 60 magnesium alloy after dynamic deformation: (a) optical metallography characteristic of shear band; (b) bright field TEM image of the microstructure in shear region; (c) TEM image of microstructure in shear band; (d) selected area diffraction pattern corresponding to regions shown in (b) and marked 1, 2, and 3 [331].

decrease in subgrain numbers. A similar recrystallized microstructure evolution is also observed in AM60B magnesium alloy as demonstrated by Zou et al. [68].

A similar evolution of the microstructure is observed in zirconium hat-shape specimens subjected to forced localization deformation [124]. Fig. 40 (a) shows the detailed microstructure of the shear band, the matrix, and a narrow 2–5 μm transition region. In the transition region, evidence of plastic flow is revealed as the initially equiaxed grains are starting to flow along the shear direction. Fig. 40(b) illustrates the elongated grains in the transition zone between shear band and matrix. Outside of the shear band, the grains retain their initial size and shape. The appearance of an equiaxed microstructure with diameter of ~ 200 nm is evident inside the shear band. The dominant diffraction spots in the insert of Fig. 40 (c) depict splitting or clustering, as marked by white arrows, revealing the initial stages of orientation changes. In the case of a larger deformation under a larger shear strain presented in Fig. 40 (d), the grain size within the shear band is 200 nm, similar to that of Fig. 40 (c). The well-developed ring diffraction pattern indicates a small grain size and randomized texture. By comparing these two diffraction patterns, the misorientation between grains appears to increase with the increase of shear strain in the shear band.

In Fig. 41, the parallel band-like structures with a length about 100–500 nm are revealed in the severely deformed band of Ti-6Al-4V under quasi-static compression (Fig. 41 (a)) [338]. These are assumed to be deformation twins which are normally observed in titanium alloys [298]. In this case, the formation of the ultrafine-equiaxed grains was attributed to twinning, and it was proposed as a twinning-induced rotational dynamic recrystallization mechanism [336]. However, a high density of dislocations was found in ASBs at a strain-rate of 1500 s^{-1} (Fig. 41 (b)), while the deformation twins seem to be restricted. Nanosized equiaxed grains with high-angle grain boundaries were observed within the ASB, as shown in Fig. 41(c).

11.1.2. FCC alloys

Materials with FCC crystal structure, such as aluminum alloys, copper alloys and nickel-based alloys have been extensively investigated by split-Hopkinson pressure bar (SHPB) using cylindrical and hat-shaped specimens, electromagnetic impact upsetting or external explosive loading (thick-walled cylinder), and Taylor impact techniques.

Substructures due to dislocation reorganization are remarkably based on the stacking-fault energies in FCC metals. The tendency for dislocation cross-slip is decreased and for dislocation pile-up increases as stacking-fault energy decreases. Thus, perfect dislocations decompose into two partial dislocations more easily, with a stacking fault between them. In addition, it was discovered that the stacking faults may overlap with each other during slip on parallel slip planes; the intrinsic and extrinsic stacking faults are bound by partial dislocations [342].

Aluminum and its alloys have relatively high stacking-fault energy, resulting in dislocation slip as a dominant mechanism during plastic deformation. Fig. 42 (a)-(c) show multiple slip microstructures inside the shear band [104]. Many equiaxed recrystallized grains dispersed inside the slip bands (with lamellar structures), are shown in Fig. 42 (d) and (e). The size of these grains is not uniform and ranges from 50 to 100 nm. Based on the corresponding diffraction pattern in Fig. 42 (e), the grain misorientation was randomly distributed with primary high-angle grain boundaries. Some recrystallized grains contain a high density of dislocations, indicating the severe shear deformation. These structures were similar to the subgrains evolved from dislocated cells.

In low-nickel austenitic stainless steel, Wang et al. [343] found that the grains were elongated along the shear band. Equiaxed

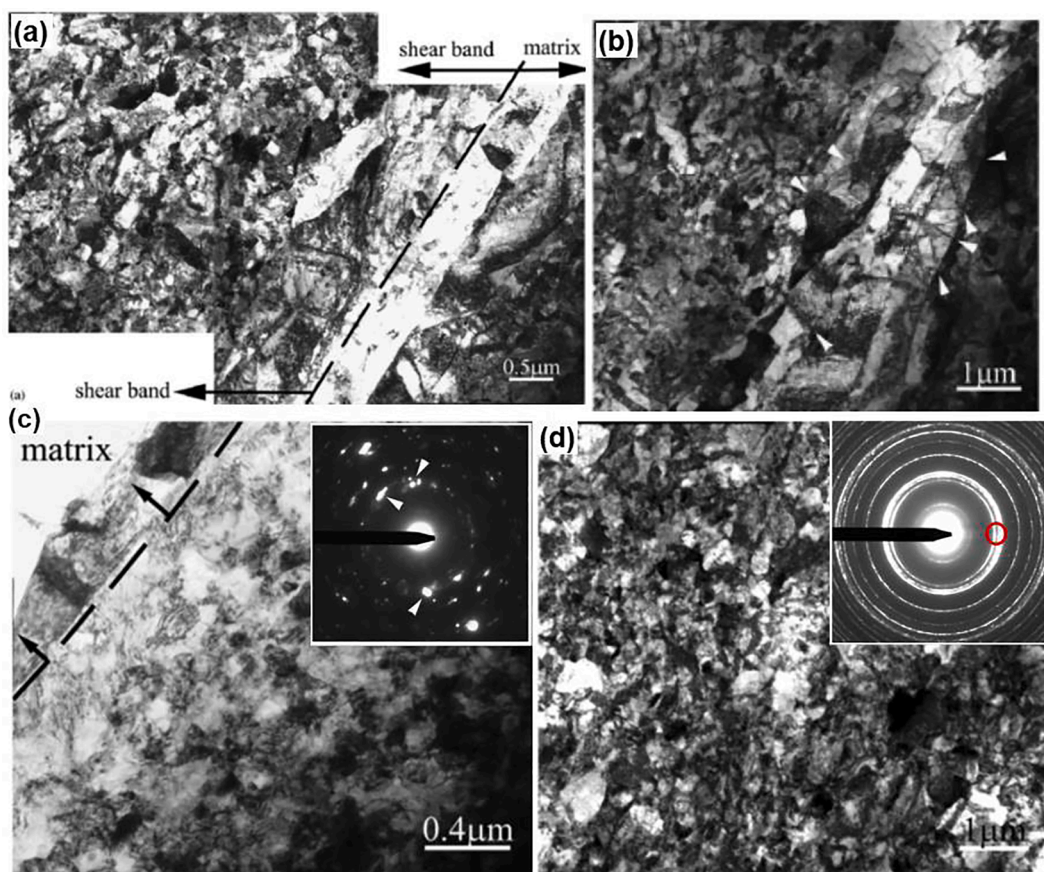


Fig. 40. Microstructure evolution in shear band of zirconium: (a) composite structure of the shear band (left), matrix (right), and the matrix/shear band (dashed region) interface; (b) fine details of deformation bands (arrows) along the pancake-like grain; (c) coarse grains evolve into a well-established fine-grained structure; (d) the microstructure with fine grains of 200 nm and the diffraction evidence with a well-developed ring structure indicating fine grain size and randomized texture [124].

grains with 100–300 nm size and low dislocation density locate in the center of the shear band. The ultrafine grains experienced severe deformation and the calculated maximum temperature was sufficient for recrystallization. The significant decrease of grain size is explained by the rotational dynamic recrystallization [336]. Such phenomenon was also found in the Ti-3Al-5Mo-4.5V alloy studied by Wang et al. [87].

Xue, Cerreta, and Gray [137] investigated the formation of forced adiabatic shear bands in AISI 316 stainless steel and obtained systematic and detailed characterization of the structures shown in Fig. 43. The stainless steel has undergone significant twinning by the previous cold rolling step and the structure inside the band was therefore somewhat more complicated, consisting of laths, fine rectangular grains, and the familiar equiaxed grains with a diameter of ~ 80 nm. Their formation was attributed to a continuous (rotational) dynamic recrystallization mechanism.

11.1.3. BCC alloys

For BCC metals, the strain-rate sensitivity is higher and so is reflects the yield stress dependence of strain rate [339]. Beatty et al. [337] studied the shear localization of AISI 4340 high strength steel. The TEM diffraction results show an absence of transformation inside the shear band; they are just heavily deformed pre-existing martensite structures. Extremely small nanograins, ranging from 8 nm to 20 nm, were formed as shown in Fig. 44. This clarified the issue that some white etching of a transformed band is indeed a deformed band.

The effect of strain on microstructural evolution in ASBs in a 1Cr18Ni9Ti stainless steel was examined by Yang et al. [344] using hat-shaped specimens. As the shear strain increased, an increase in dislocation density and elongated grains developed with the formation of sub-grains in the direction of shear. Upon shear band maturity, the short axis width of the elongated grains reduced and there was an increase in the misorientations in subgrains, which resulted in the formation of nano-grains. The formation of nano-grains was explained using a classical rotational dynamic recrystallization mechanism to rotate the grain boundary by about 30° .

Wang et al. [311] also investigated the adiabatic shear localization in beta type coarse-grained Ti-5Al-5Mo-5 V-1Cr-1Fe (Ti-55511) alloy using the SHPB. ASBs were found, of which the width changes slightly with increasing nominal shear strain. The width of ASBs in

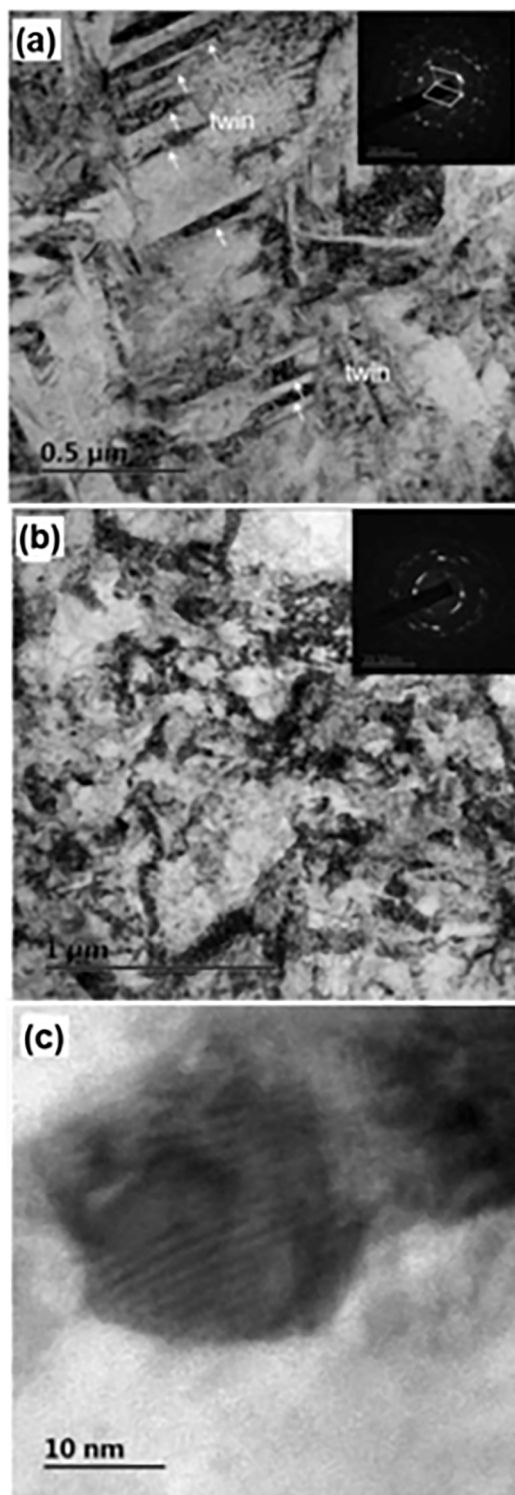


Fig. 41. TEM images of microstructure within the shear band of heat-treated Ti-6Al-4V alloy specimens deformed at the strain rate of: (a) 0.001 s^{-1} ; (b) and (c) 1500 s^{-1} . Notice nanosized equiaxed grain in (c) [338].

the fine-grained Ti-55511 alloy [305] is smaller than that in the coarse-grained materials, which is consistent with the prediction of shear band thickness in Section 5.2. From Fig. 45 (a)-(c), it can be seen that highly-elongated dislocation cells form near the boundary of sheared regions, and fine-scaled deformed grains with size of 100 nm in the center of shear band in coarse-grained Ti-55511 alloy.

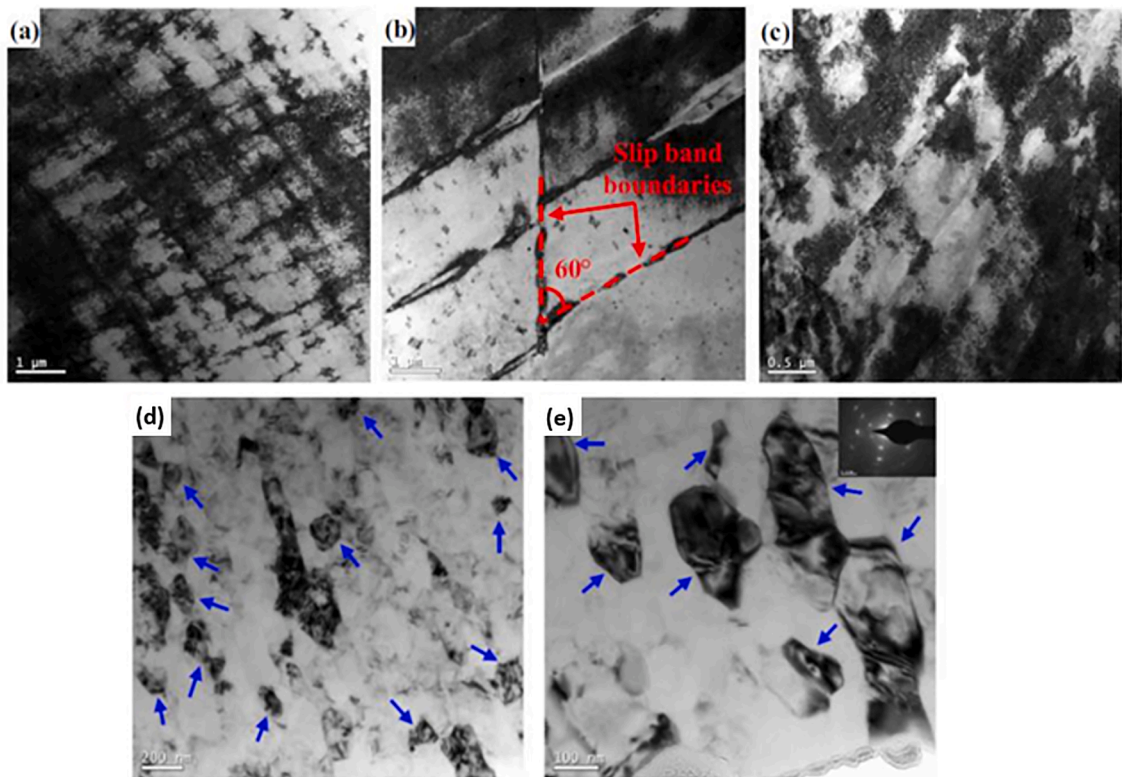


Fig. 42. Details of microstructure within the shear bands in Al-Cu alloy subjected to electromagnetic upsetting: (a) multiple groups of slip bands crossing each other; (b) partial enlarged view of slip bands; (c) dislocation patches; (d) dynamically recrystallized grains in the adiabatic shear band; (e) enlarged view of grains [104].

For comparison, the microstructure evolution during shear localization of fine-grained Ti-55511 alloy, which is composed of α and β phases (matrix), is also presented in Fig. 45 (d)-(f). The elongated cell structures are found close to the shear region, and nano-sized equiaxed grains with size of 50–200 nm with low dislocation density are formed in the core of ASB. Meanwhile, the α'' -martensite phase and α -phase grains are found in region A (Fig. 45 (f)) as the marked by dashed line, which indicate the occurrence of phase transformation from β -Ti (cubic) to orthorhombic within the shear bands. The dynamic recovery and rotational dynamic recrystallization mechanisms lead to the formation of microstructures inside the ASBs in these two Ti-55511 alloys. Wang et al. [461] revealed that Ti-5553 alloys with alpha/beta phases and bimodal microstructures obtained high strength (over 1.5 GPa) and high dynamic failure strain (~ 0.15) under dynamic loading. Beta to martensite phase transformation occurred during dynamic deformation. The area with the high dislocation density served as the nuclei site to activate martensite phase transformation. Ali et al. [464] also found that stress-induced bcc to hcp phase transformation in beta Ti-5Al-5V-5Mo-3Cr-0.5Fe alloys occurred under dynamic loading when two adjacent beta planes $(110)_\beta$ in $\langle 111 \rangle_\beta$ direction covered 1/6th of the total separating distance between the planes. Twinning and phase transformation during dynamic deformation lead to the breaking-up of coarse grains before shear localization.

Besides, a link between texture and DRX within ASB was established by Molinari et al. [341]. They applied the EBSD technique to measure the orientation of the grains for a XC-18 steel, from which the crystallographic texture was studied and the DRX was identified. They compared the orientation distribution functions from the EBSD with calculations using the self-consistent viscoplastic method. Different textures within the ASB and outside the ASB were measured, and a strong D2 component inside ASB indicated the occurrence of DRX (Fig. 46). The angles ϕ_1 , ϕ_2 , and ϕ are the Euler angles. It was shown that the main texture formation mechanism of DRX is oriented nucleation followed by generalized growth. The simulation with a self-consistent homogenization was found to be more faithful than previous relaxed constraint models [345]. However, it should be mentioned that this model does not address rotational recrystallization. It is possible that this low-carbon steel does not exhibit what is traditionally known as ‘transformed bands’ and that therefore the mechanism of texture evolution is not the same as when rotational recrystallization takes place.

11.2. Shear bands in high-entropy alloys

Due to their excellent strain hardening, most high-entropy alloys (HEAs) are expected to have remarkable resistance to shear localization in comparison with conventional alloys. Li et al. [80,346] carried out Hopkinson bar experiments using hat-shaped specimens (a forced shear localization configuration seen in Section 3.1) to examine the deformation mechanisms, especially

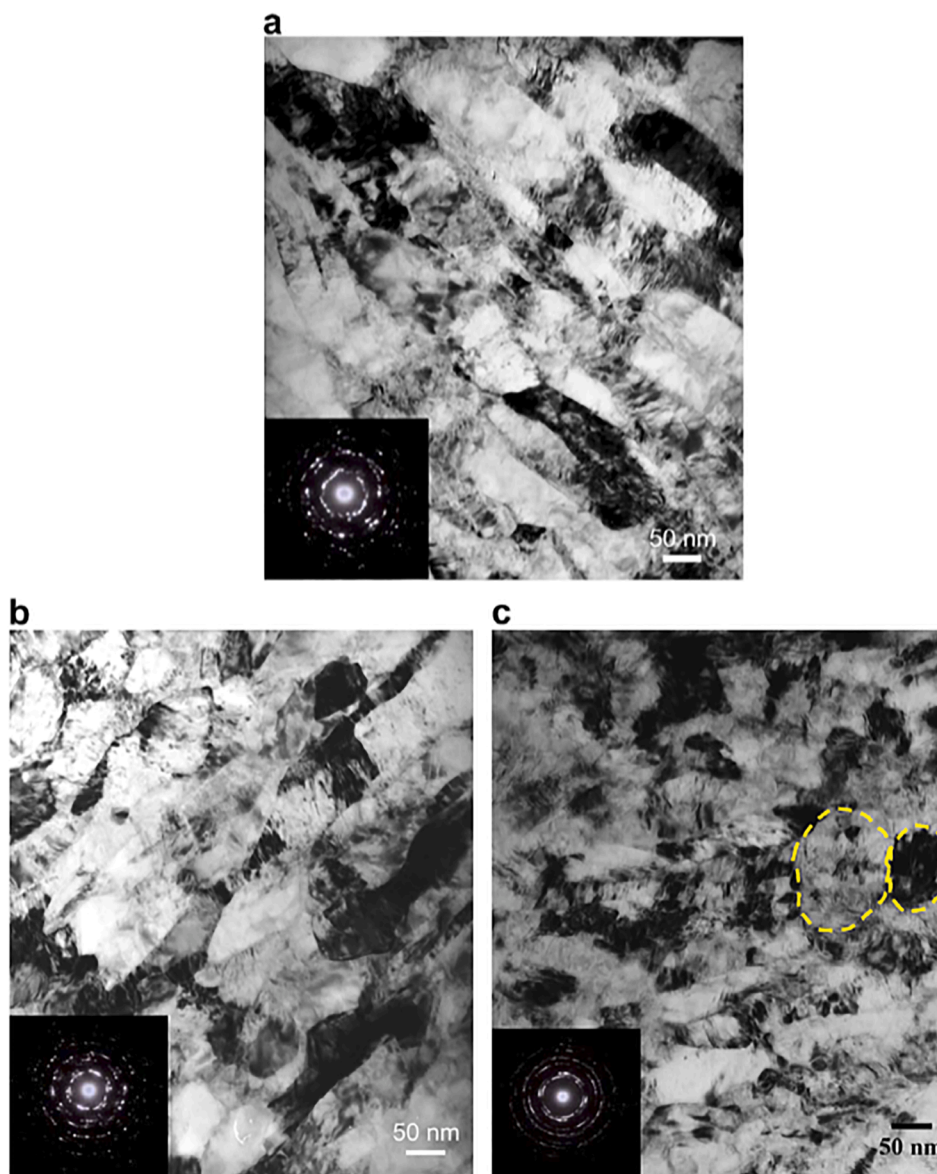


Fig. 43. Transmission electron microscopy images revealing microstructures at the center of shear bands developed in 316L stainless steel corresponding to increasing loading durations of (a) 25.1 μs ; (b) 30.0 μs and (c) 36.1 μs [137]. The increasing durations produce increasing shear strains. Structure evolves from elongated/rectangular subgrains to equiaxed nanosized grains with corresponding evolution of the diffraction pattern.

focusing on shear localization, for two types of HEAs. One is a coarse-grained $\text{Al}_{0.3}\text{CoCrFeNi}$ HEA with a grain size of $\sim 500 \mu\text{m}$, the other is a CrMnFeCoNi HEA with an average grain size of about $10 \mu\text{m}$. The strain-hardening rate of the $\text{Al}_{0.3}\text{CoCrFeNi}$ HEA is significantly higher (above 1000 MPa) than coarse-grained pure Al at low and high strain-rates. The combined multiple strengthening mechanisms such as solid-solution hardening, forest dislocation hardening (Fig. 47 (a) and (b)), and mechanical twinning (Fig. 47 (c)) lead to an excellent strain hardening rate, as shown in Fig. 47 (d). And thus, no ASB is observed at a shear strain of ~ 1.1 . Fig. 47 (f) and (g) show the formation of a significant amount of mechanical twins near the end notch of the hat-shaped specimen, confirming twinning-induced continuous work-hardening in competition with the thermal softening effect, which suppresses shear localization.

High strain-rate tests of a series of hat-shaped specimens with the application of stopper rings to control shear displacements were performed [346], focusing on the critical shear strain for shear localization in the CrMnFeCoNi high-entropy alloy. Fig. 48(a) demonstrates that the specimen localizes only at a high shear strain of ~ 7 . The calculated temperature rises in the shear band reached the recrystallization temperature of $\sim 0.4 T_{\text{melting}}$. Fig. 48(b) shows the formation of a narrow shear band with a thickness of about $10 \mu\text{m}$. Nanostructured grains with size of 100–300 nm are found inside the shear band, Fig. 48(c). The evolution of shear deformation, coupled with the temperature rise (Fig. 48(a)), leads to the formation of a dislocated/twinned microstructure that breaks up the initial

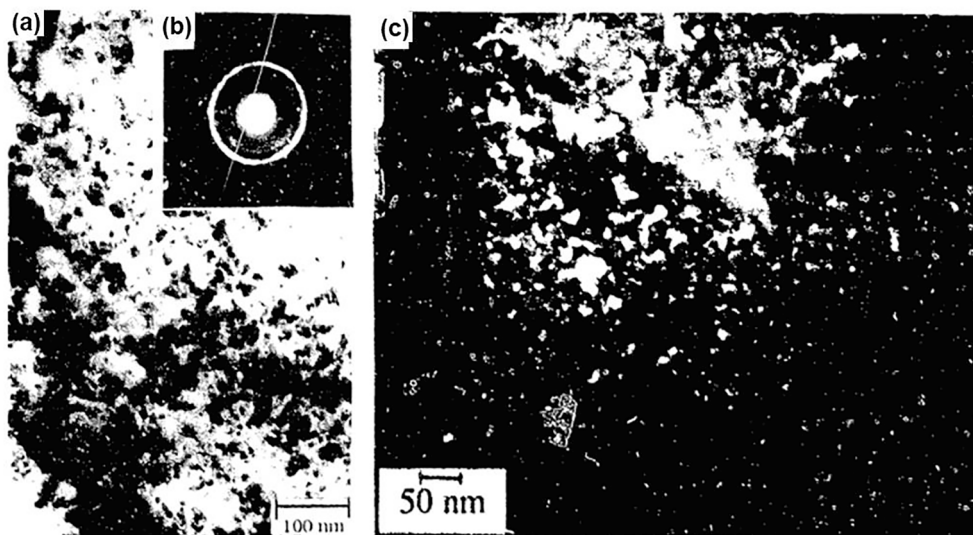


Fig. 44. (a) TEM bright-field image of microstructure inside the shear band of AISI 4340 high strength steel; (b) Diffraction pattern in image (a); (c) Dark-field image showing nanometer grains ranging from 8 nm to 20 nm inside the shear band [337].

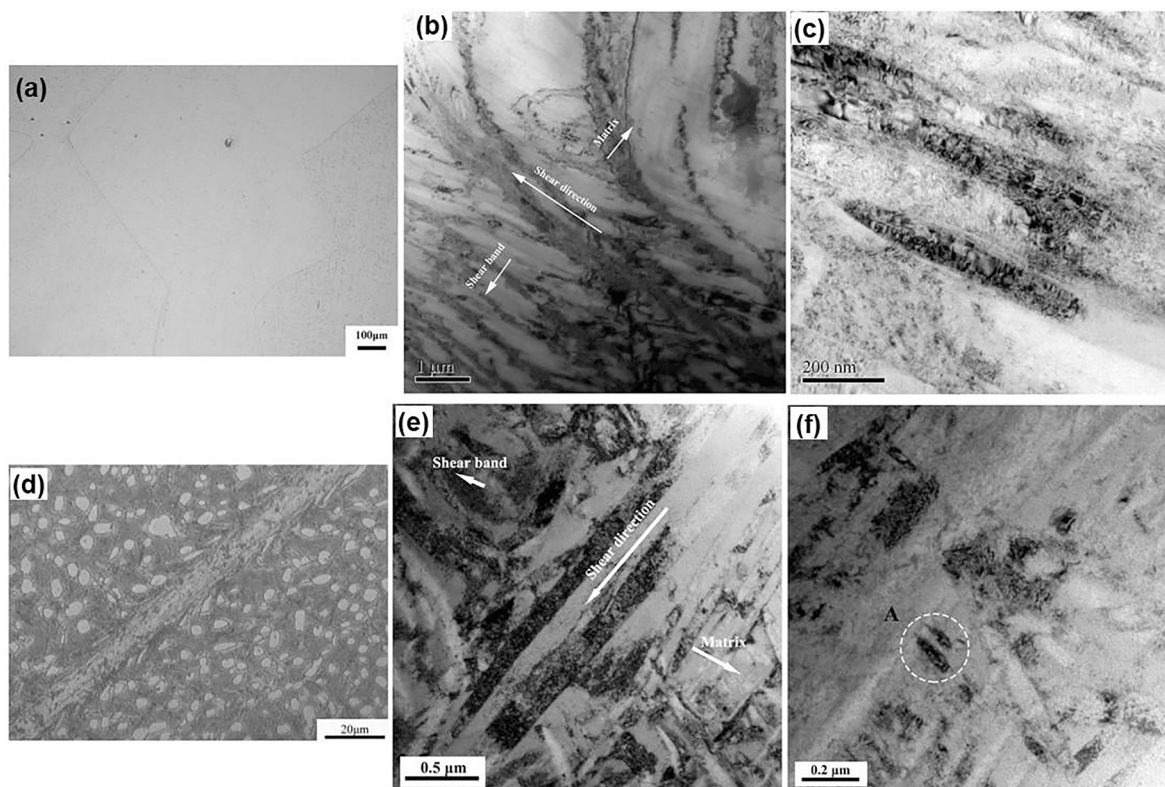


Fig. 45. The morphology of shear band in titanium alloy (Ti-5Al-5Mo-5V-1Cr-1Fe) with coarse-grained beta microstructure (a)-(c) and fine-grained near-beta microstructure (d)-(f): (a) original microstructure of coarse-grained titanium alloy; (d) optical micrograph of the shear band in fine-grained specimen; (b) and (e) the interface region between shear band and matrix; (c) and (f) the microstructure in the center of the shear band [305,311].

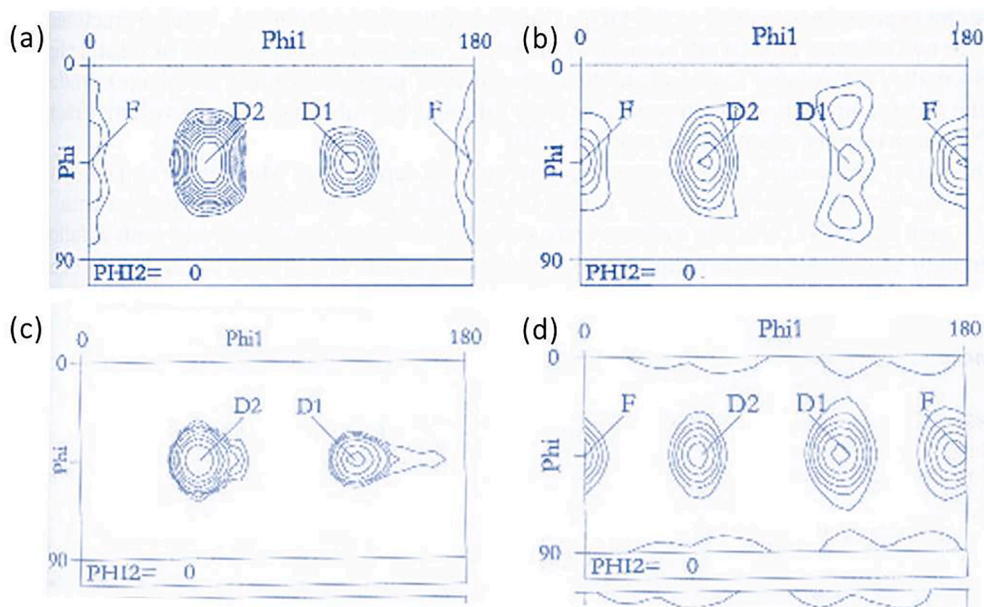


Fig. 46. Orientation Distribution Functions (ODFs) obtained inside (a), (c) and outside (b), (d) the shear band for a XC18 (AISI-1020) steel subjected to shear deformation with a shear strain equals 5. (a) and (b): experimental measured texture from EBSD; (c) and (d): simulated results. Notice the concentration of D2 within the bands in both experimental and simulated cases. ϕ_1 , ϕ_2 , and ϕ are Euler angles [341].

coarse-grained grains into small regions. Recrystallization twins are found within grains inside the shear band in Fig. 48(d) and are due to the dynamic recrystallization process in CrMnFeCoNi HEA (which has a low stacking-fault energy of ~ 20 mJ/m²). Fig. 49(a) shows the excellent work-hardening ability of Al_{0.3}CoCrFeNi and CrMnFeCoNi HEAs at high strain rates. Fig. 49(d) compares the experimentally observed and predicted critical shear strains for shear localization in seven materials [80,346] using the Staker criterion (Eq. (8)). The CrMnFeCoNi HEA shows the most remarkable resistance to shear localization among the seven metals and alloys. As mentioned earlier, this is caused by the high strain-hardening ability as seen in Fig. 49(b) and low thermal softening effect as shown in Fig. 49(c) [80,346].

Recently, medium-entropy alloys (MEAs) have emerged as an interesting class of metallic materials, which exhibit unique mechanical properties [347]. Ma et al. [348] investigated the dynamic response of FCC CrCoNi MEA by a series of SHPB experiments at both room and cryogenic temperatures. Excellent dynamic performance, propitiated by a combination of high dynamic shear strength and shear failure strain, were observed. Such superior strain hardening under dynamic conditions was attributed to the dynamic grain refinement and deformation twinning. Phase transformation from FCC to HCP phase was found, sustaining high strain hardening rate at cryogenic temperatures. In addition to these FCC HEAs with high strain-hardening ability, the dynamic behavior of many other HEAs still needs to be explored.

11.3. Shear bands in nanocrystalline metals

Nanocrystalline and ultrafine-grained materials are discussed here. The effect of grain size on the strain-rate sensitivity of materials is presented in Fig. 50 [332,349]. The increase in strain-rate sensitivity for FCC and decrease for BCC metals with the decrease of grain size are noted. The materials in the shadowed region with BCC structure except for Cu may fail by localization.

ASB formation in nanostructured alloys with FCC structure and with different stacking-fault energies (SFEs) was studied by Li et al. [350]. They employed the SHPB at a strain rate of $\sim 4 \times 10^3$ s⁻¹ for Cu-Al alloys with different SFEs, which were deformed through 8 passes by Equal Channel Angular Pressing (ECAP) at room temperature. It was revealed that ASBs were more susceptible to be formed in the alloys with lower stacking fault energy, even though higher work-hardening behavior was shown when decreasing stacking fault energy under quasi-static loading. Shear localization was observed, and flow lines were apparent. The thickness of the shear band is about 25 μ m in Fig. 51 (a). Different microstructures inside and outside the shear band are obtained by TEM and shown in Fig. 51 (b) and (c). The grain sizes outside the band are much larger and have a higher density of defects. The selected area diffraction pattern demonstrates the existence of deformation twins in the area which are marked by a dashed circle. Fully recrystallized grains and nearly defect-free inside the shear band are associated with the temperature rise.

On the other hand, Mishra et al. [82] studied the high strain-rate response of pure copper with an ultrafine grained structure produced by ECAP. On further examination, the structure of these bands was quite different from the initial material, with a large scatter in grain size ranging from 0.2 μ m to 4 μ m. Fig. 52 shows the structure of shear band as revealed by (a) SEM, (b) TEM and (c) EBSD. The large grains arise from heat-induced static recrystallization inside the shear band and heat-affected zone near the band; meanwhile, most of the ultrafine grains are retained outside the deformation areas. Thus, the enhanced strain-rate sensitivity and

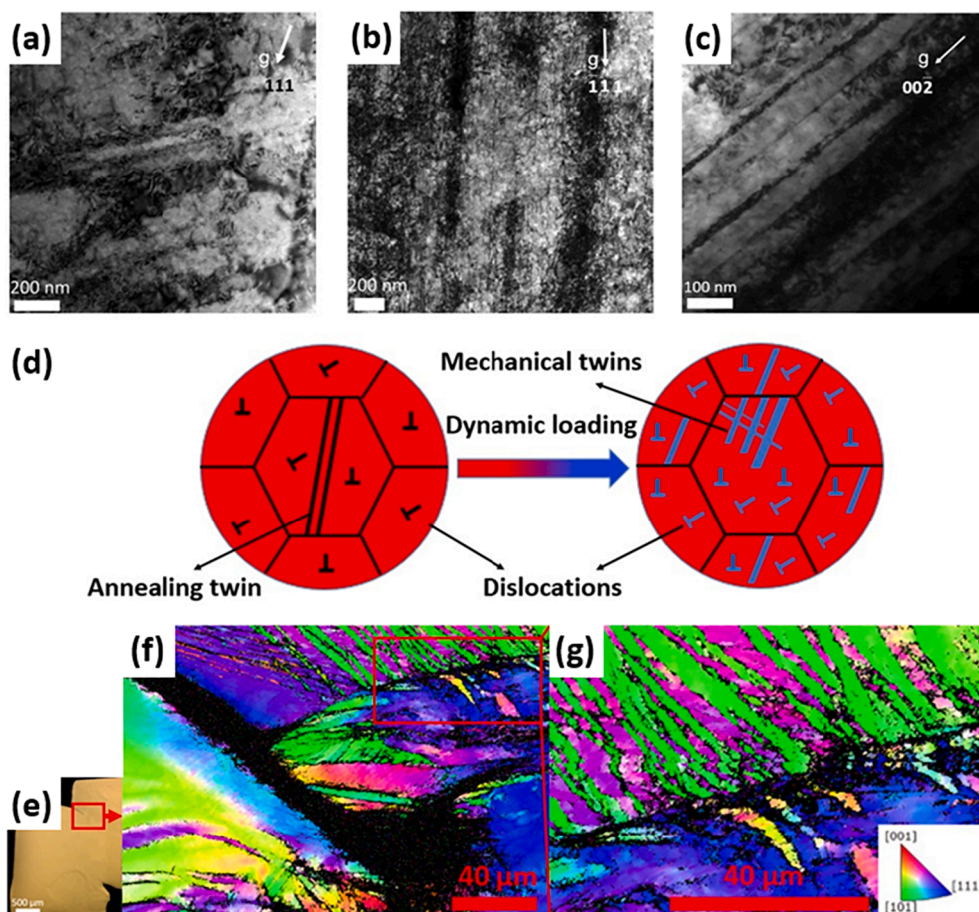


Fig. 47. Resistance to shear localization in $\text{Al}_{0.3}\text{CrFeCoNi}$ high-entropy alloy at shear strain of 1 and TEM bright-field images of the deformed samples at the strain-rates of: (a) 10^{-4} s^{-1} ; (b) and (c) 1800 s^{-1} ; (d) schematic sketches showing the deformation mechanisms in dynamic loading; (e) optical microscopy image of the deformed hat-shaped sample; (f) EBSD image near the deformation tip; (g) EBSD image showing deformation twins near the deformation tip [80].

decreased shear band thickness in UFG copper as compared with conventional polycrystalline copper can be attributed to an enhanced thermal softening and inherent instability observed in the UFG materials.

Adiabatic shear localization in ultrafine-grained $\sim 120 \text{ nm}$ titanium was studied in a forced shear hat-shaped specimen [81]. Fig. 53 depicts the microstructure inside the ASB, which consists of equiaxed nanocrystalline grains ($\sim 40 \text{ nm}$) which are about one third of the size of the initial grains ($\sim 120 \text{ nm}$). The formation of these nanograins was modeled through a combination of shear deformation and rotational dynamic recrystallization. The decrease in grain size inside the shear band is similar to other severe plastic deformation techniques such as high-pressure torsion (HPT). The UFG titanium was found to be more prone to shear localization due to increased thermal softening and decreased work hardening, in comparison with coarse-grained titanium. The reduced thermal diffusivity was also suggested to play a role.

11.4. Shear bands in metallic glasses

The initiation and development of shear bands are dominant in the deformation of most metallic glasses, and in many cases, bulk metallic glasses (BMGs), which typically fail by shear localization [24]. First, a number of shear localization regions form. Finally, a few shear bands develop and dominate the dynamic deformation process. Since metallic glasses are quite different from traditional crystalline alloys, lacking long-range order and only possessing short-range order, crystalline defects such as dislocations and grain boundaries cannot exist in such unique structures. The characteristic thickness of the shear localized zone is about $\sim 10 \text{ nm}$ [351]. Such an extremely localized flow mode induces very limited ductility prior to catastrophic fracture, impeding many technological applications of metallic glasses. It is therefore of importance to clarify the mechanism of shear banding in metallic glasses. Shear banding in metallic glasses has attracted substantial attention during last decades, and the reviews by Greer et al. [24] and Dodd & Bai [10] are notable. These have been developed since the seventies and assumed that stress is a function of strain, strain rate, and temperature.

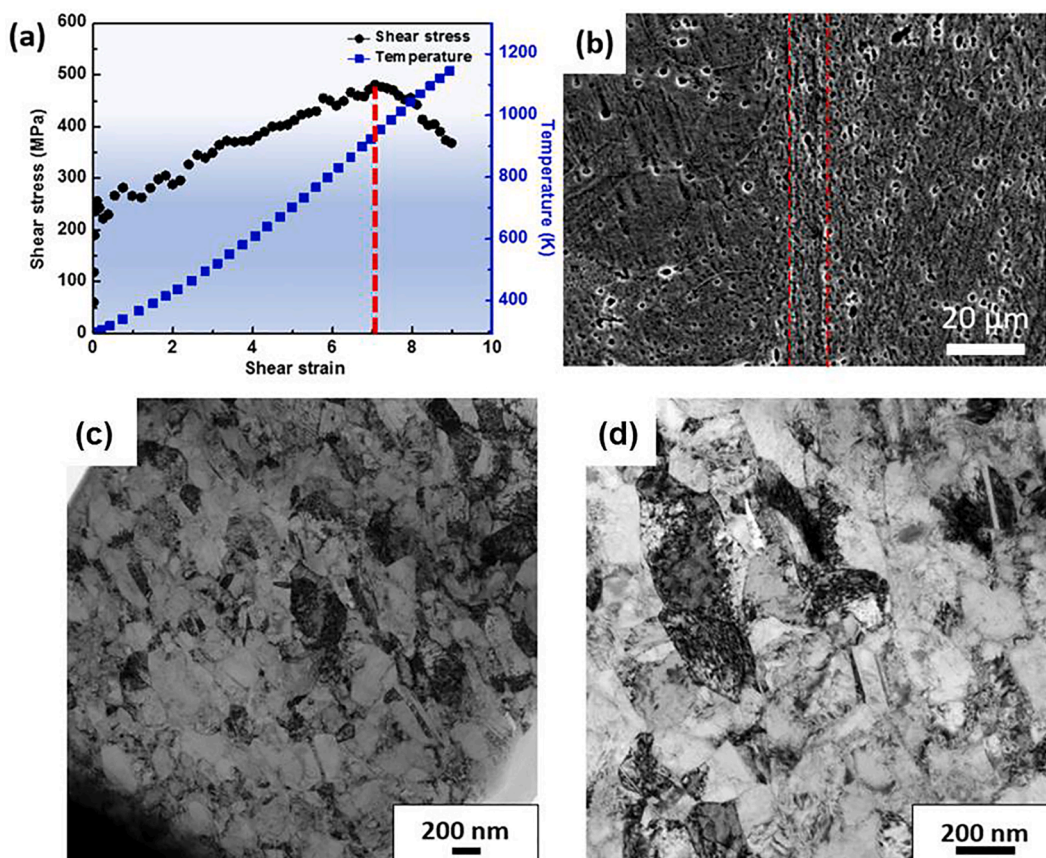


Fig. 48. (a) Shear stress vs. shear strain and temperature evolution of the shear band of the CrMnFeCoNi high-entropy alloy; (b) scanning electron microscope (SEM) image showing the width of shear band is about 10 μm ; (c) transmission electron microscopy images of microstructure inside the shear band in CrMnFeCoNi HEA; (d) recrystallized nanotwins inside the equiaxed nanosized grains formed by the rotational dynamic recrystallization [346].

There are two views on the softening mechanism leading to localization in metallic glasses: thermal softening, reported by Leamy et al. [352] and free-volume softening, proposed by Spaepen [353]. The “free-volume softening” hypothesis essentially contends that shear banding in metallic glasses has an athermal, structural origin. However, the “thermal-softening” hypothesis has gained evidence from the melting phenomena on final fracture surfaces [354] and the significant temperature rise associated with shear banding [355]. Dai et al. [356] revealed that the shear banding in metallic glasses is essentially a coupled thermomechanical process dominated by free volume softening, but assisted by thermal softening. They also proposed an analytical perturbation model which describes the shear flow in metallic glasses considering the free volume and thermal viscoplastic features. The shear-banding instability was found to initiate from local free volume creation, whereas the temperature rise is its consequence (Fig. 54 (a)) [357].

Shear-band evolution in metallic glasses was determined by the dynamic balance between free volume diffusion and momentum diffusion, associated with thermal dissipation, as presented in Fig. 54 (b) [358]. This is different in crystalline materials, which are dominated by the competition between the momentum dissipation and the energy (heating) dissipation. The optimum dissipated energy occurs in a narrow shear-band region, about 10 nm, while momentum dissipation dominates the shear-band spacing. By taking the structural softening, the momentum diffusion, and the energy conservation into account, Chen et al. [359] developed a theoretical model for the evolution dynamics of multiple shear banding in metallic glasses which achieves a quantitative characterization of the shear band evolution in line with experiments. A competing map of shear band nucleation and propagation was further constructed to understand the collective behavior of multiple shear bands in metallic glasses (Fig. 54 (c)). Jiang et al. [360] proposed an explicit expression to predict the thickness of shear bands in metallic glasses, demonstrating the underlying relationship with the activation size of the shear transformation zone (STZ) and the activation free volume concentration, which was consistent with experimental observations (Fig. 54 (d)).

Wright et al. [333,361] investigated the deformation characteristics and shear bands in metallic glasses subjected to uniaxial compression and studied the serrated flow in detail, as presented in Fig. 55 (a). The evolution of load and displacement as a function of time was analyzed to predict the temperature increase in the shear band. One of these examples, based on Pd₄₀Ni₄₀P₂₀ bulk metallic glass, is presented in Fig. 55 (c) and (d). The temperature increase predicted for heating during a single serration is on the order of a few degrees Kelvin. The small temperature increment would not be a possible cause for serrated flow. A temperature rise of 280 K is also

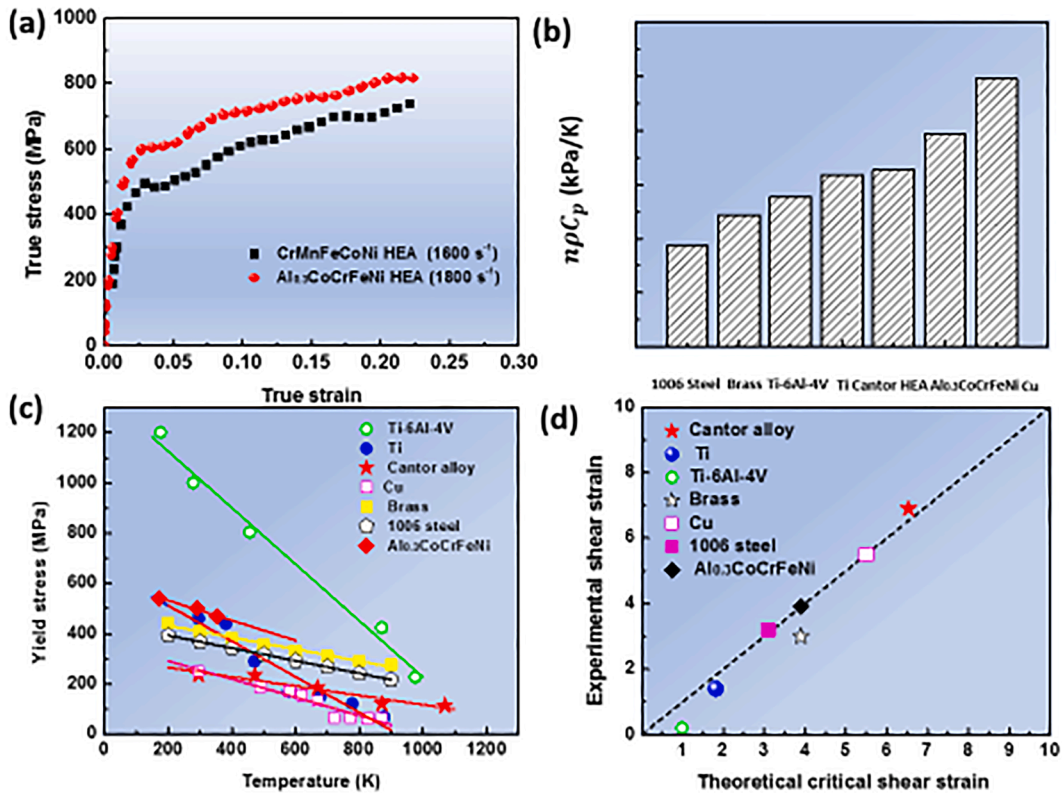


Fig. 49. (a) Mechanical response of Al_{0.3}CoCrFeNi and Cantor high-entropy alloys under high strain-rates; (b) the value of $n\rho C_p$ for pure Ti [37], Ti-6Al-4V alloy [327], 1006-Steel [452], Copper [452], Brass [452], Al_{0.3}CoCrFeNi HEA [80] and the Cantor alloy [346]; (c) thermal-softening effect of different materials; (d) predicted (Staker equation) and experimental critical shear strain for shear localization.

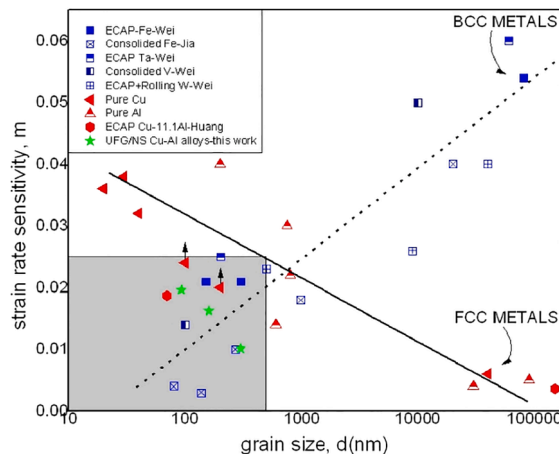


Fig. 50. Strain-rate sensitivity of BCC and FCC metals or alloys as a function of grain size; the squares stand for BCC and the triangles stand for FCC metals. The metals or alloys included in the shadowed region all failed via localized shearing deformation except for the two red triangles which represent the pure copper [349]. (For interpretation of the references to color in this figure legend, the reader is referred to the web version of this article.)

predicted for the final failure event, which may be underestimated due to the uncertainty of parameters in the calculations. Thus, the local adiabatic heating is proposed not to be the main reason of flow localization in metallic glasses. Resolidified spheroidal droplets do appear on the fracture surface, which suggests the localized melting during the final failure event.

Experiments performed by Zhang and coworkers [362] show that that the compressive and tensile strengths of BMGs are not identical. Typical curves are shown in Fig. 55 for Ti-, Pd-, and Zr-based BMGs [363,364]. Load drops are observed in compression tests

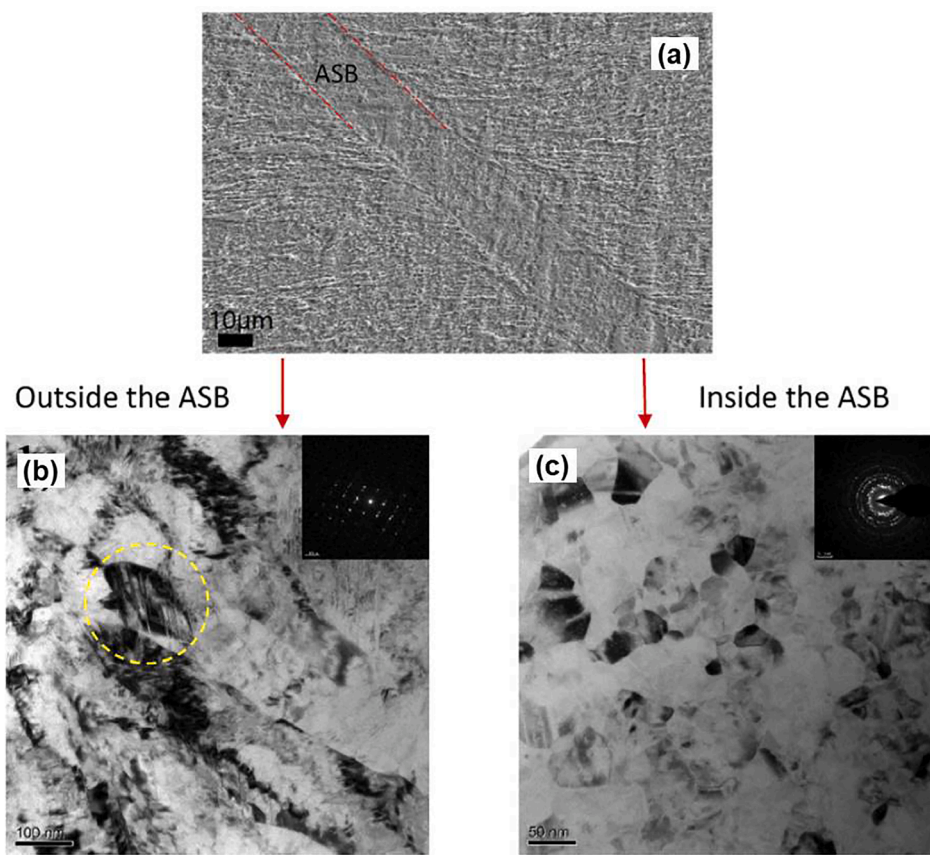


Fig. 51. Microstructure of shear band in nanostructured Cu-11.4 at% Al under dynamic loading at a strain rate of $\sim 4 \times 10^3 \text{ s}^{-1}$: (a) overall view of region; (b) TEM outside of ASB; (c) TEM inside ASB showing nanocrystalline structure [350].

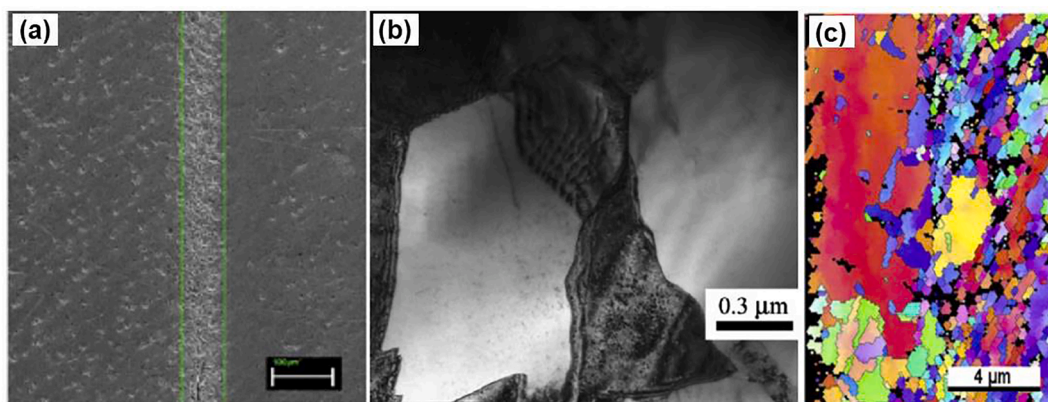


Fig. 52. Forced shear band formed in hat shaped specimen in ultrafine grained copper with size of $\sim 200 \text{ nm}$: (a) SEM showing shear band with width $\sim 50 \mu\text{m}$; (b) TEM showing larger recrystallized grains; (c) EBSD image showing enlarged grains inside shear band (fractured along band area) [82].

of the three BMGs, which present the same nature as just mentioned [333,361]. The compressive strength is slightly higher ($\sim 15\%$) than the tensile strength (Fig. 55 (b)). The failure by tension and compression deformation occurs by shear banding, as presented in the fractured $\text{Pd}_{40}\text{Ni}_{40}\text{P}_{20}$ materials in Fig. 56 [365]. The compressive fracture angle of 42° , which is smaller than the maximum shear stress direction 45° , indicating that yielding of Pd-based BMG obeys a Mohr-Coulomb criterion instead of the von-Mises criterion. Indeed, the angle of the shear band with the loading axis in tension was 56° . Zhang et al. [366] proposed a new failure criterion, modified from the Mohr-Coulomb theory, aiming at explaining this phenomenon.

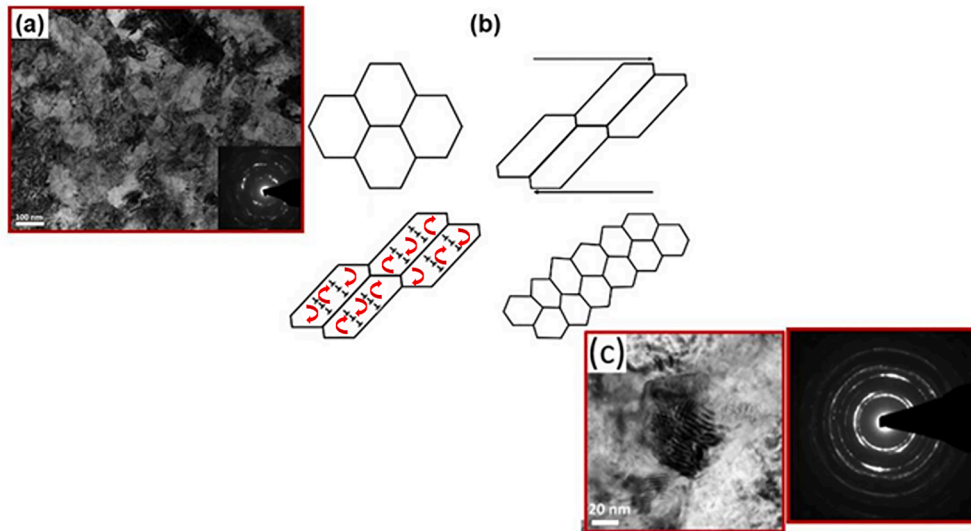


Fig. 53. Sequence of microstructure breakdown and formation of ultrafine grained titanium produced by Equal Channel Angular Pressing (ECAP): (a) TEM micrograph of cross-section of as-received titanium; (b) schematic illustration of microstructural evolution inside the shear band; (c) equiaxed grains inside shear band. Although the initial grain size is 120 nm, there is further refinement inside shear band [81].

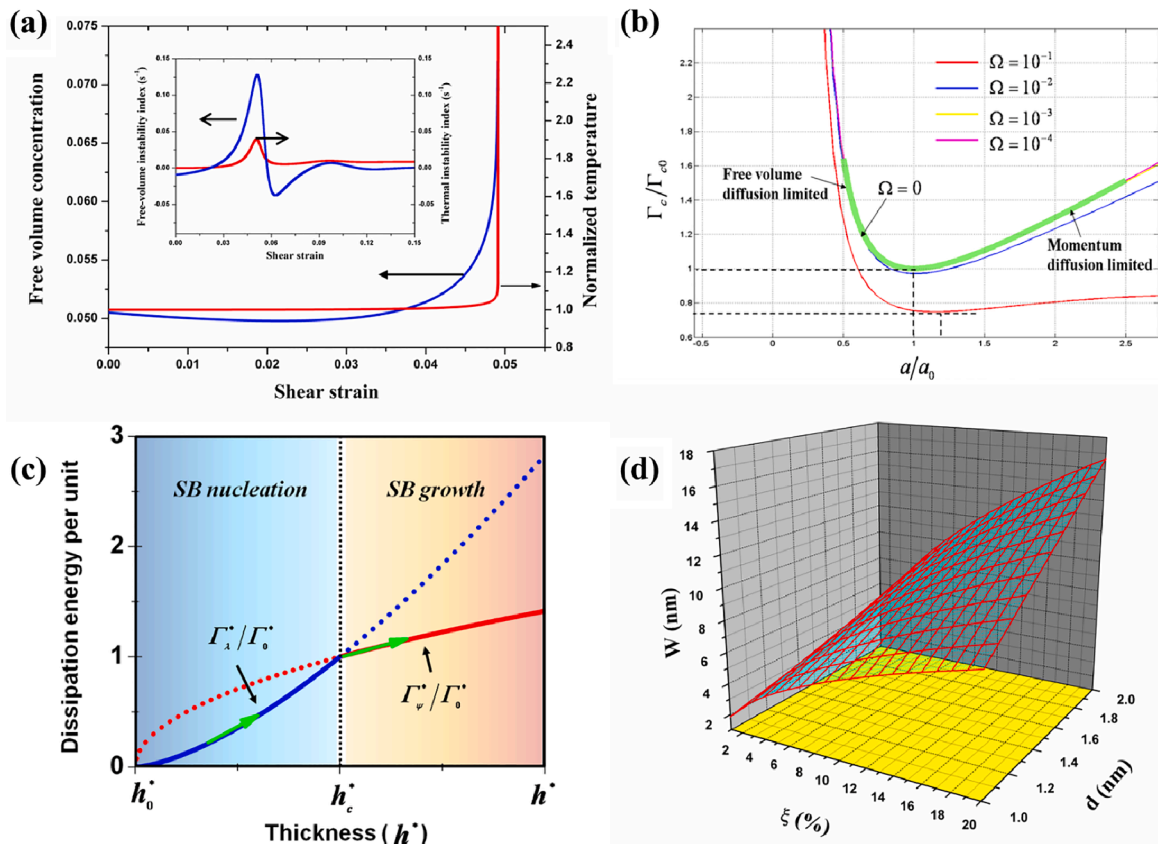


Fig. 54. Shear-banding mechanism in metallic glasses: (a) local free-volume creation and temperature rise in shear band; inset shows evolution of free-volume instability index and thermal instability index before shear band instability [357]; (b) critical energy dissipated in SB (shear band toughness) versus shear band thickness with different thermal-effect coefficients [358]; (c) a competing map of shear-banding nucleation and growth [359]; (d) prediction of shear band thickness as a function of activation free volume concentration and shear transformation zone size [360].

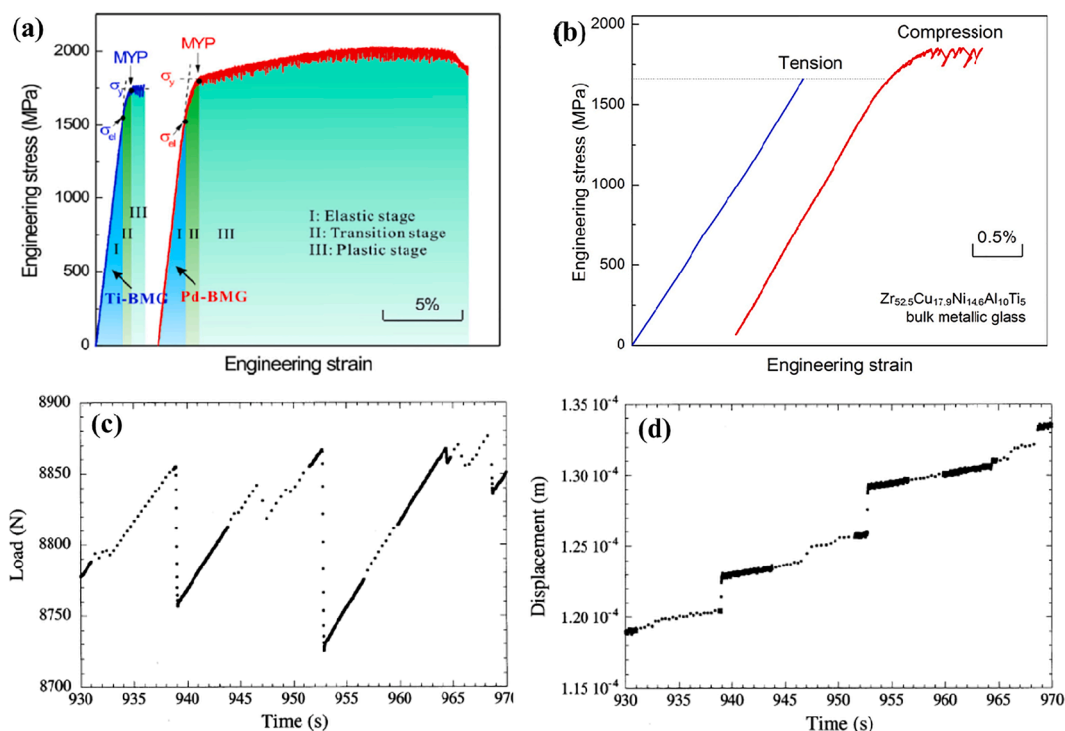


Fig. 55. Typical engineering stress–strain curves for Ti-, Zr-, and Pd-based bulk metallic glasses (BMGs): (a) dynamic response of Ti- and Pd-BMGs under compression; (b) comparison of engineering stress–strain curves of Zr-BMG in tension and compression [363,364]; (c) load and (d) total displacement as a function of time in serrated flow region in Pd₄₀Ni₄₀P₂₀ BMG in uniaxial compression [361].

Fig. 57 (a) shows a sequence of deformation events in compression testing [10]. A shear band starts at the surface, and progresses at a velocity V_1 . As mentioned earlier, plastic deformation in metallic glasses takes place by two possible mechanisms: the free volume formation, due to Spaepen [353,367] and shear transformation zones (STZs), due to Argon [368] and Langer [369,370]. The latter can expand, initiating larger shear bands. The thermally softened region reaches a length a_1 . When the shear band propagates downwards, the region away from the band cools down and forms the “Frozen” band. This reduces the driving energy for the band, resulting in the smaller length of the softened region to a_2 . Thus, one speculates a corresponding reduction in propagation velocity to V_2 . The velocity finally decreases to zero, when the softened region length comes to a critical size a_3 . Each formation and arrest process results in a load drop. Thus, the BMG shows a limited ductility in compression, propitiated by the continuous formation and “freezing” of shear bands.

This is different from tensile deformation [10]. Once the shear band forms from the expansion of a shear transformation zone and softening of the material, one crack can easily form at the surface and develop along the band. Under such condition, as presented in the sequence of Fig. 57 (b), the crack follows the propagation of the shear band. The band advances at a velocity V_1 and is followed by the crack opening. The scenarios presented in Fig. 57 require thermal softening within the band and support the theory that thermal softening acts as a crucial drive for shear localization [352].

A new mode of atomic cluster motion, i.e. tension transformation zone (TTZ) was proposed by Jiang et al. [371] to understand the fracture mechanism induced by shear banding. As illustrated in Fig. 58, the classical STZ pioneered by Argon [374] is the basic plastic flow or shear-banding event, and describes the shear-dominated motion of local clusters under deviatoric stress, whereas the TTZ describes the dilatation/cavitation-dominated motion of local clusters under hydrostatic tension stress. It is clarified that, at the atomic cluster level, the fracture energy dissipation in amorphous alloys is dominated by two competitive processes, STZs and TTZs, underlying shear banding and nanoscale cavitation ahead of the crack tip, respectively. This STZ vs. TTZ mechanism has been widely used to understand and predict the fracture behavior of various metallic glasses [372,373].

Jiang and Atzmon [374] performed TEM on Al₉₀Fe₅Gd₅ and observed nanocrystallization in both shear band and fracture surface formed during compression deformation. Nanocrystallites formed in shear bands, which they interpreted as, due to a kinetic effect by uniformly distributed free volume; the formation of the nanocrystallites at the fracture surfaces was due to adiabatic temperature rise. The nanocrystals were evenly distributed in the shear band.

Different mechanisms operate in different BMGs [374] and the occurrence of thermal softening in no manner diminishes the significance of free volume softening, which otherwise dominates under certain conditions. Under the other conditions, shear transformation zones might grow and give rise to bands.

Maaß et al. [119] isolated a single shear band from a Zr-based BMG (Zr_{52.2}Ti₅Cu_{17.9}Ni_{14.6}Al₁₀), presenting a non-serrated flow curve recorded at 273 K, as shown in Fig. 57 (a). The evolution from serrated to non-serrated flow is based on the dynamics of shear-band propagation and is not due to kinetic limitations during shear-band nucleation, leading to an increased concentration of shear

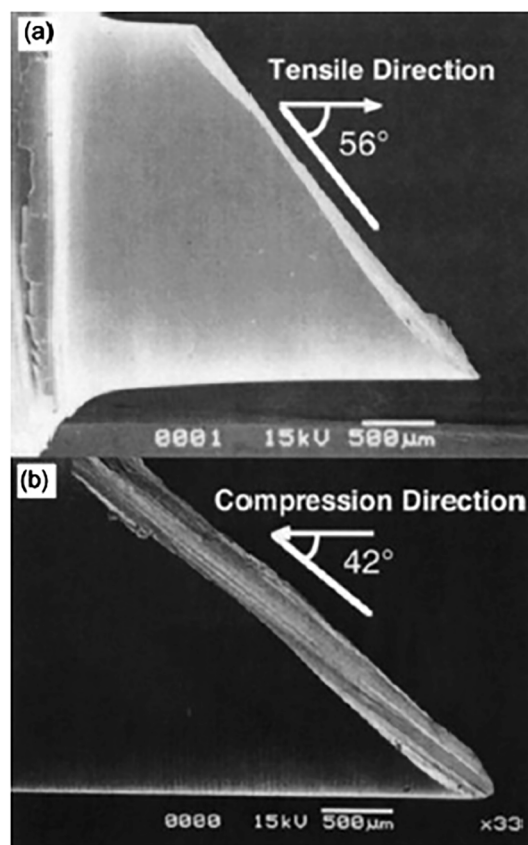


Fig. 56. Typical shear fracture modes of Pd₄₀Ni₄₀P₂₀ bulk metallic glass: The side view after shear fracture in (a) tension and (b) compression respectively [365].

bands. Non-serrated flow is due to continuous propagation of a shear band without arrest. The macroscopic view of the polished surface in Fig. 57 (b) demonstrates the location of shear band, which is indicated by the solid line. Nano-indentation was performed to reveal structural changes perpendicular to the shear band. The indentation hardness profiles in Fig. 57 (c) exhibit structural softening within the affected zone with width exceeding tens of micrometers. The variation of hardness related to the formation of shear bands is discussed in Section 10.

11.5. Crystalline to amorphous transition within shear band

Phase transformations, such as martensitic phase transformation [305] and amorphization in some metallic materials [375], do occur during shear localization. Meyers et al. [106] firstly reported the glassy region confirmed by the characteristic ring patterns formed in the center of a shear band in AISI 304 stainless steel, indicating the existence of a phase transformation from crystalline to amorphous state. Li et al. [376] also reported the coexistence of amorphous and nanocrystalline structures in dynamically deformed TWIP steel. The transition from the amorphous state to a fine-scaled nanocrystalline phase within the center of shear region clearly suggests that melting inside the shear bands occurred. They proposed a deformation mechanism for the TWIP steel at high strain rate including melting and quenching processes, required for the formation of amorphous and nanocrystalline grains. These observations and analyses confirm the transformation from crystalline to amorphous under dynamic loading.

Zhao et al. carried out laser ablation-driven shock compression of covalently bonded materials, such as silicon [211], germanium [75], boron carbide [76], and silicon carbide [77]. Nanoscale amorphous shear bands were found in those materials, as presented in Figs. 59 and 60. High resolution TEM as well as molecular dynamics simulation suggest that dislocation activity is the precursor to amorphization [377]. A high density of stacking faults was revealed at the crystalline/amorphous interface in silicon and germanium while the interfaces of boron carbide and silicon carbide are relatively “defect free” [375]. It was proposed that the high deviatoric shear stress plays a very important role in this process. The thickness of the amorphous band is much lower than the ones obtained by other techniques, owing to the higher strain rate of laser shock ($\sim 10^8 \text{ s}^{-1}$) and higher strength of the covalently-bonded materials.

Fig. 61 shows the SEM and TEM images of shear bands for 45 vol% and 65 vol% Ti₂B/Al composites [378]. Fluid-like melted aluminum accumulation with no clear boundary, regular shape or certain flowing orientation, was observed on the fracture surfaces of the 45 vol% Ti₂B/Al composite (Fig. 61 (a)). Meanwhile, a flat and smooth melted aluminum region with a width of 20 μm is observed

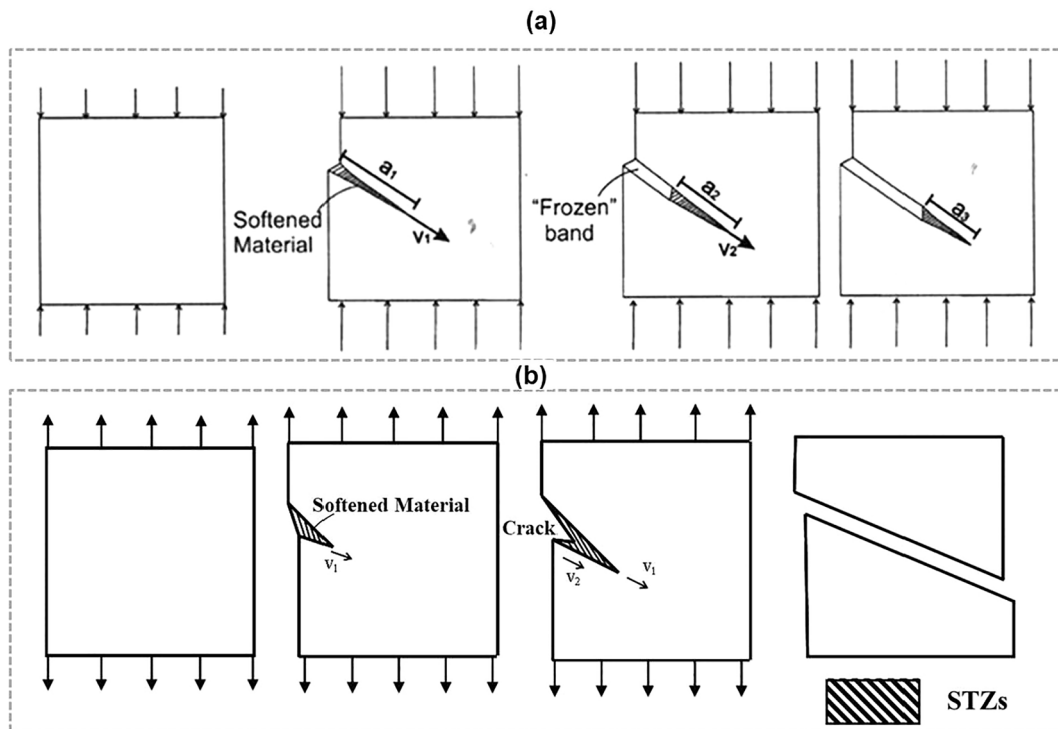


Fig. 57. Schematic sequence showing (a) how a shear band initiates, propagates, and arrests in a metallic glass subjected to quasistatic compression and (b) how a shear band initiates in tension from an existing shear transformation zone (STZ) as well as how a crack propagates along the softened path eventually overcoming band and fracturing in bulk metallic glass [10].

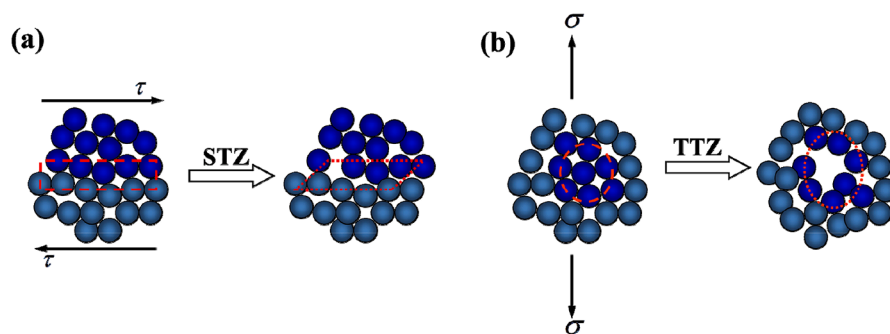


Fig. 58. Basic modes of atomic cluster motions in metallic glasses: (a) shear transformation zone and (b) tension transformation zone [371].

on the fracture surfaces of 65 vol% Ti₂B/Al composites (Fig. 61 (b)). A high density of dislocations was found near the boundary of the shear band, as presented in Fig. 61 (c). From the edge to the center of the band, fine grains are found aligning along a particular orientation with the size < 100 nm (Fig. 61 (d)). An important finding is that nano-crystalline and ultrafine-grains can be identified by means of high-resolution TEM in the center of the shear band. Furthermore, an amorphous area observed in Fig. 61 (e) is also confirmed by the corresponding selected area diffraction (SAD) pattern from site 1, which consists of a series of rings and is a typical pattern of the amorphous state. SAD patterns correspond to sites 2 and 3 are characterized by discontinuous spots, which are characteristic of nano-crystalline grains. These results indicate that melting and phase transformation occurred, which were induced by local adiabatic temperature rise.

11.6. Spacing and Self-organization of shear bands

Most of the studies analyze a single shear band propagating along a fixed direction. However, the formation of shear bands in a material is clearly not such a simple process. From the mathematical point-of-view, the formation of a spontaneous ASB is an instability process. Linear instability and localization analyses predict when ASBs may occur and how fast the growth rate could be at early post-

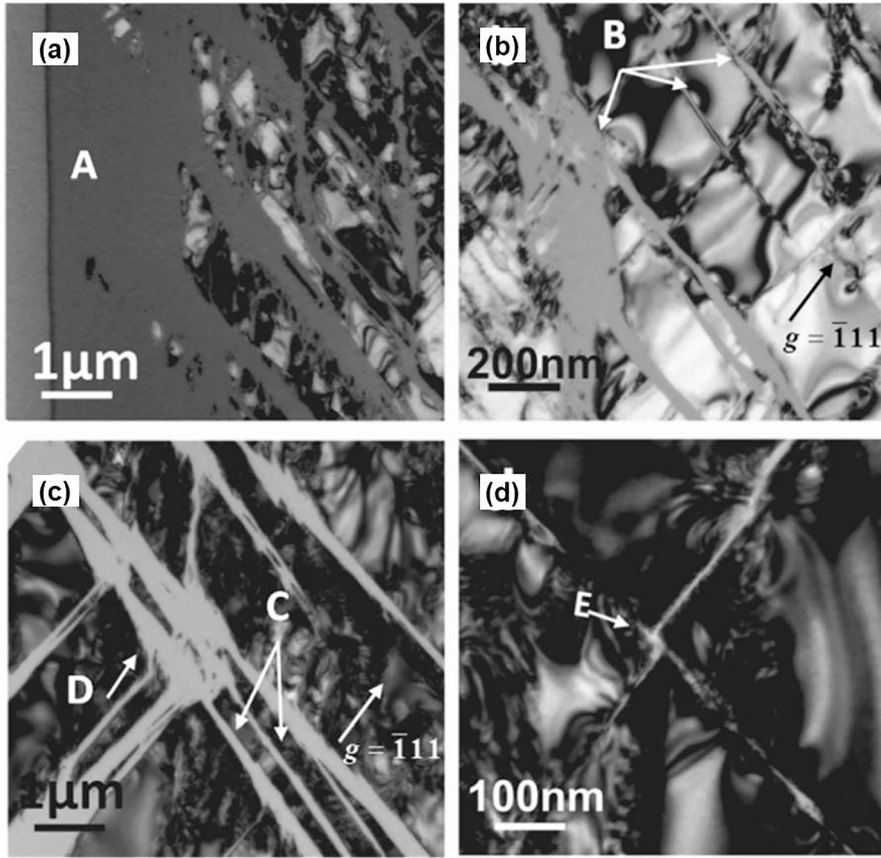


Fig. 59. TEM images of the complex amorphous pattern in shock-impacted silicon: (a) broad region of the amorphous material on the top surface on which the laser energy is deposited, marked by A, below which multiple amorphous bands penetrate into the crystal; (b) pattern of the amorphous bands B decreasing in thickness with depth; (c) termination D, bifurcations and feathering, marked by C, usually observed along with the primary bands and different variants of the bands eventually intersect; (d) the intersection leads to the formation of a jog/kink feature and is indicated by E [377].

instability. Grain boundaries, precipitates, second phase particles, inclusions, and dislocation structures are all-natural perturbation sources in metals. Temperature disturbances have also been considered as perturbation sources to activate the formation of shear bands. However, one cannot ignore the fact that shear bands interact.

Grady [379,380] was a pioneer in proposing a perturbation solution for shear instability in brittle materials. Later, Grady and Kipp [161] developed another theoretical model for the determination of shear-band spacing. According to them, the rapid loss of strength across the developing shear band influences neighboring material by forcing it to unload. This leads to the estimate of the spacing between bands. The shear-band spacing L corresponds to the minimum localization time:

$$L_{GK} = 2 \left(\frac{9C_v \lambda}{\dot{\gamma}_0^3 \alpha^2 \sigma_0} \right)^{1/4} \quad (31)$$

where the parameters were previously defined for Eq. (22), which predicts the width of an individual band. σ_0 is initial flow stress, and $\dot{\gamma}_0$ is initial shear strain rate.

Wright and Ockendon [162] used an alternative approach and applied the perturbation analysis to the conservation equations. The equation comes from small growing disturbances in the localization region. The Wright-Ockendon model adds the strain-rate sensitivity m to the Grady-Kipp model as follows:

$$L_{WO} = 2\pi \left[\frac{m^3 \lambda C_v}{\dot{\gamma}_0^3 \alpha^2 \tau_0} \right]^{1/4} \quad (32)$$

where τ_0 is the reference shear stress. Since $m \ll 1$ for most metals, $L_{WO} < L_{GK}$.

Molinari [163] also carried out an analysis of ASB spacing based on a one-dimensional formulation and related the minimum

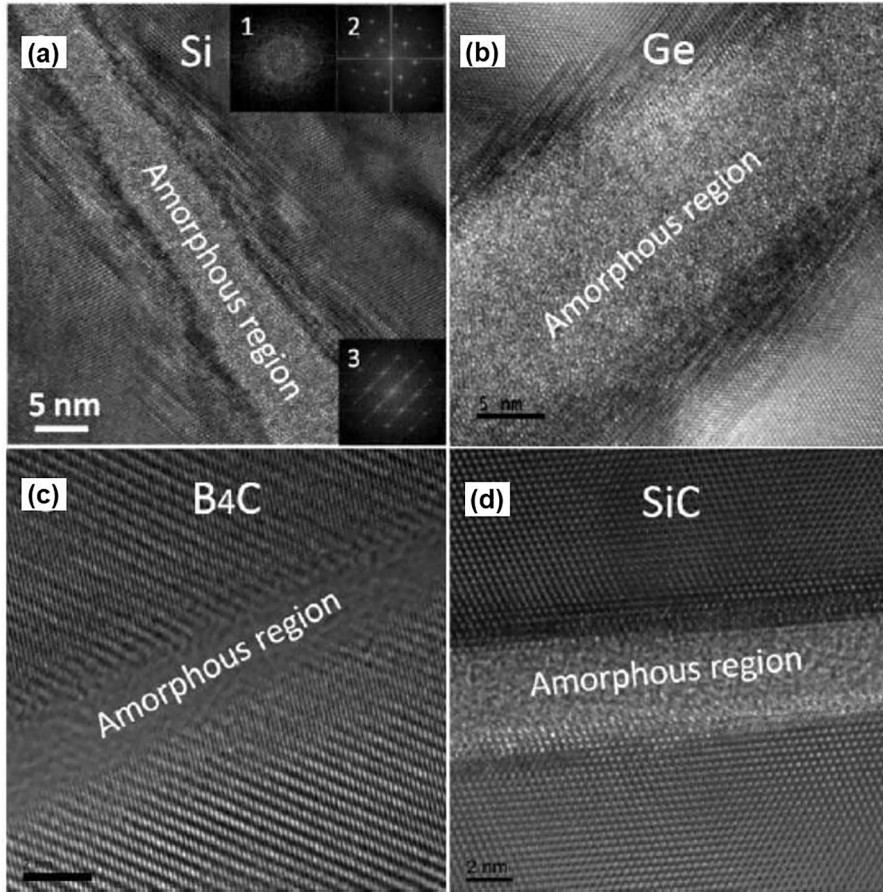


Fig. 60. High resolution TEM micrographs of amorphous bands in four different covalently bonded materials subjected to high-amplitude short pulse duration tests using pulsed lasers (1–10 ns): (a) silicon; (b) germanium; (c) boron carbide; (d) silicon carbide [375].

spacing of shear bands to the characteristic wavelength of the dominant instability mode. An explicit solution for shear-band spacing was derived for those materials without strain hardening, when a modified linear thermal softening coefficient was applied:

$$L_M = 2\pi \left[\frac{m^3 \lambda C_v (1 - \alpha T_0)^2}{\left(1 + \frac{1}{m}\right) \beta^2 \dot{\gamma}_0^3 \alpha^2 \tau_0} \right]^{1/4} \quad (33)$$

Asymptotic developments are also performed for strain-hardening materials, which demonstrate that the strain hardening n has a great influence on the spacing of shear bands.

The above theories cannot properly explain the increased spacing when the shear-band size rises, as they are based on one-dimensional analysis. As shear-band interactions are more complex than the one-dimensional condition, their spacing cannot be analyzed by the one-dimensional perturbation theories. The interaction among shear bands leads to an increase in the spacing as they grow. This is produced by shielding from the stress fields of the larger bands. Similar to trees in a forest, the larger trees create shade and impede the growth of the smaller ones, so that the mean spacing of trees increases with their size. This has been done conceptually for fragmentation of dynamically expanding rings by Mott and coworkers [169] in WW2 with the purpose of determining fragmentation of shells. More advanced analysis methods were used by Rodriguez-Martinez [381], who used three calculational techniques: finite element computations of the radial expansion of ductile rings, numerical simulations of unitary axisymmetric cells with sinusoidal spatial imperfections subjected to tensile loading and a linear perturbation technique.

An evaluation was conducted by Xue et al. [327,382], who considered that the analysis has to consider elements that are shown below:

(a) *Nucleation rate of shear bands.* The probability of nucleation, $p(V_0, S_0)$, in a reference volume V_0 , or surface S_0 can be depicted by a Weibull distribution. The stress has to be replaced by strain as the independent variable. The new Weibull parameters defining the distribution are the critical strain for nucleation, a mean nucleation strain, and a Weibull modulus. It is also possible to incorporate shielding at the nucleation stage, depending on the relative values of the rate of nucleation and rate of growth.

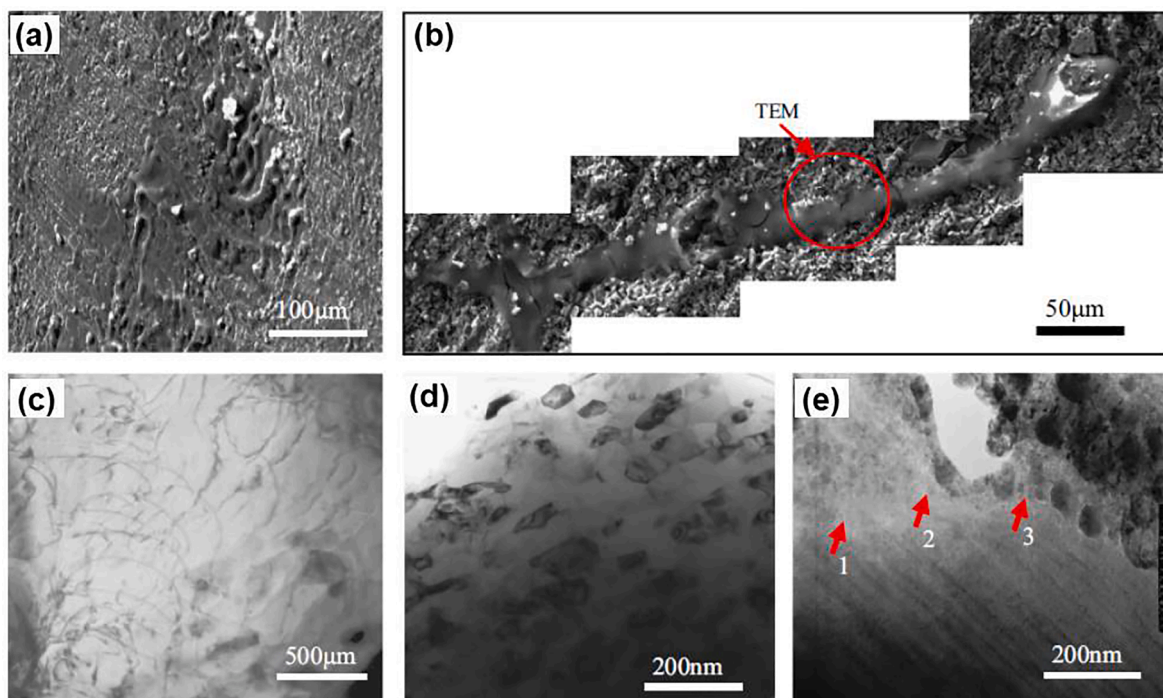


Fig. 61. SEM morphologies of shear bands in $\text{Ti}_2\text{B}/\text{Al}$ composites and TEM characteristics from the edge to the center of the bands: (a) fluid-like bands; (b) narrow band; (c) dislocations; (d) fine grains (<100 nm); (e) amorphous and nano-crystalline grains [378].

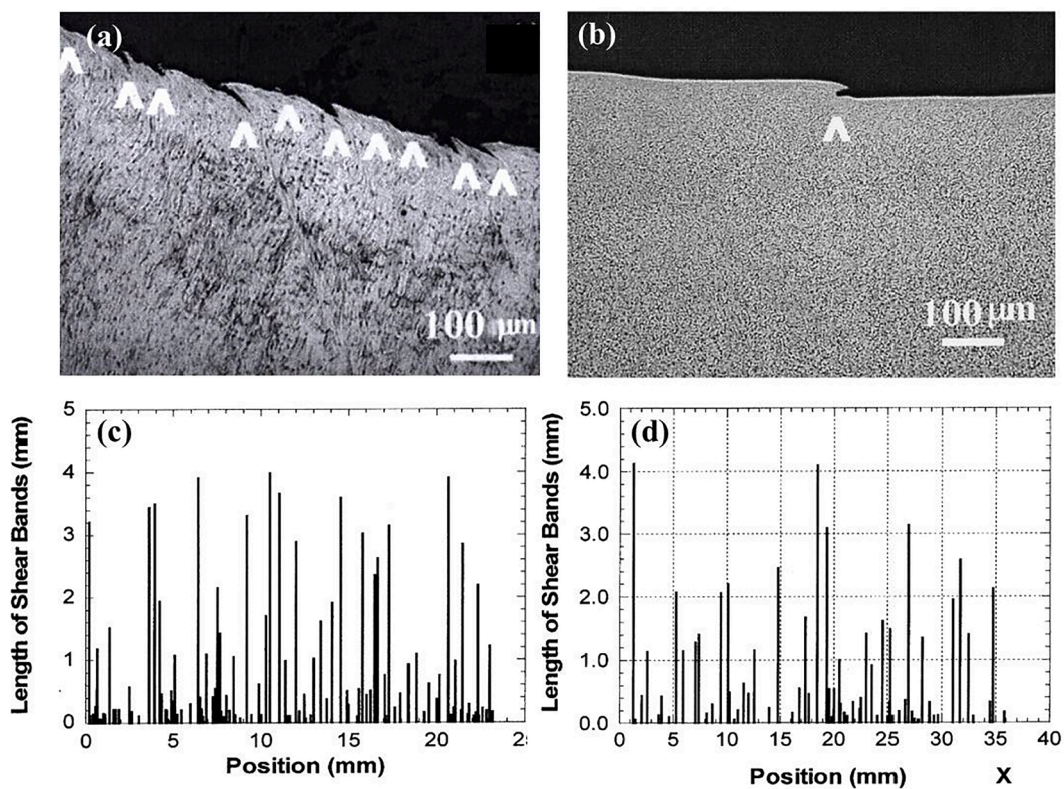


Fig. 62. Shear-band pattern in different materials subjected to explosive implosion in thick-walled cylinder configuration. Comparison of shear-band spacing for (a) stainless steel and (b) Ti-6Al-4V; spatial distribution in (c) CP Ti for $\epsilon_{\text{eff}} = 0.92$ and (d) Ti-6Al-4V for $\epsilon_{\text{eff}} = 0.26$ [106,327].

(b) *Rate of growth, or velocity of propagation.* Shear bands compete among themselves and continuously change their patterns as they evolve. An initially significant number of small bands gradually evolves into a smaller number of large bands, because of the stress shielding during growth, as described in Fig. 62. The external traction is considered to be constant during the evolution process.

The implosion of a thick-walled cylinder is an excellent technique to quantitatively estimate the parameters. This method is described in Section 3.3. Shear bands are initiated at the inner wall of the cylinder, where the strain is maximum, and propagate outwards, along trajectories of maximum shear strain, which form helicoids. The initial spacing and its evolution can be closely monitored.

This methodology developed by Xue et al. [157,327] has been applied to metals and alloys, and has been proven to be an effective and reliable means to probe the collective behavior of shear bands. They studied the self-organization of shear bands at a high strain rate $\sim 10^4 \text{ s}^{-1}$. The proposed two-dimensional model correctly describes the shear-band spacings of Ti and Ti-6Al-4V alloy, as presented in Fig. 63 [327]. The first stage is the nucleation stage in the preferred location at time t_0 . The shielding effect can be expressed by S :

$$S = \frac{\bar{t} - t_{cr}}{\bar{t}} \quad (34)$$

where, \bar{t} is the characteristic time for the complete nucleation and t_{cr} is a critical time when a complete shielding effect happens. Under different shielding effects S , some of nuclei can no longer be activated as shown in Fig. 63. The increment in shielding effect S generates increasing growth velocity V , reducing strain rate $\dot{\epsilon}$, and reducing natural spacing L . During the growth stage, the spacing is L_i at a certain length l_i . The growth becomes unstable at a critical length $l_{cr,i}$ and alternate shear bands growth with a new spacing L_{i+1} ; the other shear bands stop the growth. The theory describes well the collective behavior of shear localization.

One example is Ti-6Al-4V alloy, which was impacted through the radial collapse technique by a thick-walled cylinder under explosive deformation [327]. Shear-band initiation, propagation as well as spatial distribution, were studied under increasing global strains. Fig. 64 (a) shows the pattern of helicoidal shear bands in a Ti-6Al-4V specimen at a global effective strain 0.541, whereas Fig. 64 (b) describes the size and spatial distribution of shear bands at a larger global effective strain of 0.915 [10]. The shear bands initiate at the surface boundary of the specimens and reach a periodical distribution at an early stage.

Fig. 62 (a) and (b) show that the shear-band spacing is quite distinct in different materials. The differences of mechanical properties between the two alloys are responsible for significant differences in the evolution of the shear-band patterns. The same differences are found between commercial pure (CP) titanium and Ti-6Al-4V alloy, as seen in Fig. 62 (a) and (b).

Fig. 65 presents how the shear-band spacing and its evolution determine the fracture of a cylindrical specimen. As the length increases, so does the spacing. There are considerable differences between materials. For example, the number of shear bands initiated in Ti (spacing of 0.18 mm) is considerably larger than that in Ti-6Al-4V (spacing of 0.53 mm). The experimental values of the initial shear-band spacings correspond well with theoretical predictions by GK, and WO and M, given in Eqs. 31–33.

Liu et al. [383] also proposed a multi-stage model for shear bands, in which the perturbation sources are incorporated through Gaussian distribution to depict the inhomogeneity of the material. The simulation results of collapsing cylinders were compared with the experimental observations reported by Xue et al. [157,382]. Therefore, a close agreement is established for various typical characteristics of ASBs, like spacing and the propagating velocity of the shear band. This obviously calls for additional works.

11.7. Effect of dynamic strain aging

Many alloys, including steels [5,6], iron [384], aluminum alloys [385], Ni-C alloys [386,387], titanium and its alloys [388–390],

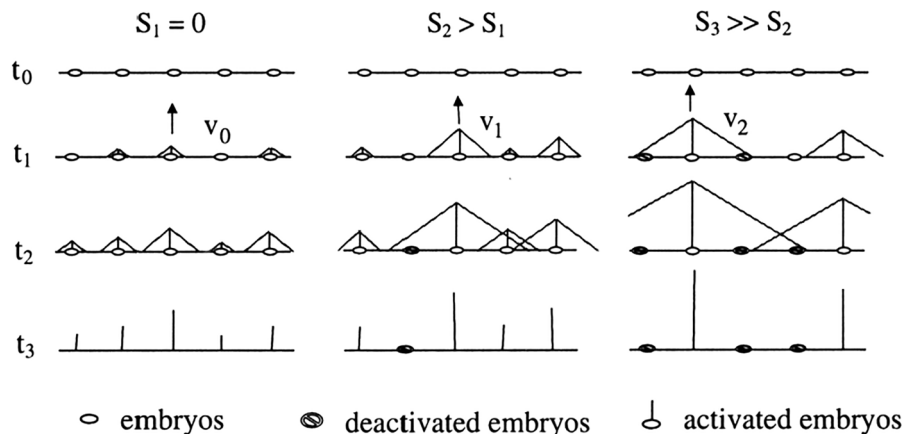


Fig. 63. Two-dimensional representation of concurrent nucleation and shielding. S is a shielding parameter; as S increases, the release of stress produced by growing shear band deactivates embryos. For $S_1 = 0$, all embryos are activated and shear-band spacing is small. For large value of shielding S_3 , (right band side) only a fraction of embryos are activated [327].

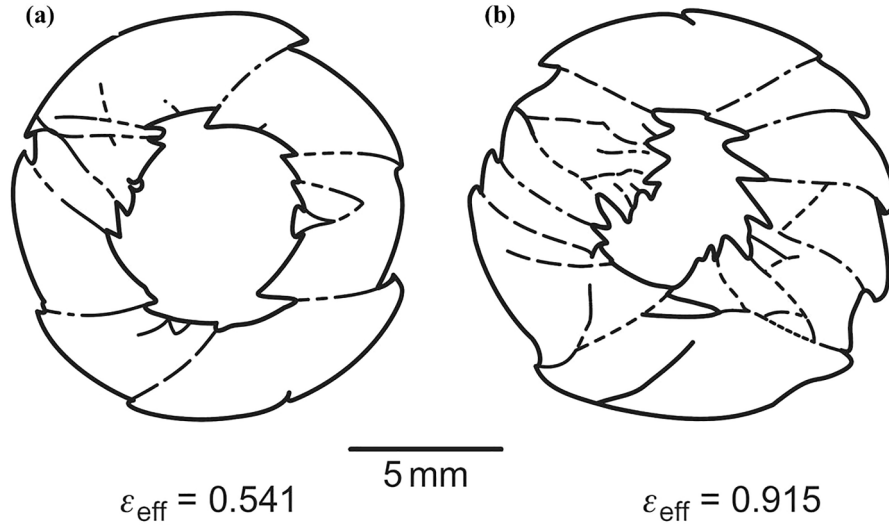


Fig. 64. Evolution of the shear band pattern in Ti-6Al-4V alloy for the imploding explosive geometry of a thick-walled cylinder: (a) $\varepsilon_{\text{eff}} = 0.541$; (b) $\varepsilon_{\text{eff}} = 0.915$ [10].

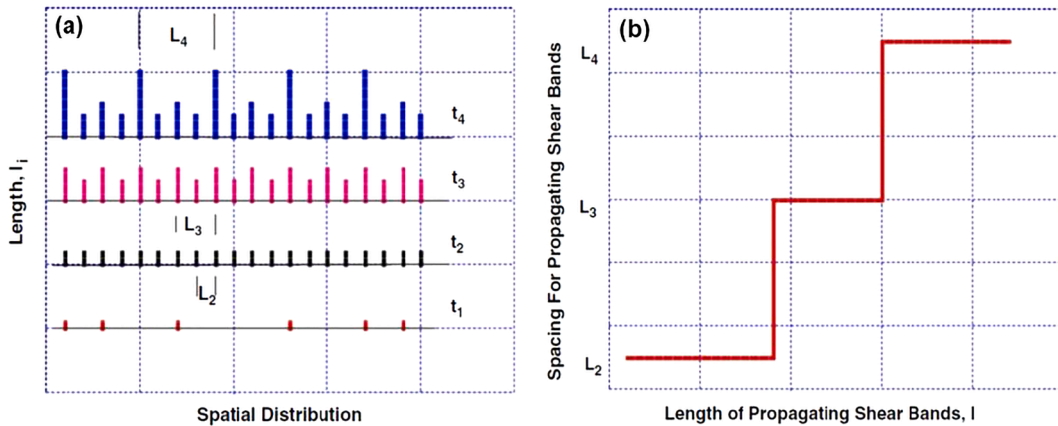


Fig. 65. (a) Schematic diagram of the evolution of shear band spacing at different levels. (t_1 -Random initiation; t_2 - self organization into “periodic” pattern among nuclei; t_3 -some shear bands grow faster suppressing others; t_4 -self-organization of developed shear bands); (b) Spacing of propagating SBs as a function of length [327].

and high entropy alloys [391], which undergo dynamic strain aging (DSA) are also sensitive to shear localization. The repetitive interaction of dislocations with solute atoms leads to a reduced and sometimes negative strain-rate sensitivity, which promotes the onset of shear localization.

Dynamic strain aging is a phenomenon originated from in the interaction of mobile dislocations with solute atoms. Cottrell [384,392] attributed the yield point phenomenon to the migration of solute atoms toward free dislocations. The resulting effect is that dislocations become surrounded by solute atoms in the form of an atmospheres. Thus, two scenarios can be expected: (1) if the applied stress is too small, the dislocations can hardly escape from the atmospheres and thus solutes will migrate with dislocations, yielding an extra back force on the dislocation motion; (2) if the applied stress is sufficiently high, dislocations can be torn from the atmospheres and therefore solute atoms will not be able to retard the dislocation motion, resulting in plastic flow under a smaller force. The latter case generates an acute upper yield point followed by the flow to a lower yield point. Cottrell [384,392] proved that solute atoms could form atmospheres around free dislocations and retard their motion. Ham [393] proposed that the minimum strain rate $\dot{\varepsilon}_m$, when serrated flow initiates, is:

$$\dot{\varepsilon}_m = C \exp\left(\frac{-E_m}{k_B T}\right) \quad (35)$$

where, E_m is the effective activation energy for the exchange of vacancies and substitutional solute atoms, C is a constant related to dislocations, solute atoms and vacancies, and k_B is the Boltzmann constant.

The trapping of mobile dislocations by solute atoms leads to a range of mechanical effects: serrations in the stress–strain curve, which is also called Portevin-Le Chatelier effect [394,395], increased strain hardening rate, reduced ductility (the blue brittleness of steels), and a change in thermal softening that results in thermal hardening in the extreme case.

The literature abounds with dynamic strain aging measurements and calculations. Fig. 66 (a) shows the flow stress (at a plastic strain 0.05) for AISI 1008 steel [6], varying temperatures at strain rates of 1.75×10^{-4} , 1.75×10^{-3} , and $1.75 \times 10^{-2} \text{ s}^{-1}$. Two effects have been observed: (a) the flow stress increases with temperature ranging from 350 to 500 K; (b) the peak temperature increases with strain rate. This has also been seen by Gilat and Wu [396], as presented in Fig. 66 (b). The same effect is observed: a shift in the hump to higher temperatures at higher strain rate. The results by Gilat and Wu [396] extend to a much higher strain rate and the hump is at $\sim 700 \text{ K}$ for a strain rate of 2 s^{-1} . It is concluded that the temperature for the hump is dependent on strain rate instead of solute content.

Recently, there have been several systematic studies of dynamic strain aging in severely plastic deformed materials [397,398]. It has been shown in ultrafine grained Al-Mg alloys [397] and titanium [398] that the Portevin-le Chatelier effect is promoted by severe plastic deformation, yet the influence is complex since the deformation microstructure is heterogeneous.

Two effects could modify the susceptibility to the formation of shear band due to the influence of dynamic strain aging:

- thermal softening is enhanced by the reduction of grain size, as the increase of the volume fraction of the grain boundary leads to an enhanced phonon scattering effect, which eventually lowers the thermal conductivity of the materials. The deformation-induced heat, therefore, is more difficult to be dissipated, leading materials to deform in non-uniform manner.
- the strain-rate sensitivity is largely reduced and in many cases negative. This leads to a non-uniform deformation and an enhanced susceptibility to shear localization.

11.8. Shear-induced chemical reactions

The importance of shear-induced chemical reactions was first reported by Bridgman [399], who proposed that the shock pressure can “break down” the electronic structure of atoms, and lead to the modification of material properties. Later, it was demonstrated by Vereshchagin et al. [400], Teller [401] and Enikolopyan et al. [402], that simultaneous pressure and shear can enhance reactivity of materials. Thadhani [403] revealed shock-induced chemical reactions and synthesis of materials. During shock compression, the coexistence of strong hydrostatic and deviatoric stresses often creates mechanical responses unique to this extreme regime. An unusual combination of “structural defects” and “powder packing characteristics” is generated, which can significantly promote chemical reactivity of powders and result in accelerated mass transport kinetics. Under such unique conditions, not only can metal and ceramic powders be dynamically consolidated [404,405] or undergo solid-state structural phase transformations [406–408], but there can also be molecular decomposition of compounds [409,410], chemical reactions in powder mixtures [411–413], as well as the synthesis of compounds [414–416].

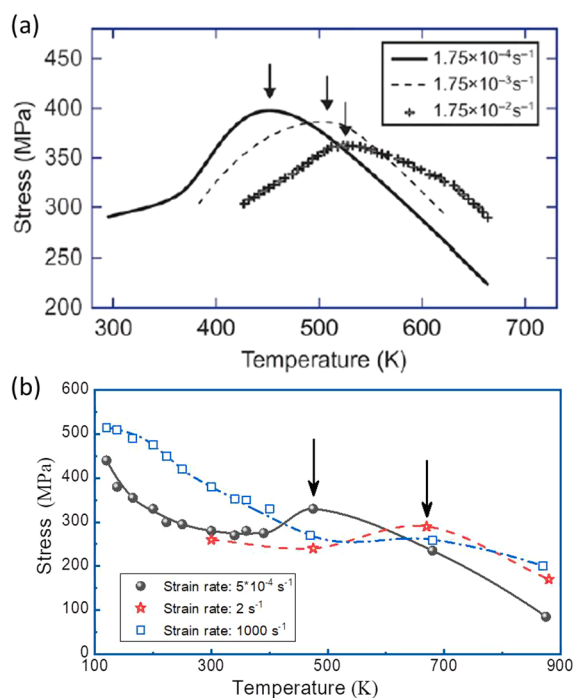


Fig. 66. (a) Effects of temperature and strain rate on flow stress (5% plastic strain) of AISI 1008 steel [6]; (b) Effect of temperature at high strain rates on flow stress of AISI 1020 steel [396].

Shock densification experiments conducted on Mo-Si, Ti-Si, Nb-Si, Ni-Ti, or Ni-Al powder mixtures by Meyers et al. [417,418], Dunbar et al. [419], Thadhani [420,421], Xu et al. [422] and Nesterenko et al. [423], found the formation of localized reactions in nonuniformly deformed areas. These studies also demonstrated that the intensely deformed powder mixtures in the localized areas underwent chemical reaction even at pressures lower than the shock threshold pressure. The extent of induced reactions was found to increase with the shock energy and temperature. Nesterenko et al. [423] carried out controlled shear experiments at a shock pressure lower than 1 GPa and showed that intense shear deformation above a threshold level can trigger and propagate chemical reactions. In the cylindrical implosion geometry, shock/shear initiated reactions followed regions of intense shear generated by ASBs. Based on experiments in Nb-Si and Mo-Si powders, different extents of shock-induced or shock-assisted chemical reactions were found in three concentric regions, (1) fully reacted; (2) partially reacted; and (3) unreacted. The shock energy dissipated by plastic deformation indeed plays a significant role in the initiation of the chemical reaction. It was proposed that the Krueger-Vreeland threshold energy for chemical reactions should be modified to take into account the plastic deformation energy. The analysis of partially reacted regions enabled the identification of the reaction micro-mechanisms according to the model proposed by Meyers et al. [418].

Recently, Zhao and Meyers [211,424,425] reported laser-shock induced amorphization in four covalently bonded solids, namely silicon (Si), germanium (Ge), boron carbide (B₄C) and silicon carbide (SiC), as shown in Fig. 60. Such amorphization (presented in Section 11.5) is supposed to be a new deformation mechanism of covalently bonded materials at ultrahigh strain rate ($>10^7$ s⁻¹) when other mechanisms such as dislocation slip, twinning, phase transformation and fracture are kinetically less favorable. The fact that the occurrence of amorphization can potentially suppress catastrophic failure of these brittle materials provides a new route for materials engineering.

Bryant et al. [426] carried out laser-driven shock-compression experiments including velocimetry and soft recovery on Ce₃Al metallic glass ribbon samples. At shock pressures below 1.8 GPa, no obvious deformation or structural changes are evidenced via XRD analysis. When the shock conditions were above the magnitude of this precursor elastic limit, visible deformation and crystallization was found. The overall results demonstrate possible densification of the glass due to delocalization of 4f electrons in Ce at lower laser shock pressures and increased crystallization with preferred orientation and distortion of the nanocrystals at higher shock compression conditions.

Thus, plastic flow in shock waves leads to the appearance of a characteristic mass-transfer mechanism which gives rise to diffusion processes during the very short period of shock-wave compression. Meanwhile, phase transitions, such as polymorphic, melting, and freezing are of significant consequence under shock-wave loading conditions. Based on the above considerations, Dai et al. [59] proposed an explosive welding method; a typical Zr-based BMG and a commercial Cu-based crystalline alloy were successfully joined based on the thick-walled cylinder technique. The mutual diffusion of component atoms in these two welded materials was observed in the interface regime and the increase of the diffusion coefficient was estimated to be about 10–100, which suggests that there is a violent coupled thermo-mechanical state near the interface after the high-speed collision. The material melting facilitated the welding process by reducing the initial surface roughness due to explosion impact. The dissimilar joining of the non-crystalline to crystalline alloy based on the shear-induced chemical reactions extends the application of bulk metallic glasses as structural and functional materials.

Shock-induced reaction synthesis, which incorporates a combination of self-sustained, high-temperature (2000–3000 K) reactions and a shock compression wave, demonstrates a unique method to produce advanced materials. It has been applied to many reactive systems, promoting the synthesis of a significant number of solid compounds and phase transformations including boron nitride [427], borides [428], silicides [429], and aluminides [430], as well as a novel welding approach [59].

12. Microstructural evolution inside shear bands

12.1. Dynamic recrystallization

The results presented in Section 11 show ample evidence for the formation of a nanocrystalline /ultrafine-grained structure that is accepted as being due to dynamic recrystallization. The recognition that dynamic recrystallization is responsible for generating nanocrystalline/ultrafine-grained microstructures in the shear bands dates from 1980s [298] and the realization that this mechanism was of a rotational and not migrational nature was a gradual process. The mechanistic understanding evolved from simple qualitative description to more complex quantitative treatments. The repeated observations of nanocrystalline and ultrafine grained structures within shear bands and a low dislocation density suggested a dynamic recovery/recrystallization process, which was proposed by Andrade et al. [108] for copper and Beatty et al. [337] for high strength steel. Since copper does not form shear bands because of its high strain hardening capability, Meyers et al. [431] and Andrade et al. [108] pre-shocked it to a high pressure (~50 GPa) using a flyer plate technique driven by an explosive charge. This introduced a highly hardened structure consisting of dislocation cells and twins and decreased significantly the strain hardening. In this condition, the hat-shaped specimens yielded a region of forced localization when subjected to high local strains.

It should be mentioned that dynamic recrystallization is also present in quartz [379], sodium nitrate [432], and other minerals. The two principal dynamic recrystallization mechanisms are, as classified by Derby [433], migrational and rotational. The deformation time for shear localization, at a high strain-rate about 10^4 s⁻¹, is of approximately $0.2\text{--}0.4 \times 10^{-4}$ s. The cooling times were calculated by Meyers et al. [19], and Hines and Vecchio [434] and are around 10^{-3} s. These are shown in Fig. 67.

In the migrational dynamic recrystallization regime, the grain boundaries have to travel distances comparable with the sizes observed. Grain-boundary migration calculations conducted by Meyers et al. [336], and Hines and Vecchio [434], predict the distances of:

Ta: 8.6×10^{-1} nm [336]

Ti: 3.9×10^{-1} nm [336]

Cu: 3×10^{-3} nm [434]

These distances are much smaller than the observed grains, with sizes of 20–200 nm. Thus, migrational recrystallization is not a dominant factor during deformation. Nevertheless, as described by Andrade et al. [108], it can contribute to some increase to the size of the grains during the cooling stage which is longer, by an order of magnitude, than the deformation stage. More detailed calculations are presented in Section 12.2.

12.2. Migration of grain boundaries and kinetics of grain growth

This section will explore the hypothesis of migrational recrystallization in a greater detail. The mobility of a grain boundary was established by applying the theory proposed by Rath and Hu [435,436]. The driving force for the motion of one grain boundary was simply calculated by equating the force working on a curved section of length dS with the energy of grain boundary, γ_{GB} . The total force F acting on the grain boundary in the y direction (Fig. 68 (a) [437]) is expressed as (in this two-dimensional approximation):

$$F = 2\gamma_{GB}\sin\frac{d\theta}{2} \approx \gamma_{GB}d\theta \quad (\text{because } \theta \text{ is considered small}) \quad (36)$$

Therefore,

$$\frac{F}{dS} = \frac{\gamma_{GB}d\theta}{R_{GB}d\theta} = \frac{\gamma_{GB}}{R_{GB}} \quad (37)$$

The motion velocity of the boundary, v , is related to the driving free force F for migration acting on the boundary dS :

$$v \propto \frac{\gamma_{GB}}{R_{GB}} = M_{GB} \frac{\gamma_{GB}}{R_{GB}} \quad (38)$$

where M_{GB} is a constant describing grain-boundary mobility, and R_{GB} is the radius of the grain boundary. This mobility is exponentially dependent on temperature through the classic Arrhenius-type relationship [436]:

$$M_{GB} = M_0 \exp(-Q/RT) \quad (39)$$

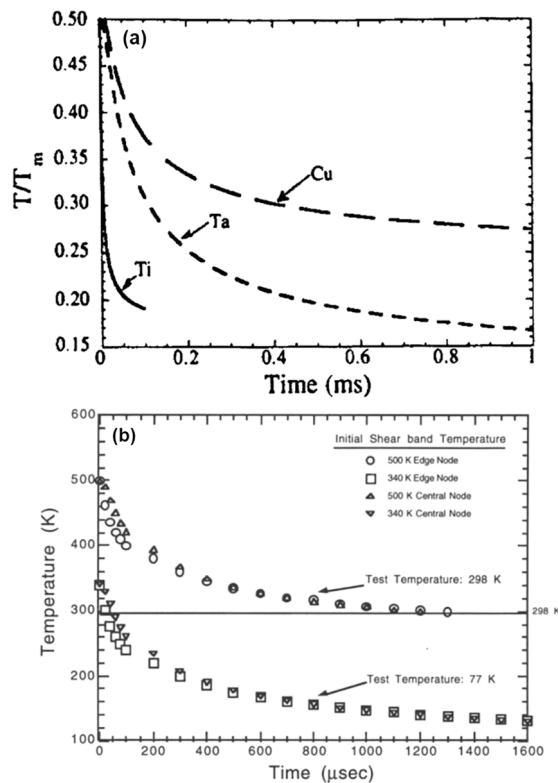


Fig. 67. Calculated temperature during shear band cooling as a function of time: (a) Cu, Ta, Ti [19]; (b) Cu at initial temperatures before deformation of 298 and 77 K [434].

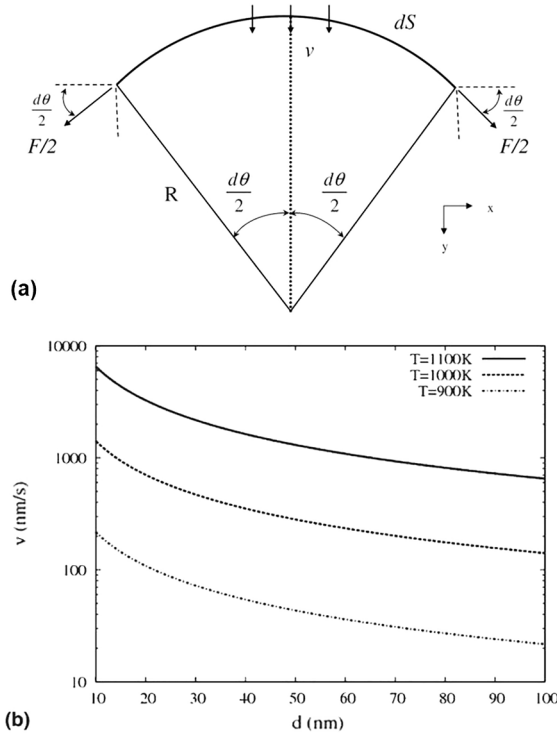


Fig. 68. (a) Schematic representation of a grain boundary with curvature $1/R$; (b) Calculated velocity of a grain boundary migration from the Rath-Hu equation at three temperatures: 900, 1000, and 1100 K [437].

For steel [438]: $Q = 140 \text{ kJ/mol}$, $M_0 = 3.5 \times 10^{-7} \text{ m}^4 \text{J}^{-1} \text{s}^{-1}$, $\gamma_{GB} = 0.835 \text{ J/m}^2$. Rath and Hu [435] use a similar equation, except for the exponent, p , which depends on the misorientation and purity of the grain boundary:

$$v = M_{GB} \Delta F^m = M_{GB} \left(\frac{\gamma_{GB}}{R_{GB}} \right)^m \quad (40)$$

Through experimental fit, p was calculated to vary from 1 to 4.

Considering $d/2 = R_{GB}$, where d represents the grain size, the velocity of grain boundary is expressed as a function of grain size in Fig. 68 (b) for various temperatures, from 900 to 1100 K. For a grain size of 100 nm, the velocity was estimated to be 22 nm/s at 900 K. The curves at 1000 K and 1100 K present higher velocities: $v = 141$ and 652 nm/s, respectively. A grain boundary displacement of 22 nm at 900 K would take 1 s. The cooling usually takes place in time scales of fractions of milliseconds. This time is not sufficient to reorganize the sub-grain configuration by migrational (continuous) recrystallization. Assuming 1 ms (Section 12.4) and $d = 100 \text{ nm}$ ($v = 0.01 \text{ m/s}$), a movement of 10 nm is reached. This model of grain-boundary mobility calculation shows that no significant grain growth happens during the cooling process and thus rotation of boundaries is indeed necessary during deformation.

An alternative approach incorporating both nucleation and growth of grains based on grain boundary energy change and diffusion mechanism was implemented by Li et al. [142]. The grains nucleate either homogeneously or heterogeneously at the elongated substructural boundaries in the deformed sample. Li et al. [142] showed that the growth of these new nuclei of recrystallized grains should incorporate both strain rate and atomic thermal migration. Including shear strain rate $\dot{\gamma}$, the growth rate for a grain associated with a certain strain, the change in diameter \dot{D}_2 can be represented as:

$$\dot{D}_2 = \frac{\alpha \mu b}{2\eta} D_2^2 \sqrt{\frac{2\rho_m \dot{\gamma}}{3}} \quad \text{or} \quad \frac{dD_2}{d\gamma} = \frac{\alpha \mu b}{2\eta} D_2^2 \sqrt{\frac{2\rho_m}{3}} \quad (41)$$

Based on Eq. 41, $D_2 = D_1 \left(\frac{1}{1 - B(\dot{\gamma} - \dot{\gamma}_c) D_1} \right)$, is an average recrystallized grain size, D_1 is the equivalent diameter of cell structure or sub-

grains, $B = \frac{\alpha \mu b}{2\eta} \sqrt{\frac{2\rho_m}{3}}$, η is the boundary energy density, $\dot{\gamma}_c$ is the critical shear strain related to the stopping of rotation and starting of the migration of sub-grain, $\alpha \mu b^2$ is the energy per unit length of dislocation (where α is a constant of 0.5–1.0) [439], δ is the width of the cell wall, ρ_m is the mobile dislocation density, and $\dot{\gamma}$ is the instantaneous strain. On the other hand, a temperature rise has been observed inside the shear band, resulting in the growth of recrystallized grains. The growth rate of these grains has to be associated with the atomic thermal migration and it is expressed as:

$$\frac{dD_3}{dt} = (D_{B_0} + k_1 \dot{\gamma} D_B^v t) \left(\frac{2\eta}{D_3} + \frac{2\tau_i^2}{E} \right) \frac{\Omega}{\delta k_B T} \quad (42)$$

where, D_3 is the instantaneous grain size, $D_{B_0} = D'_0 \exp(-Q_B/RT)$ and $D_B^v = D''_0 \exp(-Q_B/RT)$, where, D_B^v is the vacancy diffusion coefficient in the grain boundary, D_{B_0} is a grain-boundary diffusion coefficient, $\Omega = b^3$ is the atomic volume, k_1 is a constant, τ_i is the applied shear stress, E is the elastic modulus. Q_B is the activation energy for grain-boundary diffusion, D'_0 and D''_0 are pre-exponential factors, R is the gas constant, and T is the absolute temperature.

Strain-rate and temperature influence are considered during the nucleation and growth process of dynamic recrystallization. The first one is an athermal part, and the latter one is the result of thermal diffusion. Li et al. [142] combined these two parts and predicted the grain growth rate during shear localization within the narrow bands:

$$\frac{dD}{dt} = (D_{B_0} + k_1 \dot{\gamma} D_B^v t) \left(\frac{\eta}{D} + \frac{\tau_i^2}{E} \right) \frac{2\Omega}{\delta k_B T} + \frac{\alpha \mu b}{2\eta} D^2 \sqrt{\frac{2\rho_m \dot{\gamma}}{3}} \quad (43)$$

This equation can be solved numerically. The calculation demonstrates that the recrystallized new grain diameter D increases almost linearly as a function of time t , and, after several microseconds it will shift to an exponential growth. Nevertheless, the deformation time is around 20–40 microseconds, so the resulting grain growth is actually very limited at this point, indicating that grain growth could hardly occur during the dynamic loading. This calculation essentially confirms the previous calculation in the beginning of this section. Li et al. [142] analyzed the recrystallized grain size in a Ni-Cu-Al alloy, and the grain size which ranges from 13 to 200 nm in diameter is confirmed by TEM observations.

12.3. Evolution of structure: from dislocations to sub-grains and equiaxed grains

The realization that migrational (discontinuous) recrystallization could not take place led to the search for alternative mechanisms.

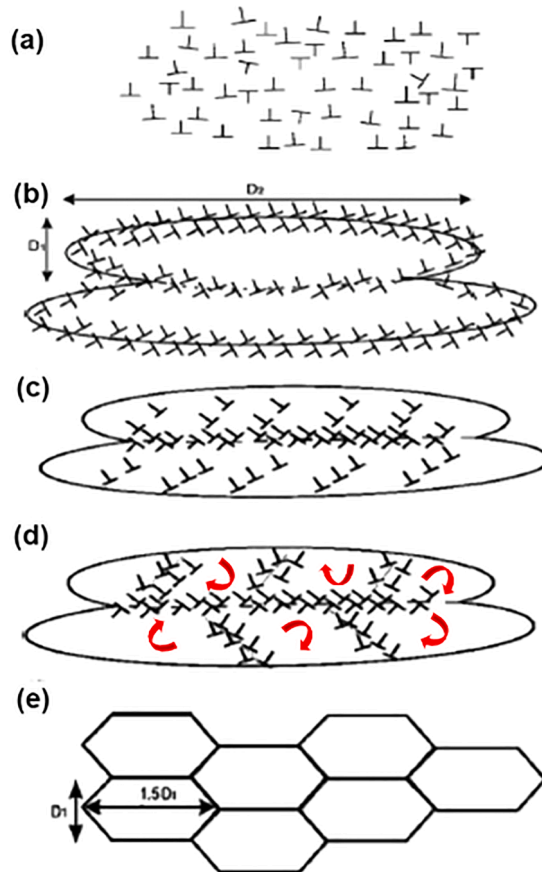


Fig. 69. Schematic of microstructural evolution leading to rotational recrystallization during severe dynamic plastic deformation: (a) homogeneous dislocation distribution; (b) reorganization into elongated cells/subgrains at critical strain/temperature; (c) continued deformation and increase in subgrain misorientation; (d) cell formation inside of subgrains and their breakup; (e) formation of equiaxed nano-/ultrafine-sized grains by rotation of grain boundaries by 30° [441].

As mentioned earlier, rotational (or continuous) recrystallization is already well known for minerals (e. g., Derby [440]).

The formation mechanism of these recrystallized grains is interpreted as consisting of a first stage, in which elongated sub-grains are formed, followed by their breakup to form equiaxed grains. This requires breakup of the elongated subgrains by rotation of individual segments; they gradually acquire different orientations. Strain-gradient effects become prominent at this stage. This evolution model was proposed by Meyers et al. [336] and expanded by Meyers et al. [19] using dislocation dynamics. The sequence of events is shown in Fig. 69.

The strain energy E_1 for randomly distributed dislocations in configuration a is represented in Fig. 69 by the expression:

$$E_1 = \rho_d \left(\frac{A\mu b^2}{4\pi} \right) \ln \left(\frac{a}{2b\rho_d^{1/2}} \right) \quad (44)$$

where ρ_d is the dislocation density, A is a constant depending on the character of the dislocations, μ is the shear modulus, b is the Burgers vector, and a is a parameter which is related to the core energy of the dislocations. It is assumed that, when a critical strain or temperature is reached, the homogeneous dislocation distribution is transformed into a subgrain structure by the movement of dislocations to the cell walls. The temperature-induced mobility of the dislocations enables such a change, at a critical point (strain or temperature, or a combination of both). The dislocation density evolution is governed by an evolution of, for instance, the Mecking-Kocks equation:

$$\frac{d\rho_d}{dt} = k_g \sqrt{\rho_d} + k_a \rho_d \quad (45)$$

where, k_g represents a hardening, or dislocation generation factor, and k_a represents a softening, or dislocation annihilation factor.

If the dislocations evolve into the subgrain structure, the energy is changed. The elongated cells are simplified to be of an ellipsoidal shape. This is represented by the configuration in Fig. 69 (b). The cell walls are assumed as tilt low-angle grain boundaries. For an ellipsoid shape with the aspect ratio r , the surface area S and volume V are expressed as:

$$S = 2\pi f(r)W^2 \quad (46)$$

$$V = \frac{4}{3}\pi rW^3 \quad (47)$$

$$f(r) = 1 + \frac{r^2}{\sqrt{r^2-1}} \sin^{-1} \left(\frac{\sqrt{r^2-1}}{r} \right) \quad (48)$$

where W is half of the cell width. All dislocations are assumed to be absorbed into the cell walls. The following equation represents the energy of dislocation subgrains, E_2 , which has its origin in low-angle grain boundaries:

$$E_2 = \rho_d \left(\frac{A\mu b^2}{4\pi} \right) \ln \left(\frac{ea}{4\pi b} \left(\frac{S}{V} \right) \frac{1}{\rho_d} \right) \quad (49)$$

where D_d , the dislocation spacing at the tilt (cell) boundaries, generates a misorientation of the low-angle grain boundaries, θ , through:

$$D_d = \frac{b}{2\sin(\theta/2)} \cong \frac{b}{\theta} \quad (50)$$

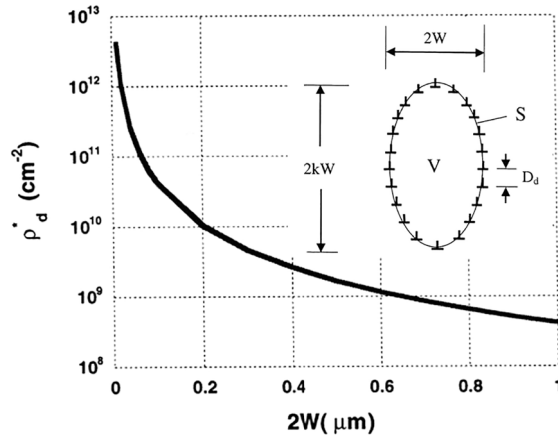


Fig. 70. Relationship between critical dislocation density ρ_d^* and subgrain width [19].

Eqs. (44) and (49) represent the total energy per unit volume with dislocation configurations a and b, in Fig. 69, respectively. The condition $E_1 = E_2$ yields the critical width W , and misorientation angle θ^* at a dislocation density ρ^*_d :

$$W = \frac{3ef(k)\rho_d^{*-1/2}}{4\pi k} \quad (51)$$

$$\theta^* = \frac{3}{4} \left(\frac{e}{\pi} \right)^2 \left(\frac{f(r)}{r} \right) \left(\frac{b}{W} \right) \quad (52)$$

Thus, the higher the dislocation density at which they reorganize, the smaller will, on its turn, be W . The energy difference between configurations a and b reaches a maximum when $r \rightarrow +\infty$, where $f(r)/r = \pi/2$.

This derivation corresponds well with the TEM observations. A typical dislocation cell size varies from 50 to 300 nm, with a rise of temperature ~ 400 K. This is associated with a dislocation density of 10^{10} cm^{-2} , approximately. Fig. 70 provides the relationship between the critical dislocation density ρ^*_d (ranging from 10^8 to 10^{13} cm^{-2}) and the width W .

After the formation of subgrains, there is a continuous increment in dislocation density with increased plastic deformation. If this increase is mainly accommodated by subgrain boundaries, the misorientation of grain boundaries can increase if cells do not dissociate (consistent with experimental observations). Cells gradually become sub-grains with the increase of misorientation. Beyond $\theta^* = 10^\circ$, the adjacent grains define high-angle boundaries. These boundaries build barriers for the dislocation motion. As experiments demonstrate, these elongated cells finally break up (Fig. 69 (d)), this is attributed to limited ability of the elongated cells to accommodate deformation. This results in a reorganization of dislocations inside subgrains to low-energy grain boundaries perpendicular to the cell boundaries. Indeed, Xue et al. [136] describe such an intermediate structure for 316L stainless steel. A similar structure was also observed by Meyers et al. [56] in tantalum, at a strain below the one for equiaxed grains. The break-up of the elongated subgrains to form near-equiaxed micro- or nano-grains is the following stage, which requires thermal energy and diffusional evolution (albeit in a very small region), corresponding to the transition from d to e in Fig. 69. The individual equiaxed grains are formed by rotation of the segments and driven by the continued requirement to move dislocations to accommodate the plastic strain. Rotations of grain-boundaries by small angles are required and the driving force is the decrease of the overall grain boundaries energy. This will be seen in the next section.

12.4. Rotation of grain boundaries

Once the elongated cells are formed and upon continued plastic deformation, they break up. Meyers et al. [106] proposed a theory of grain-boundary rotation to demonstrate the evolution of the structure during the dynamic recrystallization. To demonstrate this, it has to be confirmed that grain-boundary rotation can be finished within the time/temperature history during shear localization. The mechanism can also be applied to other severe plastic deformation processes during dynamic recrystallization and indeed this was applied by Mishra et al. [441] to ultra-fine-grained copper prepared by Equal Channel Angular Pressing (ECAP). The relaxation of the misoriented segmented grains to a more equiaxed grain configuration can be accomplished by small rotations of the grain boundaries. Fig. 71 (a) and (b) show that a rotation of 30° of the boundaries leads to the transformation from segmented subgrains to an equiaxed microstructure. If each subgrain segment rotates by an angle θ , an equiaxed or near equiaxed structure would be formed. This process can be assisted by the diffusion (flux of atoms) along the grain boundary, which normally is orders of magnitude faster than that in the bulk. Fick's law, which is associated with a potential energy gradient, is applied. This is a crucial idea of this model: a mechanical stress drives the diffusion by assuming an applied force \vec{F} acting on a particle:

$$\vec{F} = \nabla V \quad (53)$$

where ∇V represents the gradient of the potential energy field. Thus, the average diffusion velocity \vec{v} is expressed as the product of the mobility of diffusion species M by the driving force: $\vec{v} = M\vec{F}$. The flux J along a grain boundary with thickness δ and depth L_2 (cross-sectional area $L_2\delta$) is thus represented as:

$$J = L_2\delta C_m M F = \left(\frac{L_2\delta D C_m}{k_B T} \right) F \quad (54)$$

where C_m is the concentration of the mobile species (mass per unit volume), D is the diffusion coefficient, (which will be the grain-boundary diffusion coefficient D_{GB}), and k_B is Boltzmann constant.

The decrease of the interfacial energy drives the rotation of subgrains. The force applied on the grain boundaries is expressed as:

$$F = \gamma_{GB} \left(1 - 2\cos\frac{\theta_3}{2} \right) L_2 \quad (55)$$

The relationship between the degree of grain rotation and the flow volume, dV , is expressed as:

$$\frac{L^2 d\theta}{4L_2} = dV \quad (56)$$

where L_2 is the thickness and dV is the volume transferred. L is the instant boundary length of the subgrain (shown in Fig. 71 (b)) and

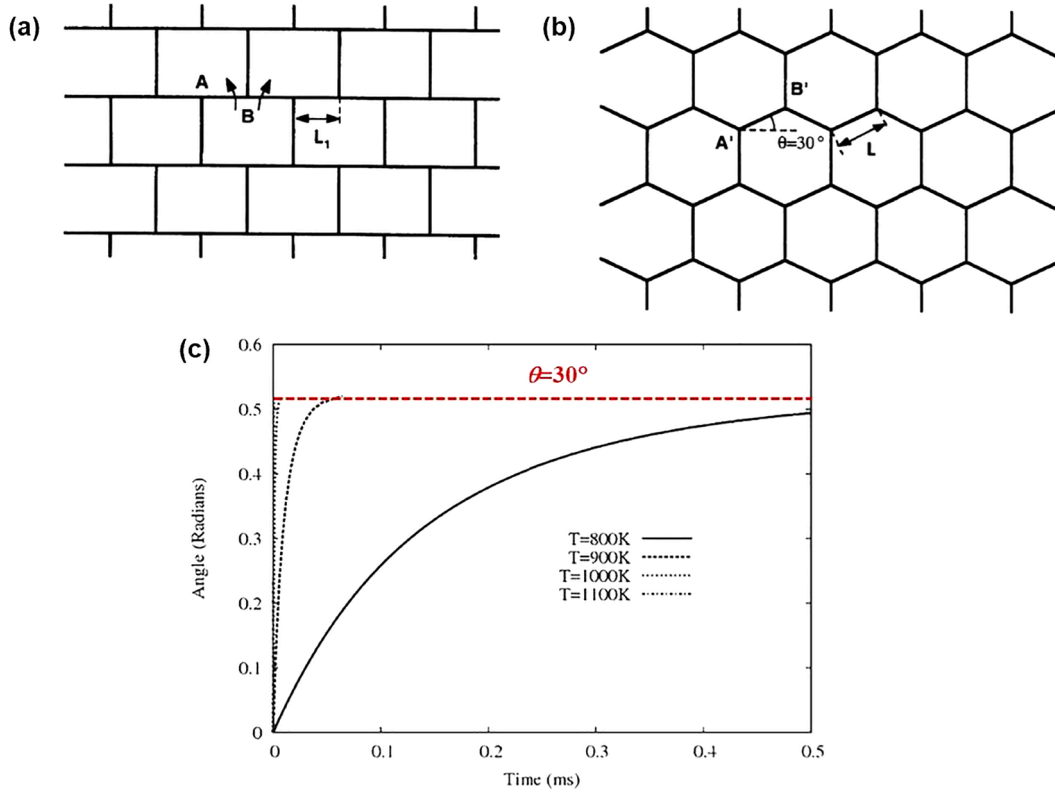


Fig. 71. (a) and (b) Representation of the last stage of rotational recrystallization leading from rectangular sub-grains to equiaxed ultrafine grains through rotation of grain boundaries: (a) a grain boundary AB under effect of interfacial energies; (b) material flux through grain boundary diffusion and rotation of AB to A'B'; (c) calculated rotation angle of boundaries from a grain size of 200 nm as a function of time for different temperatures [106,437].

equals to:

$$L = \frac{L_1}{\cos\theta} \quad (57)$$

where L_1 is the initial length, as indicated by AB in Fig. 71 (a). Thus, from Eq. (56):

$$\frac{d\theta}{dt} = \frac{4\cos^2\theta}{L_2L_1^2} \frac{dV}{dt} = \frac{4\cos^2\theta}{L_2L_1^2\rho} \frac{dm}{dt} \quad (58)$$

where dm/dt is the mass change along boundaries, which is equal to the rate of volume change multiplied by density ρ .

The rate of mass change, dm/dt , incorporated into Eq. (58), represents the flux, J . Substituting Eq. (54) into 58:

$$\frac{d\theta}{dt} = \frac{4\cos^2\theta}{L_2L_1^2\rho} J = \frac{4\cos^2\theta}{L_2L_1^2\rho} \left(\frac{L_2\delta D_{GB}C_m}{k_B T} \right) F \quad (59)$$

$$\frac{d\theta}{dt} = \frac{4\cos^2\theta}{L_1^2\rho} \frac{\delta D_{GB}C_m}{k_B T} \gamma_{GB} (1 - 2\sin\theta) L_2 \quad (60)$$

Assuming that the grains formed are equiaxed, $L_2 \approx L_1$.

$$\frac{4\delta D_{GB}\gamma_{GB}}{L_1 k_B T} t = \int_0^\theta \frac{d\theta}{\cos^2\theta (1 - 2\sin\theta)} \quad (61)$$

By integrating Eq. (61), one obtains:

$$t = \frac{L_1 k_B T}{4\delta D_{GB}\gamma_{GB}} f(\theta) \quad (62)$$

in which:

$$f(\theta) = \frac{\tan\theta - \frac{2}{3}\cos\theta}{(1 - 2\sin\theta)} + \frac{4}{3\sqrt{3}} \frac{\ln \frac{\tan\frac{\theta}{2} - 2 - \sqrt{3}}{\tan\frac{\theta}{2} - 2 + \sqrt{3}}}{\tan\frac{\theta}{2} - 2 + \sqrt{3}} + \frac{2}{3} - \frac{4}{3\sqrt{3}} \frac{\ln \frac{2 + \sqrt{3}}{2 - \sqrt{3}}}{2 - \sqrt{3}} \quad (63)$$

The most significant parameter in Eq. (62) is the grain-boundary diffusion coefficient D_{GB} , which contributes to the diffusion coefficient D . It is multiplied by the grain-boundary thickness δ and is given, based on Frost and Ashby [442], for AISI 304 stainless steel [106], as:

$$\delta D_{GB} = 2.0 \times 10^{-13} \exp\left[\frac{-167 \times 10^3}{RT}\right] (m^3 s^{-1}) \quad (64)$$

As an illustration here, we utilize the parameters for stainless steel to demonstrate the application of Eq. (62). The subgrain size is taken as 200 nm in stainless steel to estimate the grain rotation time [106]. For $T = 900, 1000, 1100$ K, the represented relationship of the degree of rotation and time are shown in Fig. 71 (c). The thickness of grain-boundary δ , taken as 0.5–1 nm, is not necessary here, because it is already incorporated into Eq. 64. The rate of rotation reduces with increasing θ and asymptotically reaches 30° , at which point the grains are equiaxed and the driving force becomes zero. The temperature T is calculated separately, as shown in Section 5.1. The above temperatures ($T = 900, 1000, 1100$ K) are within the range of recrystallization temperatures. Meyers et al. [106] estimated for stainless steel a temperature rise to be about 800 K at a shear strain of 10 and equal to about 1000 K when shear strain reaches 35. Fig. 71 demonstrates that the rotation of a 200 nm grain from a rectangular to an equiaxed shape occurs in a short time of 0.5 ms. This is within the same order as the deformation time. Thus, the equiaxed configuration formed during shear localization has been demonstrated by both experiments and theory. The coexistence of elongated and rectangular subgrains observed inside the shear bands in 304L stainless steel, is significant evidence for this mechanism of equiaxed grain formation by the rotation dynamic recrystallization mechanism as presented above.

12.5. Dynamic deformation/adiabatic shear band formation

Fig. 71 (c) shows that a grain rotation of 30° occurs in 1.4 μ s at the temperature of 1100 K, whereas with decreasing temperature in the shear band, it takes a relatively longer time. For a higher temperature, a rotation of 30° takes ~ 0.9 ms at 800 K. These calculations predict progressive rotations of the grain boundary within the deformation time (1–64 μ s) at temperatures between 900 K and 1100 K

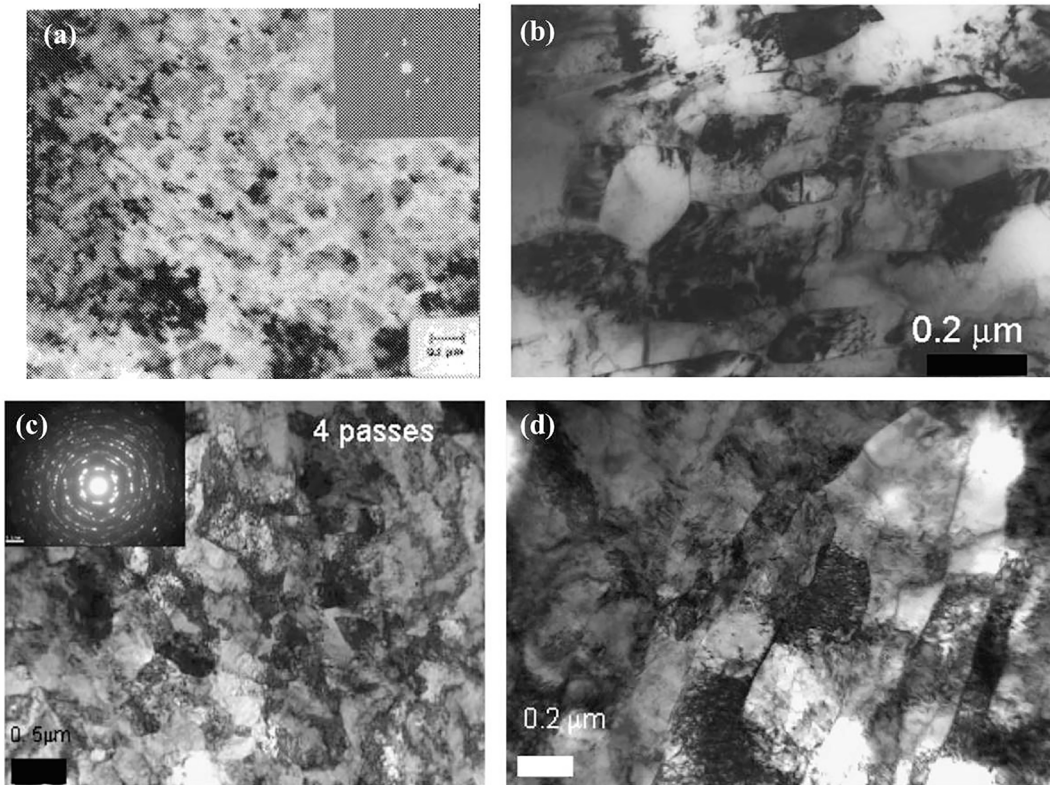


Fig. 72. TEM images of Cu subjected to shear strain of 4: (a) and (b) microstructure inside the shear band of impacted hat-shaped specimen (strain rate of about 10^4 s^{-1}); (c) and (d) microstructure generated by equal channel angular pressing (ECAP) after 4 passes under a strain rate of 1 s^{-1} [108,441].

for grain sizes between 0.1 and 0.3 μm [437]. However, this does not exclude the existence of reorientation or accommodation of the grain boundaries at the cooling (post deformation) stage.

12.6. Comparison of shear localization with conventional low-strain-rate severe plastic deformation

It is instructive to compare the structures generated by severe plastic deformation and adiabatic shear band formation. This was done by Mishra et al. [441] who concluded that the same mechanism operates in both cases. The similarity between the recrystallized ultrafine- or nano-grains prepared by ECAP and the microstructures generated within shear bands is striking, despite the obvious difference in thermomechanical history. For comparison purposes, Fig. 72 (a) and (b) show the ultrafine-grained copper achieved in a hat-shaped specimen which was constrained by the plastic deformation in a narrow 200 μm band [108]. The shear strain was measured to be about 4 and a size of 100–200 nm grains was revealed. Fig. 72 (c) and (d) illustrate the structure obtained by ECAP with an equivalent shear strain of 4 through four passes. The grain size is relatively similar, with more obvious grain-boundary waviness by ECAP, as described by Mishra et al. [441]. This is indeed very surprising, considering the significant differences in strain-rate (approximately 1 s^{-1} for ECAP and 10^4 s^{-1} for the dynamic testing) and thermal history (successive thermal spikes after each pass for ECAP and adiabatic temperature rise to $\sim 600 \text{ K}$ for the hat-shaped specimen).

This similarity is clarified by comparing the Zener-Hollomon parameters, Z , for these two processes. The Zener-Hollomon parameter includes both temperature, T , and strain rate, $\dot{\epsilon}$, in one equation which has the activation energy for diffusion, Q [36]:

$$Z = \dot{\epsilon} \exp(Q/RT) \quad (65)$$

For the formation of a shear band in hat-shaped specimen, the strain rate is taken as 10^4 s^{-1} . Using $Q = 72.5 \text{ kJ/mol}$ (the activation energy for grain-boundary diffusion in copper) and an estimated temperature $T = 500 \text{ K}$, one obtains $\ln Z = 27$. For ECAP, the strain rate is about 1 s^{-1} . The temperature rise is very minor. We take, as a first approximation, $T = 350 \text{ K}$ (this is calculated using the expressions in Section 5.1). Using the same activation energy, one can get $\ln Z = 25$. Thus, the conditions in both adiabatic shear localization and ECAP favor thermal recovery in the same manner. The similarity of the value of $\ln Z$ results in the similar subgrain size. Li et al. [443] generalized this, discovering that deformation-induced grain refinement increases at higher Z values and the average grain size drops from 320 to 66 nm when $\ln Z$ increases from 22 to 66. The grain refinement mechanism is dominated by dislocation activity in low- Z processes, while deformation twinning plays a significant role in high- Z deformation. A significant increase in yield strength from 390 to 610 MPa was revealed in deformed Cu when increasing Z , attributed to a significant grain refinement by deformation nanotwins.

12.7. Dynamic recrystallization: does it precede or follow localization?

The question whether dynamic recrystallization generates shear localization or is a product thereof is difficult to answer. It is akin to the ‘Chicken-and-egg’ conundrum. Molinari and Clifton [243] and Molinari [453] showed that thermal softening alone can lead to localization when the accumulated plastic strain reaches a critical value. One should not forget that thermal softening is the result of the interaction of dislocations with short-range obstacles. Rotational dynamic recrystallization results in the breakup of the dislocation structure into well-defined sub-grains and subsequent formation of grains with diameter of $\sim 200 \text{ nm}$. Dislocations are also involved in the formation of these low-angle boundaries between adjacent sub-grains which gradually increase in misorientation. Would this be a vindication of the ‘crystallite theory’ of plastic deformation of the beginning of the Twentieth Century resulting from X-Ray line broadening? This theory was superseded in the 1930s by dislocation theory. We believe that rotational dynamic recrystallization is qualitatively distinct from strict softening due to thermal energy. It results in an acceleration in the drop of the flow stress and in a more abrupt delineation of the shear band. The simulations by Lieou and Bronkhorst [445,454] suggest that DRX results in a significant drop in dislocation density and shear stress, in contrast with thermal softening alone. The experimental results by (Guo et al. [225] (Fig. 17) are intriguing: they suggest that the formation of an ASB (at the maximum stress) precedes the drastic temperature rise. These results are not in agreement with those of Nie et al. [154] (Fig. 11) which show that localized heating precedes the maximum stress. One can conclude from the above that dynamic recrystallization is involved in the ‘transformed’ bands, whereas thermal softening leads to ‘deformed’ bands, in the old nomenclature.

13. Additional considerations and advances

Using the Manwaring-Meyer [132] hat-shaped configuration and copper specimens pre-conditioned by shock compression to $\sim 50 \text{ GPa}$ in order to increase the yield stress and decrease the work-hardening rate, Hines and Vecchio [434] confirmed the effect first observed by Andrade et al. [108]. Fig. 73 (a) shows that the shear band obtained in copper by Meyers et al. [105], and Andrade et al. [108] with deformation initiated at room temperature in Fig. 73 (b) is identical to the one obtained by Hines and Vecchio [434] on the same material with deformation initiated at 77 K. The similarity between the two specimens is obvious, with the width of the forced localization region being the same $\sim 200 \mu\text{m}$.

Hines and Vecchio [434] also evaluated the subgrain coalescence recrystallization mechanism and concluded that it cannot operate within the deformation time. They thus concluded that a mechanically-based process would be necessary for dynamic recrystallization at high strain rates. This was modeled using a bicrystal subjected to simple shear and applying a micromechanical model incorporating rate-dependence and lattice rotations. These calculations provided a mechanistic interpretation for the progressive rotations between

the two subgrains and annihilation of dislocations, generating high-angle grain boundaries. This progressive subgrain misorientation generates rotational recrystallization and is akin to the evolution of dislocations into subgrains presented by Meyers et al. [336]. Fig. 74 shows the sequence of structural rearrangement steps under shear starting with a monocrystal (a) which subdivides into elongated cells (b), which on their turn break down into equiaxed subgrains that continue to rotate (c), leading to the final structure (d). Thus, they also point to rotational recrystallization as the mechanism responsible for the generation of the ultra-fine and nanocrystalline grains, as presented in Fig. 75 [444].

Rittel and coworkers [281] investigated the evolution of microhardness in pure titanium and two-phase titanium alloys Ti-6Al-4V and observed nanosized recrystallization grains at applied strains that were only one half of the localization strain. They argue that dynamic recrystallization precedes shear-band formation and is not the result of localization. Fig. 76 (a) shows one such region, with nanograins indicated by arrows. For titanium, in a similar manner, discontinuous islands of recrystallized grains nucleate and grow with strain, eventually coalescing and forming a continuous band, which in essence is the shear band. Localization, marked by a rapid drop in stress, corresponds to the complete band formation. This discontinuous formation of recrystallization islands is consistent with Guduru and Ravichandran's [153] observation that the shear band contains "hot spots". These are softened by virtue of the local increase in temperature, and further by the annihilation of dislocations when recrystallization takes place. Plastic deformation and temperature inhomogeneities are the probable causes for the recrystallization islands observed by Rittel et al. [281]. Another aspect to consider is the non-homogeneous plastic deformation, a characteristic feature of plastic deformation in polycrystals and especially of bi-phase alloys, such as Ti-6Al-4V. In order to illustrate such phenomenon, Fig. 76 (b) shows the larger magnification optical microscopy images of the well-developed and the onset regions of an ASB. Local differences of deformation pattern are readily seen. Thus, the plastic deformation in specific areas might exceed considerably the global strain. This can be a further cause of "early" recrystallization observed by Rittel and collaborators [281].

The mechanistic incorporation of this complex phenomenon of recrystallization in shear bands has been taken up by Lieou and Bronkhorst [445]. A rigorous mechanics analysis incorporating thermodynamics and the entropy of dislocation configurations was conducted in an ideal material (pseudo-titanium) used as model and compared with experiments by Li et al. [81]. The grain size and dislocation density evolution are compared and significant differences in the response are observed between specimens which undergo dynamic recrystallization and those who do not. The recrystallized grains have significantly reduced dislocations. The shear stress vs. shear strain curve has a more pronounced drop with dynamic recrystallization, as shown in Fig. 77 (a). This simulation was performed

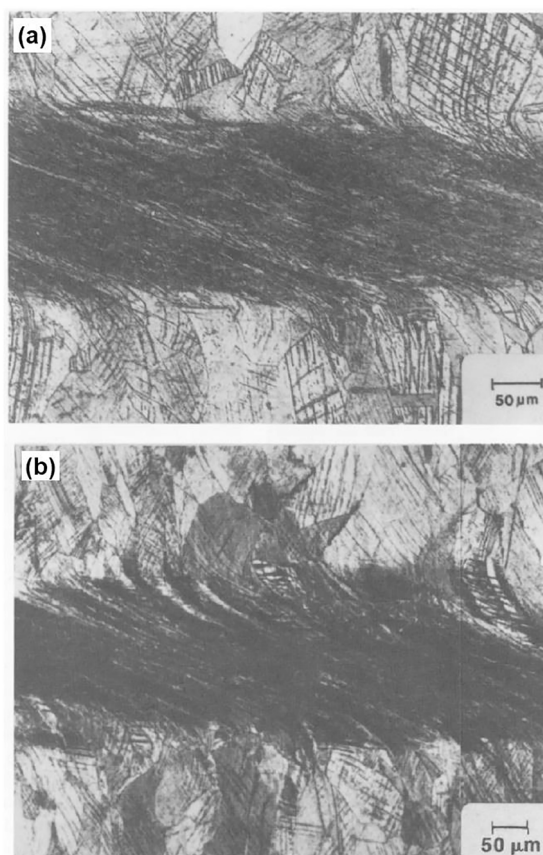


Fig. 73. Shear localization regions in pre-shocked copper (to a pressure of ~ 50 GPa) [105] deformed at (a) room temperature (298 K) and (b) 77 K [434]. Note similar thickness and characteristics of bands.

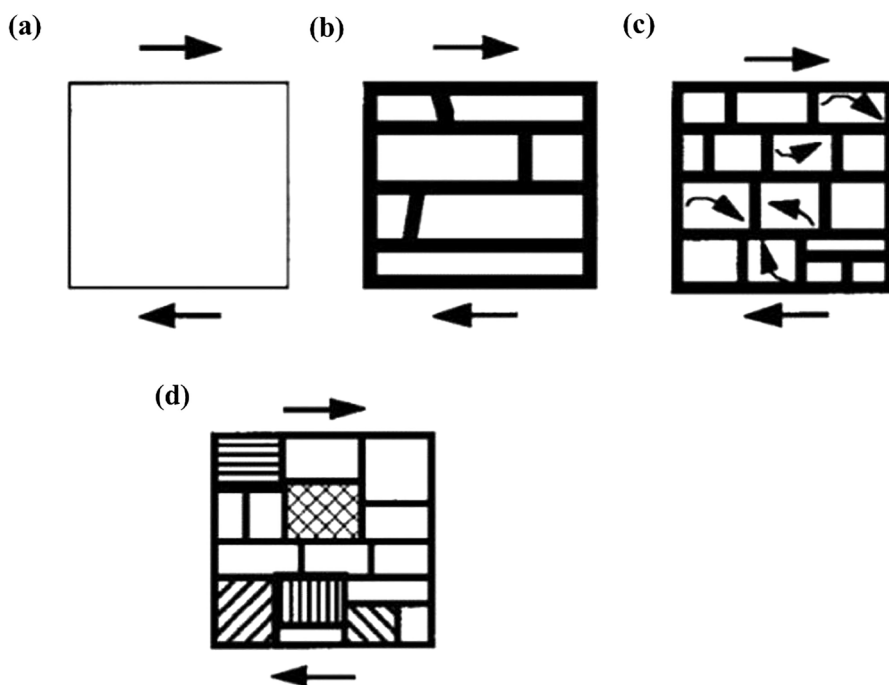


Fig. 74. Sequence showing rotational recrystallization model by Hines et al. [444] based on crystal plasticity, which enabled nano-/ultrafine-sized grains to rotate: (a) starting single crystal; (b) formation of elongated subgrains; (c) rotation of equiaxed subgrains; (d) high-angle misorientations between some subgrains.

at a high strain rate, $\sim 5 \times 10^4 \text{ s}^{-1}$. The corresponding dislocation density evolution is presented in Fig. 77 (b), where the dimensionless ordinate represents a normalized dislocation density (dislocation density/initial density). This reduced dislocation density, in turn, affects the flow stress. In the absence of dynamic recrystallization, the density produces saturation beyond a shear strain of 4, whereas it undergoes a significant drop in the case of DRX. These results represent a quantitative mechanistic understanding of the structural evolution of shear localization which incorporates rotational recrystallization.

Fig. 78 summarizes the micromechanical behavior of nanocrystalline NiTi (with average grain size 65 nm) [446]. The compression deformation of the micropillars leads to the formation of localized nano-shear bands with significant strain bursts, leading to extreme amorphization and further grain-size decrease from an initial 65 to 11 nm inside the shear band. This shear-induced amorphization is akin to the one analyzed by Zhao et al. [375] for Si, Ge, and has also been observed by Luo et al. [447] in the intermetallic compound SmCo₅. The phase transformation mechanism still needs to be examined, originating from its unstable thermodynamic status.

14. Conclusions

Shear localization is a process of plastic deformation which precedes the failure of materials under external loading. When the rate of application of the load, and consequently the rate of generation of heat in a narrow region becomes higher than the rate of heat extraction, the local temperature rises. In the extreme case where the heat extracted is negligible, the process becomes adiabatic, with a maximum of temperature rise. This regime of localization produces what is commonly referred as “adiabatic shear bands (ASBs)” which have well defined characteristics and exhibit a commonality of microstructural evolution features across the different classes of metals: FCC, BCC, HCP alloys, metallic glasses, and composites. We evaluate the broad literature published on ASBs (totaling $\sim 2,000$ papers) in this review, focusing on the more recent work and presenting the principal experimental techniques, mechanical and microstructural features. The following are important elements in our evaluation:

1. *Industrial and military applications.* Adiabatic shear bands are an important localized deformation mechanism which has great importance in machining, forging, and other industrial operations. In forging and forming it is undesirable, whereas in cutting and machining it is often desirable. The relevance of ASBs in ballistic applications is also recognized globally. Armor designers develop materials that can resist this dramatic shear localization, which causes plugging of the target with increased vulnerability. Similarly, ASB formation in projectiles is precursor to catastrophic failure. One exception is tungsten-based kinetic energy penetrators which are replacing depleted uranium. The formation of ASBs at the tip, during the penetration process, keeps the projectile sharp and increases its effectiveness. Cheng et al. [462] developed a novel multiphase tungsten alloy. The failure of this alloy under dynamic compression was mainly attributed to the shearing in the loading direction without

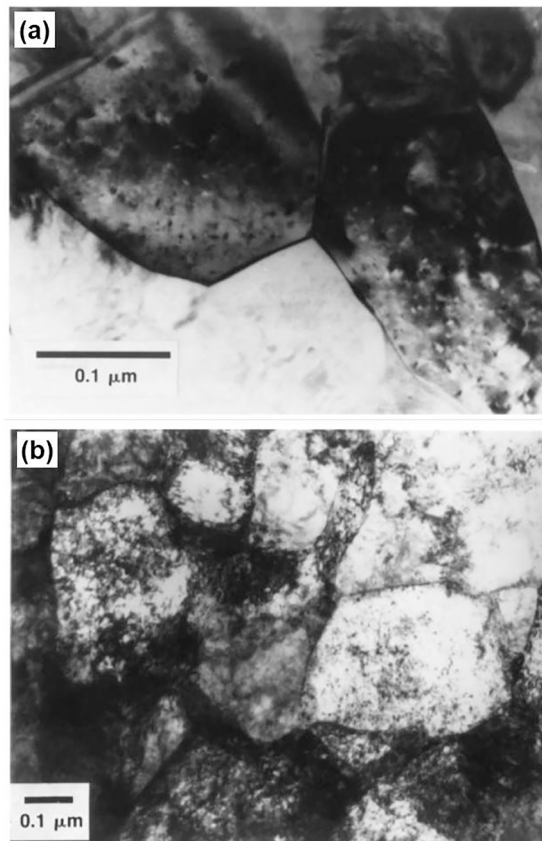


Fig. 75. Transmission electron micrograph of the micrometer-sized grains with diameters of approximately $0.2\ \mu\text{m}$ in an adiabatic shear band: (a) formed in copper at 40,000/s and an initial temperature of 77 K; (b) formed in tantalum at 30,000/s and an initial temperature of 298 K [444].

significant plastic deformation. The experimental and numerical simulation studies [463] prove that its unique ‘self-sharpening’ property (due to the formation of shear bands at the tip of projectiles) can improve the penetration performance.

2. *Experimental techniques.* There have been, since the early 1878 experiments by Tresca and the 1928 Kravz-Tarnavskii identification of shear bands, numerous techniques utilized to generate shear bands and, in the limit, adiabatic shear bands [455]. These can be roughly classified into:
 - (a) Compression Hopkinson (Kolsky) bar experiments using a variety of specimen geometries, varying from simple cylinders to more complex shapes and generating controlled simple shear in prescribed regions.
 - (b) Torsional Hopkinson (Kolsky) bar experiments on specimens with a hollow cylinder shape. A torsional elastic wave is launched into the incident bar and generates a simple shear stress state in the reduced portion cylinder, which can be assumed to be homogeneous.
 - (c) Contained cylindrical explosive geometry with the explosive either placed inside or outside a hollow specimen; special fixtures to generate prescribed and controlled strains have been successfully developed. This geometry leads itself well to the study of the collective behavior of shear bands.
 - (d) Ballistic experiments where a projectile is fired against a target, generating shear bands in both.
 - (e) Machining experiments generating chips with shear bands.
3. *Simple criteria for shear-band initiation.* These have been developed since the seventies and assumed that stress is a function of strain, strain rate, and temperature. These simple criteria assume that the process is adiabatic. The critical strain for localization is defined at the point at which the stress change with increased strain becomes negative. These criteria are named after their originators: Culver [2], Recht [1], and Staker [40] are prominent among them.
4. *More advanced criteria for shear localization.* The incorporation of heat transfer into the analysis requires the use of perturbation methods. This was done by Clifton [229], Bai [43], Fressengeas and Molinari [250], Molinari [457] as well as Burns and Trucano [41]. These analyses are more exact and provide different critical strains which depend on strain rates. As strain rates increase, critical strains in general decrease because of the decrease in thermal diffusion.
5. *Shear-band width.* The thickness of the adiabatic shear bands depends on a number of material parameters; expressions were proposed by Bai-Dodd [268], Grady [161], and Molinari [270]. Their predictions are significantly different but nevertheless of the same order of magnitude, which is in the micrometer range, for most metallic materials: 5–200 μm . In general, the width

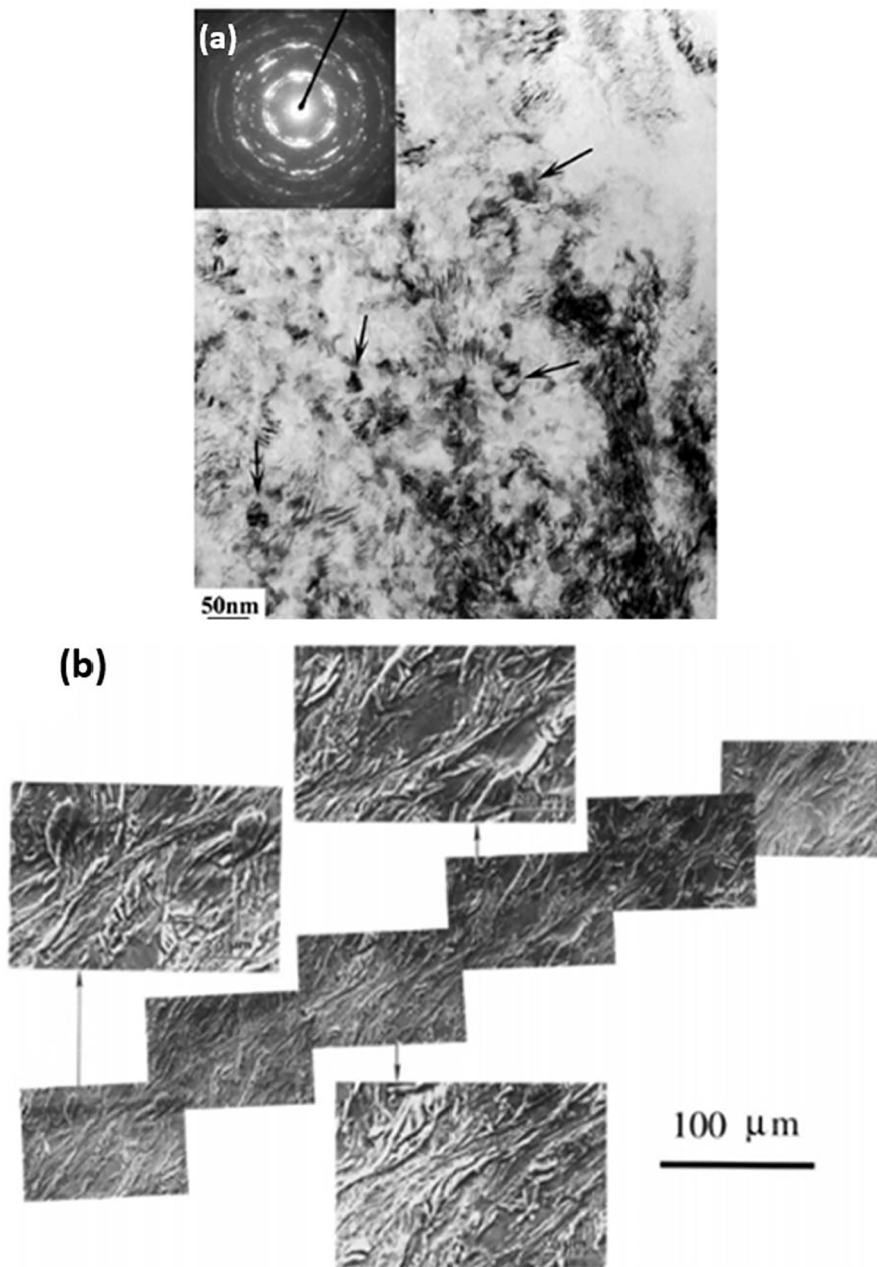


Fig. 76. (a) TEM micrograph in the fillet area from interrupted dynamic tests, the dynamically recrystallized grains formed in the highly dislocated area are indicated by arrows [281]; (b) Montage of SEM micrographs of a shear-band tip showing variation in shear deformation from grain to grain [158].

decreases with increasing strength, thermal softening, and with decreasing initial temperature, heat capacity and thermal diffusivity.

6. *Temperature rise.* The deformation times and temperature excursion inside shear band have been calculated at increasing levels of complexity. Simple closed-form analyses assume adiabatic heating as a first stage and heat extraction from the band to the surrounding, as a second stage. More advanced approaches involve finite elements and concurrent deformation and heat transfer. Measurements are being conducted with increasing accuracy using diagnostics with the capability of focusing on smaller areas; however, these are still larger than the shear-band thickness.
7. *Spacing of shear bands.* Both contained external and internal explosive systems in a cylindrical geometry have been used to determine the spacing of shear bands. The shear-band spacing has been established in steels, titanium and its alloys, and has been successfully compared with mathematical predictions by Wright and Ockendon [162] and Molinari [163] (based on the

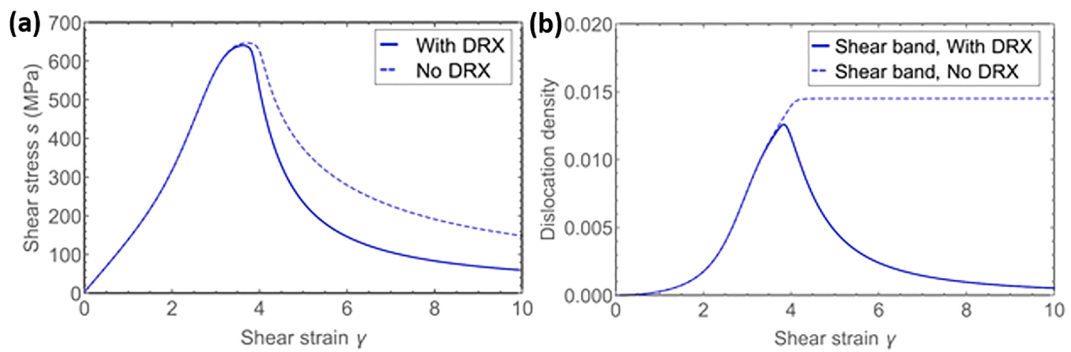


Fig. 77. (a) Shear stress as a function of accumulated shear strain for titanium undergoing dynamic recrystallization (solid curve) and pseudo-titanium which does not (dashed curve). Upon the onset of ASB, titanium becomes softer than pseudo-titanium because of DRX; (b) Dislocation densities in the shear band as a function of accumulated shear strain for titanium (solid curve) and pseudo-titanium (dashed curve). DRX produces a collapse of dislocation density. The applied strain rate is $5 \times 10^4 \text{ s}^{-1}$ [445].

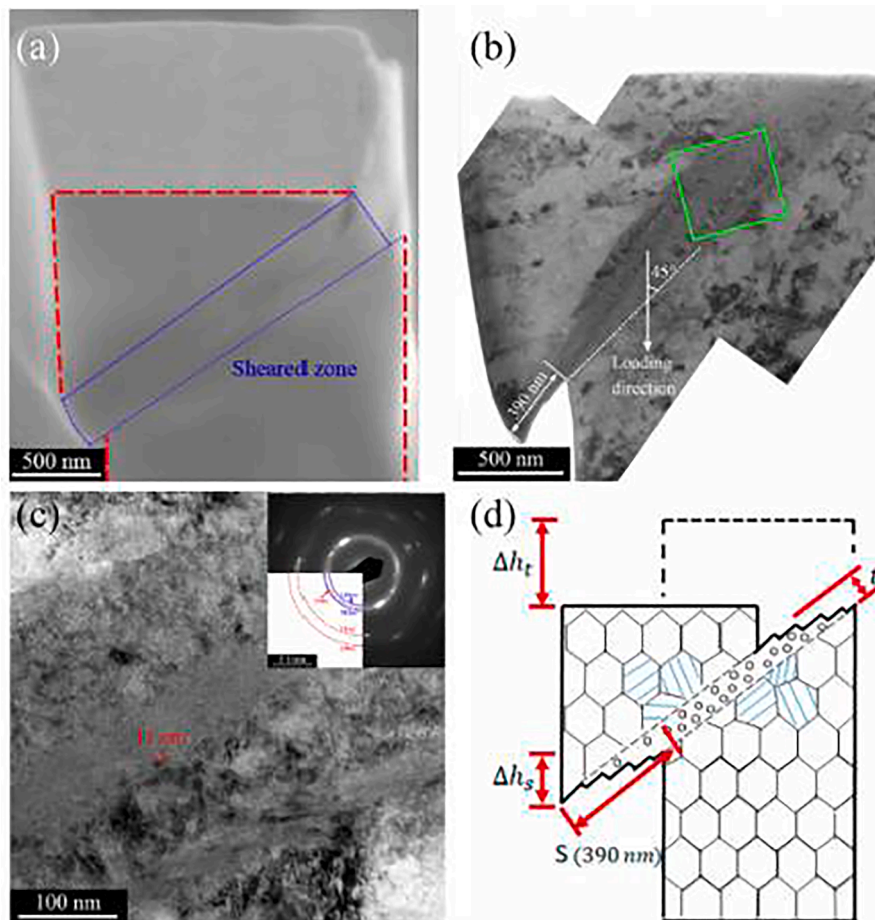


Fig. 78. Grain refinement and amorphization in monocrystalline NiTi micropillars under uniaxial compression [446]: (a) SEM micrograph of the plastically-deformed micropillar; (b) bright-field TEM micrograph of the localized shear band oriented at an angle of 45° to the loading direction; (c) a magnified image and the SADP of the region marked with a green box in (b); (d) a schematic drawing shows the plastic deformation of the nanocrystalline NiTi micropillar where the blue lines represent the residual martensite.

fastest growth rate of perturbations), and Grady and Kipp [161] (based on momentum diffusion). The evolution of shear-band spacing in these materials has also been studied, and the spacing increases with the propagation distance; this latter is due to the shielding effect by the leading shear bands.

8. *Micro/nanostructural evolution.* The microstructural evolution in shear bands might include a number of processes dictated by the phase transformation and internal structural reorganizations required by severe plastic deformation. The traditional literature divided the shear bands into deformed and transformed, based on optical microscopy observations. The use of modern characterization tools, and especially transmission electron microscopy, pioneered by Me-bar and Shechtman [62] and Meyers and Pak [326] has revealed a greater complexity in the structures. Many of the bands that were classified into “transformed” by virtue of being virtually featureless in optical microscopy observation actually had the same crystallographic structure as the matrix. However, grains were so small (50–200 nm) that they escaped optical observation, being beyond its resolution.
9. *Propagation velocity of ASBs.* The early experiments by Marchand and Duffy [101] already showed that the shear band has a front. Continuum and finite element calculations by Molinari and coworkers [275,276] established the relationship between applied velocity and ASB propagation velocity in simple shear. Kalthoff [183], Zhou et al. [115], Wright [458] and Guduru et al. [153] developed experiments designed to obtain the relationship between imparted velocity to system and ASB propagation velocity.
10. *Recrystallization within shear bands.* In the absence of phase transformation, it has been found that the structure within the shear band evolves from dislocations to the formation of sub-grains, which progressively break up into equiaxed grains with dimensions of diameter in 50–200 nm. This evolution is a rotational dynamic recrystallization (DRX) process which was proposed in 1996 [336]. The appearance of these nano and ultrafine grains is associated with a drastic decrease in the dislocation density and associated flow stress and significant rotations.
11. *Metallic glasses and nanocrystalline materials.* The virtual absence of work hardening in metallic glasses makes them especially prone to shear localization, which can develop at quasistatic loading rates. One may consider this as an isothermal process, but experiments by Lewandowski and Greer [355] showed a significant temperature rise. Although there is considerable debate over this point, thermal softening can play a significant role in the deformation and localization in metallic glasses. Nanocrystalline metallic materials exhibit, mostly, a very low work hardening rate and this predisposes them to shear localization. For titanium, it was observed that the shear band in the ultrafine grained condition (100 nm) is thinner (~10 μm) than the coarse-grained counterpart (~30 μm).
12. *Constitutive equations.* Throughout the literature and in this review, a broad range of constitutive equations have been introduced to treat ASBs either analytically or computationally. We emphasize that all equations have their value and their most important characteristic is their ability to describe as faithfully as possible the thermomechanical response. As an illustration, we list here the various equations in this overview by their numbers, starting with the general formulation expressed in Eq. (1). These equations use power, exponential, and linear functions to describe the main effects of work hardening, strain rate hardening, and thermal softening. They also use normal stresses and strains and alternatively, shear or effective (or equivalent) stresses and strains. These equations, which permeate the text, are: 9, 15, 16, 23, and 28.

15. Critical evaluation and recommendations

Both the mathematics and the materials/mechanical aspects of adiabatic shear localization have been the object of monographs, among which one by Wright [12] and one by Dodd and Bai [9–11]. The latter is a collection of authoritative articles by globally recognized experts and includes, in addition to metals, polymers and granular materials. The large number of specialized papers, over one thousand, could induce an outsider to think that this is a ‘dead’ field and that little knowledge can be gained by further pursuing it. However, this is not the case, and the development of new experimental and computational methods is revealing new aspects and addressing points that have yet to be resolved.

The deformation involved in impact, explosions, penetration, shatter, fragmentation, and in a variety of rapid deposition of energy events requires specialized diagnostics, since the phenomena take place in an extreme regime where times ranging from tens to millionths of a second. Significant progress has been made in our understanding enabled by innovative diagnostics, advanced analysis, state-of-the-art characterization, and ever more realistic modeling methods. On the characterization side, the focused ion beam (FIB) is playing an important role in extracting samples from very narrow regions for subsequent observation. Transmission electron microscopy (TEM) has been used since the 1980s but novel characterization techniques such as HRTEM and SEM-EBSD are playing an increasingly important role in this endeavor. On the analytical side, crystal plasticity and molecular dynamics are increasingly contributing. The development of experimental setups whereby the sample surface can be monitored as deformation proceeds is also an added approach for the further investigation of the formation procedure of the ASB or shear fracture. The following are the most important aspects in the study of ASBs that need further study:

1. *In-situ* experimental examination of the two-dimensional deformation evolution of shear band: This has three components:

- (a) Propagation velocity as a function of applied stress. Zhou et al. [115] obtained for the first time an extremely essential characteristic of shear bands: their propagation velocity. This is far from a closed subject and it would be desirable to establish experimentally how the velocity is related to the applied stress and, more generally, to the constitutive response in metals and alloys. The Mercier-Molinari [448] theory which predicts this velocity should be tested for different materials and stress levels.
- (b) The temperature rise. It plays the most significant role in the formation of the shear bands, and is being established with growing precision as the experimental methods evolve and enable the measurement over smaller and smaller dimensions [456]. A study that has shown this in an excellent manner is the work by Guo et al. [225].
- (c) Thermal softening effect at high rates. The microstructural transformations that are well documented undoubtedly affect the thermal softening since they determine the strength. We do not know softening other than the simple evaluation by Andrade and

Meyers [108] and detailed analysis by Lieou and Bronkhorst [445,454]. The width and spacing of shear bands are directly related to this softening. The constitutive modeling by Molinari and Ravichandran [449] should be extended and generalized.

2. A better understanding of the rate sensitivity on work hardening is needed for improved constitutive description at high rates and temperatures, leading to the major structural changes in shear bands. The Los Alamos MTS model pioneered by Kocks and coworkers [450] includes the effect of rate sensitivity of work hardening through a dislocation evolution term (dislocation generation and annihilation), but the physical basis needs experimental verification in this extreme regime.

3. An ultrafine grain/nanocrystalline structure is universally observed in shear bands, but the relative contributions of rotational recrystallization, post-deformation recrystallization and grain growth processes have still not been quantified.

4. The self-organization of the bands has been conducted for a number of materials. However, the change in spacing of shear bands as their length increases has not yet been successfully modeled. This is a problem that lends itself well to FEM analysis. Further combined experimental/analytical investigation is needed to develop a predictive understanding of this behavior including two-dimensional effects.

5. Grady [160,161] proposed the concept of shear-band toughness as a quantitative measure of the resistance of a material to shear localization. This line of research should be continued with the goal of generating operational parameters that assist in materials selection.

6. The evolution of the structure in adiabatic shear bands shows great similarities with severe plastic deformation (SPD) processes such as ECAP and high-pressure torsion (HPT). This has been interpreted in terms of the equivalence of the Zener-Hollomon parameter. Li et al. [443] extended this analysis to incorporate other effects, such as the dislocation density. This can lead to a modified Zener-Hollomon parameter, possibly through the addition of an energetic term.

7. The exact nature of the interaction between solute atoms and dislocations in dynamic strain aging at high strain rates requires more experiments and modeling. While thermal softening is elevated, the strain rate sensitivity is reduced (or even negative), the tendency for shear localization is raised. New theories, especially in the atomistic scale, need to be incorporated to understand the influence of dynamic strain aging on the shear localization of materials. For instance, it has been suggested recently that dynamic strain aging does not require a long-distance diffusion, but rather atomistic "hopping" in the vicinity of the dislocation core [451], suggesting that the DSA effect is stronger than expected, even in the high strain-rate regime where shear localization is expected.

8. Cold spray fabrication. This is an important method by which metal particles are accelerated to high velocities (500–1,000 m/s) and impact a target, bonding to it. Although it has been claimed that adiabatic shear localization plays a key role in the bonding process, this is still a matter of contention.

9. Bulk metallic glasses. The precise mechanisms of initiation and propagation of shear bands in BMGs are still not understood. Nevertheless, they play a seminal role in their deformation. Molecular dynamics simulations have been used with a special filtering method to reveal the formation of the STZs. Non affine displacements, local heterogeneities, and shear localization were identified. This is an example of a computational approach that can distinguish between the different atomic movement processes and separate free volume from thermal contributions to softening and shear localization. Additional studies of this nature are needed.

As a final remark, the confluence of mechanics and materials has always yielded the most rapid progress in our understanding of the relationship between the structure and mechanical properties of materials, and shear bands are a sterling example where this close interaction has led to the fastest progress. Mechanicians develop analytical and computational models which can be tested through carefully planned experiments. These experiments have to be designed with the testing of mechanics hypotheses in mind. Materials Scientists conduct advanced characterization experiments which were initially on recovered specimens but are increasingly being in situ to document the structural changes prior to, during, and after localization. The communication between these two disciplines will continue to drive the progress in our understanding of ASBs.

Declaration of Competing Interest

The authors declare that they have no known competing financial interests or personal relationships that could have appeared to influence the work reported in this paper.

Acknowledgements

Support for the writing of this review as well as for the experiments whose results are presented herein are provided by the National Natural Science Foundation of China (Grant Nos. 51871186, 52074230), the China Council Fellowship for Dr. Na Yan (201706295045), and a China Scholarship Council for Zezhou Li (201508020004). This research was supported by the US Army Research Office programs at UCSD in the 1988-1998 period and by the US National Science Foundation Division of Engineering (Institute for Mechanics and Materials). In the recent past, the support was provided by the UCSD Center for High Energy Density Science (UCOP LAB FEES GRANT ID: LFR-17-449059), the U.S. Department of Energy through grant NNSA/SSAP (DE-NA0002080), and the NNSA/DOE (DE-NA0003842). Support by the Center for Matter under Extreme Pressure Conditions (CMEC) is gratefully acknowledged. Collaborations and discussions with former students and colleagues are greatly appreciated: U.R. Andrade, S. S. Batsanov, J.H. Beatty, E. Cerreta, Y. J. Chen, J. C. La Salvia, J.- M. Ehlers, G.T. Gray, A. Grebe, X. L. Huang, J. Isaacs, B.K. Kad, D. Kong, H. Li, Q. Li, Z. Ling, L.W. Meyer, L. E. Murr, A. Molinari, S. Nemat-Nasser, V.F. Nesterenko, T. Perez-Prado, G. Ravichandran, B. A. Remington, T. Shen, G. Subhash, K.S. Vecchio, S. Walley, Z. G. Wang, C. L. Wittman, B. F. Wang, T. W. Wright, Q. Xue, J. Q. Yu, J.H. Zhang, L. Wang, X.W. Cheng, Z. F. Zhang, S. T. Zhao, and W. L. Zhong.

References

- [1] Recht R. Catastrophic thermoplastic shear. *J Appl Mech* 1964;31:189–93.
- [2] Culver RS. Thermal instability strain in dynamic plastic deformation. *Metallurgical effects at high strain rates*: Springer; 1973. p. 519–30.
- [3] Longo WP, Reed-Hill RE. Work softening in polycrystalline metals. *Scr Metall* 1970;4:765–70.
- [4] Meyers MA. Work softening in shock-loaded nickel. *Metall Trans A* 1977;8:1581–3.
- [5] Baird J. The theory of strain ageing. *Iron Steel* 1963;36:326–34.
- [6] Li CC, Leslie WC. Effects of dynamic strain aging on the subsequent mechanical properties of carbon steels. *Metall Trans A* 1978;9:1765–75.
- [7] Zaretsky E, Kanel GI. Plastic flow in shock-loaded silver at strain rates from 10^4 s^{-1} to 10^7 s^{-1} and temperatures from 296 K to 1233 K. *J Appl Phys* 2011;110:073502.
- [8] El Ters P, Shehadeh MA. Modeling the temperature and high strain rate sensitivity in BCC iron: Atomistically informed multiscale dislocation dynamics simulations. *Int J Plast* 2019;112:257–77.
- [9] Bai Y, Dodd B. *Adiabatic shear localization: occurrence, theories, and applications*. Pergamon Press; 1992.
- [10] Dodd B, Bai Y. *Adiabatic shear localization: frontiers and advances*. Elsevier 2012.
- [11] Dodd B, Bai Y. *Introduction to adiabatic shear localization: Revised Edition*: Imperial College Press; 2014.
- [12] Wright TW. *The physics and mathematics of adiabatic shear bands*. Cambridge University Press; 2002.
- [13] Chen W, Song B, editors. *Split hopkinson (kolsky) bar: design, testing and applications*. Boston, MA: Springer, US; 2011.
- [14] Shukla A, Ravichandran G, Rajapakse YDS, editors. *Dynamic failure of materials and structures*. Boston, MA: Springer, US; 2010.
- [15] Rogers HC. Adiabatic plastic deformation. *Annu Rev Mater Sci* 1979;9:283–311.
- [16] Timothy S. The structure of adiabatic shear bands in metals: a critical review. *Acta Metall* 1987;35:301–6.
- [17] Gilman JJ. Micromechanics of shear banding. *Mech Mater* 1994;17:83–96.
- [18] Klepaczko J. Remarks on impact shearing. *J Mech Phys Solids* 1998;46:2139–53.
- [19] Meyers MA, Nesterenko VF, LaSalvia JC, Xue Q. Shear localization in dynamic deformation of materials: microstructural evolution and self-organization. *Mater Sci Eng, A* 2001;317:204–25.
- [20] Ben-Dor G, Dubinsky A, Elperin T. Ballistic impact: recent advances in analytical modeling of plate penetration dynamics—a review. *Appl Mech Rev* 2005;58:355–71.
- [21] Walley S. Shear localization: a historical overview. *Metall Mater Transactions A* 2007;38:2629–54.
- [22] Armstrong RW, Walley SM. High strain rate properties of metals and alloys. *Int Mater Rev* 2008;53:105–28.
- [23] Xu Y, Zhang J, Bai Y, Meyers MA. Shear localization in dynamic deformation: microstructural evolution. *Metall Mater Trans A* 2008;39:811.
- [24] Greer A, Cheng Y, Ma E. Shear bands in metallic glasses. *Mater Sci Eng R* 2013;74:71–132.
- [25] Antolovich SD, Armstrong RW. Plastic strain localization in metals: origins and consequences. *Prog Mater Sci* 2014;59:1–160.
- [26] Molinari A. Shear band analysis. *Solid State Phenom* 1988;3–4:447–67.
- [27] Salvado FC, Teixeira-Dias F, Walley SM, Lea LJ, Cardoso JB. A review on the strain rate dependency of the dynamic viscoplastic response of FCC metals. *Prog Mater Sci* 2017;88:186–231.
- [28] Tresca MH. On further applications of the flow of solids. *Proc Inst Mech Eng* 1878;29:301–45.
- [29] Massey HF. The flow of metal during forging. *Proc Manchester Assoc Eng* 1921:21–6.
- [30] Johnson W, Baraya GL, Slater RAC. On heat lines or lines of thermal discontinuity. *Int J Mech Sci* 1964;6:409–14.
- [31] Johnson W. Henri Tresca as the originator of adiabatic heat lines. *Int J Mech Sci* 1987;29:301–10.
- [32] Kravz-Tarnavskii VP. A peculiar band discovered in steel (in Russian). *Zeitschrift der Russischen Metallurgischen* 1928;3:162–7.
- [33] Dodd B, Walley SM, Yang R, Nesterenko VF. Major steps in the discovery of adiabatic shear bands. *Metall Mater Trans A* 2015;46:4454–8.
- [34] Taylor GI, Quinney H. The latent energy remaining in a metal after cold working. *Proc Royal Soc A* 1934;143:307–26.
- [35] Davidenko N, Miroslubov I. Eine besondere art der stauchdeformation von stahl: Der krawz-tarnavskij effekt. *Tech Phys USSR* 1935;2:281–98.
- [36] Zener C, Hollomon JH. Effect of strain rate upon plastic flow of steel. *J Appl Phys* 1944;15:22–32.
- [37] Meyers MA, Subhash G, Kad B, Prasad L. Evolution of microstructure and shear-band formation in α -hcp titanium. *Mech Mater* 1994;17:175–93.
- [38] Campbell J, Ferguson W. The temperature and strain-rate dependence of the shear strength of mild steel. *Phil Mag* 1970;21:63–82.
- [39] Argon A. A theory for the low-temperature plastic deformation of glassy polymers. *Phil Mag* 1973;28:839–65.
- [40] Staker M. The relation between adiabatic shear instability strain and material properties. *Acta Metall* 1981;29:683–9.
- [41] Burns T, Trucano T. Instability in simple shear deformations of strain-softening materials. *Mech Mater* 1982;1:313–24.
- [42] Clifton R. Material response to ultra high loading rates. NRC National Material Advisory Board (US). Report 1980;356:129–42.
- [43] Bai Y. A criterion for thermo-plastic shear instability. *Shock waves and high-strain-rate phenomena in metals*. Springer 1981:277–84.
- [44] Bai Y. Thermo-plastic instability in simple shear. *J Mech Phys Solids* 1982;30:195–207.
- [45] Gama BA, Lopatnikov SL, Gillespie JW. Hopkinson bar experimental technique: a critical review. *Appl Mech Rev* 2004;57:223–50.
- [46] Duffy J, Campbell J, Hawley R. On the use of a torsional split Hopkinson bar to study rate effects in 1100–0 aluminum. *J Appl Mech* 1971;38:83–91.
- [47] Davies E, Hunter S. The dynamic compression testing of solids by the method of the split Hopkinson pressure bar. *J Mech Phys Solids* 1963;11:155–79.
- [48] Chandrasekaran H, M'saoubi R, Chazal H. Modelling of material flow stress in chip formation process from orthogonal milling and split Hopkinson bar tests. *Mach Sci Technol* 2005;9:131–45.
- [49] Frew D, Forrestal MJ, Chen W. Pulse shaping techniques for testing brittle materials with a split Hopkinson pressure bar. *Exp Mech* 2002;42:93–106.
- [50] Hartley K, Duffy J, Hawley R. The torsional Kolsky (split-Hopkinson) bar. *ASM metals handbook* 1985;8:218–28.
- [51] Lifshitz J, Leber H. Data processing in the split Hopkinson pressure bar tests. *Int J Impact Eng* 1994;15:723–33.
- [52] Xue Q, Shen L, Bai Y. A modified split Hopkinson torsional bar in studying shear localization. *Meas Sci Technol* 1995;6:1557.
- [53] Zhao H, Gary G, Klepaczko JR. On the use of a viscoelastic split Hopkinson pressure bar. *Int J Impact Eng* 1997;19:319–30.
- [54] Zhao PD, Lu FY, Chen R, Lin YL, Li JL, Lu L, et al. A technique for combined dynamic compression-shear test. *Rev Sci Instrum* 2011;82:035110.
- [55] Nesterenko V, Bondar M. Investigation of deformation localization by the “thick-walled cylinder” method. *DYMAT J* 1994;1:245–51.
- [56] Meyers MA, Nesterenko V, Chen Y, LaSalvia J, Bondar M, Lukyanov Y. High-strain, high-strain-rate deformation of titanium: the thick-walled cylinder method. *Metallurgical and materials applications of shock-wave and high-strain-rate phenomena*. Amsterdam: Elsevier; 1995. p. 487.
- [57] Lovinger Z, Rikanaati A, Rosenberg Z, Rittel D. Electro-magnetic collapse of thick-walled cylinders to investigate spontaneous shear localization. *Int J Impact Eng* 2011;38:918–29.
- [58] Liu M, Li Y, Hu H, Hu X. A numerical model for adiabatic shear bands with application to a thick-walled cylinder in 304 stainless steel. *Modell Simul Mater Sci Eng* 2013;22:015005.
- [59] Jiang M-Q, Huang BM, Jiang ZJ, Lu C, Dai L-H. Joining of bulk metallic glass to brass by thick-walled cylinder explosion. *Scr Mater* 2015;97:17–20.
- [60] Nesterenko V. Localization of deformation in collapse of a thick walled cylinder. *Combustion, Explosion and Shock Waves* 1994;30:500–9.
- [61] Kad BK, Schoenfeld SE, Burkins MS. Through thickness dynamic impact response in textured Ti-6Al-4V plates. *Mater Sci Eng, A* 2002;322:241–51.
- [62] Me-Bar Y, Shechtman D. On the adiabatic shear of Ti-6Al-4V ballistic targets. *Mater Sci Eng* 1983;58:181–8.
- [63] Mangelino S, Abbott K. Metallurgical factors affecting the ballistic behavior of steel targets. *J Mater* 1972;7:231–9.
- [64] Sangoy L, Meunier Y, Pont G. Steels for ballistic protection. *Israel J Technol* 1988;24:319–26.
- [65] Meyer Jr HW, Kleponis DS. Modeling the high strain rate behavior of titanium undergoing ballistic impact and penetration. *Int J Impact Eng* 2001;26:509–21.
- [66] Murr L, Ramirez A, Gaytan S, Lopez M, Martinez E, Hernandez D, et al. Microstructure evolution associated with adiabatic shear bands and shear band failure in ballistic plug formation in Ti-6Al-4V targets. *Mater Sci Eng, A* 2009;516:205–16.
- [67] Iqbal M, Gupta G, Diwakar A, Gupta N. Effect of projectile nose shape on the ballistic resistance of ductile targets. *Eur J Mech-A/Solids* 2010;29:683–94.

- [68] Zou D, Zhen L, Xu C, Shao W. Characterization of adiabatic shear bands in AM60B magnesium alloy under ballistic impact. *Mater Charact* 2011;62:496–502.
- [69] O'Donnell RG, Woodward RL. Instability during high strain rate compression of 2024 T351 aluminium. *J Mater Sci* 1988;23:3578–87.
- [70] Altenaïji M, Guan ZW, Cantwell WJ, Zhao Y, Schleyer GK. Characterisation of aluminium matrix syntactic foams under drop weight impact. *Mater Des* 2014;59:296–302.
- [71] Wong EH, Selvanayagam CS, Seah SKW. al. e. Stress–strain characteristics of tin-based solder alloys at medium strain rate. *Mater Lett* 2008;62:3031–4.
- [72] Remington TP, Remington BA, Hahn EN, Meyers MA. Deformation and failure in extreme regimes by high-energy pulsed lasers: A review. *Mater Sci Eng, A* 2017;688:429–58.
- [73] Fairand B, Clauer A. Laser generation of high-amplitude stress waves in materials. *J Appl Phys* 1979;50:1497–502.
- [74] Clauer AH, Holbrook JH, Fairand BP. Effects of laser induced shock waves on metals. In: *Shock waves and high-strain-rate phenomena in metals*. Springer; 1981. p. 675–702.
- [75] Zhao S, Kad B, Wehrenberg CE, Remington BA, Hahn EN, More KL, et al. Generating gradient germanium nanostructures by shock-induced amorphization and crystallization. *Proc Natl Acad Sci* 2017;114:9791–6.
- [76] Zhao S, Kad B, Remington BA, LaSalvia JC, Wehrenberg CE, Behler KD, et al. Directional amorphization of boron carbide subjected to laser shock compression. *Proc Natl Acad Sci* 2016;113:12088–93.
- [77] Zhao S, Flanagan R, Hahn EN, Kad B, Remington BA, Wehrenberg CE, et al. Shock-induced amorphization in silicon carbide. *Acta Mater* 2018;158:206–13.
- [78] Zhang QB, Zhao J. A review of dynamic experimental techniques and mechanical behaviour of rock materials. *Rock Mech Rock Eng* 2014;47:1411–78.
- [79] Xu Y, Zhong W, Chen Y, Shen L, Liu Q, Bai Y, et al. Shear localization and recrystallization in dynamic deformation of 8090 Al–Li alloy. *Mater Sci Eng, A* 2001;299:287–95.
- [80] Li Z, Zhao S, Diao H, Liaw P, Meyers MA. High-velocity deformation of Al_{0.3}CoCrFeNi high-entropy alloy: Remarkable resistance to shear failure. *Sci Rep* 2017;7:42742.
- [81] Li Z, Wang B, Zhao S, Valiev RZ, Vecchio KS, Meyers MA. Dynamic deformation and failure of ultrafine-grained titanium. *Acta Mater* 2017;125:210–8.
- [82] Mishra A, Martin M, Thadhani N, Kad B, Kenik EA, Meyers MA. High-strain-rate response of ultra-fine-grained copper. *Acta Mater* 2008;56:2770–83.
- [83] Xu Y, Bai Y, Meyers MA. Deformation, phase transformation and recrystallization in the shear bands induced by high-strain rate loading in titanium and its alloys. *J Mater Sci Technol* 2006;22:737–46.
- [84] Yang Y, Luo S, Hu H, Tang T, Zhang Q. Diffusive transformation at high strain rate: On instantaneous dissolution of precipitates in aluminum alloy during adiabatic shear deformation. *J Mater Res* 2016;31:1220–8.
- [85] Yang Y, Chen Y, Jiang L, Li M, Zhang Q, Tang T. Study on the characteristics and thermal stability of nanostructures in adiabatic shear band of 2195 Al–Li alloy. *Appl Phys A* 2015;121:1277–84.
- [86] Jiang Y, Chen Z, Zhan C, Chen T, Wang R, Liu C. Adiabatic shear localization in pure titanium deformed by dynamic loading: Microstructure and microtexture characteristic. *Mater Sci Eng, A* 2015;640:436–42.
- [87] Wang BF, Yang Y. Microstructure evolution in adiabatic shear band in fine-grain-sized Ti–3Al–5Mo–4.5V alloy. *Mater Sci Eng, A* 2008;473:306–11.
- [88] Hopkinson J. Further experiments on the rupture of iron wire. *Proc Literary and Philosophical Society of Manchester* 1872;1:119–21.
- [89] Hopkinson B. A method of measuring the pressure produced in the detonation of high explosives or by the impact of bullets. *Philos T R Soc A* 1914;213:437–56.
- [90] Kolsky H. An investigation of the mechanical properties of materials at very high rates of loading. *Proc Phys Soc Sect B* 1949;62:676.
- [91] Davies R. A critical study of the Hopkinson pressure bar. *Philos T R Soc A* 1948;240:375–457.
- [92] Hauser FE. Techniques for measuring stress-strain relations at high strain rates. *Exp Mech* 1966;6:395–402.
- [93] Lindholm U, Yeakley L. High strain-rate testing: tension and compression. *Exp Mech* 1968;8:1–9.
- [94] Chiddister J, Malvern L. Compression-impact testing of aluminum at elevated temperatures. *Exp Mech* 1963;3:81–90.
- [95] Harding J, Welsh LM. A tensile testing technique for fibre-reinforced composites at impact rates of strain. *J Mater Sci* 1983;18:1810–26.
- [96] Dunand M, Gary G, Mohr D. Load-inversion device for the high strain rate tensile testing of sheet materials with Hopkinson pressure bars. *Exp Mech* 2013;53:1177–88.
- [97] Roth CC, Gary G, Mohr D. Compact SHPB system for intermediate and high strain rate plasticity and fracture testing of sheet metal. *Exp Mech* 2015;55:1803–11.
- [98] Nemat-Nasser S, Isaacs JB, Starrett JE. Hopkinson techniques for dynamic recovery experiments. *Proceedings of the Royal Society of London Series A: Mathematical and Physical Sciences*. 1991;435:371–91.
- [99] Baker WE, Yew C. Strain-rate effects in the propagation of torsional plastic waves. *J Appl Mech* 1966;33:917–23.
- [100] Xue Q, Shen L, Bai Y. Elimination of loading reverberation in the split Hopkinson torsional bar. *Rev Sci Instrum* 1995;66:5298–304.
- [101] Marchand A, Duffy J. An experimental study of the formation process of adiabatic shear bands in a structural steel. *J Mech Phys Solids* 1988;36:251–83.
- [102] Bai Y, Xue Q, Xu Y, Shen L. Characteristics and microstructure in the evolution of shear localization in Ti-6Al-4V alloy. *Mech Mater* 1994;17:155–64.
- [103] Chichili D, Ramesh K. Recovery experiments for adiabatic shear localization: a novel experimental technique. *J Appl Mech* 1999;66:10–20.
- [104] Zhang X, Cui J, Li GY. Microstructural mechanism in adiabatic shear bands of Al–Cu alloy bars using electromagnetic impact upsetting. *Mater Lett* 2017;194:62–5.
- [105] Meyers MA, Andrade UR, Chokshi AH. The effect of grain size on the high-strain, high-strain-rate behavior of copper. *Metall Mater Trans A* 1995;26:2881–93.
- [106] Meyers MA, Xu Y, Xue Q, Perez-Prado M, McNelley T. Microstructural evolution in adiabatic shear localization in stainless steel. *Acta Mater* 2003;51:1307–25.
- [107] Mishra B, Mondal C, Goyal R, Ghosal P, Kumar KS, Madhu V. Plastic flow behavior of 7017 and 7055 aluminum alloys under different high strain rate test methods. *Mater Sci Eng A* 2014;612:343–53.
- [108] Andrade U, Meyers MA, Vecchio K, Chokshi A. Dynamic recrystallization in high-strain, high-strain-rate plastic deformation of copper. *Acta Metall Mater* 1994;42:3183–95.
- [109] Peirs J, Tirry W, Amin-Ahmadi B, Coghe F, Verleysen P, Rabet L, et al. Microstructure of adiabatic shear bands in Ti-6Al-4V. *Mater Charact* 2013;75:79–92.
- [110] Klepaczko J. An experimental technique for shear testing at high and very high strain rates. The case of a mild steel. *Int J Impact Eng* 1994;15:25–39.
- [111] Glema A, Lodygowski T, Sumelka W. Nowacki's double shear test in the framework of the anisotropic thermo-elasto-viscoplastic material model. *J Theoretical Appl Mech* 2010;48:973–1001.
- [112] Li Q, Jones N. Response and failure of a double-shear beam subjected to mass impact. *Int J Solids Struct* 2002;39:1919–47.
- [113] Kalthoff JF. Transition in the failure behavior of dynamically shear loaded cracks. *Appl Mech Rev* 1990;43:S247–50.
- [114] Kalthoff JF. Modes of dynamic shear failure in solids. *Int J Fract* 2000;101:1–31.
- [115] Zhou M, Rosakis A, Ravichandran G. Dynamically propagating shear bands in impact-loaded prenotched plates—I. Experimental investigations of temperature signatures and propagation speed. *J Mech Phys Solids* 1996;44:981–1006.
- [116] Zhou M, Ravichandran G, Rosakis A. Dynamically propagating shear bands in impact-loaded prenotched plates—II. Numerical simulations. *J Mech Phys Solids* 1996;44:1007–32.
- [117] Gray GT, Vecchio KS, Livescu V. Compact forced simple-shear sample for studying shear localization in materials. *Acta Mater* 2016;103:12–22.
- [118] Dowling A. The dynamic punching of metals. *J Inst Met* 1970;98:215–24.
- [119] Maaß R, Samwer K, Arnold W, Volkert C. A single shear band in a metallic glass: Local core and wide soft zone. *Appl Phys Lett* 2014;105:171902.
- [120] Clifton RJ, Klopp RW. Pressure-shear plate impact testing *Metals handbook* 1985;8:230–9.
- [121] Rittel D, Lee S, Ravichandran G. A shear-compression specimen for large strain testing. *Exp Mech* 2002;42:58–64.
- [122] Dorogoy A, Rittel D, Godinger A. Modification of the shear-compression specimen for large strain testing. *Exp Mech* 2015;55:1627–39.
- [123] Lee WS, Sue WC, Lin CF, Wu CJ. The strain rate and temperature dependence of the dynamic impact properties of 7075 aluminum alloy. *J Mater Process Technol* 2000;100:116–22.
- [124] Kad BK, Gebert JM, Perez-Prado MT, Kassner ME, Meyers MA. Ultrafine-grain-sized zirconium by dynamic deformation. *Acta Mater* 2006;54:4111–27.

- [125] Wang B, Huang X, Liu Y, Liu B. Mechanical properties and shear localization of high entropy alloy CoCrFeMnNi prepared by powder metallurgy. TMS Annual Meeting & Exhibition: Springer 2018:469–80.
- [126] Walley S, Radford D, Chapman D. The effect of aspect ratio on the compressive high rate deformation of three metallic alloys. Journal de Physique IV (Proceedings): EDP sciences 2006:851–6.
- [127] Siviour CR, Walley SM. Inertial and frictional effects in dynamic compression testing. In: Othman R, editor. The Kolsky-Hopkinson bar machine: selected topics. Cham: Springer International Publishing; 2018. p. 205–47.
- [128] Dougherty L, Cerreta E, Gray G, Trujillo C, Lopez M, Vecchio K, et al. Mechanical behavior and microstructural development of low-carbon steel and microcomposite steel reinforcement bars deformed under quasi-static and dynamic shear loading. Metall Mater Trans A 2009;40:1835–50.
- [129] Xue Q, Liao X, Zhu Y, Gray G. Formation mechanisms of nanostructures in stainless steel during high-strain-rate severe plastic deformation. Mater Sci Eng, A 2005;410:252–6.
- [130] Cerreta E, Frank I, Gray G, Trujillo C, Korzekwa D, Dougherty L. The influence of microstructure on the mechanical response of copper in shear. Mater Sci Eng A 2009;501:207–19.
- [131] Cerreta E, Bingert J, Gray G, Trujillo C, Lopez M, Bronkhorst C, et al. Microstructural examination of quasi-static and dynamic shear in high-purity iron. Int J Plast 2013;40:23–38.
- [132] Meyer L, Manwaring S. Critical adiabatic shear strength of low alloyed steel under compressive loading. In: International Conference on Metallurgical Applications of Shock-Wave and High-Strain-Rate Phenomena (EXPLOMET85); 1985. p. 657-74.
- [133] Peirs J, Verleysen P, Degrieck J, Coghe F. The use of hat-shaped specimens to study the high strain rate shear behaviour of Ti–6Al–4V. Int J Impact Eng 2010; 37:703–14.
- [134] Nemat-Nasser S, Isaacs JB, Liu MQ. Microstructure of high-strain, high-strain-rate deformed tantalum. Acta Mater 1998;46:1307–25.
- [135] Chen YJ, Meyers MA, Nesterenko VF. Spontaneous and forced shear localization in high-strain-rate deformation of tantalum. Mater Sci Eng A 1999;268:70–82.
- [136] Xue Q, Gray GT. Development of adiabatic shear bands in annealed 316L stainless steel: Part I. Correlation between evolving microstructure and mechanical behavior. Metall Mater Trans A 2006;37:2435–46.
- [137] Xue Q, Cerreta E, Gray G. Microstructural characteristics of post-shear localization in cold-rolled 316L stainless steel. Acta Mater 2007;55:691–704.
- [138] Bronkhorst C, Cerreta E, Xue Q, Maudlin P, Mason T, Gray Iii G. An experimental and numerical study of the localization behavior of tantalum and stainless steel. Int J Plast 2006;22:1304–35.
- [139] Li J, Suo T, Huang C, Li Y, Wang H, Liu J. Adiabatic shear localization in nanostructured face centered cubic metals under uniaxial compression. Mater Des 2016;105:262–7.
- [140] Wang Z, Chen Z, Zhan C, Kuang L, Shao J, Wang R, et al. Quasi-static and dynamic forced shear deformation behaviors of Ti-5Mo-5V-8Cr-3Al alloy. Mater Sci Eng A 2017;691:51–9.
- [141] Meyer LW, Halle T. Shear strength and shear failure, overview of testing and behavior of ductile metals. Mech Time-Dependent Mater 2011;15:327–40.
- [142] Li Q, Xu Y, Lai Z, Shen L, Bai Y. Dynamic recrystallization induced by plastic deformation at high strain rate in a Monel alloy. Mater Sci Eng A 2000;276:250–6.
- [143] Hartmann KH, Kunze HD, Meyer LW. Metallurgical effects on impact loaded materials. In: Shock waves and high-strain-rate phenomena in metals. Springer; 1981. p. 325–37.
- [144] Liu L, Dai L, Bai Y, Wei B. Initiation and propagation of shear bands in Zr-based bulk metallic glass under quasi-static and dynamic shear loadings. J Non-Cryst Solids 2005;351:3259–70.
- [145] Zhu C, Harrington T, Livescu V, Gray GT, Vecchio KS. Determination of geometrically necessary dislocations in large shear strain localization in aluminum. Acta Mater 2016;118:383–94.
- [146] Vural M, Ravichandran G, Rittel D. Large strain mechanical behavior of 1018 cold-rolled steel over a wide range of strain rates. Metall Mater Trans A 2003;34: 2873–85.
- [147] Dorogoy A, Rittel D, Godinger A. A shear-tension specimen for large strain testing. Exp Mech 2016;56:437–49.
- [148] Oussouaddi O, Klepaczko J. Analysis of transition from isothermal to adiabatic deformation in the case of a twisted tube. J Phys 1991;III(1):323–30.
- [149] Xu Z, Ding X, Zhang W, Huang F. A novel method in dynamic shear testing of bulk materials using the traditional SHPB technique. Int J Impact Eng 2017;101: 90–104.
- [150] Xu Z, Liu Y, Sun Z, Hu H, Huang F. On shear failure behaviors of an armor steel over a large range of strain rates. Int J Impact Eng 2018;118:24–38.
- [151] Hudspeth M, Claus B, Dubelman S, Black J, Mondal A, Parab N, et al. High speed synchrotron x-ray phase contrast imaging of dynamic material response to split Hopkinson bar loading. Rev Sci Instrum 2013;84:025102.
- [152] Chen WW, Hudspeth MC, Claus B, Parab ND, Black JT, Fezzaa K, et al. In situ damage assessment using synchrotron X-rays in materials loaded by a Hopkinson bar. Philos T R Soc 2014;372:20130191.
- [153] Guduru P, Rosakis A, Ravichandran G. Dynamic shear bands: an investigation using high speed optical and infrared diagnostics. Mech Mater 2001;33:371–402.
- [154] Nie Y, Claus B, Gao J, Zhai X, Kedir N, Chu J, et al. In situ observation of adiabatic shear band formation in aluminum alloys. Exp Mech 2020;60:153–63.
- [155] Shockey D, Erlich D. Metallurgical influences on shear band activity. In: Meyers MA, Murr LE, editors. Shock waves and high-strain-rate phenomena in metals. Springer; 1981. p. 249–61.
- [156] Yang Y, Zheng H, Zhao Z, Zhang Q, Zhang Q, Jiang F, et al. Effect of phase composition on self-organization of shear bands in Ti-1300 titanium alloy. Mater Sci Eng A 2011;528:7506–13.
- [157] Xue Q, Nesterenko VF, Meyers MA. Evaluation of the collapsing thick-walled cylinder technique for shear-band spacing. Int J Impact Eng 2003;28:257–80.
- [158] Nesterenko V, Meyers MA, Wright T. Self-organization in the initiation of adiabatic shear bands. Acta Mater 1998;46:327–40.
- [159] Stokes J, Nesterenko V, Shlachter J, Fulton R, Indrakanti S, Gu Y. Comparative behavior of Ti and 304 stainless steel in a magnetically-driven implosion at the Pegasus-II facility. Fundamental issues and applications of shock-wave and high-strain-rate phenomena,(Proceedings of the EXPLOMET'2000). New York: Elsevier Science Ltd.; 2001. p. 585–92.
- [160] Grady D. Dissipation in adiabatic shear bands. Mech Mater 1994;17:289–93.
- [161] Grady D, Kipp M. The growth of unstable thermoplastic shear with application to steady-wave shock compression in solids. J Mech Phys Solids 1987;35: 95–119.
- [162] Wright T, Ockendon H. A scaling law for the effect of inertia on the formation of adiabatic shear bands. Int J Plast 1996;12:927–34.
- [163] Molinari A. Collective behavior and spacing of adiabatic shear bands. J Mech Phys Solids 1997;45:1551–75.
- [164] Mott NF, Linfoot EH. A Theory of Fragmentation. Fragmentation of Rings and Shells: The Legacy of NF Mott. Berlin, Heidelberg: Springer Berlin Heidelberg; 2006. p. 207–25.
- [165] Mott NF, Grady Fragmentation of DHE. Shells: a Theoretical Formula for the Distribution of Weights of Fragments. In: Grady D, editor. Fragmentation of Rings and Shells. Springer; 2006. p. 227–41.
- [166] Mott NF. A Theory of the Fragmentation of Shells and Bombs. In: Grady D, editor. Fragmentation of Rings and Shells: The Legacy of NF Mott. Berlin, Heidelberg: Springer; 2006. p. 243–94.
- [167] Mott NF. Fragmentation of shell casings and the theory of rupture in metals. In: Grady D, editor. Fragmentation of rings and shells: The legacy of NF mott. Berlin, Heidelberg: Springer; 2006. p. 295–325.
- [168] Mott NF. A theory of fragmentation: application to wire wound bombs such as the American 20 lb, F. In: Grady D, editor. Fragmentation of rings and shells: The legacy of NF Mott. Berlin, Heidelberg: Springer; 2006. p. 327–48.
- [169] Mott NF. Fragmentation of shell cases. Proc Roy Soc London A 1947;189:300–8.
- [170] Liu J, Fan Q, Cai H, Wang F. Underlying mechanism of periodical adiabatic shear bands generated in Ti–6Al–4V target by projectile impact. Mater Des 2015; 87:231–7.
- [171] DeMange JJ, Prakash V, Pereira JM. Effects of material microstructure on blunt projectile penetration of a nickel-based super alloy. Int J Impact Eng 2009;36: 1027–43.

- [172] Chen X, Zhou X, Li X. On perforation of ductile metallic plates by blunt rigid projectile. *Eur J Mech-A/Solids* 2009;28:273–83.
- [173] Zaid A, El-Kalay A, Travis F. An examination of the perforation of a mild steel plate by a flat-ended cylindrical projectile. *Int J Mech Sci* 1973;15:129–43.
- [174] Jenq S, Goldsmith W, Kelly J. Effect of target bending in normal impact of a flat-ended cylindrical projectile near the ballistic limit. *Int J Solids Struct* 1988;24:1243–66.
- [175] Rusinek A, Rodríguez-Martínez JA, Arias A, Klepaczko JR, López-Puente J. Influence of conical projectile diameter on perpendicular impact of thin steel plate. *Eng Fract Mech* 2008;75:2946–67.
- [176] Rodríguez-Millán M, Vaz-Romero A, Rusinek A, Rodríguez-Martínez J, Arias A. Experimental study on the perforation process of 5754–H111 and 6082–T6 aluminium plates subjected to normal impact by conical, hemispherical and blunt projectiles. *Exp Mech* 2014;54:729–42.
- [177] Rodríguez-Martínez JA, Rusinek A, Pesci R, Zaera R. Experimental and numerical analysis of the martensitic transformation in AISI 304 steel sheets subjected to perforation by conical and hemispherical projectiles. *Int J Solids Struct* 2013;50:339–51.
- [178] Arias A, Rodríguez-Martínez JA, Rusinek A. Numerical simulations of impact behaviour of thin steel plates subjected to cylindrical, conical and hemispherical non-deformable projectiles. *Eng Fract Mech* 2008;75:1635–56.
- [179] Meyers MA, Wittman CL. Effect of metallurgical parameters on shear band formation in low-carbon (~ 0.20 Wt Pct) steels. *Metall Trans A* 1990;21:3153–64.
- [180] Solberg JK, Leinun JR, Embury JD, Dey S, Børvik T, Hopperstad OS. Localised shear banding in Weldox steel plates impacted by projectiles. *Mech Mater* 2007;39:865–80.
- [181] Craig J, Stock T. Microstructural damage adjacent to bullet holes in 70–30 brass. *J Aust Inst Met* 1970;15:1–5.
- [182] Kalthoff JF, Winkler S. Failure mode transition at high rates of shear loading. *Impact Loading and Dynamic Behavior of Materials* 1987;1:185–95.
- [183] Kalthoff JF. Shadow optical analysis of dynamic shear fracture. *Opt Eng* 1988;27:271035.
- [184] Gu L, Kang G, Chen H, Wang M. On adiabatic shear fracture in high-speed machining of martensitic precipitation-hardening stainless steel. *J Mater Process Technol* 2016;234:208–16.
- [185] Hou ZB, Komanduri R. Modeling of thermomechanical shear instability in machining. *Int J Mech Sci* 1997;39:1273–314.
- [186] Bakkal M, Shih AJ, Scattergood RO, Liu C. Machining of a Zr–Ti–Al–Cu–Ni metallic glass. *Scr Mater* 2004;50:583–8.
- [187] Velásquez JP, Bolle B, Chevrier P, Geandier G, Tidu A. Metallurgical study on chips obtained by high speed machining of a Ti–6 wt.% Al–4 wt.% V alloy. *Mater Sci Eng A* 2007;452:469–74.
- [188] Molinari A, Musquar C, Sutter G. Adiabatic shear banding in high speed machining of Ti–6Al–4V: experiments and modeling. *Int J Plast* 2002;18:443–59.
- [189] Achouri M, Germain G, Dal Santo P, Saidane D. Experimental and numerical analysis of micromechanical damage in the punching process for High-Strength Low-Alloy steels. *Mater Des* 2014;56:657–70.
- [190] Sedgwick R, Hageman L, Herrmann R, Waddell J. Numerical investigations in penetration mechanics. *Int J Eng Sci* 1978;16:859–69.
- [191] Kennedy C, Murr LE. Comparison of tungsten heavy-alloy rod penetration into ductile and hard metal targets: microstructural analysis and computer simulations. *Mater Sci Eng A* 2002;325:131–43.
- [192] Stock T, Thompson K. Penetration of aluminum alloys by projectiles. *Metallurgical Transactions* 1970;1:219–24.
- [193] Semiatin S, Lahoti G. Deformation and unstable flow in hot forging of Ti–6Al–2Sn–4Zr–2Mo–0.1Si. *Metall Trans A* 1981;12:1705–17.
- [194] Park NK, Yeom JT, Na YS. Characterization of deformation stability in hot forging of conventional Ti–6Al–4V using processing maps. *J Mater Process Technol* 2002;130:540–5.
- [195] Xue W, Gao S, Duan D, Liu Y, Li S. Material transfer behaviour between a Ti6Al4V blade and an aluminium hexagonal boron nitride abrasible coating during high-speed rubbing. *Wear* 2015;322:76–90.
- [196] Correa E, Alcántara N, Valeriano L, Barbedo N, Chaves R. The effect of microstructure on abrasive wear of a Fe–Cr–C–Nb hardfacing alloy deposited by the open arc welding process. *Surf Coat Technol* 2015;276:479–84.
- [197] Meyers MA. *Dynamic behavior of materials*. John Wiley & Sons 1994.
- [198] Komanduri R, Von Turkovich BF. New observations on the mechanism of chip formation when machining titanium alloys. *Wear* 1981;69:179–88.
- [199] Ye G, Xue S, Jiang M, Tong X, Dai L. Modeling periodic adiabatic shear band evolution during high speed machining Ti–6Al–4V alloy. *Int J Plast* 2013;40:39–55.
- [200] Barry J, Byrne G. The mechanisms of chip formation in machining hardened steels. *J Manuf Sci Eng* 2002;124:528–35.
- [201] Dong G, Zhaopeng H, Rongdi H, Yanli C, Muguthu JN. Study of cutting deformation in machining nickel-based alloy Inconel 718. *Int J Mach Tools Manuf* 2011;51:520–7.
- [202] Bakkal M, Shih AJ, Scattergood RO. Chip formation, cutting forces, and tool wear in turning of Zr-based bulk metallic glass. *Int J Mach Tools Manuf* 2004;44:915–25.
- [203] Burns TJ, Davies MA. On repeated adiabatic shear band formation during high-speed machining. *Int J Plast* 2002;18:487–506.
- [204] Chen G, Ren C, Yang X, Jin X, Guo T. Finite element simulation of high-speed machining of titanium alloy (Ti–6Al–4V) based on ductile failure model. *The Int J Adv Manuf Technol* 2011;56:1027–38.
- [205] Calamaz M, Coupard D, Girof F. A new material model for 2D numerical simulation of serrated chip formation when machining titanium alloy Ti–6Al–4V. *Int J Mach Tools Manuf* 2008;48:275–88.
- [206] Molinari A, Cherguene R, Miguélez H. Numerical and analytical modeling of orthogonal cutting: the link between local variables and global contact characteristics. *Int J Mech Sci* 2011;53:183–206.
- [207] Molinari A, Cherguene R, Miguélez H. Contact variables and thermal effects at the tool–chip interface in orthogonal cutting. *Int J Solids Struct* 2012;49:3774–96.
- [208] Molinari A, Soldani X, Miguélez M. Adiabatic shear banding and scaling laws in chip formation with application to cutting of Ti–6Al–4V. *J Mech Phys Solids* 2013;61:2331–59.
- [209] Field JE, Walley SM, Proud WG, Goldrein HT, Siviour CR. Review of experimental techniques for high rate deformation and shock studies. *Int J Impact Eng* 2004;30:725–75.
- [210] Gebbeken N, Greulich S, Pietzsch A. Hugoniot properties for concrete determined by full-scale detonation experiments and flyer-plate-impact tests. *Int J Impact Eng* 2006;32:2017–31.
- [211] Zhao S, Kad B, Hahn E, Remington BA, Wehrenberg C, Huntington C, et al. Pressure and shear-induced amorphization of silicon. *Extreme Mech Lett* 2015;5:74–80.
- [212] Platt JP, Behr WM. Grain size evolution in ductile shear zones: Implications for strain localization and the strength of the lithosphere. *J Struct Geol* 2011;33:537–50.
- [213] Platt JP. Influence of shear heating on microstructurally defined plate boundary shear zones. *J Struct Geol* 2015;79:80–9.
- [214] Platt JP, De Bresser JHP. Stress dependence of microstructures in experimentally deformed calcite. *J Struct Geol* 2017;105:80–7.
- [215] Cross AJ, Skemer P. Rates of dynamic recrystallization in geologic materials. *J Geophys Res Solid Earth* 2019;124:1324–42.
- [216] Andò E, Hall SA, Viggiani G, Desrues J, Bésuelle P. Grain-scale experimental investigation of localised deformation in sand: a discrete particle tracking approach. *Acta Geotech* 2012;7:1–13.
- [217] LaRouche S, Mikkola D. Shock hardening behavior of Cu–8.7 Ge at very short pulse durations. *Scr Metall* 1978;12:543–7.
- [218] Costin LS, Duffy J. The effect of loading rate and temperature on the initiation of fracture in a mild, rate-sensitive steel. *J Eng Mater Technol* 1979;101:258–64.
- [219] Hartley K, Duffy J, Hawley R. Measurement of the temperature profile during shear band formation in steels deforming at high strain rates. *J Mech Phys Solids* 1987;35:283–301.
- [220] Ranc N, Taravella L, Pina V, Herve P. Temperature field measurement in titanium alloy during high strain rate loading-Adiabatic shear bands phenomenon. *Mech Mater* 2008;40:255–70.
- [221] Liu J, Shim VPW. La-based bulk metallic glass failure analysis under static and dynamic loading. *Int J Impact Eng* 2013;60:37–43.
- [222] Giovanola JH. Adiabatic shear banding under pure shear loading Part I: direct observation of strain localization and energy-dissipation measurements. *Mech Mater* 1988;7:59–71.

- [223] Benzing JT, Poling WA, Pierce DT, Bentley J, Findley KO, Raabe D, et al. Effects of strain rate on mechanical properties and deformation behavior of an austenitic Fe-25Mn-3Al-3Si TWIP-TRIP steel. *Mater Sci Eng A* 2018;711:78–92.
- [224] Wu S, Bie B, Fan D, Sun T, Fezzaa K, Feng Z, et al. Dynamic shear localization of a titanium alloy under high-rate tension characterized by x-ray digital image correlation. *Mater Charact* 2018;137:58–66.
- [225] Guo Y, Ruan Q, Zhu S, Wei Q, Chen HS, Lu J, et al. Temperature rise associated with adiabatic shear band: causality clarified. *Phys Rev Lett* 2019;122:015503.
- [226] Shih CJ, Nesterenko VF, Meyers MA. High-strain-rate deformation and comminution of silicon carbide. *J Appl Phys* 1998;83:4660–71.
- [227] Shih CJ, Meyers MA, Nesterenko VF. High-strain-rate deformation of granular silicon carbide. *Acta Mater* 1998;46:4037–65.
- [228] Lindholm US. Review of dynamic testing techniques and material behaviour. Oxford: publisher; 1974. p. 3–21.
- [229] Clifton R, Duffey J, Hartley K, Shawki T. On critical conditions for shear band formation at high strain rates. *Scr Metall* 1984;18:443–8.
- [230] Chen Y, Ghosh S. Micromechanical analysis of strain rate-dependent deformation and failure in composite microstructures under dynamic loading conditions. *Int J Plast* 2012;32:218–47.
- [231] Khan AS, Suh YS, Kazmi R. Quasi-static and dynamic loading responses and constitutive modeling of titanium alloys. *Int J Plast* 2004;20:2233–48.
- [232] Chichili D, Ramesh K, Hemker K. The high-strain-rate response of alpha-titanium: experiments, deformation mechanisms and modeling. *Acta Mater* 1998;46:1025–43.
- [233] Follansbee P, Gray G. An analysis of the low temperature, low and high strain-rate deformation of Ti–6Al–4V. *Metall Trans A* 1989;20:863–74.
- [234] Rosakis P, Rosakis A, Ravichandran G, Hodowany J. A thermodynamic internal variable model for the partition of plastic work into heat and stored energy in metals. *J Mech Phys Solids* 2000;48:581–607.
- [235] Austin RA, McDowell DL. A dislocation-based constitutive model for viscoplastic deformation of fcc metals at very high strain rates. *Int J Plast* 2011;27:1–24.
- [236] Clayton J. Dynamic plasticity and fracture in high density polycrystals: constitutive modeling and numerical simulation. *J Mech Phys Solids* 2005;53:261–301.
- [237] Lloyd J, Clayton J, Becker R, McDowell D. Simulation of shock wave propagation in single crystal and polycrystalline aluminum. *Int J Plast* 2014;60:118–44.
- [238] Armstrong RW, Coffey CS, Elban WL. Adiabatic heating at a dislocation pile-up avalanche. *Acta Metall* 1982;30:2111–6.
- [239] Armstrong RW, Zerilli FJ. Dislocation mechanics aspects of plastic instability and shear banding. *Mech Mater* 1994;17:319–27.
- [240] Mason JJ, Rosakis AJ, Ravichandran G. On the strain and strain rate dependence of the fraction of plastic work converted to heat: an experimental study using high speed infrared detectors and the Kolsky bar. *Mech Mater* 1994;17:135–45.
- [241] Smith JL, Seidt JD, Gilat A. Full-Field Determination of the Taylor-Quinney Coefficient in Tension Tests of Ti-6Al-4V at Strain Rates up to 7000 s⁻¹. In: Lamberti L, Lin MT, Furlong C, Sciammarella C, Reu PL, Sutton MA, editors. *Advancement of Optical Methods & Digital Image Correlation in Experimental Mechanics*. Cham: Springer International Publishing; 2019. p. 133–9.
- [242] Shawki T, Clifton R, Majda G. Analysis of Shear Strain Localization in Thermal Visco-Plastic Materials. *Brown Univ Providence Ri Div Of. Engineering* 1983.
- [243] Molinari A, Clifton R. Analytical characterization of shear localization in thermoviscoplastic materials. *J Appl Mech* 1987;54:806–12.
- [244] Burns TJ. Approximate linear stability analysis of a model of adiabatic shear band formation. *Q Appl Math* 1985;43:65–84.
- [245] Anand L, Kim K, Shawki T. Onset of shear localization in viscoplastic solids. *J Mech Phys Solids* 1987;35:407–29.
- [246] Wright TW, Batra RC. The initiation and growth of adiabatic shear bands. *Int J Plast* 1985;1:205–12.
- [247] Wright TW, Batra RC. Further results on the initiation and growth of adiabatic shear bands at high strain rates. *Le Journal de Physique Colloques* 1985;46:C5–323-330.
- [248] Wright TW, Walter JW. On stress collapse in adiabatic shear bands. *J Mech Phys Solids* 1987;35:701–20.
- [249] Wright TW. Approximate analysis for the formation of adiabatic shear bands. *J Mech Phys Solids* 1990;38:515–30.
- [250] Fressengeas C, Molinari A. Instability and localization of plastic flow in shear at high strain rates. *J Mech Phys Solids* 1987;35:185–211.
- [251] Xu Y, Bai Y, Xue Q, Shen L. Formation, microstructure and development of the localized shear deformation in low-carbon steels. *Acta Mater* 1996;44:1917–26.
- [252] Flockhart C, Woodward R, Lam Y, O'donnell R. The use of velocity discontinuities to define shear failure trajectories in dynamic plastic deformation. *Int J Impact Eng* 1991;11:93–106.
- [253] Xing D, Bai YL, Chen CM, Huang XL. On post-instability processes in adiabatic shear in hot rolled steel. *J Mech Phys Solids* 1991;39:1017–42.
- [254] Schoenfeld SE, Kad B. Texture effects on shear response in Ti–6Al–4V plates. *Int J Plast* 2002;18:461–86.
- [255] Clayton JD. Modeling effects of crystalline microstructure, energy storage mechanisms, and residual volume changes on penetration resistance of precipitate-hardened aluminum alloys. *Compos Part B-Eng* 2009;40:443–50.
- [256] Dolinski M, Rittel D, Dorogoy A. Modeling adiabatic shear failure from energy considerations. *J Mech Phys Solids* 2010;58:1759–75.
- [257] Kuriyama S, Meyers MA. Numerical modeling of the propagation of an adiabatic shear band. *Metall Trans A* 1986;17:443.
- [258] Medyanik SN, Liu WK, Li S. On criteria for dynamic adiabatic shear band propagation. *J Mech Phys Solids* 2007;55:1439–61.
- [259] Landau P, Osovski S, Venkert A, Gärtnerová V, Rittel D. The genesis of adiabatic shear bands. *Sci Rep* 2016;6:37226.
- [260] Rittel D. A different viewpoint on adiabatic shear localization. *J Phys D: Appl Phys* 2009;42:214009.
- [261] Longère P. Respective/combined roles of thermal softening and dynamic recrystallization in adiabatic shear banding initiation. *Mech Mater* 2018;117:81–90.
- [262] Needleman A, Tvergaard V. Analysis of a brittle-ductile transition under dynamic shear loading. *Int J Solids Struct* 1995;32:2571–90.
- [263] Cowie JG, Azrin M, Olson GB. Microvoid formation during shear deformation of ultrahigh strength steels. *Metall Trans A* 1989;20:143–53.
- [264] Kudryashov N, Ryabov P, Zakharchenko A. Self-organization of adiabatic shear bands in OFHC copper and HY-100 steel. *J Mech Phys Solids* 2015;76:180–92.
- [265] Zhang Z, Eakins DE, Dunne FP. On the formation of adiabatic shear bands in textured HCP polycrystals. *Int J Plast* 2016;79:196–216.
- [266] Teng X, Wierzbicki T, Couque H. On the transition from adiabatic shear banding to fracture. *Mech Mater* 2007;39:107–25.
- [267] Carslaw HS, Jaeger JC. *Conduction of heat in solids*. 2nd ed. Oxford: Clarendon Press; 1959.
- [268] Dodd B, Bai Y. Width of adiabatic shear bands formed under combined stresses. *Mater Sci Technol* 1989;5:557–9.
- [269] Bai YL, Cheng CM, Yu SB. On evolution of thermo-plastic shear band. *Acta Mech Sin* 1986;2:1.
- [270] Dinzart F, Molinari A. Structure of adiabatic shear bands in thermo-viscoplastic materials. *Eur J Mech A* 1998;17:923–38.
- [271] Wright TW, Ockendon H. A model for fully formed shear bands. *J Mech Phys Solids* 1992;40:1217–26.
- [272] Grady DE. Properties of an adiabatic shear-band process zone. *J Mech Phys Solids* 1992;40:1197–215.
- [273] Batra RC, Zhang X. On the propagation of a shear band in a steel tube. *J Eng Mater Technol* 1994;116:155–61.
- [274] Gioia G, Ortiz M. The two-dimensional structure of dynamic boundary layers and shear bands in thermoviscoplastic solids. *J Mech Phys Solids* 1996;44:251–92.
- [275] Mercier S, Molinari A. Steady-State shear band propagation under dynamic conditions. *J Mech Phys Solids* 1998;46:1463–95.
- [276] Bonnet-Lebouvier AS, Molinari A, Lipinski P. Analysis of the dynamic propagation of adiabatic shear bands. *Int J Solids Struct* 2002;39:4249–69.
- [277] Yiadom SB, Khan AK, Bassim N. Effect of microstructure on the nucleation and initiation of adiabatic shear bands (ASBs) during impact. *Mater Sci Eng A* 2014;615:373–94.
- [278] Batra R, Zhu Z. Dynamic adiabatic shear band development in a bimetallic body containing a void. *Int J Solids Struct* 1991;27:1829–54.
- [279] Batra R, Adulla C, Wright T. Effect of defect shape and size on the initiation of adiabatic shear bands. *Acta Mech* 1996;116:239–43.
- [280] Meyer L, Staskewitsch E, Burlibies A. Adiabatic shear failure under biaxial dynamic compression/shear loading. *Mech Mater* 1994;17:203–14.
- [281] Rittel D, Landau P, Venkert A. Dynamic recrystallization as a potential cause for adiabatic shear failure. *Phys Rev Lett* 2008;101:165501.
- [282] Molinari A, Leroy YM. Structures in shear zones due to thermal effects. *Mech Solids* 1991;313:7–13.
- [283] Dai LH, Liu LF, Bai YL. Formation of adiabatic shear band in metal matrix composites. *Int J Solids Struct* 2004;41:5979–93.
- [284] Liu LF, Dai LH, Yang GW. Strain gradient effects on deformation strengthening behavior of particle reinforced metal matrix composites. *Mater Sci Eng A* 2003;345:190–6.
- [285] Lee S, Cho KM, Kim KC, Choi WB. Adiabatic shear band formation in Al-SiC w composites. *Metall Trans A* 1993;24:895–900.
- [286] Owolabi GM, Odeshi AG, Singh MNK, Bassim MN. Dynamic shear band formation in Aluminum 6061–T6 and Aluminum 6061–T6/Al₂O₃ composites. *Mater Sci Eng A* 2007;457:114–9.

- [287] Dai LH, Liu LF, Bai YL. Effect of particle size on the formation of adiabatic shear band in particle reinforced metal matrix composites. *Mater Lett* 2004;58:1773–6.
- [288] Xu X, Ling Z, Wu X, Bai Y. Evolution of thermoplastic shear localization and related microstructures in Al₇/SiCp composites under dynamic compression. *J Mater Sci Technol* 2002;18:504–8.
- [289] Zhou M. The growth of shear bands in composite microstructures. *Int J Plast* 1998;14:733–54.
- [290] Boakye-Yiadom S, Khan AK, Bassim N. A systematic study of grain refinement during impact of 4340 steel. *Mater Sci Eng A* 2014;605:270–85.
- [291] Dai LH, Ling Z, Bai YL. Size-dependent inelastic behavior of particle-reinforced metal–matrix composites. *Compos Sci Technol* 2001;61:1057–63.
- [292] Backman ME, Finnegan SA. The propagation of adiabatic shear. *Metallurgical Effects at High Strain Rates*; Springer; 1973. p. 531–43.
- [293] Miguélez MH, Soldani X, Molinari A. Analysis of adiabatic shear banding in orthogonal cutting of Ti alloy. *Int J Mech Sci* 2013;75:212–22.
- [294] Lapovok R, Tóth LS, Molinari A, Estrin Y. Strain localisation patterns under equal-channel angular pressing. *J Mech Phys Solids* 2009;57:122–36.
- [295] Welsh N. Frictional heating and its influence on the wear of steel. *J Appl Phys* 1957;28:960–8.
- [296] Cho K, Chi Y, Duffy J. Microscopic observations of adiabatic shear bands in three different steels. *Metall Trans A* 1990;21:1161–75.
- [297] Zurek AK. The study of adiabatic shear band instability in a pearlitic 4340 steel using a dynamic punch test. *Metall Mater Trans A* 1994;25:2483–9.
- [298] Grebe HA, Pak H-R, Meyers MA. Adiabatic shear localization in titanium and Ti-6 pct Al-4 pct V alloy. *Metall Trans A* 1985;16:761–75.
- [299] Timothy S, Hutchings I. Initiation and growth of microfractures along adiabatic shear bands in Ti-6Al-4V. *Mater Sci Technol* 1985;1:526–30.
- [300] Liao SC, Duffy J. Adiabatic shear bands in a Ti-6Al-4V titanium alloy. *J Mech Phys Solids* 1998;46:2201–31.
- [301] Wei Q, Pan ZL, Wu XL, Schuster BE, Kecskes LJ, Valiev RZ. Microstructure and mechanical properties at different length scales and strain rates of nanocrystalline tantalum produced by high-pressure torsion. *Acta Mater* 2011;59:2423–36.
- [302] Dorogoy A, Rittel D. Dynamic large strain characterization of tantalum using shear-compression and shear-tension testing. *Mech Mater* 2017;112:143–53.
- [303] Zhang X, Cui J, Xu J, Li G. Microstructure investigations on 2A10 aluminum alloy bars subjected to electromagnetic impact upsetting. *Mater Sci Eng A* 2017;702:142–52.
- [304] Kim H, Lee JH, Lee C, Bang W, Ahn S, Chang Y. Shear band formation during hot compression of AZ31 Mg alloy sheets. *Mater Sci Eng A* 2012;558:431–8.
- [305] Wang B, Sun J, Wang X, Fu A. Adiabatic shear localization in a near beta Ti-5Al-5Mo-5 V-1Cr-1Fe alloy. *Mater Sci Eng A* 2015;639:526–33.
- [306] Chichili DR, Ramesh K, Hemker KJ. Adiabatic shear localization in α -titanium: experiments, modeling and microstructural evolution. *J Mech Phys Solids* 2004;52:1889–909.
- [307] Li D, Yang Y, Xu T, Zheng H, Zhu Q, Zhang Q. Observation of the microstructure in the adiabatic shear band of 7075 aluminum alloy. *Mater Sci Eng A* 2010;527:3529–35.
- [308] Trent EM. The formation and properties of Martensite on the surface of rope wire: Reprint from the Journal. *J Iron Steel Inst* 1941;1.
- [309] Wittman C, Meyers MA, Pak H-R. Observation of an adiabatic shear band in AISI 4340 steel by high-voltage transmission electron microscopy. *Metall Trans A* 1990;21:707–16.
- [310] Derep J. Microstructure transformation induced by adiabatic shearing in armour steel. *Acta Metall* 1987;35:1245–9.
- [311] Wang B, Wang X, Li Z, Ma R, Zhao S, Xie F, et al. Shear localization and microstructure in coarse grained beta titanium alloy. *Mater Sci Eng A* 2016;652:287–95.
- [312] Edwards NJ, Song W, Cimpoeru SJ, Ruan D, Lu G, Herzog N. Mechanical and microstructural properties of 2024-T351 aluminium using a hat-shaped specimen at high strain rates. *Mater Sci Eng A* 2018;720:203–13.
- [313] Yang Y, Wang Z, Jiang L. Evolution of precipitates in ZK60 magnesium alloy during high strain rate deformation. *J Alloy Compd* 2017;705:566–71.
- [314] Yang Y, Jiang L. Effect of heat treatment on adiabatic shear susceptibility in ZK60 magnesium alloy. *Mater Sci Eng A* 2016;664:146–54.
- [315] Zou D, Zhen L, Zhu Y, Xu C, Shao W, Pang B. Deformed microstructure evolution in AM60B Mg alloy under hypervelocity impact at a velocity of 5 km s⁻¹. *Mater Des* 2010;31:3708–15.
- [316] Rogers H. The tensile fracture of ductile metals. *Metal Society AIME* 1960;218:498–506.
- [317] Zhen L, Zou D, Xu C, Shao W. Microstructure evolution of adiabatic shear bands in AM60B magnesium alloy under ballistic impact. *Mater Sci Eng A* 2010;527:5728–33.
- [318] Rittel D, Ravichandran G, Venkert A. The mechanical response of pure iron at high strain rates under dominant shear. *Mater Sci Eng A* 2006;432:191–201.
- [319] Yuan F, Jiang P, Wu X. Annealing effect on the evolution of adiabatic shear band under dynamic shear loading in ultra-fine-grained iron. *Int J Impact Eng* 2012;50:1–8.
- [320] Xing J, Yuan F, Wu X. Enhanced quasi-static and dynamic shear properties by heterogeneous gradient and lamella structures in 301 stainless steels. *Mater Sci Eng A* 2017;680:305–16.
- [321] Lesuer D, Syn C, Sherby O. Severe plastic deformation through adiabatic shear banding in Fe–C steels. *Mater Sci Eng A* 2005;410:222–5.
- [322] Boakye-Yiadom S, Bassim N. Microstructural evolution of adiabatic shear bands in pure copper during impact at high strain rates. *Mater Sci Eng A* 2018;711:182–94.
- [323] Duan CZ, Wang MJ. Characteristics of adiabatic shear bands in the orthogonal, cutting of 30CrNi₃MoV steel. *J Mater Process Technol* 2005;168:102–6.
- [324] Wang P, Kumar KS. Dynamic deformation response of a high-strength, high-toughness Fe–10Ni–0.1C steel. *Mater Sci Eng A* 2009;519:184–97.
- [325] Li J, Yang H, Yang P. Prolonged work hardening range in high manganese TRIP steel during adiabatic shear band formation. *Mater Lett* 2014;134:180–3.
- [326] Meyers MA, Pak HR. Observation of an adiabatic shear band in titanium by high-voltage transmission electron microscopy. *Acta Metall* 1986;34:2493–9.
- [327] Xue Q, Meyers MA, Nesterenko V. Self-organization of shear bands in titanium and Ti-6Al-4V alloy. *Acta Mater* 2002;50:575–96.
- [328] Padilla H, Lambros J, Beaudoin A, Robertson I. Relating inhomogeneous deformation to local texture in zirconium through grain-scale digital image correlation strain mapping experiments. *Int J Solids Struct* 2012;49:18–31.
- [329] Zou DL, Luan BF, Liu Q, Chai LJ, Chen JW. Characterization of adiabatic shear bands in the zirconium alloy impacted by split Hopkinson pressure bar at a strain rate of 6000 s⁻¹. *Mater Sci Eng A* 2012;558:517–24.
- [330] Tang L, Chen ZY, Zhan CK, Yang XY, Liu CM, Cai HN. Microstructural evolution in adiabatic shear bands of copper at high strain rates: Electron backscatter diffraction characterization. *Mater Charact* 2012;64:21–6.
- [331] Jiang L, Yang Y, Wang Z, Hu H. Microstructure evolution within adiabatic shear band in peak aged ZK60 magnesium alloy. *Mater Sci Eng A* 2018;711:317–24.
- [332] Wei Q. Strain rate effects in the ultrafine grain and nanocrystalline regimes—influence on some constitutive responses. *J Mater Sci* 2007;42:1709–27.
- [333] Wright WJ, Saha R, Nix WD. Deformation mechanisms of the Zr₄₀Ti₁₄Ni₁₀Cu₁₂Be₂₄ bulk metallic glass. *Mater Trans* 2001;42:642–9.
- [334] Johnson GR, Hoegfeldt JM, Lindholm US, Nagy A. Response of various metals to large torsional strains over a large range of strain rates—part 1: Ductile metals. *J Eng Mater Technol, Trans ASME* 1983;105:42–7.
- [335] Dalla Torre FH, Dubach A, Schallibaum J, Löffler JF. Shear striations and deformation kinetics in highly deformed Zr-based bulk metallic glasses. *Acta Mater* 2008;56:4635–46.
- [336] Meyers MA, LaSalvia J, Nesterenko VF, Chen Y, Kad B. Dynamic recrystallization in high strain rate deformation. In: McNelley T, editor. *Recrystallization and related phenomena*. Monterey: publisher; 1997.
- [337] Beatty H, Meyer L, Meyers MA, Nemat-Nasser S. Formation of Controlled Adiabatic Shear Bands in AISI 4340 High Strength Steel. U.S. Army Materials Technology Laboratory, MTL TR; 1990. p. 90–54.
- [338] Yao J, Suo T, Zhang S, Zhao F, Wang H, Liu J, et al. Influence of heat-treatment on the dynamic behavior of 3D laser-deposited Ti-6Al-4V alloy. *Mater Sci Eng A* 2016;677:153–62.
- [339] Ulacia I, Dudamell N, Gálvez F, Yi S, Pérez-Prado M, Hurtado I. Mechanical behavior and microstructural evolution of a Mg AZ31 sheet at dynamic strain rates. *Acta Mater* 2010;58:2988–98.
- [340] Shahan AR, Taheri AK. Adiabatic shear bands in titanium and titanium alloys: a critical review. *Mater Des* 1993;14:243–50.
- [341] Toth L, Hildenbrand A, Molinari A. Dynamic recrystallisation in adiabatic shear bands. *Le. J Phys IV* 2000. Pr9-365.

- [342] Yang H, Zhang J, Xu Y, Meyers MA. Microstructural Characterization of the Shear Bands in Fe-Cr-Ni Single Crystal by EBSD. *J Mater Sci Technol* 2008;24:819–28.
- [343] Wang B, Liu Z, Wang X, Li Z. An EBSD investigation on deformation-induced shear bands in a low nickel austenitic stainless steel under controlled shock-loading conditions. *Mater Sci Eng A* 2014;610:301–8.
- [344] Yang Y, Jiang L, Luo S, Hu H, Tang T, Zhang Q. Effect of Strain on Microstructure Evolution of 1Cr18Ni9Ti Stainless Steel During Adiabatic Shearing. *J Mater Eng Perform* 2016;25:29–37.
- [345] Hildenbrand A, Tóth LS, Molinari A, Baczynski J, Jonas JJ. Self-consistent polycrystal modelling of dynamic recrystallization during the shear deformation of a Ti IF steel. *Acta Mater* 1999;47:447–60.
- [346] Li Z, Zhao S, Alotaibi SM, Liu Y, Wang B, Meyers MA. Adiabatic shear localization in the CrMnFeCoNi high-entropy alloy. *Acta Mater* 2018;151:424–31.
- [347] Gludovatz B, Hohenwarter A, Thurston KVS, Bei H, Wu Z, George EP, et al. Exceptional damage-tolerance of a medium-entropy alloy CrCoNi at cryogenic temperatures. *Nat Commun* 2016;7:10602.
- [348] Ma Y, Yuan F, Yang M, Jiang P, Ma E, Wu X. Dynamic shear deformation of a CrCoNi medium-entropy alloy with heterogeneous grain structures. *Acta Mater* 2018;148:407–18.
- [349] Li J, Li Y, Huang C, Suo T. Mechanical responses and dynamic failure of nanostructure Cu–Al alloys under uniaxial compression. *Mech Mater* 2017;114:147–60.
- [350] Li J, Li Y, Huang C, Suo T, Wei Q. On adiabatic shear localization in nanostructured face-centered cubic alloys with different stacking fault energies. *Acta Mater* 2017;141:163–82.
- [351] Zhang Y, Greer AL. Thickness of shear bands in metallic glasses. *Appl Phys Lett* 2006;89:071907.
- [352] Leamy HJ, Wang TT, Chen HS. Plastic flow and fracture of metallic glass. *Metall Mater Trans B* 1972;3:699.
- [353] Spaepen F. A microscopic mechanism for steady state inhomogeneous flow in metallic glasses. *Acta Metall* 1977;25:407–15.
- [354] Georgarakis K, Aljerf M, Li Y, LeMoulec A, Charlot F, Yavari AR, et al. Shear band melting and serrated flow in metallic glasses. *Appl Phys Lett* 2008;93:031907.
- [355] Lewandowski J, Greer A. Temperature rise at shear bands in metallic glasses. *Nat Mater* 2006;5:15.
- [356] Dai LH, Yan M, Liu LF, Bai YL. Adiabatic shear banding instability in bulk metallic glasses. *Appl Phys Lett* 2005;87:3.
- [357] Jiang MQ, Dai LH. On the origin of shear banding instability in metallic glasses. *J Mech Phys Solids* 2009;57:1267–92.
- [358] Jiang MQ, Dai LH. Shear-band toughness of bulk metallic glasses. *Acta Mater* 2011;59:4525–37.
- [359] Chen Y, Jiang MQ, Dai LH. Collective evolution dynamics of multiple shear bands in bulk metallic glasses. *Int J Plast* 2013;50:18–36.
- [360] Jiang MQ, Wang WH, Dai LH. Prediction of shear-band thickness in metallic glasses. *Scr Mater* 2009;60:1004–7.
- [361] Wright WJ, Schwarz RB, Nix WD. Localized heating during serrated plastic flow in bulk metallic glasses. *Mater Sci Eng A* 2001;319:229–32.
- [362] Zhang Z, Eckert J, Schultz L. Difference in compressive and tensile fracture mechanisms of Zr₅₉Cu₂₀Al₁₀Ni₈Ti₃ bulk metallic glass. *Acta Mater* 2003;51:1167–79.
- [363] Qu RT, Liu ZQ, Wang G, Zhang ZF. Progressive shear band propagation in metallic glasses under compression. *Acta Mater* 2015;91:19–33.
- [364] Qu R, Eckert J, Zhang Z. Tensile fracture criterion of metallic glass. *J Appl Phys* 2011;109:083544.
- [365] Mukai T, Nieh TG, Kawamura Y, Inoue A, Higashi K. Effect of strain rate on compressive behavior of a Pd₄₀Ni₄₀P₂₀ bulk metallic glass. *Intermetallics* 2002;10:1071–7.
- [366] Zhang Z, Eckert J. Unified tensile fracture criterion. *Phys Rev Lett* 2005;94:094301.
- [367] Spaepen F. Metallic glasses: Must shear bands be hot? *Nat Mater* 2006;5:7.
- [368] Argon A. Plastic deformation in metallic glasses. *Acta Metall* 1979;27:47–58.
- [369] Langer JS. Microstructural shear localization in plastic deformation of amorphous solids. *Phys Rev E* 2001;64:011504.
- [370] Langer JS. Shear-transformation-zone theory of deformation in metallic glasses. *Scr Mater* 2006;54:375–9.
- [371] Jiang MQ, Ling Z, Meng JX, Dai LH. Energy dissipation in fracture of bulk metallic glasses via inherent competition between local softening and quasi-cleavage. *Phil Mag* 2008;88:407–26.
- [372] Wang G, Chan KC, Xu XH, Wang WH. Instability of crack propagation in brittle bulk metallic glass. *Acta Mater* 2008;56:5845–60.
- [373] Raghavan R, Murali P, Ramamurthy U. On factors influencing the ductile-to-brittle transition in a bulk metallic glass. *Acta Mater* 2009;57:3332–40.
- [374] Jiang W, Atzmon M. The effect of compression and tension on shear-band structure and nanocrystallization in amorphous Al₉₀Fe₅Gd₅: a high-resolution transmission electron microscopy study. *Acta Mater* 2003;51:4095–105.
- [375] Zhao S, Kad B, Hahn E, Chen L, Opachi Y, More K, et al. Shock-induced Amorphization in Covalently Bonded Solids. *EPJ Web Conference* 2018;183:03027.
- [376] Li N, Wang Y, Peng RL, Sun X, Liaw PK, Wu G, et al. Localized amorphism after high-strain-rate deformation in TWIP steel. *Acta Mater* 2011;59:6369–77.
- [377] Zhao S, Hahn EN, Kad B, Remington BA, Wehrenberg CE, Bringa EM, et al. Amorphization and nanocrystallization of silicon under shock compression. *Acta Mater* 2016;103:519–33.
- [378] Zhu D, Zheng Z, Chen Q. Adiabatic shear failure of aluminum matrix composites and microstructural characteristics of transformed bands. *Mater Sci Eng A* 2014;595:241–6.
- [379] Grady DE. Shock deformation of brittle solids. *J Geophys Res Solid Earth* 1980;85:913–24.
- [380] Grady DE, Lipkin J. Criteria for impulsive rock fracture. *Geophys Res Lett* 1980;7:255–8.
- [381] Rodríguez-Martínez JA, Vadillo G, Fernández-Sáez J, Molinari A. Identification of the critical wavelength responsible for the fragmentation of ductile rings expanding at very high strain rates. *J Mech Phys Solids* 2013;61:1357–76.
- [382] Xue Q, Meyers MA, Nesterenko V. Self organization of shear bands in stainless steel. *Mater Sci Eng A* 2004;384:35–46.
- [383] Liu M, Li Y, Hu H, Hu X. A numerical model for adiabatic shear bands with application to a thick-walled cylinder in 304 stainless steel. *Modell Simul Mater Sci Eng* 2014;22:5005.
- [384] Cottrell AH, Bilby B. Dislocation theory of yielding and strain ageing of iron. *Proceedings of the Physical Society A* 1949;62:49.
- [385] Morris J. Dynamic strain aging in aluminum alloys. *Mater Sci Eng* 1974;13:101–8.
- [386] Mulford RA, Kocks UF. New observations on the mechanisms of dynamic strain aging and of jerky flow. *Acta Metall* 1979;27:1125–34.
- [387] Kocks UF, Cook RE, Mulford RA. Strain aging and strain hardening in Ni-C alloys. *Acta Metall* 1985;33:623–38.
- [388] Cheng J, Nemat-Nasser S. A model for experimentally-observed high-strain-rate dynamic strain aging in titanium. *Acta Mater* 2000;48:3131–44.
- [389] Garde A, Santhanam A, Reed-Hill R. The significance of dynamic strain aging in titanium. *Acta Metall* 1972;20:215–20.
- [390] Yang R, Zhang H, Shen L, Xu Y, Bai Y, Dodd B. A modified split Hopkinson torsional bar system for correlated study of τ - γ relations, shear localization and microstructural evolution. *Philosophical Transactions A* 2014;372:20130208.
- [391] Zhang Y, Zuo TT, Tang Z, Gao MC, Dahmen KA, Liaw PK, et al. Microstructures and properties of high-entropy alloys. *Prog Mater Sci* 2014;61:1–93.
- [392] Cottrell Alan H, Jaswon MA, Mott Nevill F. Distribution of solute atoms round a slow dislocation. *Proceedings of the Royal Society A* 1949;199:104–14.
- [393] Ham RK, Jaffrey D. Dislocation multiplication, vacancy accumulation, and the onset of jerky flow during forward and reverse 1 strain in Cu-3.2 at. % Sn. *Phil Mag* 1967;15:247–56.
- [394] Hähner P. On the physics of the Portevin-Le Châtelier effect part 1: The statistics of dynamic strain ageing. *Mater Sci Eng A* 1996;207:208–15.
- [395] Hähner P. On the physics of the Portevin-Le Châtelier effect part 2: from microscopic to macroscopic behaviour. *Mater Sci Eng A* 1996;207:216–23.
- [396] Gilat A, Wu X. Plastic deformation of 1020 steel over a wide range of strain rates and temperatures. *Int J Plast* 1997;13:611–32.
- [397] Zhao S, Meng C, Mao F, Hu W, Gottstein G. Influence of severe plastic deformation on dynamic strain aging of ultrafine grained Al–Mg alloys. *Acta Mater* 2014;76:54–67.
- [398] Lopes FPD, Lu CH, Zhao S, Monteiro SN, Meyers MA. Room Temperature Dynamic Strain Aging in Ultrafine-Grained Titanium. *Metall Mater Trans A* 2015;46:4468–77.
- [399] Bridgman PW. Effects of High Shearing Stress Combined with High Hydrostatic Pressure. *Phys Rev* 1935;48:825.

- [400] Vereshchagin LF, Zubova EV, Burdina KP. Dense modifications of germanium and silicon produced under the simultaneous action of high pressure and shear. *Doklady Akademii Nauk SSSR* 1966;168:314.
- [401] Teller E. On the speed of reactions at high pressures. *J Chem Phys* 1962;36:901–3.
- [402] Enikolopyan N, Vol'eva V, Khzardzhyan A, Ershov V. Explosive chemical reactions in solids. *Dokl Phys Chem* 1987;292:1.
- [403] Thadhani NN. Shock-induced chemical reactions and synthesis of materials. *Prog Mater Sci* 1993;37:117–226.
- [404] Gourdin WH. Dynamic consolidation of metal powders. *Prog Mater Sci* 1986;30:39–80.
- [405] Meyers MA, Thadhani N, Chang S. Martensitic transformation induced by tensile stress pulses. *Le Journal de Physique Colloques* 1988;49:355–62.
- [406] Meyers MA. An estimate of the nucleation time in the martensitic transformation. *Metall Trans A* 1979;10:1723–7.
- [407] DeCarli PS, Jamieson JC. Formation of diamond by explosive shock. *Science* 1961;133:1821.
- [408] Duvall GE, Graham RA. Phase transitions under shock-wave loading. *Rev Mod Phys* 1977;49:523.
- [409] Ryabinin YN. About Some Experiences for Dynamic Compacting of Substances. *Technical Physics Review* 1956;26:2661–6.
- [410] Dremin AN, Breusov ON. Processes occurring in solids under the action of powerful shock waves. *Russ Chem Rev* 1968;37:392.
- [411] Nesterenko VF, Meyers MA, Chen HC, LaSalvia JC. The structure of controlled shear bands in dynamically deformed reactive mixtures. *Metall Mater Trans A* 1995;26:2511–9.
- [412] Thadhani NN, Graham RA, Royal T, Dunbar E, Anderson MU, Holman GT. Shock-induced chemical reactions in titanium–silicon powder mixtures of different morphologies: Time-resolved pressure measurements and materials analysis. *J Appl Phys* 1997;82:1113–28.
- [413] Eakins D, Thadhani NN. Shock compression of reactive powder mixtures. *Int Mater Rev* 2009;54:181–213.
- [414] Bennett LS, Sorrell FY, Simonsen IK, Horie Y, Iyer KR. Ultrafast chemical reactions between nickel and aluminum powders during shock loading. *Appl Phys Lett* 1992;61:520–1.
- [415] Vecchio KS, Yu L-H, Meyers MA. Shock synthesis of silicides—I. experimentation and microstructural evolution. *Acta Metall Mater* 1994;42:701–14.
- [416] Mang C, Kontny A, Fritz J, Schneider R. Shock experiments up to 30 GPa and their consequences on microstructures and magnetic properties in pyrrhotite. *Geochim Geophys Geosyst* 2013;14:64–85.
- [417] Meyers MA, Batsanov SS, Gavrillkin SM, Chen HC, LaSalvia JC, Marquis FDS. Effect of shock pressure and plastic strain on chemical reactions in Nb-Si and Mo-Si systems. *Mater Sci Eng A* 1995;201:150–8.
- [418] Meyers MA, Yu LH, Vecchio KS. Shock synthesis of silicides—II. Thermodynamics and kinetics. *Acta Metall Mater* 1994;42:715–29.
- [419] Dunbar E, Thadhani NN, Graham RA. High-pressure shock activation and mixing of nickel-aluminum powder mixtures. *J Mater Sci* 1993;28:2903–14.
- [420] Thadhani NN, Work S, Graham RA, Hammett WF. Shock-induced reaction synthesis (SRS) of nickel aluminides. *J Mater Res* 1992;7:1063.
- [421] Namjoshi SA, Thadhani NN. Modeling the reaction synthesis of shock-densified titanium-silicon powder mixture compacts. *Metall Mater Trans B* 2000;31:307–16.
- [422] Xu X, Thadhani NN. Investigation of shock-induced reaction behavior of as-blended and ball-milled Ni+Ti powder mixtures using time-resolved stress measurements. *J Appl Phys* 2004;96:2000–9.
- [423] Nesterenko VF, Meyers MA, Chen HC, LaSalvia JC. Controlled high-rate localized shear in porous reactive media. *Appl Phys Lett* 1994;65:3069–71.
- [424] Zhao S, Kad B, Wehrenberg CE, Remington BA, Hahn EN, More KL, et al. Generating gradient germanium nanostructures by shock-induced amorphization and crystallization. *Proc Natl Acad Sci* 2017;114:9791–6.
- [425] Zhao S, Kad B, Remington BA, LaSalvia JC, Wehrenberg CE, Behler KD, et al. Directional amorphization of boron carbide subjected to laser shock compression. *Proc Natl Acad Sci* 2016;113:12088–93.
- [426] Bryant AW, Scripka D, Alamgir FM, Thadhani NN. Laser shock compression induced crystallization of Ce₃Al metallic glass. *J Appl Phys* 2018;124:035904.
- [427] Shang SS, Hokamoto K, Meyers MA. Hot dynamic consolidation of hard ceramics. *J Mater Sci* 1992;27:5470–6.
- [428] Kurita T, Matsumoto H, Sakamoto K, Shimada T, Osada T, Ojima K, et al. Effects of shock compression on powder mixtures of nickel and boron. *J Alloy Compd* 2005;396:133–8.
- [429] Krueger BR, Mutz Jr AH. TV. Correlation of shock initiated and thermally initiated chemical reactions in a 1:1 atomic ratio nickel-silicon mixture. *J Appl Phys* 1991;70:5362–8.
- [430] Reeves RV, Mukasyan AS, Son SF. Transition from Impact-induced Thermal Runaway to Prompt Mechanochemical Explosion in Nanoscaled Ni/Al Reactive Systems. *Propellants Explos Pyrotech* 2013;38:611–21.
- [431] Meyers MA, Murr LE, Staudhammer KP. international conference on shock-wave and high-strain-rate phenomena in materials. *EXPLOMET* 90.1992..
- [432] Tungatt PD, Humphreys FJ. An in-situ optical investigation of the deformation behaviour of sodium nitrate — an analogue for calcite. *Tectonophysics* 1981;78:661–75.
- [433] Derby B. The dependence of grain size on stress during dynamic recrystallisation. *Acta Metall Mater* 1991;39:955–62.
- [434] Hines J, Vecchio K. Recrystallization kinetics within adiabatic shear bands. *Acta Mater* 1997;45:635–49.
- [435] Hu H, Rath BB. On the time exponent in isothermal grain growth. *Metallurgical Transactions* 1970;1:3181–4.
- [436] Hu H, Rath BB. Influence of Solutes on the Mobility of Tilt Boundaries. In: Hu H, editor. *The Nature and Behavior of Grain Boundaries: A Symposium held at the TMS-AIME Fall Meeting in Detroit, Michigan, October 18–19, 1971*. Springer, US: New York, NY; 1972. p. 405–35.
- [437] Yang H, Xu Y, Seki Y, Nesterenko VF, Meyers MA. Analysis and characterization by electron backscatter diffraction of microstructural evolution in the adiabatic shear bands in Fe–Cr–Ni alloys. *J Mater Res* 2009;24:2617–27.
- [438] Humphreys FJ, Hatherly M. *Recrystallization and related annealing phenomena*. Elsevier 2012.
- [439] Hirth J, Lothe J. *Theory of Dislocations*. Materials Science and Engineering: McGraw-Hill; 1968.
- [440] Derby B, Ashby MF. On dynamic recrystallisation. *Scr Metall* 1987;21:879–84.
- [441] Mishra A, Kad BK, Gregori F, Meyers MA. Microstructural evolution in copper subjected to severe plastic deformation: Experiments and analysis. *Acta Mater* 2007;55:13–28.
- [442] Frost HJ, Ashby MF. *Deformation mechanism maps: the plasticity and creep of metals and ceramics*. Pergamon press; 1982.
- [443] Li Y, Zhang Y, Tao N, Lu K. Effect of the Zener-Hollomon parameter on the microstructures and mechanical properties of Cu subjected to plastic deformation. *Acta Mater* 2009;57:761–72.
- [444] Hines JA, Vecchio KS, Ahzi S. A model for microstructure evolution in adiabatic shear bands. *Metall Mater Trans A* 1998;29:191–203.
- [445] Lieou KKC, Bronkhorst CA. Dynamic recrystallization in adiabatic shear banding: Effective-temperature model and comparison to experiments in ultrafine-grained titanium. *Int J Plast* 2018;111:107–21.
- [446] Hua P, Chu K, Sun Q. Grain refinement and amorphization in nanocrystalline NiTi micropillars under uniaxial compression. *Scr Mater* 2018;154:123–6.
- [447] Luo H, Sheng H, Zhang H, Wang F, Fan J, Du J, et al. Plasticity without dislocations in a polycrystalline intermetallic. *Nat Commun* 2019;10:3587.
- [448] El Mai S, Mercier S, Petit J, Molinari A. An extension of the linear stability analysis for the prediction of multiple necking during dynamic extension of round bar. *Int J Solids Struct* 2014;51:3491–507.
- [449] Molinari A, Ravichandran G. Constitutive modeling of high-strain-rate deformation in metals based on the evolution of an effective microstructural length. *Mech Mater* 2005;37:737–52.
- [450] Follansbee PS, Kocks UF. A constitutive description of the deformation of copper based on the use of the mechanical threshold stress as an internal state variable. *Acta Metall* 1988;36:81–93.
- [451] Curtin WA, Olmsted DL, Hector LG. A predictive mechanism for dynamic strain ageing in aluminium–magnesium alloys. *Nat Mater* 2006;5:875–80.
- [452] Lindholm US, Johnson GR. Strain-Rate Effects in Metals at Large Shear Strains. In: Mescal J, Weiss V, editors. *Material Behavior Under High Stress and Ultrahigh Loading Rates*. Boston, MA: Springer, US; 1983. p. 61–79.
- [453] Estrin Y, Molinari A, Mercier S. The Role of Rate Effects and of Thermomechanical Coupling in Shear Localization. *J Eng Mater Technol* 1997;119:322–31.
- [454] Lieou KKC, Mourad HM, Bronkhorst CA. Strain localization and dynamic recrystallization in polycrystalline metals: Thermodynamic theory and simulation framework. *Int J Plast* 2019;119:171–87.

- [455] Walley SM. Highways and byways in the history of high rate mechanical testing. *J Dyn Behav Mater* 2020;6:113–58.
- [456] Nieto-Fuentes JC, Osovski S, Venkert A, Rittel D. Reassessment of the Dynamic Thermomechanical Conversion in Metals. *Phys Rev Lett* 2019;123:6.
- [457] Molinari A. Thermoviscoplastic instability in simple shear. *J Theor Appl Mech* 1985;4:659–84.
- [458] Wright TW. On the speed of an unconstrained shear band in a perfectly plastic material. *Int J Solids Struct* 2003;40:871–9.
- [459] Austin RA. Elastic precursor wave decay in shock-compressed aluminum over a wide range of temperature. *J Appl Phys* 2018;123.
- [460] Zheng C, Wang F, Cheng X, Fu K, Liu J, Wang Y, et al. Effect of microstructures on ballistic impact property of Ti–6Al–4V targets. *Mater Sci Eng A* 2014;608:53–62.
- [461] Wang L, Wang Y, Xu X, Liu C. Dynamic behaviour and shock-induced martensite transformation in near-beta Ti-5553 alloy under high strain rate loading. *EPJ Web of Conferences* 2015;94:02026.
- [462] Cheng XW, Wang F, Li S, Yuan S. Research on novel self-sharpen tungsten alloys. *Rare Metal Mater Eng* 2006;35(11):1762.
- [463] Cheng XW, Wang F, Li S, Wang L. Numerical Simulation on the Penetrations of Long-rod Projectiles with Different Nose Shapes. *Acta Arm* 2007;28(8).
- [464] Ali T, Wang L, Cheng XW, Liu A, Xu X. Omega phase formation and deformation mechanism in heat treated Ti-5553 alloy under high strain rate compression. *Mater Lett* 2019;236:163–6.
- [465] Zheng C, Wang F, Cheng XW, Liu J, Liu T, Zhu Z, Yang K, Peng M, Jin D. Capturing of the propagating processes of adiabatic shear band in Ti–6Al–4V alloys under dynamic compression. *Mater Sci Eng A* 2016;658:60–7.



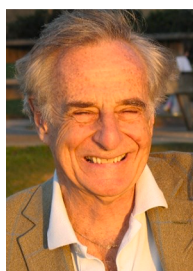
Na Yan holds a Ph. D degree in condensed matter physics from Northwestern Polytechnical University in 2011. Currently, she is a Professor in the School of Physical Science and Technology in Northwestern Polytechnical University. She is a Fellow of MRS-China and an editor of the *Journal of Materials Engineering*. She was a Visiting Scholar at the University of California, San Diego. She co-organized (with Marc André Meyers) the first symposium on dynamic behaviour of materials within PRICM 10, establishing a new area of activity. Her focus is in materials physics. Within this field, she has worked in three areas: 1) Processing of materials; 2) Structural and mechanical properties of materials and 3) Material acoustics. Her most significant contributions are: 1) Relationship between microstructures and mechanical properties in nickel-based alloys; 2) Discovery of dual phase separation events in ternary complex immiscible alloy; 3) A thermodynamic criterion for metastable phase separation in cobalt/copper-based alloys; 4) Design of a novel acoustic levitator with two confronting ultrasonic waves. She has been supported by the National Natural Science Foundation, Shaanxi Industrial Science and Technology Project, Fundamental Research Funds for the Central Universities, and Specialized Research Fund for the Doctoral Program of Higher Education. These research activities have led to the publication of more than 30 peer reviewed papers and Shaanxi Province Science and Technology Award (second-prize, 2019).



Zezhou Li is a graduate (PhD) from the Department of Mechanical and Aerospace Engineering (Materials Science and Engineering program) of the University of California, San Diego. He obtained his Bachelor's degree in Materials Science and Engineering at the University of Science and Technology, Beijing, in 2013, before completing a Master of Science at University of California, San Diego in 2014. His research focuses on the linkage of structure and properties of materials, as well as high strain-rate behaviour, nanocrystalline materials, high-entropy alloys. He has significant expertise in transmission electron microscopy.



Yongbo Xu is Professor, Institute of Metal Research, Chinese Academy of Sciences. He graduated from the Dept. of Physics of Jilin University in 1964, and served as the deputy director of the State Key Laboratory for Fatigue and Fracture of Materials (1989-1997). He was funded by the Chinese State Department (1994-). He visited McMaster University, Canada (1983-1984), University of Virginia, USA (1991-1993), and UCSD as a Visiting Scholar. The principal theme of his research is the relationship of mechanical behaviour to the microstructures for advanced materials, as well as microstructure and fracture behaviour at the crack-tip at atomic level. He is the author or co-author of approximately 200 scientific papers. He has been the recipient of several awards, including National Nature Science Award (second-prize, 1993), Chinese Academy of Sciences Award (second-prize, 1989), State Education Commission (second-prize, 2012), Science and Technology award from China Aviation Society (second-class, 2010), Chinese Academy of Sciences award (third-prize, 1990, 1992, 1993), Liaoning province Science and technology award (third-prize, 1993, 2011). At IMR, he supervised doctoral students of CAS. He served as a member of the Editorial Board for *Acta Metallurgica Sinica* (2009-2014, and 2008-2012), *Scientific Journal of Materials Science* (2007-2009), and the *International Journal of Advanced Materials* (2003-2006).



Marc André Meyers is a Distinguished Professor of Materials Science at the University of California, San Diego. His research is in the field of the mechanical behavior of materials. Within this field, he has focused on three areas: dynamic behavior of materials, nanocrystalline materials, and biological materials. In the dynamic behaviour of materials, the unifying theme is the high rate at which events occur. He initiated this work in 1972 and has dedicated forty-eight uninterrupted years to it, unifying it by emphasizing the fundamental physical and chemical phenomena. This has been defined in his now-classic book, *Dynamic Behavior of Materials* (1994). He is the co-author of *Mechanical Metallurgy*, *Mechanical Behavior of Materials*, *Biological Materials Science* (2014), and approximately 490 papers. His honors include Fellow, TMS, APS, ASM, and Explorers Club as well as awards in the US (APS Duvall, ASM Albert White and Sauveur, TMS Mehl, Cohen, Leadership, and Educator, Acta Materialia Materials and Society, SMD/TMS Distinguished Engineer/Scientist and Service), in Europe (Humboldt, DGM Heyn, DYMAT Rinehart, and Grand Prix en Sciences, Luxembourg), in China (Lee Hsun), and member of the Brazilian and Luxembourg Academies of Sciences. He was co-founder of the Center for Explosives Technology Research, New Mexico Tech, and of the EXPLOMET conference series (1980–2000), as well as Associate Director and Director of the UCSD Institute for Mechanics and Materials, where he co-organized four summer schools. He co-chaired the first three Pan American Materials Conferences, which he co-founded. He also writes fiction.